TOPICS IN QUANTUM DYNAMICS OF SOLID STATE QUBITS

by

Canran Xu

A dissertation submitted in partial fulfillment of the requirements for the degree of

Doctor of Philosophy
(Physics)

at the

University of Wisconsin - Madison 2015

Defended on 7 July, 2015

Dissertation approved by the following members of the Final Oral Committee:

Maxim Vavilov · Associate Professor of Physics

Robert McDermott \cdot Professor of Physics

Robert Joynt \cdot Professor of Physics

Mark Eriksson \cdot Professor of Physics

Irena Knezevic \cdot Professor of Electrical and Computer Engineering

© Copyright Canran Xu2015

Some rights reserved under the Creative Commons BY-NC-SA license. For more information, please refer to http://creativecommons.org/licenses/.

Abstract

This thesis explores several theoretical aspects of quantum information processing. First we examine several questions regarding circuit quantum electrodynamics architecture with a double quantum dot system. We find that there exists a quantum signature in the photovoltaic effects in the current spectrum through the unbiased DQD when the microwave resonator is subject to an AC drive. We demonstrate that this signature is due to the entanglement between the single photon field and the charge states in the DQD. We additionally show that this entanglement is essential to consider the photon statistics, which exhibits both a sub-Poissonian distribution and antibunching. This photon statistics can be measured by the current progress in Josephson photomultipliers.

We then investigate the dynamics of a two-level system with slow varying external parameters and weakly coupled to an Ohmic environment. Specifically, we generalize the Bloch-Redfield approach to time-dependent problems in a perturbative manner, and apply this formalism to two well-suited problems. For a qubit subject to a rotating magnetic field, we demonstrated that the Berry curvature, and hence the Berry phase are immune to quantum fluctuations arising from the environment at zero temperature. For the Landau-Zener problem, on the other hand, it is evident that the incoherent excitation and relaxation processes are leading mechanism.

Next, we consider a Hamiltonian for many-body localization, a generalized example of Anderson localization in interacting quantum many-body systems. Previously literatures stated that for such systems, the eigenstate thermalization hypothesis fails to work. To have a deeper understanding this statement, we apply a local quench to the system and analyze the response of the system. We show that the level spacing statistics and inverse participation ratio both suggest a clear difference between localized and delocalized phase. We further demonstrate that the edges of the localized states can be visualized by the mobility edge via local spin measurements, and by using the same sets of data, the many-body localization length can be evaluated as well.

Lastly, we apply a harmonic drive to the many-body localized Hamiltonian. Benefited

from the Floquet theory, we evaluate the Bures displacement of the system in the Hilbert space caused by the drive for both phases, in which the distinction in the average value of Bures displacement can be revealed for a system with ten spins or so. We also show that from thermodynamics point of view, the two phases can be distinguished by von Neumann entropy, energy fluctuations and spin diffusions.

Acknowledgements

I would never have been able to finish my dissertation without the help and support of countless individuals during my time at UW-Madison.

First and foremost, I would like to express my sincere gratitude for the support and guidance of my advisor, Prof. Maxim Vavilov. I am grateful for his effort and time to helping me understand the relevant research area. His extensive knowledge and experience has been crucial to the progress in my research. I would not have completed my work in a timely manner without his quick response to my questions and proper guidance. I am deeply indebted to him.

I have also received remarkable assistance from Prof. Robert McDermott, who, along with Maxim, offered lots of opportunities for me to understand the practical aspects in superconducting qubits. As an experimentalist, his experience and insights were pivotal to the success of lots of interesting development in the field.

I also would like to thank my collaborators Prof. Frank Wilhem-Mauch, Prof. Britton Plourde, Luke Govia, Dr. Emily Pritchett, for their help and discussions with the project for qubit readout with a JPM, and Dr. Amrit Poudel for the project of nonadiabatic qubit dynamics. I also would like to thank Prof. Vadim Oganesyan and Prof. Hakan Türeci who offered great opportunities for discussions while I was visiting New York and Princeton. I am grateful to Prof. Andrey Chubukov, Prof. Natalia Perkins, Prof. Alex Levchenko, Dr. Clement Wong, Dr. André Saraiva, Dr. Guanyu Zhu, Dr. Ke Wang, who have been always available for help and sharing their valuable knowledge.

I would like to express my appreciation to my thesis committee, Profs. Maxim Vavilov, Robert McDermott, Robert Joynt, Mark Eriksson and Irena Knezevic, for their encouragements and valuable comments. I would also thank Prof. Matthew Herndon for his service in my preliminary exam.

Finally, I wish to thank my families for their love that I have been replying upon. Both educated as theoretical physicists, my parents have a profound impact on my choice of career, and always show a great passion to support me, throughout my entire life.

The work presented in this thesis was supported by the NSF Grant No. DMR-1105178 and DMR-0955500, LPS Grant No. W911NF-11-1-0030 and ARO under contract W911NF-14-1-0080.

I dedicate this thesis to my parents.

Contents

	Abs	tract	i
	Ack	nowledgements	iii
C	onter	nts	vi
Li	${f st}$ of	Figures	x
Li	${f st}$ of	Tables	xxii
1	Intr	roduction	1
	1.1	Introduction to quantum information	1
	1.2	Quantum computing with solid state qubits	4
		Double Quantum Dots	4
		Superconducting qubits	7
		Circuit Quantum Electrodynamics	9
		Adiabatic quantum computation and many-body localization	11
	1.3	Open quantum systems	12
		The Bloch-Redfield master equation	14
		The Lindblad master equation	16
	1.4	Outline of the thesis	17
	1.5	Publication List	20
2	Qua	antum photovoltaic effect in double quantum dots	22
	2.1	Introduction	22

	2.2	$Model \ldots \ldots \ldots \ldots \ldots$	24
	2.3	Results	29
	2.4	Discussion and Conclusion	34
3	Full	Counting Statistics of Photons Emitted by Double Quantum Dot	37
	3.1	Introduction	37
	3.2	Counting Statistics Formalism	39
		Double quantum dot coupled to a resonator	39
		Quantum jump approach	41
		Computation of the Fano factor	43
		Charge full counting statistics	45
	3.3	Ideal Photon Counter	47
	3.4	Adiabatic elimination of photon degrees of freedom	51
	3.5	Photon Counting Statistics Measured By Josephson Photomultipliers	53
	3.6	Conclusions	56
4	Non	adiabatic dynamics of a slowly driven dissipative two-level system	58
	4.1	Introduction	58
	4.2	Bloch–Redfield approach to time-dependent Hamiltonians	61
	4.3	Qubit rotation in a plane	66
		Environment field perpendicular to the rotation plane	69
		Environment field in the rotation plane	73
		Longitudinal coupling to environment	75
		Coupling to a strongly damped Quantum oscillator	76
	4.4	Landau–Zener Transition	78
		Zero temperature dissipative environment	83
		Finite temperatures	85
		Longitudinal coupling	90
		Longitudinal coupling	

		Rotating field	93
		Landau–Zener problem	94
	4.6	Discussion and Conclusions	96
	4.7	appendix	99
		Solution of rate equations for the avoided level crossing	99
		Solution of rate equations for the avoided level crossing for environment with	
		longitudinal coupling	101
5	Res	sponse to a local quench of a system near many body localization	
	trai	nsition	103
	5.1	Introduction	103
	5.2	Level Spacing Statistics of the MBL Hamiltonian	107
	5.3	Level Spacing Statistics of the Quenched Hamiltonian	109
	5.4	Long Time Dynamics of Local Quench	115
	5.5	Summary	122
6	Ma	ny-body localization in a quantum system subject to a local periodic	
	driv	⁄e	12 4
	6.1	Introduction	124
	6.2	Evolution in the Floquet Representation	125
	6.3	Relation between Floquet amplitudes and hopping matrix	128
	6.4	Statistical properties of the hopping matrix	131
	6.5	Thermodynamic characteristics	136
		Time evolution	136
		Energy Fluctuations	137
		Spin Diffusion	138
		Bures distance and inverse partition ratio	140
		Von Neumann entropy	142
	6.6	Summary	1/13

1	V
_ 1	Λ

7	Conclusion	145
Bil	oliography	148

List of Figures

1.1	(a) Micrograph of a DQD device with gate voltages applied to gates L , R and	
	$T.$ Gates L and R are used to adjust the detuning, ε , and gate T sets the	
	coherent interdot tunnel amplitude \mathcal{T} . The conductance g_s of a nearby quantum	
	point contact monitors the occupation of each dot. (b) The transport properties	
	of a DQD that attached two leads are defined by coherent amplitude $\mathcal T$ and	
	incoherent rates $\Gamma_L(R)$. (c) Energy diagram of the DQD qubit, which can be	
	manipulated by a radiative drive with frequency ω	6
1.2	Schematic energy levels of superconducting LC-circuit (a) without a Josephson	
	junction or (b) with a Josephson junction	8
2.1	(a) An illustration of a DQD and a transmission line resonator coupled to an	
	external microwave source μ w. (b) A schematic view of the DQD. Electrons are	
	confined to the left (L) and right (R) dots by barrier gates BL, BM, and BR	
	that also control electron tunneling rates between the source, S, and the left	
	dot, the left and right dots, and the right dot and the drain, D, respectively.	
	Electrostatic energies of two quantum dots are defined by the plunger gates, PL	
	and PR, and the PL gate is also connected to an antinode of the resonator, see	
	e.g. Refs.[29, 31]. (c) Electronic states of the DQD are presented in both the	
	eigenstate basis (solid lines) and the left–right basis (dashed lines). Tunneling	
	from the excited state, $ e\rangle$, to the left/right lead, with rate $\Gamma_{e,L/R}$ and from the	
	left/right lead to the ground state, $ g\rangle$, with rate $\Gamma_{L/R,g}$ are illustrated by arrows.	23

2.2	The average number of photons in the resonator and the photovoltaic current as	
	functions of level bias ε for $\mathcal{T}/2\pi = 1$ GHz, $F = 50~\mu\text{s}^{-1}$ and $\omega_0/2\pi = 8$ GHz.	
	The current is generated near the resonant condition when $\varepsilon = \pm \sqrt{\hbar^2 \omega_0^2 - 4T^2}$	
	(vertical lines). The three curves represent different dephasing rates γ_{ϕ} the DQD.	27
2.3	The average number of photons in the resonator and the photovoltaic current	
	as a function of the frequency ω of the microwave drive for $\mathcal{T}/2\pi=1$ GHz,	
	$F=50~\mu {\rm s}^{-1}$ and $\Omega=\omega_0=2\pi\times 8~{\rm GHz},~g/2\pi=48.5~{\rm MHz}.$ For $\gamma_\phi=0,$ both	
	average number of photons \bar{N} and the photovoltaic current show local minima	
	at $\omega = \omega_0$ and local maxima near $\omega = (E_{1,\pm} - E_0)/\hbar$, shown by vertical lines.	
	As the dephasing rate γ_{ϕ} increases, the double peaks merge to a single peak at	
	$\omega = \omega_0.$	28
2.4	The average number of photons in the resonator and the photovoltaic current	
	as a function of the frequency ω of the microwave drive for detuned DQD and	
	resonator system with $\Omega/2\pi=8.1$ GHz, $\omega_0/2\pi=8.0$ GHz, the intradot tunnel-	
	ing $\mathcal{T}/2\pi=1$ GHz, and the drive amplitude $F=50$ MHz. The photon average	
	number has a peak at $\omega = (E_{1,-} - E_0)/\hbar$, Eq. (2.10), while the photovoltaic	
	current exhibits a double peak feature at $\omega = (E_{1,\pm} - E_0)/\hbar$ (vertical lines)	30
2.5	(a) The average number of photons in the resonator and the photovoltaic current	
	as a function of the frequency ω of the microwave drive for $\Omega = \omega_0 = 2\pi \times 8$ GHz,	
	the intradot tunneling $\mathcal{T}/2\pi=1$ GHz, and the drive amplitude $F/2\pi=30$ MHz	
	and extremely low tunneling rates to the leads and the energy relaxation rate,	
	$\Gamma_l = \Gamma_r = \gamma = 2\pi \times 100$ kHz. The photon average number and the photocurrent	
	have several peaks at $\omega_{n,\pm}=(E_{n,\pm}-E_0)/n\hbar$ with $n=1,2,3,$ these frequencies,	
	calculated from Eq. (2.10) are shown by vertical lines). (b) The histogram	
	presents the probabilities P_n to have n photons in the resonator steady state	
	at drive frequency ω_1 (dark bars) and ω_2 (grey bars). (c) The diagram is a	
	schematic picture for the Jaynes-Cummings energy levels showing single and	
	two photon excitations	33

2.0	Dependence of the average photon number and the current on inicrowave fre-	
	quency ω for several values of the drive amplitude $F/2\pi=5,10,15$ MHz, at	
	zero dephasing $\gamma_{\phi}=0$ and other parameters are the same as in data in Fig-	
	ure 3.3. As the amplitude of the drive increases, the two peaks merge together	
	to a single peak at $\omega = \omega_0$	35
3.1	(a) An illustration of a DQD and a resonator (a $\lambda/2$ -transmission line) coupled	
	to a photon counter (PC). (b) In the DQD, electrons are confined to the left	
	(L) and right (R) dots by barrier gates BL, BM, and BR that also control	
	electron tunneling rates between the source, S, and the left dot, the left and right	
	dots, and the right dot and the drain, D, respectively. Electrostatic energies of	
	two quantum dots are defined by the plunger gates, PL and PR, and the PL	
	gate is also connected to an antinode of the transmutation line. (c) Electronic	
	eigenstates of the DQD and tunneling from the left lead to the ground/excited	
	state with rate $\Gamma_{L,g/e}$, and from the ground/excited state to the right lead with	
	rate $\Gamma_{g/e,R}$	38
3.2	Dependences of (a) the electric current I through the DQD, (b) the average	
	photon number \bar{N} in the resonator, (c) the electron Fano factor $F_{\rm el}$ and (d) the	
	Fano factor $F_{\rm ph}$ for emitted photons are shown as functions of the electrostatic	
	bias $\hbar \varepsilon$ near the resonance at $\varepsilon_0 = -\sqrt{\omega_0^2 - 4T^2}$. Solid (dashed) lines represent	
	the case for $\gamma_r = 0$ ($\gamma_r = 2\Gamma$). Other system parameters are $\Gamma_{l,r} = \Gamma$, $\omega_0 = 800\Gamma$,	
	$\mathcal{T} = 200\Gamma$, $g_0 = 5\Gamma$, $\kappa = 2\Gamma$ and $\gamma_{\phi} = 0$. Dotted line in panel (a) refers to elastic	
	electric current through a non-interacting DQD	45

(a) The second order correlation function $g_{\rm ph}^2(2)(\tau)$ for photons as a function of time τ at resonant condition $\Omega = \omega_0$ for different values of energy, γ_r , and phase, γ_{ϕ} , relaxation rates. (b) The photon Fano factor $F_{\rm ph}$ as a function of relaxation rate γ in three cases $\gamma_r = \gamma_\phi = \gamma$ (solid line), $\gamma_r = \gamma$ and $\gamma_\phi = 0$ (dotted line), $\gamma_{\phi} = \gamma$ and $\gamma_r = 0$ (dashed line). (c) $F_{\rm ph}$ as a function of photon detection rate κ shows a flat behavior for $\kappa \gtrsim \Gamma$. Other system parameters in both panels are $\Gamma_{l,r} = \Gamma$, $\omega_0 = 800\Gamma$, $\mathcal{T} = 200\Gamma$, $g_0 = 5\Gamma$, $\kappa = 2\Gamma$ and $\gamma_{\phi} = 0$ [for (a) and (b)]... 47 Probabilities P_n to have n emitted photons during time t at resonance $\Omega = \omega_0$ for (a) an ideal DQD without decoherence of electronic states, $\gamma_r = \gamma_\phi = 0$ and $t=75/\Gamma;$ (b) a DQD with inelastic relaxation $\gamma_r=2\Gamma,\,\gamma_\phi=0$ and $t=145/\Gamma.$ Other system parameters in both panels are $\Gamma_{l,r} = \Gamma$, $\omega_0 = 800\Gamma$, $\mathcal{T} = 200\Gamma$, $g_0 = 5\Gamma$ and $\kappa = 2\Gamma$. A thin curve in both panels represents the corresponding Poisson distribution $P_n^{(P)} = e^{-\bar{n}} \bar{n}^n / n!$ with $\bar{n} = \sum_n n P_n$ equal to the average number of emitted photons. 48 Dependence of photon noise Fano factor on (a) photon detection rate κ and (b) the bare coupling constant g_0 . In panel (a), the bare coupling constant is fixed $g_0 = 5\Gamma$ and in panel (b) the photon detection rate is fixed $\kappa = 10\Gamma$. Solid (dashed) lines represent results for numerical (analytical) calculations with method described in Sec. 3.2(Sec. 3.4). Other system parameters are $\Gamma_{l,r} = \Gamma$, $\omega_0 = 800\Gamma$, $\mathcal{T} = 200\Gamma$. Both plots indicate that the analytical results agree with 50 Comparison of Fano factor measured by an ideal photon detector and JPM with the same set of parameters of a DQD. Other additional parameters for JPM model are $g_{\rm JPM} = 5\Gamma$, $\omega_{\rm JPM} = \omega_0$, $\kappa_0 = 0.6\Gamma$, $\gamma_{\rm cap} = 1.5\Gamma$ and $\gamma_{\rm t} = 1.5\Gamma$. When we introduce the energy relaxation rate $\gamma_d = 1.5\Gamma$ for the JPM, the resultant 55

3.7	Probabilities P_n to have n JJ recordings during time t at resonance $\Omega = \omega_0$	
	for (a) an ideal DQD without decoherence of electronic states, $\gamma_r = \gamma_\phi = 0$ and	
	$t=132/\Gamma$; (b) a DQD with inelastic relaxation $\gamma_r=2\Gamma,\gamma_\phi=0$ and $t=293.3/\Gamma.$	
	Other system parameters in both panels are $\Gamma_{l,r} = \Gamma$, $\omega_0 = 800\Gamma$, $\mathcal{T} = 200\Gamma$,	
	$g_0 = 5\Gamma$ and $\kappa = 2\Gamma$. A thin curve in both panels represents the corresponding	
	Poisson distribution $P_n^{(P)} = e^{-\bar{n}} \bar{n}^n / n!$ with $\bar{n} = \sum_n n P_n$ equal to the average	
	number of emitted photons.	56
4.1	The Bloch sphere representation of the qubit state in the diabetic basis with	
	$\Omega=0.2\Delta$ and initial condition $z=1$ for (a) $\alpha=0$ and (b) $\alpha=0.02$ at $T=0$.	
	For the dissipationless dynamics the trajectory of the qubit state form cycloids	
	along the equator $y = 0$. However, for the dissipative dynamics the cycloidal	
	trajectory flattens to a circular one with a finite value $m_y(\infty)$	68
4.2	Time dependence of the out-of-plane polarization, $m_y(t)$, at zero temperature of	
	environment for $\alpha=0.02$ (solid line) and $\alpha=0.05$ for fluctuating environment	
	field out of the plane of rotation, $\mathbf{n} = \hat{\mathbf{y}}$. The pure dephasing rate is zero, $J_0 = 0$.	
	The frequency of rotation of the control field is $\Omega = 0.1\Delta$. The thin horizontal	
	line represents the asymptotic values of $m_y(\infty)$	69
4.3	Time dependence of the out-of-plane polarization, $m_y(t)$, at various tempera-	
	tures of environment: $T=0$ (solid line), $T=0.5\Delta$ (dashed line) and $T=\Delta$	
	(dotted line) for fluctuating environment field out of the plane of rotation, $\mathbf{n} = \hat{\mathbf{y}}$.	
	The pure dephasing rate is zero, $J_0 = 0$. The frequency of rotation of the control	
	field is $\Omega = 0.1\Delta$. The coupling to environment $\alpha = 0.05$. The thin horizontal	
	lines represent the asymptotic values of $m_y(\infty)$ at different temperatures	71

environment, for $\alpha = 0.05$ (solid line) and $\alpha = 0.1$ (dashed line) for fluctuating environment field in the plane of rotation, $\mathbf{n} = \hat{\mathbf{z}}$. The pure dephasing rate is	
environment field in the plane of rotation, $\mathbf{n} = \hat{\mathbf{z}}$. The pure dephasing rate is	
zero, $J_0 = 0$. The frequency of rotation of the control field is $\Omega = 0.1\Delta$. The	
relaxation is reduced for time intervals when $\Omega t \simeq \pi n$. The thin horizontal line	
represents the asymptotic values of $m_y(\infty)$	73
4.5 Time dependence of the out-of-plane polarization, $m_y(t)$, for $\alpha = 0.1$ and $T = 0$	
(solid line), $T=0.5\Delta$ (dashed line) and $T=\Delta$ (dotted line) in case when	
fluctuating environment field is in the plane of rotation, $\mathbf{n}=\hat{\mathbf{z}}$. The pure	
dephasing rate is zero, $J_0 = 0$. The frequency of rotation of the control field is	
$\Omega = 0.1\Delta$. The thin horizontal lines represent the asymptotic values of $m_y(\infty)$	
at different temperatures	75
4.6 Time dependence of the out-of-plane polarization, $m_y(t)$, at zero temperature of	
environment for a qubit coupled to a damped harmonic oscillator with damping	
rate $\kappa = 0.2\Delta$ and coupling constant between the qubit and environment $\lambda =$	
0.1 Δ . Coupling vector $\mathbf{n} \parallel \hat{\mathbf{y}}$ (solid line) and $\mathbf{n} \parallel \hat{\mathbf{z}}$ (dash-dotted line). For	
comparison, the solution for the Bloch–Redfield equation is presented (dashed	
line) with $\alpha = 0.03$ and $J_0 = 0$. The rotation angular velocity is $\Omega = 0.1\Delta$. The	
thin horizontal line represents the asymptotic values of $m_y(\infty)$	77
4.7 Time dependence of the out-of-plane polarization, $m_y(t)$, at environment tem-	
per ature $T=0.5\Delta$ for a qubit coupled to a damped harmonic oscillator with	
damping rate $\kappa=0.2\Delta$ and coupling constant between the qubit and environ-	
ment $\lambda = 0.1\Delta$. Coupling vector $\mathbf{n} \parallel \hat{\mathbf{y}}$ (solid line) and $\mathbf{n} \parallel \hat{\mathbf{z}}$ (dash-dotted	
line). For comparison, the solution for the Bloch–Redfield equation is presented	
(dashed line) with $\alpha=0.03$ and $J_0=0$. The rotation angular velocity is	
$\Omega = 0.1\Delta$. The thin horizontal line represents the asymptotic values of $m_y(\infty)$.	78

4.8	Representation of a qubit state during the Landau–Zener process on the Bloch	
	sphere in (a) diabatic basis of states $ \uparrow\rangle$ and $\downarrow\rangle$ along fixed $\hat{\mathbf{z}}$ axis; (b) adiabatic	
	basis of the ground, $ g\rangle$, and excited, $ e\rangle$, states; (c) in the "improved" eigenstate	
	basis, $ g\rangle$ and $ e\rangle$, obtained from the diabetic basis by U_2 transformation. In	
	the diabatic basis the trajectory of qubit state moves across the sphere from	
	state $ \downarrow\rangle$ (ground state at $t\to-\infty$) towards $ \uparrow\rangle$ and slowly approaches the	
	circle of constant precession at $t \to \infty$. The trajectory in the adiabatic basis	
	and eigenstate basis shows a simpler trajectory and fast switch to the constant	
	precession circle. Level-crossing speed $v=0.5\Delta^2$ and no coupling to environment.	79
4.9	projection of a qubit state during the Landau–Zener process on the Bloch sphere	
	on $ \downarrow\rangle$ state in the diabatic basis (dash-dotted line) and on the ground state in	
	the adiabatic basis (solid line) and the "improved" eigenstate basis (dashed line).	
	In the diabatic basis the projection of the qubit state shows long oscillations with	
	amplitude decreasing as a power law in time, while the eigenstate projections	
	quickly reach the asymptotic value. Level-crossing speed $v=0.5\Delta^2$ and no	
	coupling to environment	81
4.10	The probability of occupation of the excited state in the Landau–Zener transition	
	in the U_2 basis. The temperature of environment is zero, $T=0$, the level velocity	
	is $v = 0.5\Delta^2$. We assume that the dephasing is absent, $J_0 = 0$. The asymptotic	
	curve for $E_c = \infty$ is given by Eq. (4.36b) with a proper choice of integration	
	constant C	84
4.11	The probability of occupation of the excited state, $P_e(t)$ in the Landau–Zener	
	transition in the U_2 basis at finite temperature of environment for $v=0.5\Delta^2,$	
	$\alpha = 0.05$ and $J_0 = 0$. The solid lines represent solutions of rate equations (4.41)	
	that show good agreement with the BR equations at higher temperatures	86

4.12	Transition probability P_{∞} as a function of environment temperature T , at dif-	
	ferent values of coupling between the qubit and the environment for $\mathbf{n} \ \hat{\mathbf{z}}$. Level-	
	crossing speed $v=0.5\Delta^2$, the high energy cutoff for the environment is $E_c=10\Delta$	
	and $J_0 = 0$. We take $P_{\infty} = P_e(t = 4E_c/v)$	88
4.13	Transition probability P_{∞} as a function of the coupling parameter of the qubit	
	and the environment, α , at different environment temperatures for $\mathbf{n} \ \hat{\mathbf{z}}$. Level-	
	crossing speed $v=0.5\Delta^2$, the high energy cutoff for the environment is $E_c=10\Delta$	
	and $J_0 = 0$. We take $P_{\infty} = P_e(t = 3E_c/v)$	89
4.14	Transition probability P_{∞} as a function of environment temperature T for $\mathbf{n} \ \hat{\mathbf{b}}$,	
	at different values of drive velocity. The high energy cutoff for the environment	
	is $E_c = 10\Delta$ and $J_0 = 0$. The solid lines represent solutions of rate equations	
	Eq. (4.41). We take $P_{\infty} = P_e(t = 4E_c/v)$	90
4.15	Polarization $m_y(t)$ as a function of time t for dephasing Lindblad evolution.	
	The decoherence rate $\gamma=0.1\Delta$ and rotation velocity $\Omega=0.1\Delta$. After the	
	rotation starts, polarization shows an oscillatory behavior originating from the	
	qubit precession, at longer times the precession stops and the qubit relaxes to	
	unpolarized state according to Eq. (4.52)	94
4.16	Transition probability P_{∞} as a function of daphasing rate γ for different level–	
	crossing speeds $v/\Delta^2=0.1,~0.25,~0.5.$ Solid lines are numerical solution of the	
	Lindblad equation, Eq. (4.50), and dashed lines are given by Eq. (4.53)	95

5.1	Level spacing statistics of the static Hamiltonian for 3 typical values of $W =$	
	$0.3, 4, 30$. Results are obtained with $L=14$ spins, and are averaged over 10^4	
	realizations. The corresponding bare fittings with GSP distribution are also	
	shown. In the strong disorder regime, the GSP distribution reduces to the well-	
	known result with Poisson distribution. In contrast, at weak disorder, it remains	
	unclear whether Wigner-Dyson, GSP or even more complicated distribution pro-	
	vides a correct result. Inset: the same set of data but plotted in log-log scale.	
	Instead of the overall distribution of r , the slope of the linear dependence at	
	small r limit is another method to obtain exponent α	109
5.2	Schematic of the one-dimensional spin- $1/2$ chain with periodic boundary condi-	
	tion. Along the chain, each spin is subject to a random onsite field h_i along z	
	direction and the spins are coupled by nearest neighbor Heisenberg interactions	
	with strength J . At time t_0 when the local quench is turned on, a transverse	
	magnetic field f is applied to one of the spin, labeled by i_0	110
5.3	The distribution of Δ index for the $S_z=0$ sector of the spectrum in (a) the	
	ergodic regime, $W=1,$ or (b) the localized regime, $W=10.$ Data is obtained	
	for $L=12$ with 100 disorder realizations. Insets: the pattern of states labeled	
	by different S_z in the middle of the band for one arbitrary disorder realization.	
	Different markers correspond to different S_z . In the ergodic regime, states with	
	the same S_z are more likely separated by at least one state with a different S_z ,	
	whereas for the localized regime, states with the same S_z more likely appear in	
	adjacent pairs	111
5.4	The probability distribution of r for (a) the ergodic regime, $W=1$ and (b) the	
	localized regime, $W=10$ with varying amplitude of perturbation f . Data is	
	obtained for $L=12$ with 1000 disorder realizations	113

5.5	Dependence of MD on the amplitude of perturbation f for weak $(W = 1)$ and	
	strong $(W=10)$ disorder. As a measure of deviation from Poisson statistics, the	
	MD for the ergodic regime is sensitive on f and grows quickly to $\simeq 0.24$, while for	
	the localized regime MD roughly remains constant at a small value $\simeq 0.01.$ Inset:	
	The definition of MD is given by the maximum distance between cumulative	
	distribution functions of r between Poisson statistics and actual statistics	114
5.6	(a) Averaged participation ratio over disorder realizations as functions of disor-	
	der strength W and energy density ϵ for a system of $L=12$ and 1000 realizations.	
	Marked by white color, the many body mobility edge encloses a region of de-	
	localized states with IPR $\sim 2^{-L}$. The horizontal and vertical cut indicates the	
	parameters for panel (c) and (d). (b) The histogram of $\log_2 \mathrm{IPR}$ in the middle	
	of the band for $W=0.5,4$ and 10. The distributions are concentrated for weak	
	and strong disorder, but highly fluctuating in the critical region. (c) The IPR	
	at fixed disorder $W=3$, for which case the states are delocalized in the middle	
	of the band but localized in the edges, and $W=7$ where all states are localized.	
	(d) The IPR and its standard deviation for fixed energy density $\epsilon=0.5.$	117
5.7	Scatter plot of $(P^i_{ \alpha\rangle}, Q^i_{ \alpha\rangle})$ for (a) the localized regime with $W=10$ and (b)	
	the ergodic regime with $W=2.5$ for states $ \alpha\rangle$ in the middle of the band. Data	
	obtained with $L=12$ and $N=1000$. The corresponding probability distribution	
	of P_i and Q_i for (c) the localized regime in which the single spin measurement	
	with and without a quench coincides with each other and for the (d) ergodic	
	regime the disparity in the distribution with and without the quench indicates	
	a thermalization	119

5.8	(a) Measure $C^i_{ \alpha\rangle} = P^i_{ \alpha\rangle} Q^i_{ \alpha\rangle}$ as functions of disorder strength W and energy	
	density ϵ for $L=12$ and $N=1000$. The many-body mobility edge is marked	
	in white. (b) "Euclidean distance" \mathcal{D}^i as a function of distance between moni-	
	tored spin and quenched spin (solid lines), and the corresponding fitting curve,	
	Eq. (5.11) (dashed lines). (c) The many-body localization length ξ extracted	
	from $\mathcal{D}^{(i)}$ as a function of disorder strength. The dashed line corresponds to the	
	$\xi=1$ to show that the at sufficiently strong disorder the system is localized in	
	the atomic limit.	121
6.1	Distribution of dimensionless power p , Eq. (6.20), over $N=10^4$ realizations	
	of the random magnetic field $\{h_i\}$ for a system with $L=10$ spins. The top	
	panel shows the distribution of the power itself for $W/J=0.3$ (blue long-dashed	
	line) and $W/J=3$ (green short-dashed line), while the bottom panel shows the	
	distribution of $\lg p$ for all three values of disorder for three values of the disorder	
	strength $W/J=0.3,3$ and 30 (red solid line). We scaled the distribution curves	
	for $W/J=3$ by factor two and for $W/J=30$ by factor six. The inset shows	
	the logarithm of the distribution of $\lg p$ for $W/J=30$ and the dash-dotted line	
	represents the slop $\sim p^{-1/2}$. The drive amplitude $f=J/\sqrt{10}$ and $\omega=J$	132
6.2	Average value of the logarithm of dimensionless power, $\lg(p)$, as a function of	
	disorder strength W for a spin system of size $L=8$ (circles), $L=10$ (diamonds)	
	and $L=12$ (triangles). The average is evaluated over $N=10^3$ samples for	
	$L=8,\ 10,\ {\rm and\ for}\ N=200\ {\rm for}\ L=12.$ The drive amplitude $f=J/\sqrt{10}$ and	
	$\omega = J.$	134
6.3	Measure $\overline{\lg \mathcal{T}^2}$ as functions of disorder strength W and energy density ϵ for	
	L=10 and $N=4000.$ The many-body mobility edge is marked in white	135

6.4	Average value of the normalized absorbed energy Q evaluated by using Eq. (6.39)
	as functions of the disorder strength W for a spin system of size $L=8,L=10$
	and $L=12$. The average is evaluated over $N=10^4$ samples for $L=8,10$
	and $N=200$ for $L=12$ and drive amplitudes are $f=0.1J$ and $f=J$. The
	dependence of Q on W in the localized regimes suggests that an exponential small
	overlap between thermal state with infinite temperature and actual density matrix.138
6.5	Expectation value of $\overline{S_z^2}$ as functions of disorder strength W for a spin system
	of size $L=8,10$ and 12. Parameters are the same as Figure 6.4 139
6.6	Average value of the IPR over all eigenstates defined in Eq.(40), as functions of
	disorder strength W for a system of size $L=8,L=10$ and $L=12.$ Parameters
	are the same as Figure 6.4
6.7	Averaged von Neumann entropy obtained by averaging over all eigenstates as
	initial conditions. At $f=J$ we expect that the entropy approaches to $L\ln 2\simeq$
	0.69L in the thermodynamic limit at weak disorder and drops to 0 at strong
	disorder. Parameters are the same as Figure 6.4

List of Tables

Chapter 1

Introduction

1.1 Introduction to quantum information

As suggested by Feynman in 1982[1], and succeeded by an argument provided by Deutsch in 1985[2], physicists have been inspired by the idea of quantum computation in such a way that the computation task is carried out by a number of quantum degrees of freedoms. In the classical computing, the information is stored in bits, which takes either 0 or 1, while the quantum information can be stored as a superposition of 0 and 1, due to its quantum nature. Benefitted by the quantum superposition, the number of states increases exponentially and all possible quantum information can be stored simultaneously as the system size goes up. The advantage of quantum computation can be revealed by the so called "quantum parallelism". Roughly speaking, in classical computation, the system evolves according to stochastic matrices which preserves the sum of probabilities, while the quantum computation is performed by a unitary transformation that preserves both total probabilities and phase coherence. Consequently, each single quantum operation is reversible, and moreover a combination of stochastic and unitary transformations is also allowed. In this sense, classical algorithms form a subset of quantum algorithms. As such, the huge improvement on the efficiency of manipulation of information results in numerous applications such as Shor's factoring algorithm[3], Grover's search algorithm[4] and quantum

adiabatic algorithm[5, 6].

Unfortunately, the pragmatic implementation of quantum computation remains an extraordinary challenge for scientists and engineers. One inevitable problem is the loss of quantum coherence, or named decoherence in literatures, due to the interaction between qubits with its nearby environment. One has to control over the operations of single qubit or multiple qubits to the order of thousands extremely precisely in the sense that any unknown evolution that affects the quantum states, such as decoherence, should be taken into account. Indeed, the coherence time realized by quantum error correction to date does not exceed any of the individual components, which is one of the main restrictions to realize a fault-tolerant quantum computer.

As for physical systems suitable for quantum computation, a number of potential implementation has been suggested. Of all existing proposals, most of them encode quantum information in terms of "natural" microscopic quantum states, such as photons[7], trapped ions[8], neutral atoms[9] or nuclear spins[10], for which the quantum description is naturally established. On the other hand, some macroscopic systems with a large number of atoms assembled in confined geometry can also be used, such as superconducting circuits and semiconductor quantum dots[11], both of whose fabrication and design being well developed using modern development in electronics. In these systems, the quantum information is represented by the collective degrees of freedom as a result of robust macroscopic phenomenon, that is, Josephson effects for superconducting qubits and Coulomb blockade for both cases, endowing well-defined macroscopic quantum states controlled by tunable parameters.

In contrast to a harmonic LC oscillator, in the superconducting circuits, the nonlinearity in the Josephson tunnel junction insulates the transition between the ground state and the excited state from the rest of circuit states. By tuning the relevant parameters, such as capacitance, inductance and Josephson energy, there are three basic types of qubits, namely flux, phase[12] and charge qubits, indicating the physical extent of the computational basis. In addition, improved descendants of basic designs, known as transmon[13], fluxonium[14]

and quantronium[15], are later constructed to reduce decoherence mechanism in the basic types.

In a semiconductor quantum dot, the electrons trapped at the interface forms a two dimensional electron gas, or 2DEG for abbreviation. These electrons are geometrically confined by external gate voltages into a small "box" in such way that the energy levels of the trapped electron are discrete, with its level-spacing greater than the experiment temperature. In this manner, the single electron states are well defined, so either the quantization of charge or spin can be used to encode quantum information. A typical charge qubit in double quantum dot is initialized by biasing the electrostatic potential such that single electron is well localized in one of the dot, and the manipulation of quantum states is controlled by tunnel elements and gate voltages. States with higher number of electrons are energetically penalized due to the Coulomb blockade effect. On the other hand, if one consider the spin degrees of freedom, each quantum dot has one electron, forming four possible spin states, one singlet labeled as S and three triplets labeled as T_0, T_+, T_- , respectively. The quantum information is stored in the S and T_0 states because they are both unaffected by external magnetic field and can be measured by the external current, with the benefited of the "spin blockade" technique.

One remarkable dividend of solid state qubits is that they can be strongly coupled to single photon mode, like an atom. This new class of experiment called circuit quantum electrodynamics (cQED) is achieved by the dipole moment formed by the separation of charges in such devices, coupled to a single mode microwave resonator, which is usually engineered as a coplanar waveguide to mediate long range interaction between qubits. In such hybrid device, qubit operations and readouts can be controlled by the frequency of the resonator and its external drive, by the well-developed quantum optical techniques. With small photon numbers in the resonator, high efficiency microwave photon detection enables the readout of the qubit in the regime where the qubit states and photon states are highly entangled. The underlying physics can be exemplified by preparation of maximum entangled states and parametric amplifier. It is therefore essential to explore the models

of on-chip photon detectors, and analyze the new physics in the quantum regime in the presence of coupling to an environment.

1.2 Quantum computing with solid state qubits

As mentioned above, qubits made out of solid state devices could offer appreciable advantages for practical use since in principle modern lithographic methods allows for scalability and flexibility in design. Indeed, the quantum information encoded in the computational basis of an "artificial" solid-state atoms, such that in contrast to "neutral" atoms, has specific freedom to manipulate at microwave frequency, and can be easily embedded in electronic circuits for external control. This tunability makes solid-state qubits as a superior candidates to those of "neutral" atoms. On the other hand, it is also worth mentioning that there is a large variety of unwanted decoherence sources in solid state qubits.

Double Quantum Dots

Quantum dots are fabricated nano-structures from semiconductor materials, where electrostatic potentials confine electrons into small "boxes" geometrically such that just a few discrete energy levels are obtained; these energy levels can be tuned by lithography methods, such that one can cover large areas with zillions of tiny quantum dots and control these states by lasers. This scenario is called optically activated quantum dots, since the transition between particular states are controlled by light absorption and/or emission, and they are not connected to any electrodes.

The measurement and control of discrete levels become even easier for transport quantum dots, which are attached to noninteracting electron reservoirs, also known as leads, so that the electrons can be transferred from one lead to another. The coupling between states in the dot and leads brings in broadening of the discrete levels. In the sense, to ensure the energy levels still survives, the charging energy, E_C , a energy scale which separates levels with different electron occupation numbers by ± 1 , should dominates over the broadening of individual states Γ . This is the so-called Coulomb blockade regime, in which single electron

states are well defined. Naturally, though, spin states of those confined electrons are great candidate for solid state qubits, we will only consider the qubits encoded by the charge degrees of freedom—those called charge qubits will be the only model discussed for quantum dot systems.

The simplest way to build a charge qubit is to consider a double quantum dots, with each of them in the Coulomb blockade regime. Being discrete, the energy spectrum of the electron states in both dots can be adjusted by the external gate voltages in such a way that one can align the Coulomb energies of states (1,0) and (0,1), where (N_1, N_2) denotes the state with N_1 (N_2) electrons in the left (right) dot. If the energy detuning of between the two states is sufficiently small compared to the charging energy, other charging states are far apart and can be disregarded. Thereby we denote the states $(1,0) \rightarrow |0\rangle$ and $(0,1) \rightarrow |1\rangle$ to construct the computational basis from a double quantum dot. As shown in Figure 1.1, the double quantum dot can be understood as a model comprising of coherent (\mathcal{T}) and incoherent $(\mathcal{T}_{L/R})$ tunneling processes, and the energy splitting between the two eigenstates can be tuned into microwave frequency for iradiative manipulation.

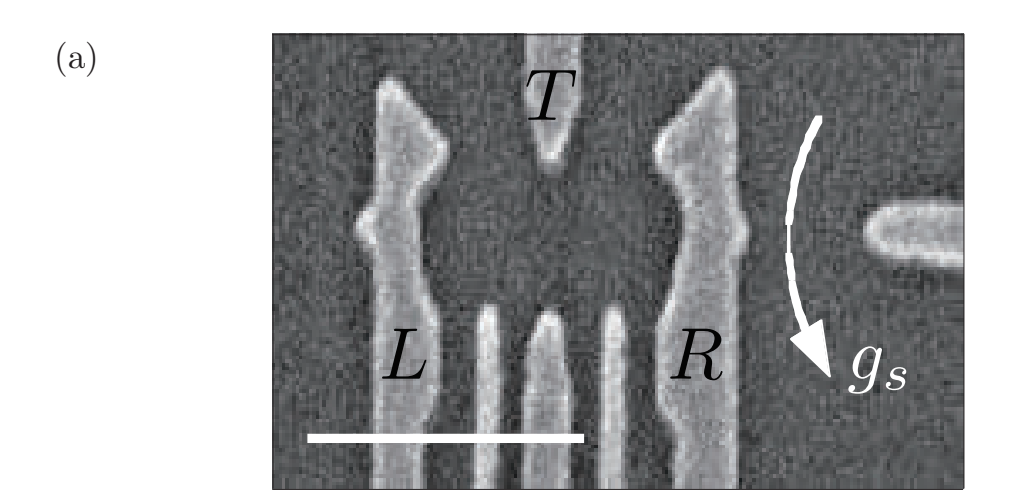
The parameters of the qubit Hamiltonian consists of energy detuning ε , as well as a coherent tunneling amplitude \mathcal{T} between the two charging states. The Hamiltonian then reads:

$$H = \begin{pmatrix} \varepsilon/2 & \mathcal{T} \\ \mathcal{T} & -\varepsilon/2 \end{pmatrix} = \frac{1}{2}\varepsilon\sigma_z + \mathcal{T}\sigma_x. \tag{1.1}$$

The ground state of the qubit is then given by

$$|G\rangle = -(|0\rangle + |1\rangle) \frac{\sin(\theta/2)}{\sqrt{2}} + (|1\rangle - |0\rangle) \frac{\cos(\theta/2)}{\sqrt{2}}, \tag{1.2}$$

where the rotating angle $\theta = \arctan(\varepsilon/2T)$. The manipulation of qubit state can be achieved by applying a resonant oscillating fields with frequency $\omega \simeq \sqrt{\varepsilon^2 + 4T^2}$ in such way that the transition between the two eigenstates of qubit can be coherently controlled. To readout the qubit, one measures the charge in the quantum dot by measuring the current in the nearby quantum point contacts (QPC) because the transmission coefficient of the QPC, \mathcal{T}_0 , depends on the number of electrons of the dot. By varying the number of electrons by ± 1 ,



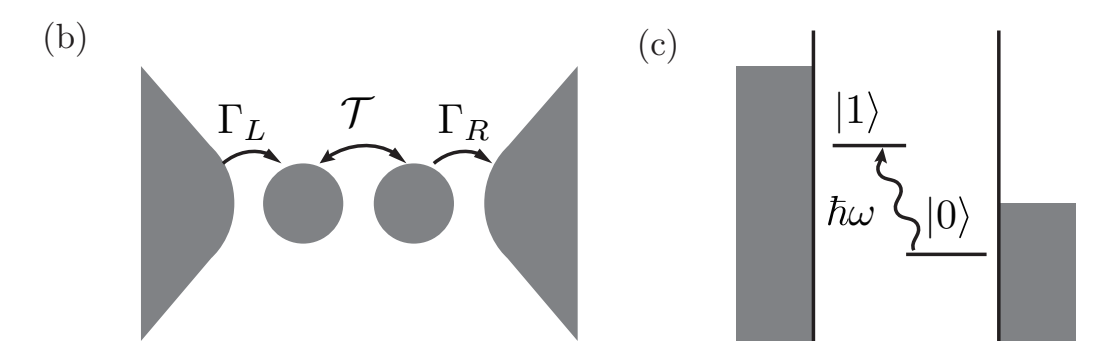


Figure 1.1: (a) Micrograph of a DQD device with gate voltages applied to gates L, R and T. Gates L and R are used to adjust the detuning, ε , and gate T sets the coherent interdot tunnel amplitude \mathcal{T} . The conductance g_s of a nearby quantum point contact monitors the occupation of each dot. (b) The transport properties of a DQD that attached two leads are defined by coherent amplitude \mathcal{T} and incoherent rates $\Gamma_L(R)$. (c) Energy diagram of the DQD qubit, which can be manipulated by a radiative drive with frequency ω .

the electrostatic potential felt by the QPC acquires a slight change, therefore leading to an increment in transmission coefficient $\delta \mathcal{T}$, or in current $\delta I = \delta \mathcal{T} e^2/\pi\hbar \simeq 1 \text{nA}$, an amount large enough to be measured within 0.2 ms. Since the net charge in each dot is either 0 or 1, the current through the QPC is quantized with two values, separated by $\simeq 1 \text{nA}$, each representing a single charge states. Therefore, the readout of charge qubit can be performed by measuring the current though the QPC.

Superconducting qubits

The superconducting qubits based on Josephson junction are so far the most successful realizations of solid state qubits that have been made. The main reason is that in order to isolate a useful qubit from the eigenstates of some small solid state device, it is necessary to have some nonlinear elements that breaks the harmonicity of the spectrum. Indeed, for superconducting circuits, the nonlinear elements are naturally embedded as a result of Josephson junction, with much less uncontrollable external fluctuations, which is the reason why superconducting qubits have a promising future.

The Josephson junction is a tunnel junction consisting of a layer of insulating material, sandwiched by two layers of superconducting material. Due to Andreev reflection, supercurrent in the superconductors is converted to normal current in the normal materials at the two interfaces, and vice versa. This is a coherent tunneling process, and the constructive interference of the electron- and hole-like excitations gives rise to the supercurrent, yielding the following Josephson equations:

$$U(\phi) = \Phi_0 \frac{\partial \phi}{\partial t} \tag{1.3}$$

$$I(\phi) = I_c \sin(\phi), \tag{1.4}$$

where $U(\phi)$ and $I(\phi)$ are the voltage and current across the Josephson junction, $\phi(t)$ is the phase difference across the junction, $\Phi_0 = \hbar/2e$ is the magnetic flux quantum, and I_c is the critical current of the Josephson junction. If the junction is current-biased with an external current above I_c , the Josephson effects break down. With the dependence of $U(\phi)$ and $I(\phi)$

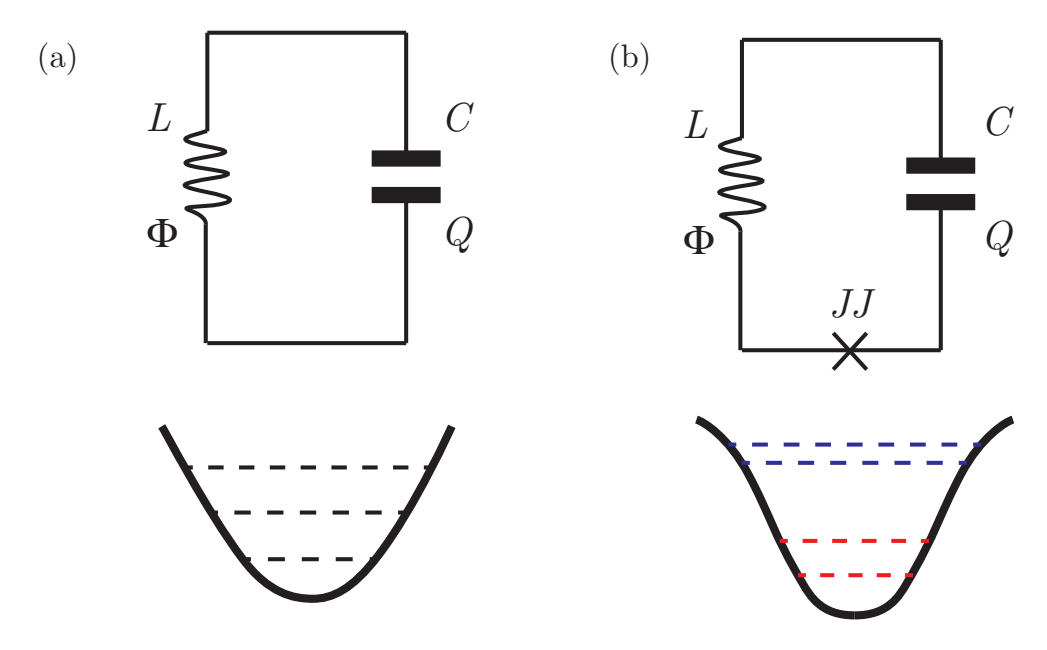


Figure 1.2: Schematic energy levels of superconducting LC-circuit (a) without a Josephson junction or (b) with a Josephson junction.

on the phase ϕ , one can construct a circuit Hamiltonian for the Josephson junction:

$$H_{JJ} = -\frac{\Phi_0 I_c}{2\pi} \cos \phi + \frac{Q^2}{2C},\tag{1.5}$$

where Q is the charge operator and C is the capacitance of the junction. In Eq. (1.5), the charge operator Q is a conjugate operator to phase ϕ , $[Q, \phi] = -2i$; indeed, the nonlinear dependence of current I as a function of phase ϕ indicates that the energy splittings in the spectrum of H_{JJ} are not equal, thereby the lowest two energy levels are well separated to others. When inserted into an LC circuit, the Josephson junction is a nonlinear element which breaks the harmonicity of spectrum, see Figure 1.2. The superconducting qubit works with the benefits of nonlinear quantum circuits.

The circuit for the phase qubit can be understood as the ground and first excited state of the metastable potential well in the Josephson junction with a biased current. Similarly the circuit for the flux qubit can be understood as a Josephson junction with external magnetic flux through the ring-shaped circuit. Flux quantization in the ring forces the supercurrent in the flux qubit to flow either clockwise or anti-clockwise, and these two states of current flow defines the qubit states. A superconducting charge qubit is formed by a tiny

superconducting island coupled by a Josephson junction. For the circuit operating in the charging regime, the number of Cooper pairs on the island is a good quantum number, and therefore the lowest two charge states form the qubit states. The corresponding Hamiltonian reads

$$H_{CQ} = E_C \left(N_g - \frac{1}{2} \right) \sigma_z - \frac{E_J}{2} \sigma_x. \tag{1.6}$$

Here, the offsite charge $N_g = C_g V_g/2e$ with C_g and V_g being the gate capacitance and gate voltage respectively. $E_J = I_c \Phi_0/2\pi$ is the Josephson energy and $E_C = (2e)^2/eC$ is the charging energy.

Even though any choice of superconducting qubits is not specifically chosen in the thesis, it worth mentioning that in the family of superconducting qubits, several modern descendants, such as transmon[13] and Xmon[16] are designed to work in the regime $E_C \gg E_J$ by shunting a large capacitance in parallel to the Josephson junction. This setting reduces the charge dispersion exponentially but the anharmonicity of the spectrum in a weak power law. As a result, the spectrum is much less sensitive to the offset charge to reduce charge noise, while maintaining sufficient anharmonicity for selective qubit states.

Circuit Quantum Electrodynamics

The interaction between quantized electromagnetic field to a two-level system was usually achieved in a tiny laser cavity. The energy exchange between the field and the system, called Rabi oscillations, occurs at a frequency Ω_R proportional to the strength of the coupling constant between the system and the field. In the strong coupling limit, the Rabi frequency Ω_R is much greater than both the decoherence rate of the two level systems and the cavity field, and the underlying physics is called cavity quantum electrodynamics.

For the last decades, however, such setting was successfully achieved in a hybrid system consisting of a microwave resonator and a superconducting qubit or quantum dot qubit. The coupling between these devices is achieved either by galvanic or direct electrostatic coupling, while the qubit is fabricated inside the resonator, or by capacitive or inductive coupling while the qubit is fabricated ouside the resonator. In all cases, the Rabi interaction

between the microwave resonator and the qubit is described by the Hamiltonian

$$H_{\text{Rabi}} = \frac{1}{2}\omega_q \sigma_z + \omega_r a^{\dagger} a + g \sigma_x \left(a + a^{\dagger} \right), \tag{1.7}$$

where a and a^{\dagger} are the annihilation and creation operators of the microwave field and ω_r is the frequency of the resonator field. In most cases that $\omega \simeq \omega_0$ and $\omega \gg g$, it is reasonable to make a rotating wave approximation to drops off the so-called counter-rotating terms, $a\sigma^-$ and $a^{\dagger}\sigma^+$, where σ^+ and σ^- are the raising and lowering operators of the qubit. The resulting expression is the well-known Jaynes-Cummings model:

$$H_{JC} = \frac{1}{2}\omega_q \sigma_z + \omega_r a^{\dagger} a + g(\sigma^+ a + \sigma^- a^{\dagger}). \tag{1.8}$$

The Jaynes-Cummings model is exactly solvable because the interaction term $g(a\sigma^+ + a^{\dagger}\sigma^-)$ only connects the states in the subspace $|n-1,\uparrow\rangle$ and $|n,\downarrow\rangle$, which leads to a block-diagonal Hamiltonian. This allows for an exact analytic solution for the eigenstates

$$|0\rangle = |0,\downarrow\rangle,\tag{1.9}$$

$$|n, +\rangle = \cos \theta_n |n - 1, \uparrow\rangle + \sin \theta_n |n, \downarrow\rangle,$$
 (1.10)

$$|n, -\rangle = -\sin \theta_n |n - 1, \uparrow\rangle + \cos \theta_n |n, \downarrow\rangle,$$
 (1.11)

and for the eigenvalues

$$E_0 = -\frac{\Delta}{2},\tag{1.12}$$

$$E_{n,\pm} = n\omega_r \pm \frac{1}{2}\sqrt{4g^2n + \Delta^2},$$
 (1.13)

for $n=1,2,\ldots$ denoting the number of photons and $\Delta=\omega_q-\omega_r$ is the qubit-resonator detuning and θ_n yields

$$\tan(2\theta_n) = \frac{2g\sqrt{n}}{\Lambda}.\tag{1.14}$$

These general solutions of the Hamiltonian are called dressed states. When $\Delta = 0$, the angles $\theta_n = \pi/4$, resulting in maximum entangled states between photon and qubit.

In the experiment, the coupling constant g depends on the specific implementation of the setting of the qubit as well as the geometry of the microwave resonator.

Adiabatic quantum computation and many-body localization

In regarding of conventional quantum computation, the computation scheme works similarly to a classical computer in such a way that the qubits are connected as a circuit through quantum gates to perform fundamental computation tasks.

However, as proposed in Ref.[5], benefited from the quantum adiabatic theorem, a new computational scheme called adiabatic quantum computation could be an efficient candidate for quantum computation as well. It works as following: At time t = 0, the quantum mechanical system is described by a Hamiltonian H_i , whose eigenstates are easy to prepare. Next, the system is slowly evolved into a more complicated final Hamiltonian H_f . By the adiabatic theorem, for a adiabatic process, the system remains in its instantaneous eigenstate if there is a gap between the eigenvalue and the rest of the spectrum. Further details about AQC can be found in the review article Ref.[17].

While in principle the AQC is a universal scheme for quantum computing, actually performing operations on this machines are equivalent to quantum simulation of the ground states (and sometimes the entire spectrum) of a complicated Hamiltonian. Therefore for any two quantum spin systems whose Hamiltonians are connected by a simple function of external parameters, the AQC scheme can be applied to understand the ground state of a unsolvable Hamiltonian. For instance, as an active research field recently, the many-body localization (MBL) physics is a regime which can be found in interacting one-dimensional spin systems with quench disorder. Recently, extensive numerical and analytical efforts have been devoted to understand the thermal and dynamical properties of the 1D random field Heisenberg model,

$$H = \sum_{i} h_i \sigma_z + J \sum_{i} \vec{\sigma}_i \cdot \vec{\sigma}_{i+1}, \qquad (1.15)$$

where $h_i \in [-W, W]$ are random numbers, and concluded that for this model there is a transition of state with localized spins to a delocalized state when W is below the critical value W_c while remain J fixed. From an experimental perspective, in each simulation one can fix the disorder realization $\{h_i\}$ for an noninteracting spin system, J = 0, a regime where spins are deeply localized with eigenstates as simple product states $|\psi\rangle = \bigotimes_i |\uparrow (\downarrow)\rangle_i$.

Then one gradually turns on J, ending up with a delocalized state when W/J is below the critical value W_c/J . With such systems, we propose and examine the dynamical aspect of MBL using a local quench or a harmonic drive, both of which take advantage of accurate methods for quantum control. The details will be discussed later in the thesis.

1.3 Open quantum systems

In practice, all quantum systems are open to the environment to some extent, and the larger a system of interest is, the more important its coupling to the nearby environment would be. For solid state qubits, the computational basis usually consists of macroscopic quantum states, and therefore the coupling leads to very severe decoherence, a term implies irreversible process that turns quantum superposition into classical mixtures. Specifically, starting with a pure state $|\psi\rangle$, the system is entangled with the environment upon time evolution, and eventually turned into a mixed state ρ . Besides, quantum information processing is less useful until a measurement of quantum states is made. So to speak, the measuring apparatus (usually as a quantum-classical interface) is indeed coupled to the system of interest, and for this reason the quantum state cannot be described by a pure state.

For a particular class of problems, the Born and Markov approximations are both valid. The essential idea is that the system couples weakly to an environment which consists of a large number of degrees of freedom in such a way that the system is not greatly affected by the environment which relaxes itself in a short time scale.

The standard approach to derive the equations of motion for a system interacting with the environment is to trace out the environmental degrees of freedom. After the truncation, the resulting time evolution of the reduced density matrix for the system is called master equation, for historical reasons. Decomposing the entire Hamiltonian as $H = H_0 + V =$ $H_S + H_E + V$, where H_S is the Hamiltonian for the system, H_E is that for the environment and V is the coupling between the two, the dynamics of the entire density matrix ρ_{tot} reads

$$\dot{\rho}_{\text{tot}}(t) = -i[H, \rho_{\text{tot}}(t)]. \tag{1.16}$$

In the interaction picture, the density matrix is given by

$$\rho_{\text{tot}}(t) = \exp\left(-iH_0t\right)\rho_{\text{tot;int}}(t)\exp\left(iH_0t\right),\tag{1.17}$$

where $\rho_{\text{tot;int}}(t)$ is governed by

$$\dot{\rho}_{\text{tot;int}}(t) = -i[V_{\text{int}}(t), \rho_{\text{tot;int}}(t)], \tag{1.18}$$

with $V_{\text{int}}(t) = e^{iH_0t}Ve^{-iH_0t}$. The general solution of Eq. (1.18) and can be expanded perturbatively:

$$\rho_{\text{tot;int}}(t) = \rho_{\text{tot;int}}(0) - \int_0^t dt'[V(t'), \rho_{\text{tot;int}}(t')]. \tag{1.19}$$

Tracing out the environment degrees of freedom, the above solution correspond to the following equation of motion for the density matrix of the system:

$$\dot{\rho}_{\text{tot;int}}(t) = -i\text{Tr}_{\text{E}}[V(t), \rho_{\text{tot;int}}(t)] - \int_{0}^{t} dt' \text{Tr}_{\text{E}}[V(t), [V(t'), \rho_{\text{tot;int}}(t')]]. \tag{1.20}$$

This is an integro-differential equation for the system density matrix, which is difficult to solve because of the time dependence of ρ in the integral term. Assuming that at t=0, there is no entanglement between system and the environment, that is, $\rho_{\text{tot}}(t) = \rho(0) \otimes \rho_{\text{E}}(0)$. Typically the system couples to many energy levels of the environment that are close in energy, therefore the time variable t' for the reduced density matrix in integrand in Eq. (1.19) can be replaced by t and make the lower limit of the integral starting from $-\infty$. This is the Markov approximation, a memoryless property caused by the fast equilibration of the environment. To this end, we obtain the Born-Markov master equation:

$$\dot{\rho}(t) = -i[V(t), \rho(t)] - \int_{-\infty}^{t} dt' \text{Tr}_{E}[V(t), [V(t'), \rho(t)]]. \tag{1.21}$$

As a result, the time evolution of the system is governed by modified quantum dynamics, which is probabilistically conserved in a non-unitary way. In the following, the Born-Markov master equation will presented in more compact forms with further details. Namely, two types of approach will be introduced, as they were used extensively throughout the thesis.

The Bloch-Redfield master equation

The Born-Markov master equation is presented in arbitrary basis, and therefore is still not convenient for numerical implementation. For the particular problem of interests, one can diagonalize the system Hamiltonian $H_S = \sum_n \omega_n |n\rangle \langle n|$ and the density matrix can be written in the eigenbasis $|n\rangle$ with elements $\rho_{mn} = \langle m|\rho|n\rangle$ yielding

$$\dot{\rho}_{mn}(t) = -i\omega_{mn}\rho_{mn}(t) - \sum_{k,l} R_{mnkl}\rho_{kl}(t). \tag{1.22}$$

The first term represents the coherent part of the in the equation of motion with transition frequencies $\omega_{nm} = \omega_n - \omega_m$, and the second term describes incoherent time evolution, where R_{mnkl} is called Bloch-Redfield tensor that reads

$$R_{mnkl} = \delta_{ln} \sum_{r} \Gamma_{mrrk}^{(>)} + \delta_{mk} \sum_{r} \Gamma_{lrrn}^{(<)} - \Gamma_{lnmk}^{(>)} - \Gamma_{lnmk}^{(<)}.$$
 (1.23)

The rates $\Gamma_{mnkl}^{(>)}$ and $\Gamma_{mnkl}^{(<)}$ are expressed by Golden rule

$$\Gamma_{mnkl}^{(>)} = \int_0^\infty dt e^{-i\omega_{kl}t} \langle V_{\text{int},mn}(t)V_{\text{int},kl}(0) \rangle_E$$
 (1.24)

$$\Gamma_{mnkl}^{(<)} = \int_0^\infty dt e^{-i\omega_{mn}t} \langle V_{\text{int},mn}(0)V_{\text{int},kl}(t) \rangle_E.$$
 (1.25)

Here $\langle \dots \rangle_E = \operatorname{Tr}_E(\dots \rho_E)$ denotes the thermal average over the environment degrees of freedoms. In other words, the Redfield tensor is obtained by the Fourier transform of the correlation function $\langle V_{\mathrm{int}}(0)V_{\mathrm{int}}(t)\rangle_E$ at given frequency differences in the eigenbasis. In reality, the environment degrees of freedoms are modeled by a set of N independent harmonic oscillators whose coordinate variables are coupled to the system degrees of freedom linearly. This model is referred to as the Caldeira-Leggett model, which is useful for a system with many levels in principle. To incorporate the environmental effects into the system, we introduce the spectral density of the environmental coupling:

$$J(\omega) = \sum_{\alpha} \lambda_{\alpha}^{2} \delta(\omega - \omega_{\alpha}), \tag{1.26}$$

where α is the indices of the environmental mode and λ_{α} is the corresponding coupling constant between mode α to the system, such that the thermal average is given by

$$C(t) = \langle V_{\rm int}(t)V_{\rm int}(0)\rangle_E = \int_0^\infty d\omega J(\omega) \left[\coth\left(\frac{\beta\omega}{2}\right)\cos(\omega t) - i\sin(\omega t)\right]. \tag{1.27}$$

Therefore, the Redfield tensor is decomposed into products of system operators S and the spectral density:

$$\Gamma_{mnkl}^{(>)} = \frac{1}{2} S_{kn} S_{lm} \tilde{C}(\omega_{ml}) \tag{1.28}$$

$$\Gamma_{mnkl}^{(<)} = \frac{1}{2} S_{kn} S_{lm} \tilde{C}^{\dagger}(\omega_{ml}), \qquad (1.29)$$

with $\tilde{C}(\omega) = \int_0^\infty dt e^{i\omega t} C(t)$. With Eqs. (1.28) and (1.29) and the tensor R_{mnkl} given in Eq. (1.23) we arrived at the Bloch-Redfield master equation. The spectral density can be obtained either by spectroscopy experiment or detailed calculations, and those system operators S are listed by all possible operators associated with two eigenstates in the Hilbert space of the system that are coupled to the environment. The Bloch-Redfield equation is widely used in different aspects of physics to model decoherence and dissipation processes.

For the application in the physics of quantum information science, detailed analysis of the qubit dynamics benefits from the theoretical understanding of the dynamics of dissipative two-level systems, which could be reduced to spin-boson model under realistic conditions. The spin-boson model has been systematically studied in Ref.[18], with careful discussions about the effects of an Ohmic bath, $J(\omega) \sim \omega$, the most common case in regards to qubit dynamics. Based on Bloch-Redfield master equation, a theoretical approach to dissipative qubit dynamics of a time-dependent Hamiltonian will be discussed in Chapter 4 and Ref.[19]. Especially, Landau-Zener transition will be reexamined in the presence of a dissipative environment. At the time of writing of this thesis the author is aware that with the progresses in AQC, more profound understanding of dissipative Landau-Zener physics is seriously desired.

The Lindblad master equation

The Lindblad master equation is a equation of motion for the system state $\rho(t)$, given by

$$\dot{\rho}(t) = -i[H, \rho(t)] + \sum_{\mu} \gamma_{\mu} \mathcal{D}[L_{\mu}] \rho. \tag{1.30}$$

The first term is the von Neumann equation for the renormalized Hamiltonian H that includes the system Hamiltonian as well as the renormalization in the presence of the environment such as Lamb shifts and Stark shifts. The second term describes the dissipation of the system: γ_{μ} is the rate for the collapse operator L_{μ} and the superoperator $\mathcal{D}[A]$ called Lindblad superoperator is given by

$$\mathcal{D}[A]\rho \equiv A\rho A^{\dagger} - \frac{1}{2} \left(A^{\dagger} A \rho + \rho A^{\dagger} A \right). \tag{1.31}$$

The operators L_{μ} can be specified not only from a microscopic picture, but also in a phenomenological way.

The Lindblad master equation can be written a

$$\dot{\rho}(t) = \mathcal{L}\rho(t),\tag{1.32}$$

where \mathcal{L} is the total Liouvillian operator. Eq. (1.32) has a simple form of solution $\rho(t) = e^{\mathcal{L}t}\rho(0)$, in which the time evolution operator $\Lambda_t = e^{\mathcal{L}t}$ is a dynamical quantum map describing the state change of the open system over time t.

- 1. Λ_t is completely positive and trace preserving.
- 2. Tr $\left[\Lambda_t \rho(0)\hat{O}\right]$ is continuous in t for all valid observables \hat{O} .
- 3. Λ_t is Markovian, namely $\Lambda_{t_1+t_2} = \Lambda_{t_1} \cdot \Lambda_{t_2}$ and $\Lambda_0 = \mathcal{I}$.

The first property ensures that the dynamical quantum map connects valid quantum states, and the second property ensures that there are no discontinuity in the time evolution of observables. The third property states that Λ_t does not depend on the memory of the time evolution, only on specific point in time.

While the Lindblad master equation is easily defined with a wide range range of applications, a lot of mathematical details and their consequences will not be discussed here. However, for problems originated from quantum information processing, it is crucial to consider the time correlation functions of observables, as well as the corresponding fluctuation spectrum, which is defined in terms of the Fourier transform of the correlation function.

Suppose we have a set of system operators $\{S_i\}$, and the time evolution of their expectation values yields a closed linear combination of them,

$$\frac{d}{dt}\langle S_i(t)\rangle = \sum_j G_{ij}\langle S_j\rangle \tag{1.33}$$

with some coefficient matrix G_{ij} . With the Liouvillian operator \mathcal{L} , the relation can be rewritten as

$$\frac{d}{dt}\langle S_i(t)\rangle = \operatorname{Tr}_S\left\{S_i\mathcal{L}\rho(t)\right\} = \operatorname{Tr}_S\left\{\left(\mathcal{L}^{\dagger}S_i\right)\rho(t)\right\} = \operatorname{Tr}_S\left\{\left(\sum_j G_{ij}S_j\right)\rho(t)\right\}, \quad (1.34)$$

which leads to

$$\mathcal{L}^{\dagger} S_i = \sum_j G_{ij} S_j. \tag{1.35}$$

Therefore we obtain

$$\frac{d}{d\tau} \langle S_i(t+\tau) S_k(t) \rangle = \operatorname{Tr}_S \left\{ \left(\mathcal{L}^{\dagger} S_i \right) \Lambda_{t+\tau} \Lambda_t^{-1} S_k \rho(t) \right\}
= \sum_j G_{ij} \langle S_j(t+\tau) S_k(t) \rangle,$$
(1.36)

a conclusion called quantum regression theorem. The significance of the theorem is that it allows us to evaluate explicit expressions for the time correlation functions and naturally the fluctuation spectrum once the solution for the expectation value given by Eq. (1.33), is known.

1.4 Outline of the thesis

The thesis is structured as the following. The first part of the thesis explores realistic problems originated from quantum information processing. Chapters 2 through 4 covers

the first part. The second part of the thesis scrutinizes the dynamical aspects of many-body localization; those materials are presented in Chapter 5 and 6.

In Chapter 2, we analyze the photovoltaic current through a double quantum dot system coupled to a high-quality driven microwave resonator. The conversion of photons in the resonator to electronic excitations produces a current flow even at zero bias across the leads of the double quantum dot system. We demonstrate that due to the quantum nature of the electromagnetic field in the resonator, the photovoltaic current exhibits a double peak dependence on the frequency ω of an external microwave source. The distance between the peaks is determined by the strength of interaction between photons in the resonator and electrons in the double quantum dot. The double peak structure disappears as strengths of relaxation processes increases, recovering a simple classical condition for maximal current when the microwave frequency is equal to the resonator frequency.

In Chapter 3, we analyze the full counting statistics of photons emitted by a double quantum dot (DQD) coupled to a high-quality microwave resonator by electric dipole interaction. We show that at the resonant condition between the energy splitting of the DQD and the photon energy in the resonator, photon statistics exhibits both a sub-Poissonian distribution and antibunching. In the ideal case, when the system decoherence stems only from photodetection, the photon noise is reduced below one-half of the noise for the Poisson distribution and is consistent with current noise. The photon distribution remains sub-Poissonian even at moderate decoherence in the DQD. We demonstrate that Josephson junction based photomultipliers can be used to experimentally assess statistics of emitted photons.

In Chapter 4, we study the dynamics of a two-level system described by a slowly varying Hamiltonian and weakly coupled to the Ohmic environment. We follow the Bloch–Redfield perturbative approach to include the effect of the environment on qubit evolution and take into account modification of the spectrum and matrix elements of qubit transitions due to time-dependence of the Hamiltonian. This formalism is applied to two problems. (1) We consider a qubit, or a spin-1/2, in a rotating magnetic field. We show that once the

rotation starts, the spin has a component perpendicular to the rotation plane of the field that initially wiggles and eventually settles to the value proportional to the product of angular rotation velocity of the field and the Berry curvature. (2) We re-examine the Landau–Zener transition for a system coupled to environment at arbitrary temperature. We show that as temperature increases, the thermal excitation and relaxation become leading processes responsible for transition between states of the system. We also apply the Lindblad master equations to these two problems and compare results with those obtained from the Bloch–Redfield equations.

In Chapter 5, we consider a one dimensional spin 1/2 chain with Heisenberg interaction in a random parallel magnetic field. This system is known to exhibit the MBL transition at critical strength of random field. We analyze the response of the chain when additional perpendicular magnetic field is applied to an individual spin. We show that the response changes across the MBL transition. Then, we propose a method for accurate determination of the mobility edge via local spin measurements. We further demonstrate that the exponential decrease of the spin response with the distance between perturbed spin and measured spin can be used to characterize the localization length in the MBL phase.

In Chapter 6, we consider a one dimensional spin chain system with quenched disorder and in the presence of a local harmonic drive. We study the time evolution of the system in the Floquet basis and evaluate the Bures displacement of the system in the Hilbert space caused by the drive per one period. This displacement can be used to identify two phases of the system: (1) the many-body localized phase, in which the distribution of the distance exhibits long tails while its average value decreases rapidly as disorder increases; and (2) the ergodic phase, in which the displacement distribution is narrow and its average value weakly depends on disorder. This distinction in the average value of the displacement between the two phases develops readily for system with ten or more spins. Therefore, recently built networks of superconducting qubits subject to a local microwave drive can simulate dynamics of a system in the many-body localization regime. We also show that from thermodynamics point of view, the two phases can also be distinguished and hence

probed by von Neumann entropy, energy fluctuations and spin diffusions, as long as the drive is sufficiently weak.

1.5 Publication List

The work in this thesis is presented in six chapters. The contents of Chapter 2, 3 and 4 have appeared in three separate published works. The material of Chapter 5 and 6 is at present being prepared for publication. In addition, there is another coauthored publication, Ref.[20], whose material is not presented in the thesis.

Chapter 2 is based on Ref.[21], titled Quantum photovoltaic effect in double quantum dots, and published in January 2013. This work was completed with Maxim G. Vavilov. Support for this work was provided in part by NSF (DMR-1105178) and the Donors of the American Chemical Society Petroleum Research Fund. Fruitful discussions with R. McDermott and J. Petta were helpful.

Chapter 3 is based on Ref. [22], titled Full counting statistics of photons emitted by a double quantum dot, and published in November 2013. This work was completed with Maxim G. Vavilov. Support for this work was provided in part by NSF Grant No. DMR-1105178, ARO and LPS Grant No. W911NF-11-1-0030. Fruitful discussions with R. McDermott, H. Treci and J. Petta were helpful.

Chapter 4 is based on Ref.[19], titled Nonadiabatic dynamics of a slowly driven dissipative two-level system, and published in May 2014. This work was completed with Amrit Poudel and Maxim G. Vavilov. Support for this work was provided in part by NSF Grants No. DMR-1105178 and DMR-0955500, ARO and LPS Grant No. W911NF-11-1-0030. Fruitful discussions with I. Aleiner, A. Glaudell, F. Nori, A. Polkovnikov, S. Shevchenko and A. Levchenko were helpful.

Chapter 5 is based on a work preparing for submission, titled Response to a local quench of a system near many body localization transition, as well as a related unpublished work. This work was completed with Maxim G. Vavilov. Support for this work was provided in part by NSF Grants No. DMR-1105178 and DMR-0955500, ARO and LPS Grant No.

W911NF-11-1-0030. Fruitful discussions with D. Basko, D. Huse, L. Ioffe, R. Nandkishore and V. Oganesyan were helpful.

Chapter 5 is based on a work preparing for submission, titled Many-body localization in a quantum system subject to a local periodic drive. This work was completed with Maxim G. Vavilov. Support for this work was provided in part by NSF Grants No. DMR-1105178 and DMR-0955500, ARO and LPS Grant No. W911NF-11-1-0030. Fruitful discussions with D. Basko, D. Huse, L. Ioffe, R. Nandkishore and V. Oganesyan were helpful.

Chapter 2

Quantum photovoltaic effect in double quantum dots

2.1 Introduction

The interaction of electrons in conductors with electromagnetic fields has long been considered within a classical picture of electromagnetic (EM) radiation. A widely–known example is the photon assisted tunneling (PAT) in double quantum dot (DQD) systems[23], when the EM field brings an electron trapped at the ground state to an excited state and facilitates electron transfer. This classical description of the EM field breaks in high-quality microwave resonators based on superconducting transmission line geometry[24]. Interaction of such EM fields with electronic devices require a quantum treatment known as the circuit quantum electrodynamics (cQED)[25, 26].

Recently, several experimental groups studied systems consisting of a superconducting high quality resonator and a DQD[27, 28, 29, 30, 31] or a voltage biased Cooper pair box[32]. The coupling strength between a resonator photon mode and electron states in a DQD is characterized by the vacuum Rabi frequency g with reported values in the range of $g/2\pi \sim 10^8$ Hz. These systems call for re-examination of the PAT by taking into account a quantum description of the EM field in terms of photon excitations. One may expect at least two

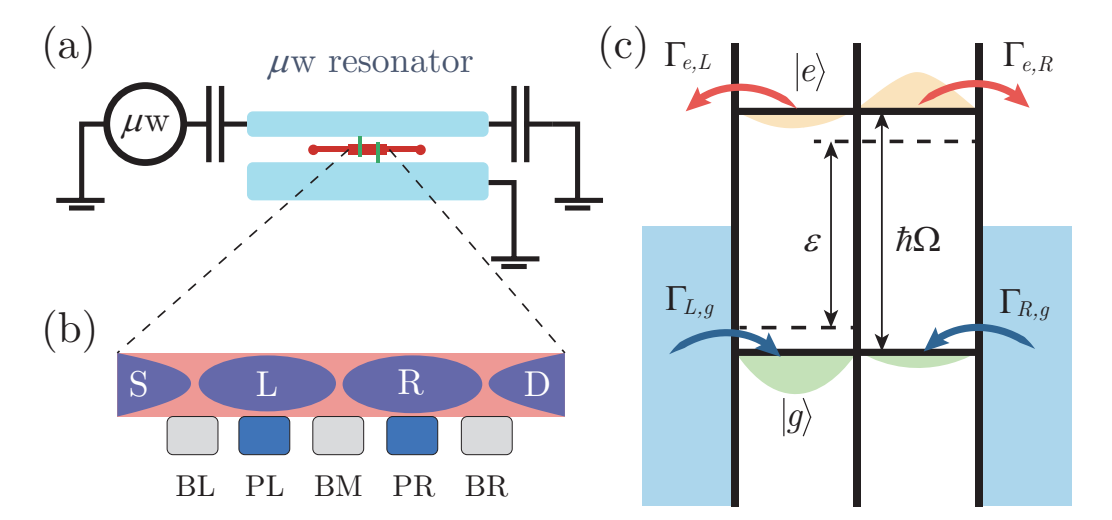


Figure 2.1: (a) An illustration of a DQD and a transmission line resonator coupled to an external microwave source μ w. (b) A schematic view of the DQD. Electrons are confined to the left (L) and right (R) dots by barrier gates BL, BM, and BR that also control electron tunneling rates between the source, S, and the left dot, the left and right dots, and the right dot and the drain, D, respectively. Electrostatic energies of two quantum dots are defined by the plunger gates, PL and PR, and the PL gate is also connected to an antinode of the resonator, see e.g. Refs.[29, 31]. (c) Electronic states of the DQD are presented in both the eigenstate basis (solid lines) and the left–right basis (dashed lines). Tunneling from the excited state, $|e\rangle$, to the left/right lead, with rate $\Gamma_{e,L/R}$ and from the left/right lead to the ground state, $|g\rangle$, with rate $\Gamma_{L/R,g}$ are illustrated by arrows.

important distinctions from the classical treatment: (1) the Lamb shift that renormalizes quantum states of electrons and photons; (2) spontaneous photon emission that breaks symmetry between absorption and emission processes and is important in systems with either a finite voltage bias between the leads[33, 34, 35] or an inhomogeneous temperature distribution[36].

In this chapter we study the photovoltaic current through a DQD coupled to a highquality microwave resonator at zero bias across the DQD. The resonator is driven by external microwave source that populates a photon mode of the resonator, see Figure. 2.1. The photons excite electrons in the DQD and produce electric current even at zero bias, similar to the classical PAT case[23, 37, 38]. We show that due to the coupling of electrons and photons, the current as a function of the source frequency has a multiple peak structure with splitting between the peaks determined by the coupling strength g and reflects the Lamb shift of electronic energy states. We also demonstrate that the interaction-induced splitting is sensitive to the energy and phase relaxation rates in the DQD.

We note that the photovoltaic effect discussed here is a common phenomenon when the current in an electronic circuit is generated by out-of-equilibrium EM environment. Examples of this phenomenon include the current response of a DQD in the vicinity of the biased quantum point contact[39] or another circuit element out of equilibrium[40] with the electronic system. However, because out-of-equilibrium photons of the environment have a broad spectrum, the generated current does not exhibit a resonant dependence on parameters of the system that we observe in a system of a single mode high quality resonator and a DQD.

2.2 Model

We consider a DQD system with each dot connected to its individual electron reservoir at zero temperature and at zero bias between the reservoirs, see Figure. 2.1(b,c). The gate voltages of the DQD are adjusted near a triple point of its stability diagram[23]. To be specific, we choose a triple degeneracy point between (N_l, N_r) , (N_l+1, N_r) and (N_l, N_r+1) electron states in the DQD and denote these states as $|0\rangle$, $|L\rangle$ and $|R\rangle$, respectively. We model the system by the Hamiltonian $\tilde{H} = H_{\text{DQD}} + H_r + H_{\text{int}}$, where H_{DQD} describes states with an extra electron in the left or right dot, $|L\rangle$ or $|R\rangle$:

$$H_{\text{DQD}} = \frac{1}{2}\varepsilon\tau_z + \mathcal{T}\tau_x,\tag{2.1}$$

with ε being the electrostatic energy difference between the two states, and \mathcal{T} being the tunnel matrix element of an electron between the dots. The Pauli matrices are defined in the subspace of states $|L\rangle$ and $|R\rangle$ as $\tau_x = |R\rangle\langle L| + |L\rangle\langle R|$ and $\tau_z = |R\rangle\langle R| - |L\rangle\langle L|$. A resonator driven by an external microwave source is described by the Hamiltonian

$$H_r = \hbar\omega_0 a^{\dagger} a + 2\hbar F(a^{\dagger} + a)\cos\omega t \tag{2.2}$$

with a (a^{\dagger}) denoting the annihilation (creation) operators for microwave photons in the resonator, $\hbar F$ being the amplitude of the external drive of the resonator and ω_0 (ω) being

frequency of the resonator (source). The interaction between the microwave field and the DQD system is represented by [33]

$$H_{\rm int} = \hbar g_0 (a^{\dagger} + a) \tau_z. \tag{2.3}$$

This interaction describes the shift of energy difference between states $|R\rangle$ and $|L\rangle$ due to the electric potential of the plunger gates defined by the microwave photon field. We assume that the photon field is distributed between the left and right plunger gates, see Figure. 2.1(b) and does not influence the source and drain voltage to avoid the rectification effects[41, 42, 43].

Further calculations are more convenient in the basis of the ground, $|g\rangle$, and excited, $|e\rangle$ states of the Hamiltonian, Eq. (3.1):

$$|e\rangle = \cos(\theta/2) |L\rangle + \sin(\theta/2) |R\rangle,$$

$$|g\rangle = -\sin(\theta/2) |L\rangle + \cos(\theta/2) |R\rangle.$$
 (2.4)

Here $\theta = \arctan(2\mathcal{T}/\varepsilon)$ characterizes the hybridization of the $|L\rangle$ or $|R\rangle$ states. The energy splitting between the eigenstates $\hbar\Omega = \sqrt{\varepsilon^2 + 4\mathcal{T}^2}$ can be tuned independently by varying ε and \mathcal{T} via dc gate voltages. We further eliminate the time-dependence in Hamiltonian Eq.(2.2) by applying unitary operator $\mathcal{U} = \exp(-i\omega t(a^{\dagger}a + \sigma_z/2))$ and utilize the rotating frame approximation to obtain [33, 35]

$$\frac{H}{\hbar} = \frac{1}{\hbar} \mathcal{U}^{\dagger} \tilde{H} \mathcal{U} - i \frac{\partial \mathcal{U}^{\dagger}}{\partial t} \mathcal{U} = \frac{\Omega - \omega}{2} \sigma_z
+ (\omega_0 - \omega) a^{\dagger} a + g(a\sigma^+ + a^{\dagger}\sigma^-) + F(a^{\dagger} + a),$$
(2.5)

where $g = g_0 \sin \theta$ characterizes the actual strength of the coupling between the microwave field and DQD states responsible for photon absorption or emission, the Pauli matrices $\sigma_z = |e\rangle \langle e| - |g\rangle \langle g|, \, \sigma^- = |g\rangle \langle e| \text{ and } \sigma^+ = |e\rangle \langle g| \text{ are defined in terms of eigenstates of the}$ electron Hamiltonian, Eq. (3.1).

We analyze the behavior of the system with Hamiltonian Eq. (2.5) in the presence of relaxation in electron and photon degrees of freedom by employing the Born-Markov master

equation for the full density matrix

$$\dot{\rho} = \mathcal{L}_{\text{tot}}\rho = -\frac{i}{\hbar} \left[H, \rho \right] + \mathcal{L}_{\text{diss}}\rho. \tag{2.6}$$

The first term on the r.h.s. of Eq.(3.4) describes the unitary evolution of the system and the second term accounts for the dissipative processes in the resonator and DQD systems [39]

$$\mathcal{L}_{diss}\rho \equiv \kappa \mathcal{D}(a)\rho + \gamma \mathcal{D}(\sigma^{-})\rho + \frac{\gamma_{\phi}}{2}\mathcal{D}(\sigma_{z})\rho + (\Gamma_{L,g} + \Gamma_{R,g})\mathcal{D}(c_{g}^{\dagger})\rho + (\Gamma_{e,L} + \Gamma_{e,R})\mathcal{D}(c_{e})\rho,$$
(2.7)

where $\mathcal{D}(x)\rho = \left(2x\rho x^{\dagger} - x^{\dagger}x\rho - \rho x^{\dagger}x\right)/2$ is the Lindblad superoperator. The relaxation of the photon field in the resonator with rate κ is represented by $\kappa \mathcal{D}(a)\rho$ and the electron relaxation from the excited state $|e\rangle$ to the ground state $|g\rangle$ with rate γ is represented by $\gamma \mathcal{D}(\sigma^{-})\rho$. The last two Lindblad superoperators account for the loading of the ground state $|g\rangle$ and unloading of the excited state $|e\rangle$ of the double quantum dot via electron tunneling in terms of operators $c_{e} = |0\rangle \langle e|$ and $c_{g}^{\dagger} = |g\rangle \langle 0|$, respectively. The tunneling rates $\Gamma_{L,g} = \Gamma_{l}\cos^{2}(\theta/2)$, $\Gamma_{R,g} = \Gamma_{r}\sin^{2}(\theta/2)$, $\Gamma_{e,L} = \Gamma_{l}\sin^{2}(\theta/2)$ and $\Gamma_{e,R} = \Gamma_{r}\cos^{2}(\theta/2)$ are written in terms of tunneling rates $\Gamma_{l/r}$ in the basis of $|L\rangle$ and $|R\rangle$ states.

Note that in Eq.(3.4), the dynamics of state $|0\rangle$ only appears via the tunneling terms involving $D(c_e)\rho$ and $\mathcal{D}(c_g^{\dagger})\rho$. These terms can be categorized by whether the empty state is loaded from the left or right lead with coefficients depending on projection of the eigenstates onto the left/right states, as shown in Figure. 2.1. In this picture,[39] the photovoltaic current is given by

$$I = e\Gamma_r \left(\cos^2 \frac{\theta}{2} \langle e | \bar{\rho} | e \rangle - \sin^2 \frac{\theta}{2} \langle 0 | \bar{\rho} | 0 \rangle \right). \tag{2.8}$$

in terms of the reduced density matrix $\bar{\rho} = \text{Tr}_{ph}\{\rho\}$, where we traced out photon degrees of freedom of the resonator. We also analyze the number of photons in the resonator,

$$\bar{N} = \text{Tr}\left\{a^{\dagger}a\rho\right\},$$
 (2.9)

where we trace out both photon and electron degrees of freedom.

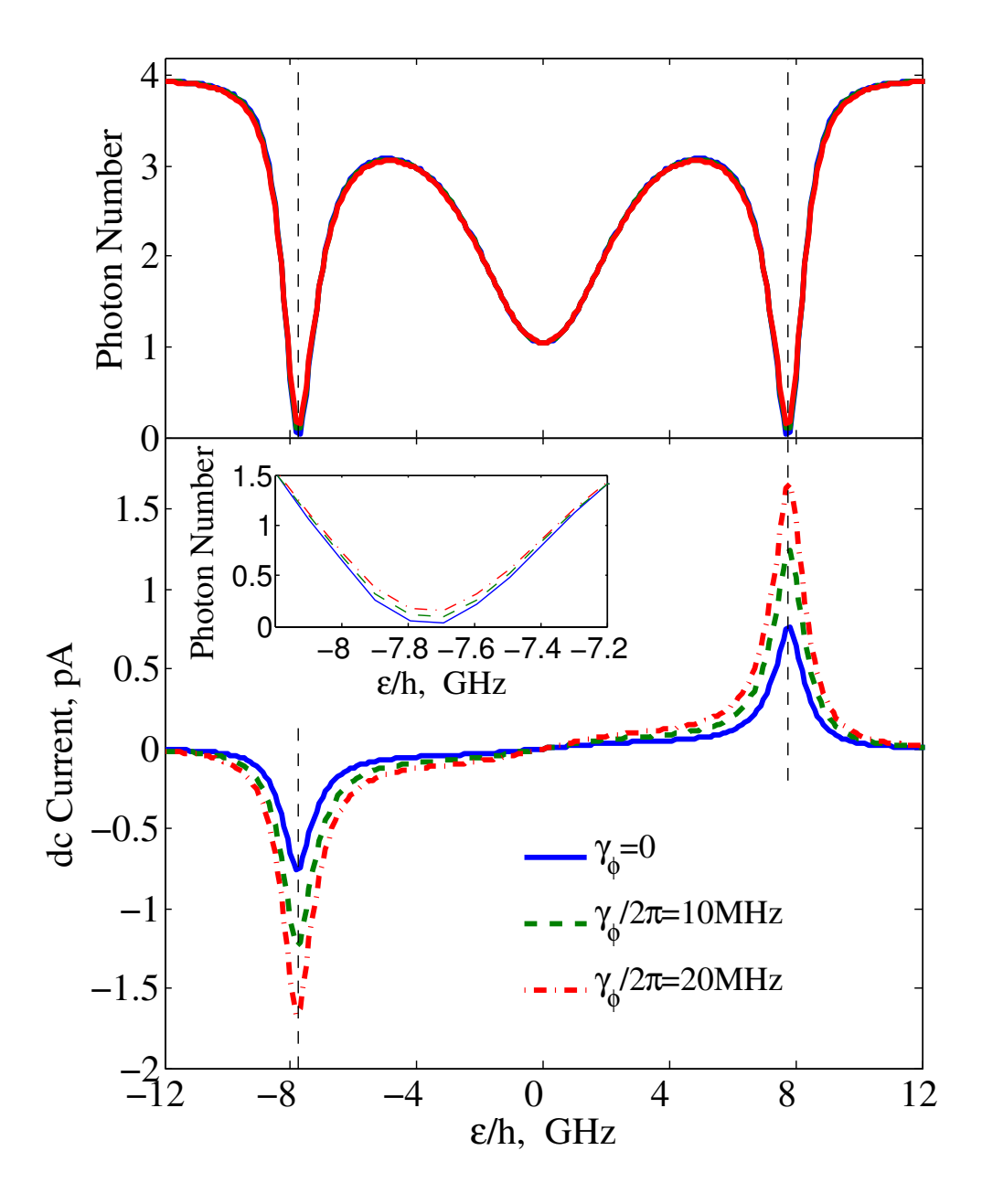


Figure 2.2: The average number of photons in the resonator and the photovoltaic current as functions of level bias ε for $\mathcal{T}/2\pi=1$ GHz, $F=50~\mu\mathrm{s}^{-1}$ and $\omega_0/2\pi=8$ GHz. The current is generated near the resonant condition when $\varepsilon=\pm\sqrt{\hbar^2\omega_0^2-4\mathcal{T}^2}$ (vertical lines). The three curves represent different dephasing rates γ_ϕ the DQD.

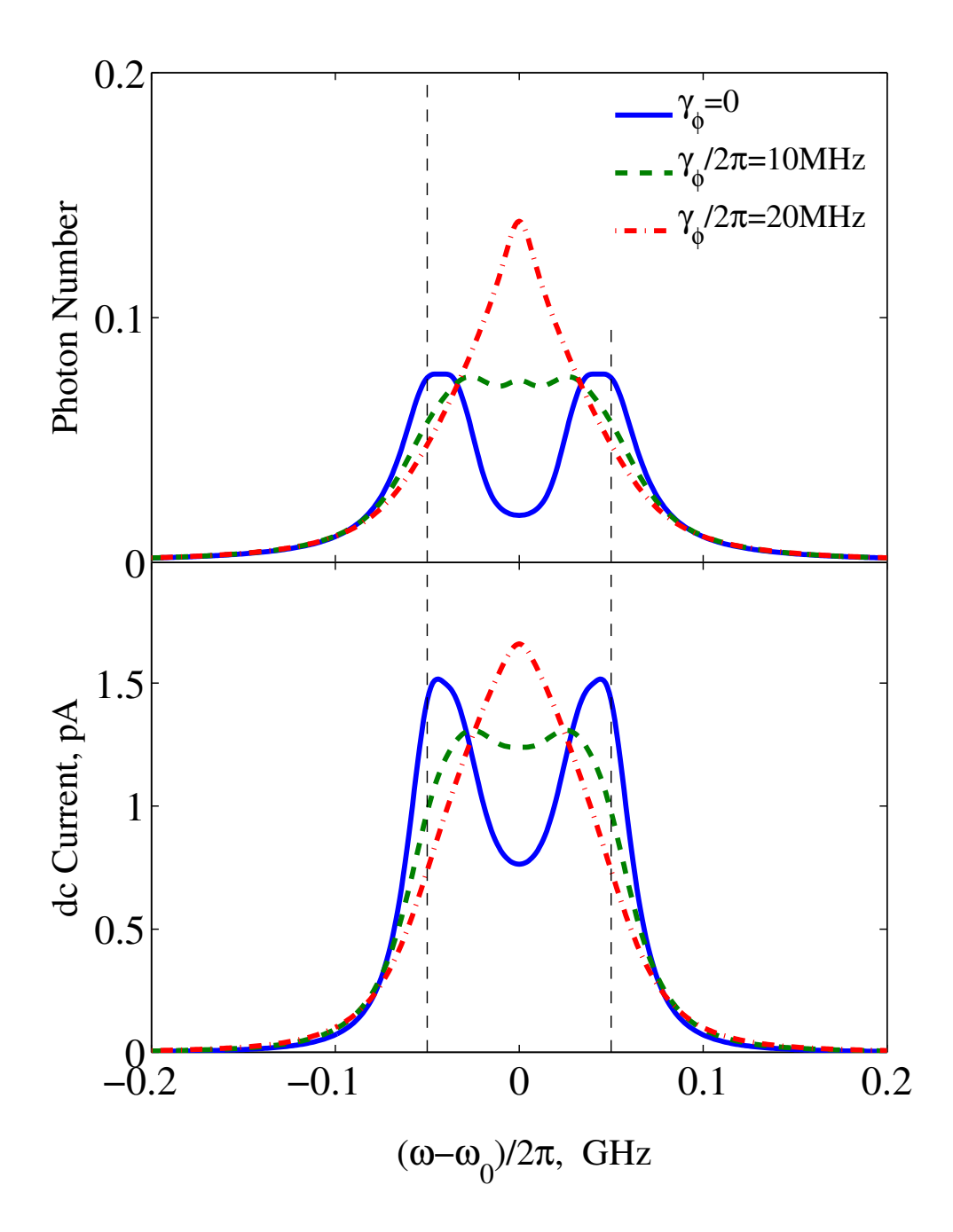


Figure 2.3: The average number of photons in the resonator and the photovoltaic current as a function of the frequency ω of the microwave drive for $\mathcal{T}/2\pi = 1$ GHz, $F = 50~\mu\text{s}^{-1}$ and $\Omega = \omega_0 = 2\pi \times 8$ GHz, $g/2\pi = 48.5$ MHz. For $\gamma_{\phi} = 0$, both average number of photons \bar{N} and the photovoltaic current show local minima at $\omega = \omega_0$ and local maxima near $\omega = (E_{1,\pm} - E_0)/\hbar$, shown by vertical lines. As the dephasing rate γ_{ϕ} increases, the double peaks merge to a single peak at $\omega = \omega_0$.

2.3 Results

The average number of photons in the resonator, \bar{N} , and the dc component of photocurrent can be found using the steady state solution of the master equation, (3.4), with $\dot{\rho} = 0$. We numerically find the full density matrix ρ for a double quantum dot and photon field of the resonator in the Fock's space using Quantum Optics Toolbox [44] and QuTiP [45], both of which provide consistent results. The steady state solution for the density matrix ρ defines the average number of photons \bar{N} , Eq. (2.9), and the photocurrent, Eq. (2.8).

Our choice of parameters is motivated by Ref. [29]. We choose the relaxation rate $\gamma = 2\pi \times 25$ MHz, the resonator relaxation rate $\kappa/2\pi = 8$ MHz, tunneling amplitude between the individual dots $\mathcal{T}/2\pi = 1$ GHz, the tunneling rate from a dot to a lead $\Gamma_{l/r} = 2\pi \times 30$ MHz, and the resonator frequency $\omega_0/2\pi = 8$ GHz. We note that to keep the coupling constant finite, we have to take $\mathcal{T} \sim \hbar\Omega$, since $g = g_0 \sin \theta$, Eq. (2.5), vanishes for $\mathcal{T} = 0$. Below we fix $g_0/2\pi = 200$ MHz.

First, we investigate dependence of the photocurrent on the separation between energy levels in the double quantum dot, controlled by the electrostatic energy difference ε . We take frequency ω of microwave source to be equal to the resonator frequency, $\omega = \omega_0$, and fix the drive amplitude $F = 50~\mu s^{-1}$. Dependence of the average number of photons in the resonator and the photocurrent on energy ε is presented in Figure. 3.2 for three values of the dephasing rate $\gamma_{\phi}/2\pi = 0$, 10, 20MHz. As the energy difference between the excited and ground states of the quantum dot goes through the resonance $\Omega = \omega_0$, we observe a significant suppression of the photon number in the resonator, see the top panel and the inset in Figure 3.2. This is expected behavior because the DQD system enhances photon absorption in the resonator at $\Omega \simeq \omega_0$. Absorbed photons cause transitions between the ground and excited electronic states. These electrons tunnel to the leads and generate electric current though the DQD. This current is shown in the lower panel of Figure 3.2 and is peaked at $\varepsilon = \pm \sqrt{\hbar^2 \omega_0^2 - 4T^2}$ or $\varepsilon/(2\pi\hbar) \simeq \pm 7.75 \text{GHz}$, indicated by dashed vertical lines.

One feature in Figure 3.2 is that the photon number is also reduced at zero bias ε , when

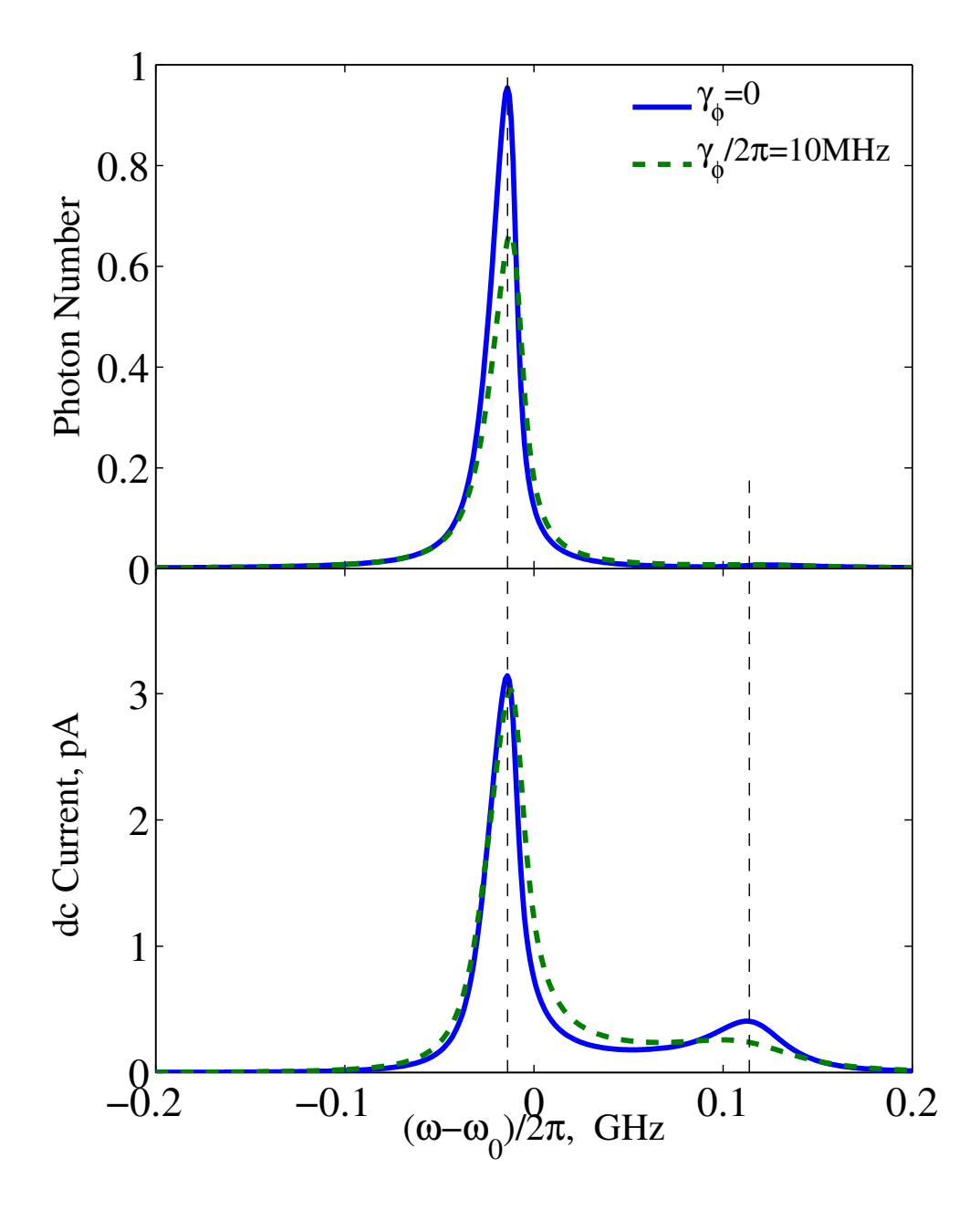


Figure 2.4: The average number of photons in the resonator and the photovoltaic current as a function of the frequency ω of the microwave drive for detuned DQD and resonator system with $\Omega/2\pi = 8.1$ GHz, $\omega_0/2\pi = 8.0$ GHz, the intradot tunneling $\mathcal{T}/2\pi = 1$ GHz, and the drive amplitude F = 50 MHz. The photon average number has a peak at $\omega = (E_{1,-} - E_0)/\hbar$, Eq. (2.10), while the photovoltaic current exhibits a double peak feature at $\omega = (E_{1,\pm} - E_0)/\hbar$ (vertical lines).

the photovoltaic current vanishes. This suppression is a result of strong enhancement of the coupling constant $g = g_0$ at $\varepsilon = 0$, resulting in stronger dissipation in the resonator and increase of off-resonant absorption rate. At the same time the photovoltaic current vanishes at $\varepsilon = 0$ due to cancellation between the two terms in Eq.(2.8).

The curves for the photon number and the current do not significantly change after the dephasing rate γ_{ϕ} is introduced in addition to the energy relaxation rate γ . Dephasing smears the resonant condition for the photon absorption by the DQD and has two effects: (1) the number of photons increases a little near the resonance $\Omega \simeq \omega_0$, see the inset in Figure 3.2; (2) the resonant absorption of photons by electrons is suppressed resulting in reduction of the photocurrent. We note that in the case presented in Figure 3.2 the first effect is stronger than the second effect and dephasing increases the magnitude of photocurrent for the case of fixed $\omega = \omega_0$.

Next, we consider the case when the frequency of the microwave source, ω , is varied while the energy splitting $\hbar\Omega$ of the DQD and the resonator frequency ω_0 are fixed. The microwave radiation is mostly reflected when its frequency does not match the difference between energies $E_{n,\pm}$ of the resonator and DQD system defined by the Jaynes-Cummings spectrum:

$$E_{n,\pm} = n\hbar\omega_0 \pm \frac{\hbar}{2}\sqrt{4g^2n + \Delta^2}, \quad E_0 = \frac{\hbar\Delta}{2}, \tag{2.10}$$

where $\Delta = \omega_0 - \Omega$ is the detuning between the DQD and the resonator. We demonstrate that for DQD with weak energy and phase relaxations, this resonant admittance of the microwave source to the resonator results in the peak structure of the average photon number and the photocurrent.

In Figure 3.3, we plot the average number of photons in the resonator and the photocurrent as a function of the drive frequency ω for $\omega_0 = \Omega$ and for the choice of other system parameters identical to those for curves in Figure 3.2. At vanishing dephasing rate, $\gamma_{\phi} = 0$, we observe a double peak feature in both photon number and photocurrent curves, see Figure 3.3. These peaks at $\omega_{\pm} = (E_{1,\pm} - E_0)/\hbar$ are defined by the level spacing of the Jaynes-Cummings Hamiltonian and are shown by vertical dashed lines in Figure 3.3.

The two peaks merge at $\omega = \omega_0$ as the dephasing rate increases and destroys quantum entanglement between photons and DQD states.

At finite detuning between the resonator and the DQD, $\Delta \gtrsim g = 2\pi \times 48.5$ MHz, the eigenstates of the system become dominantly photon states or electron states of the DQD. As a result, the microwave source increases the number of photon excitations in the resonator when the microwave frequency is in resonance with the transition between the photon-like states, $\omega_{1,-} = (E_{1,-} - E_0)/\hbar$. But the source has a weak effect at the resonance with the electron-like states at frequency $\omega_{1,+} = (E_{1,+} - E_0)/\hbar$. We present the corresponding dependence of the photon number and the photocurrent in Figure 3.4 for $\omega_0/2\pi = 8$ GHz, $\Omega/2\pi = 8.1$ GHz ($\Delta = 100$ MHz) and other parameters identical to those for in Figs. 3.2 and 3.3. We indeed observe one large peak in the photon number near the resonant condition for the dominantly photon state with energy $E_{1,-}$ while the photon number does not show significant enhancement near the second resonance, corresponding to the transition to the dominantly electronic state with energy $E_{1,+}$. The photocurrent still exhibits double peak feature, but the peak corresponding to the photon resonance is higher, when the microwave drive produces a higher photon population.

We now consider a more idealistic regime of significantly reduced tunneling and relaxation rates $\Gamma_l = \Gamma_r = \gamma = 2\pi \times 100$ kHz, the drive amplitude $F/2\pi = 30$ MHz and $\omega_0 = \Omega = 2\pi \times 8$ GHz. In this case additional resonances develop, see Figure 3.6. These resonances correspond to excitations of several photons in the cavity by the microwave source. When the frequency of the source satisfies $\hbar\omega n = E_{n,\pm} - E_0$, the DQD-resonator system experiences transitions from the ground state to the energy state $E_{n,\pm}$, cf. Ref. [46]. These multiphoton transitions result in peaks of the average photon number and the magnitude of the photocurrent. Curves in Figure 3.6 have three pairs of peaks at frequencies $\omega_{n,\pm} = \omega_0 \pm g/\sqrt{n}$ marked by vertical dashed lines for n = 1, 2, 3. We notice that for $\omega = \omega_{1,2}$ the average photon number is nearly the same, see the top panel in Figure 3.6(a), while the photon distribution function is different, Figure 3.6(b): at $\omega = \omega_{2,-}$ a non-zero P_2 develops for a probability that the resonator contains two photons. This difference in

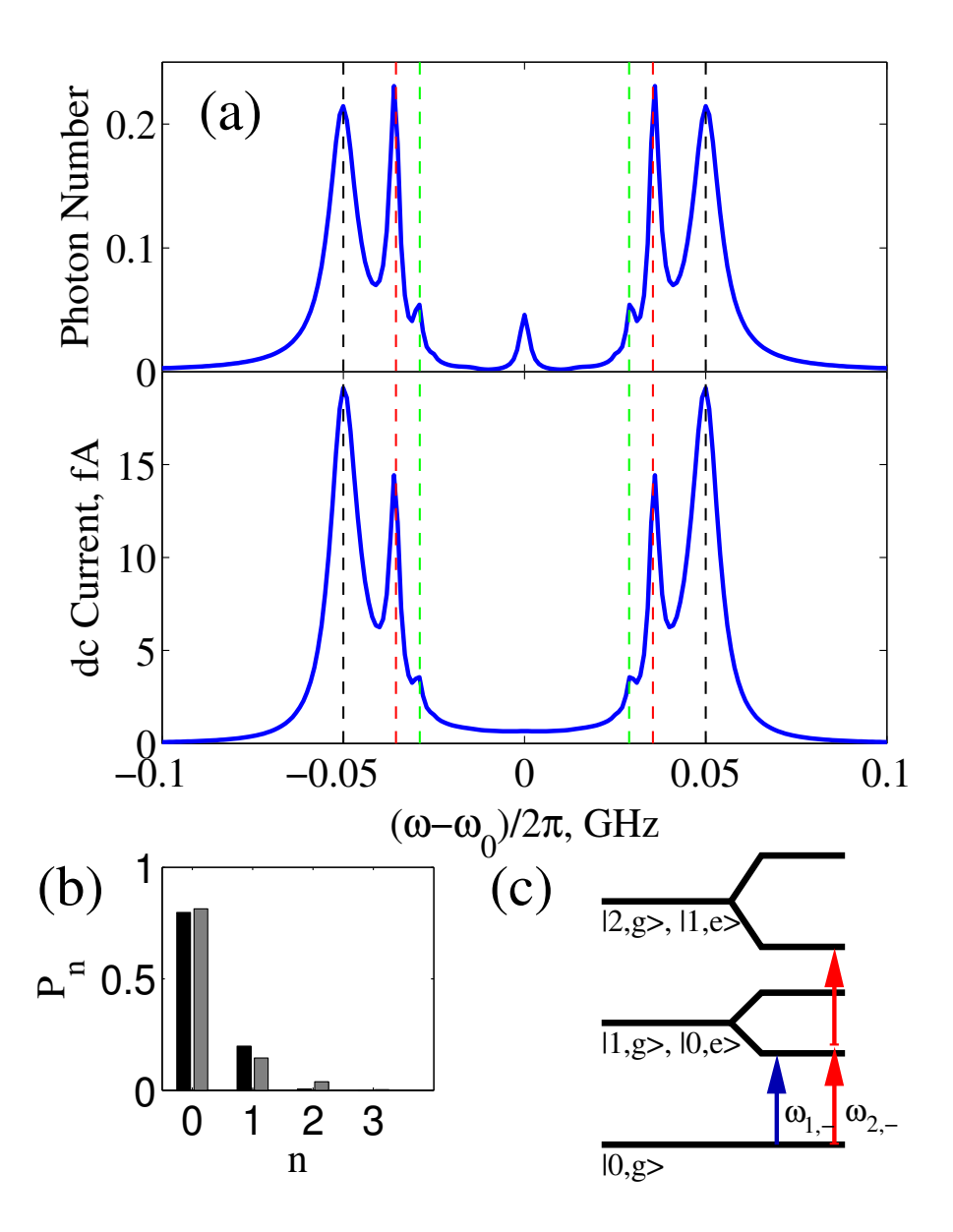


Figure 2.5: (a) The average number of photons in the resonator and the photovoltaic current as a function of the frequency ω of the microwave drive for $\Omega = \omega_0 = 2\pi \times 8$ GHz, the intradot tunneling $\mathcal{T}/2\pi = 1$ GHz, and the drive amplitude $F/2\pi = 30$ MHz and extremely low tunneling rates to the leads and the energy relaxation rate, $\Gamma_l = \Gamma_r = \gamma = 2\pi \times 100$ kHz. The photon average number and the photocurrent have several peaks at $\omega_{n,\pm} = (E_{n,\pm} - E_0)/n\hbar$ with n = 1, 2, 3, these frequencies, calculated from Eq. (2.10) are shown by vertical lines). (b) The histogram presents the probabilities P_n to have n photons in the resonator steady state at drive frequency ω_1 (dark bars) and ω_2 (grey bars). (c) The diagram is a schematic picture for the Jaynes-Cummings energy levels showing single and two photon excitations.

 P_n indicates that the microwave drive line does not match the resonator to produce a two photon occupation of the resonator at $\omega = \omega_1$, but it matches the resonator to populate the state with the energy $E_{2,\pm}$, which then decays to the lower energy states with n = 1, 0.

Next, we investigate dependence of the photon number in the resonator and the magnitude of the photovoltaic current for different amplitudes F of the drive. The above discussion was mostly focused on a resonator containing less than one photon. As the drive increases, the double peak feature evolves to a single peak at the drive frequency equal to the frequency of the resonator, $\omega = \omega_0$. We interpret this cross-over as a signature of changed hierarchy of the terms in the system Hamiltonian. At weak drive, we have a JC Hamiltonian with its peculiar energy levels, Eq.(2.10), and the drive can be viewed as a weak probe testing the spectral structure of the coupled resonator and DQD system. Once the drive reaches the strength of the g coupling, $g \simeq 2\pi \times 50$ MHz, a proper way to treat the system is to start with the Floquet-type states [38, 47, 48] of the driven resonator and then to take into account the interaction of these states with the DQD system as a perturbation. In this picture, the photon resonance happens at $\omega = \omega_0$. The coupling g is responsible for the formation of the broader "wings" in curves for the average photon number and the photocurrent. These wings are more pronounced in the photovoltaic current, which is entirely due to the coupling between resonator and DQD. This broad structure of the generated current as a function of the source frequency is preserved even at stronger drive. Thus, the shape of the photovoltaic curve might provide an experimental approach to quantify the strength of the JC coupling constant.

2.4 Discussion and Conclusion

We analyzed the photovoltaic current through a DQD system at zero voltage bias between the leads. The double quantum dot interacts through its dipole moment to a quantized electromagnetic field of a high quality microwave resonator. The interaction is described by the Jaynes–Cummings Hamiltonian of a quantized electromagnetic field and a two level quantum system, represented by ground and excited electronic states of the double quantum

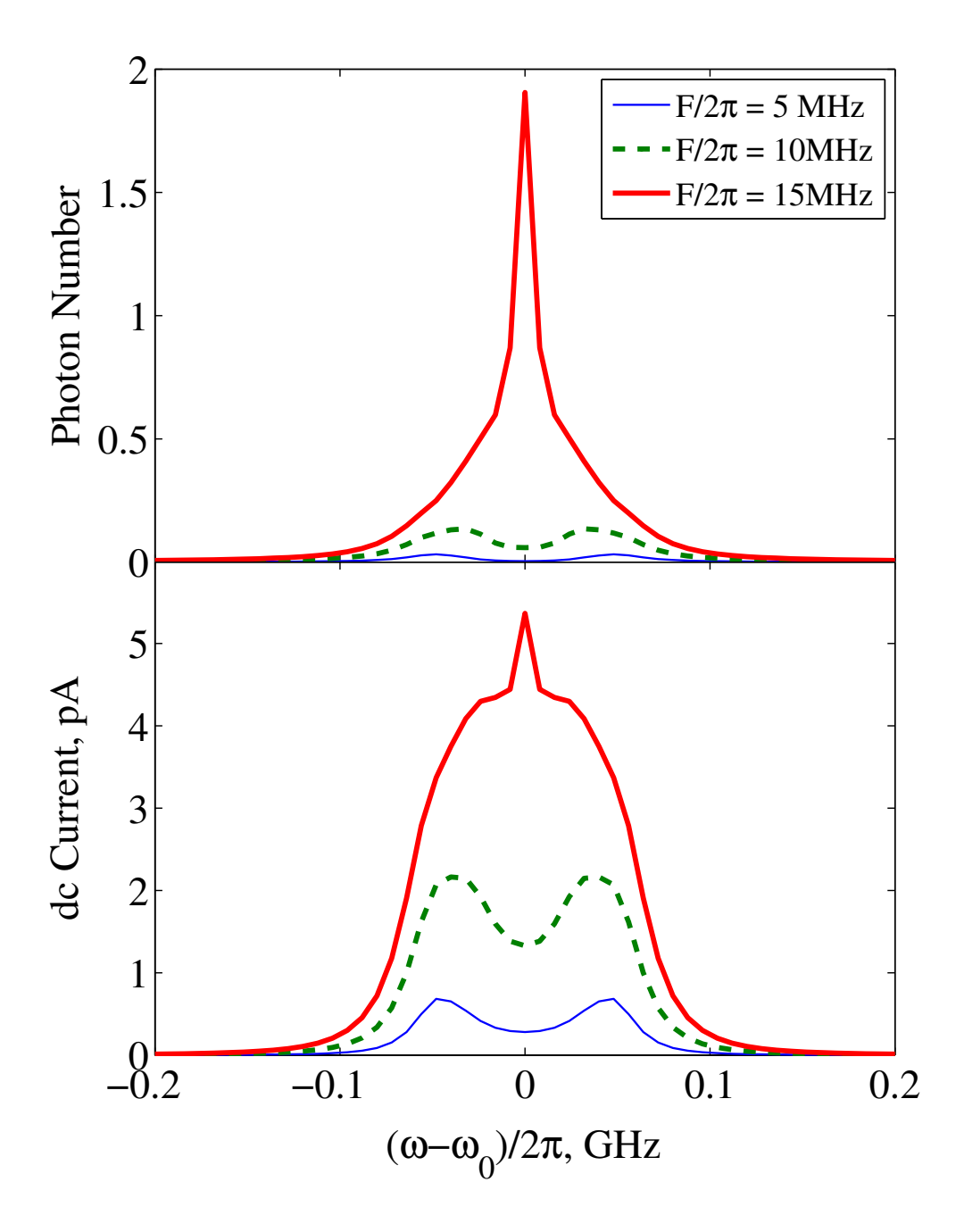


Figure 2.6: Dependence of the average photon number and the current on microwave frequency ω for several values of the drive amplitude $F/2\pi=5$, 10, 15 MHz, at zero dephasing $\gamma_{\phi}=0$ and other parameters are the same as in data in Figure 3.3. As the amplitude of the drive increases, the two peaks merge together to a single peak at $\omega=\omega_{0}$.

dot. When a weak microwave radiation is applied to the resonator, the source acts as a spectral probe that causes excitation of the system when the energy difference between its eigenstates is equal to the photon energy $\hbar\omega$ of the source. If this resonance condition is satisfied, the microwave source populates the photon mode of the resonator and generates a direct current though the double dot system even at zero bias.

We demonstrated that at finite, but still low energy and phase relaxation rates of the DQD, both the average number of photons in the resonator and the photocurrent through the DQD have a double-peak structure as functions of the frequency of the microwave source. This double peak structure reflects an avoided crossing of the energy states of the DQD and the resonator photons due to the interaction between the two subsystems and is reminiscent of the Lamb shift by a single electromagnetic mode. We also found that in the limit if extremely weak relaxation rates of the DQD, multiphoton resonances develop when the energy difference between the states of the coupled system is a multiple of $\hbar\omega$.

As energy and phase relaxation rates of the DQD increase, the peaks in the photon number and the photocurrent broaden and eventually merge in a single resonance peak at the frequency ω_0 of the resonator. In this limit, the resonator photon mode and the DQD are no longer described as an entangled quantum system and the resonant condition for the interaction of the microwave source with the system corresponds to equal frequencies of the source and the resonator mode, $\omega = \omega_0$.

At stronger microwave drive, frequency dependence of the average photon number in the resonator evolve from the Jaynes-Cummings double peaks at $\omega = \omega_0 \pm g$ to a single peak at the resonator frequency ω_0 . The single peak at $\omega = \omega_0$ is a result of multi-photon transitions at strong drive by the microwave source that all merge together due to finite width of multi-photon resonances. Similar evolution to a single peak occurs for the photocurrent response, although the photocurrent curve has a broader width as a function of the source frequency ω , this width corresponds to the strength of the coupling g between the photon mode of the resonator and the DQD and may be used to characterize the strength of this coupling in experiments.

Chapter 3

Full Counting Statistics of Photons Emitted by Double Quantum Dot

3.1 Introduction

The statistics of photons emitted by an electric current depends on the electron state of a conductor. If the electric current were classical, the photon field would be in a coherent state [49] with Poissonian statistics. An electron system with strong inelastic processes is characterized by thermal distribution and produce black-body radiation with super-Poissonian statistics of emitted photons. However, if the electron distribution is far from equilibrium, the photon counting statistics may become sub-Poissonian [50, 51, 52].

I Several experiments have recently been developed to study the statistics of photons in the GHz frequency range. Experiments [53, 54, 55] measured the photon statistics in a steady state of high quality resonator and distinguished between the thermal source and a coherent drive. The photon noise of a quantum point contact at finite bias was also investigated using an amplifier [56]. An alternative approach to study photon statistics utilizes a photon counter [57, 58]. An individual photon counter can provide the statistics of emitted photons, while a system with two counters can be used for Hanbury Brown-Twiss (HBT) interferometry [59], e.g. measurement of the second-order intensity correlation func-

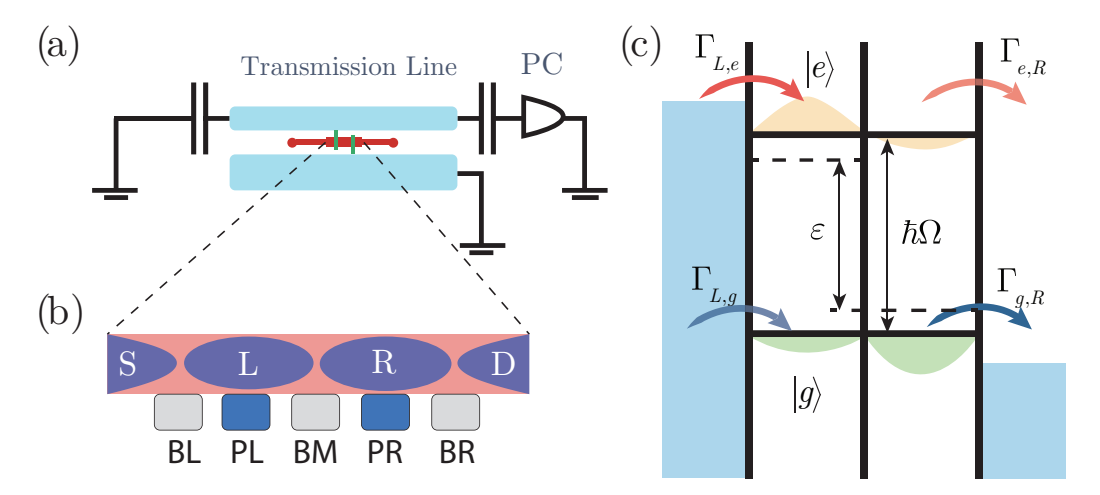


Figure 3.1: (a) An illustration of a DQD and a resonator (a $\lambda/2$ -transmission line) coupled to a photon counter (PC). (b) In the DQD, electrons are confined to the left (L) and right (R) dots by barrier gates BL, BM, and BR that also control electron tunneling rates between the source, S, and the left dot, the left and right dots, and the right dot and the drain, D, respectively. Electrostatic energies of two quantum dots are defined by the plunger gates, PL and PR, and the PL gate is also connected to an antinode of the transmutation line. (c) Electronic eigenstates of the DQD and tunneling from the left lead to the ground/excited state with rate $\Gamma_{L,q/e}$, and from the ground/excited state to the right lead with rate $\Gamma_{q/e,R}$.

tion $g^{(2)}(\tau)$. Generic HBT measurement indicates that noninteracting bosons and fermions would exhibit bunching and antibunching, respectively [60], while several more complicated examples of photon statistics caused by quantum electron transport have been proposed in systems with quantum point contact [50, 51, 52] and quantum Hall regime [61].

In this chapter we study statistics of photon radiation from a DQD coupled to a microwave resonator, a system that was recently studied experimentally by several groups [28, 27, 31, 29]. We show that photon statistics is sub-Poissonian with reduced noise in the flux of emitted photons from the resonator. This regime of reduced noise is robust for the considered system. While it is widely expected that photons produced by an electron source may show sub-Poissonian statistics, such a regime usually occurs under several stringent conditions. In particular, the emission statistics of a quantum point contact is sub-Poissonian only if the voltage bias does not exceed twice the photon energy and the contact has a single conduction channel, otherwise photons have super-Poissonian distribution [50, 51, 52]. In the setup considered here, a combination of Fermi statistics and

repulsion of electrons maintains the reduced noise in photon flux in a wide range of system parameters. Even a short dephasing time which is the main constraint for observation of quantum effects in DQDs hardly changes the distribution of emitted photons. It is the energy relaxation processes in the DQD that drive the photon distribution from sub- to super–Poissonian as the relaxation causes equilibration of the whole system and brings the photon field to a state similar to that of a thermal radiation. We argue that the system of a coupled DQD and a resonator can be used to study a cross-over from non-equilibrium to a thermal state in an interacting quantum system. Finally, our analysis indicates that the Josephson-based photon counters [57, 58] are suitable for studies of photon emission statistics by a DQD.

3.2 Counting Statistics Formalism

Double quantum dot coupled to a resonator

We study the statistical properties of photon emission by a voltage-biased DQD. The Hamiltonian for a system of a DQD and a resonator, shown in Figure 3.1, is presented as a combination of three terms, $H = H_{\text{DQD}} + H_{\text{ph}} + H_{\text{int}}$. The Hamiltonian of a DQD in the Coulomb blockade regime near a triple point in its electrostatic stability diagram [23] is represented by

$$H_{\rm DQD} = \frac{1}{2}\hbar\varepsilon\tau_z + \hbar\mathcal{T}\tau_x,\tag{3.1}$$

in the basis of electron states in the left, $|L\rangle$, and right, $|R\rangle$, quantum dots with electrostatic energy ε and the tunneling amplitude \mathcal{T} ; in this basis, $\tau_z = |L\rangle \langle L| - |R\rangle \langle R|$ and $\tau_x = |R\rangle \langle L| + |L\rangle \langle R|$. The term $H_{\rm ph} = \hbar \omega_0 a^\dagger a$ represents a noninteracting photon mode in the resonator. The interaction between charge and photon degrees of freedom is described by the Hamiltonian $H_{\rm int} = \hbar g_0 \left(a^\dagger + a \right) \tau_z$ [33, 35, 62, 21].

In further calculations, we use the eigenstates of the DQD Hamiltonian, Eq. (3.1),

namely the ground, $|g\rangle$, and excited, $|e\rangle$, states:

$$|e\rangle = \cos(\theta/2) |L\rangle + \sin(\theta/2) |R\rangle,$$

$$|g\rangle = -\sin(\theta/2) |L\rangle + \cos(\theta/2) |R\rangle.$$
(3.2)

Here $\theta = \arctan(2\mathcal{T}/\varepsilon)$ characterizes the hybridization between states $|L\rangle$ and $|R\rangle$ due to inter dot tunneling. The energy splitting between the eigenstates $\hbar\Omega = \hbar\sqrt{\varepsilon^2 + 4\mathcal{T}^2}$ can be tuned via gate voltages [23]. In the eigenstate basis, Eq. (3.2), and within rotating wave approximation, the Hamiltonian H is

$$H = \frac{\hbar\Omega}{2}\sigma_z + \hbar\omega_0 a^{\dagger} a + \hbar g(a^{\dagger}\sigma^- + a\sigma^+), \tag{3.3}$$

where $g = g_0 \sin \theta$ is the effective electron–photon coupling constant, and $\sigma^- = |g\rangle \langle e|$, $\sigma^+ = |e\rangle \langle g|$.

We analyze the behavior of the system with Hamiltonian Eq. (3.3) in the presence of decoherence in electron and photon degrees of freedom and tunneling of electrons between the DQD and the leads by employing the master equation for the full density matrix

$$\dot{\rho} = \mathcal{L}\rho = -\frac{i}{\hbar} \left[H, \rho \right] + \mathcal{D}_{\text{tot}}\rho, \tag{3.4}$$

where the commutator describes the unitary evolution of the system and

$$\mathcal{D}_{\text{tot}}\rho = \kappa \mathcal{K}(a)\rho + \mathcal{D}_{\text{DQD}}\rho \tag{3.5}$$

accounts for the total dissipative evolution described by Lindblad superoperators

$$\mathcal{K}(x)\rho = \left(2x\rho x^{\dagger} - x^{\dagger}x\rho - \rho x^{\dagger}x\right)/2. \tag{3.6}$$

The first term, $\kappa \mathcal{K}(a)\rho$, represents photon detection by an ideal photon counter with rate κ . The second term,

$$\mathcal{D}_{\text{DQD}}\rho = \gamma_r \mathcal{K}(\sigma^-)\rho + \frac{\gamma_\phi}{2} \mathcal{K}(\sigma_z)\rho + \Gamma_l \mathcal{K}(c_l^{\dagger})\rho + \Gamma_r \mathcal{K}(c_r)\rho, \tag{3.7}$$

describes dissipative dynamics of the DQD. Here, $\gamma_r \mathcal{K}(\sigma^-)\rho$ corresponds to electron relaxation from the excited to ground states at zero temperature; $\gamma_\phi \mathcal{K}(\sigma_z)\rho/2$ represents dephasing with rate γ_{ϕ} ; the last two terms in $\mathcal{D}_{\text{DQD}}\rho$ account for the processes [35] of loading state $|L\rangle$ from the source with tunneling rate Γ_l and unloading state $|R\rangle$ to the drain with tunneling rate Γ_r , see Figure 3.1, and we introduced $c_r = |0\rangle \langle R|$ and $c_l^{\dagger} = |L\rangle \langle 0|$.

We calculate the full counting statistics (FCS) of emitted photons defined as probability distribution $P_n(t)$ to count n photons during measurement time t. For a lossless resonator, the average photon count $\langle n \rangle = \sum n P_n(t) = \kappa \bar{N}t$ is determined by the photon number $\bar{N} = \langle a^{\dagger}a \rangle_{\rm st} = \text{Tr}\{\rho_{\rm st}a^{\dagger}a\}$ in the resonator and the photon detection rate [63] κ , here $\rho_{\rm st}$ is the steady state solution of Eq. (3.4): $\mathcal{L}\rho_{\rm st} = 0$. In particular, we are interested in the Fano factor, $F_{\rm ph} = [\langle n^2 \rangle - \langle n \rangle^2]/\langle n \rangle$, that characterizes its noise property. By definition, photon emission is Poissonian if $F_{\rm ph} = 1$, while for sub-(super-) Poissonian processes, $F_{\rm ph} < 1$ ($F_{\rm ph} > 1$).

Quantum jump approach

In this section we utilize the quantum jump approach [64] to calculate the FCS. The Liouvillian in Eq. (3.4) can be decomposed as

$$\dot{\rho}(t) = \mathcal{L}\rho(t) = (\mathcal{L}_0 + \mathcal{J})\,\rho(t),\tag{3.8}$$

where we have singled out the jump superopertor, $\mathcal{J}\rho = \kappa a \rho a^{\dagger}$, to describe the stochastic quantum jump associated with photon detection, and \mathcal{L}_0 governing the deterministic dynamics of the system. Since quantum jumps are discretized in counted photon numbers, the full density matrix $\rho(t)$ can be resolved in terms of individual components $\rho^{(n)}(t)$ representing a quantum trajectory with n photons being counted by the photon detector during time interval [0, t]:

$$\rho(t) = \sum_{n} \rho^{(n)}(t). \tag{3.9}$$

By definition, the equation of motions for $\rho^{(n)}(t)$ is

$$\dot{\rho}^{(n)}(t) = \mathcal{L}_0 \rho^{(n)}(t) + \mathcal{J}\rho^{(n-1)}(t). \tag{3.10}$$

These equations of motion are coupled and therefore hard to solve. It is more convenient to define the generalized density matrix

$$\tilde{\rho}(t,s) = \sum_{n} s^n \rho^{(n)}(t), \tag{3.11}$$

by introducing the counting variable for photons, s. The equations of motion for $\tilde{\rho}(t,s)$ is obtained by multiplying Eq. (3.10) by s^n and taking sum over n,

$$\dot{\tilde{\rho}}(t,s) = \mathcal{M}(s)\tilde{\rho}(t,s), \tag{3.12}$$

with

$$\mathcal{M}(s) = \mathcal{L}_0 + s\mathcal{J}. \tag{3.13}$$

For s = 1, Eq. (3.12) reduces to the original master equation Eq. (3.4). The formal solution of Eq. (3.12) is

$$\tilde{\rho}(t,s) = e^{\mathcal{M}(s)t}\tilde{\rho}(0,s), \tag{3.14}$$

where the initial state is chosen to be the steady state, $\tilde{\rho}(0,s) = \rho_{\rm st}$.

Next, we introduce moment generating function

$$\mathcal{G}(t,s) = \operatorname{Tr}\left\{\tilde{\rho}(t,s)\right\} = \operatorname{Tr}\left\{e^{\mathcal{M}(s)t}\tilde{\rho}(0,s)\right\}. \tag{3.15}$$

This function permits one to calculate the higher order moments. Indeed, the n resolved density matrix allows us to obtain the FCS of the system by taking trace of $\rho^{(n)}(t)$:

$$P_n(t) = \text{Tr}\{\rho^{(n)}(t)\}.$$
 (3.16)

Then, according to Eqs. (3.11) and (3.15), we identify

$$\mathcal{G}(t,s) = \sum_{n} s^{n} P_{n}(t). \tag{3.17}$$

The probability distribution $P_n(t)$ is given by the inverse Fourier transform in parameter $s = \exp(i\chi)$:

$$P_n(t) = \int^{2\pi} e^{-in\chi} \mathcal{G}(t, e^{i\chi}) \frac{d\chi}{2\pi}.$$
 (3.18)

The factorial moments $\langle \langle n^m \rangle \rangle_f$ of n can be obtained by derivatives of $\mathcal{G}(t,s)$:

$$\langle \langle n^m \rangle \rangle_{\rm f} = \sum_n P_n(t) \prod_{i=0}^{m-1} (n-i) = \left. \frac{\partial^m \mathcal{G}(t,s)}{\partial s^m} \right|_{s=1}.$$
 (3.19)

We note that Eq. (3.14) is understood as a Dyson series, therefore the generalized density matrix can be expanded into a sum of n photon detections:

$$\tilde{\rho}(t,s) = \mathcal{S}(t,0)\rho_{\rm st} + \sum_{n} \int_{-\infty}^{t} dt_{n} \cdots \int_{-\infty}^{t_{2}} dt_{1}$$

$$\mathcal{S}(t,t_{n})s(t_{n})\mathcal{J}(t_{n})\cdots\mathcal{S}(t_{2},t_{1})\mathcal{J}(t_{1})\mathcal{S}(t_{1},0)\rho_{\rm st},$$
(3.20)

where $S(t_1, t_2) = \exp \left[\mathcal{L}_0(t_1 - t_2) \right]$.

Computation of the Fano factor

In principle, the method described in the previous subsection can be used to calculate $P_n(t)$ and then the Fano factor in terms of the first and second order factorial moments, using Eq. (3.19). However, evaluation of factorial moments involve derivatives of generating function $\mathcal{G}(t,s)$ over s, which is not convenient in practice for numerical calculations. In this subsection, we describe a numerical method more suitable for numerical evaluation of Fano factors.

As mentioned in the previous subsection, photon counts over measurement time t are associated with evolution of the generalized density matrix subject to the corresponding quantum jump \mathcal{J} . Fluctuations in the number of counts are given by

$$\langle \delta n^2(t) \rangle = \frac{1}{2} \int_0^t dt_1 \int_0^t dt_2 \langle \{ \delta \mathcal{J}(t_1), \delta \mathcal{J}(t_2) \} \rangle, \qquad (3.21)$$

where $\delta \mathcal{J}(t) = \mathcal{J}(t) - J(t)$ is the quantum fluctuation of the photon counting measurement and $J(t) = \kappa \bar{N}(t) = \text{Tr} \mathcal{J} \rho_{\text{st}}$ is the average photon count rate; $\{A, B\}$ stands for an anticommutator. According to Eq. (3.20), we take first two orders of derivatives over s and

find the correlation function of photon counts during measurement time t:

$$\langle n^{2}(t)\rangle = \int^{t} dt_{1} \int^{t} dt_{2} \frac{\delta^{2} \operatorname{Tr} \tilde{\rho}(t, s)}{\delta s(t_{1}) \delta s(t_{2})} \Big|_{s=1}$$

$$+ \int^{t} dt \frac{\delta \operatorname{Tr} \tilde{\rho}(t, s)}{\delta s(t)} \Big|_{s=1}$$

$$= 2 \int^{t} dt_{1} \int^{t_{1}} dt_{2} \langle \mathcal{J}(t_{1}) \mathcal{S}(t_{1}, t_{2}) \mathcal{J}(t_{2}) \rangle$$

$$+ \langle n(t) \rangle.$$
(3.22)

Note that we have implied $t_1 \geq t_2$ in the second line and thus the term with $t_1 \leq t_2$ is added to symmetrize the expression with switching on time labels. Then, one can integrate Eq. (3.22) with respect to t_1 and t_2

$$\langle \delta n^{2} \rangle = \langle n^{2}(t) \rangle - \int^{t} \int^{t} dt_{1} dt_{2} J^{2}$$

$$= \langle n(t) \rangle + 2 \int^{t} d\tau (t - \tau) \left[\operatorname{Tr} \left(\mathcal{J} \mathcal{S}(\tau) \mathcal{J} \rho_{st} \right) - J^{2} \right]$$

$$= \langle n(t) \rangle + 2 J^{2} \int^{t} d\tau (t - \tau) \left(g_{ph}^{(2)}(\tau) - 1 \right),$$
(3.23)

using the second order correlation function of photon field:

$$g_{\rm ph}^{(2)}(\tau) = \frac{\langle a^{\dagger} a^{\dagger}(\tau) a(\tau) a \rangle}{\langle a^{\dagger} a \rangle^2} = \frac{\text{Tr} \left\{ a^{\dagger} a e^{\mathcal{L}\tau} \left(a \rho_{\rm st} a^{\dagger} \right) \right\}}{\text{Tr} \left\{ a^{\dagger} a \rho_{\rm st} \right\}^2}$$
(3.24)

Eq. (3.23) is the famous Mandel's photon counting formula [65]. Taking into account that t is large compared to the characteristic memory time of the system, Eq. (3.23) reduces to the expression for the photon Fano factor, independent of t [65, 66]

$$F_{\rm ph} = \frac{\langle \delta n^2 \rangle}{\langle n(t) \rangle} = 1 + 2J \int^{\infty} d\tau \operatorname{Tr} \left\{ g_{\rm ph}^{(2)}(\tau) - 1 \right\}. \tag{3.25}$$

Following Refs. [67, 68], we introduce the "Dirac notation" in Liouvillian space for steady state $|\text{st}\rangle\rangle \equiv \rho_{\text{st}}$ and a dual vector $\langle\langle e|\equiv \hat{1}$. The inner product defined in Liouvillian space is the trace over operator "ket" in state "bra". For example, the inner product of the two former objects is given by $\langle\langle e|\text{st}\rangle\rangle \equiv \text{Tr}\rho_{\text{st}} = 1$. It is then useful to define the projector $\mathcal{P} = \mathcal{P}^2 = |\text{st}\rangle\rangle\langle\langle e|$ onto the steady state as well as its complement $\mathcal{Q} = 1 - \mathcal{P}$. Note that a useful property of \mathcal{P} is $\mathcal{L}\mathcal{P} = \mathcal{L}|\text{st}\rangle\rangle\langle\langle e| = 0$ and $\mathcal{P}\mathcal{L} = 0$, and therefore $\mathcal{L} = \mathcal{Q}\mathcal{L}\mathcal{Q}$. The

propagator $S(\tau)$ in the second line of Eq. (3.23) can be decomposed as $S(\tau) = \mathcal{P} + \mathcal{Q}S(\tau)\mathcal{Q}$, and thus $\text{Tr}(\mathcal{J}\mathcal{P}\mathcal{J}\rho_{st}) = \langle \langle e|\mathcal{J}|st \rangle \rangle \langle \langle e|\mathcal{J}|st \rangle \rangle = J^2$. We obtain

$$F_{\rm ph} = 1 + \frac{2}{J} \int^{t \to \infty} d\tau \mathcal{J} \mathcal{Q} \mathcal{S}(\tau) \mathcal{Q} \mathcal{J}$$

$$= 1 - \frac{2}{J} \text{Tr} \left\{ \mathcal{J} \mathcal{Q} \mathcal{L}^{-1} \mathcal{Q} \mathcal{J} \rho_{\rm st} \right\}$$

$$= 1 - \frac{2}{J} \langle \langle e | \mathcal{J} \mathcal{R} \mathcal{J} | \text{st} \rangle \rangle,$$
(3.26)

where $\mathcal{R} = \mathcal{Q}\mathcal{L}^{-1}\mathcal{Q}$ is the inverse of the Liouvillian projected out of the steady state.

Eq. (3.26) is the key step to evaluate photon Fano factor. We also have to find the inverse of the Loiouvillian, \mathcal{R} , and project the result out of the steady state. In practice, inverse of the Liouvillian matrix with large dimension is numerically unstable, but we can evaluate the combination $|\mathcal{W}\rangle\rangle = \mathcal{R}\mathcal{J}|\text{st}\rangle\rangle$ determined by the following equation

$$\mathcal{L}|\mathcal{W}\rangle\rangle = \mathcal{L}\mathcal{R}\mathcal{J}|\mathrm{st}\rangle\rangle = \mathcal{Q}\mathcal{J}|\mathrm{st}\rangle\rangle$$
$$= \mathcal{J}|\mathrm{st}\rangle\rangle - |\mathrm{st}\rangle\rangle\langle\langle e|\mathcal{J}|\mathrm{st}\rangle\rangle, \tag{3.27}$$

where the second equality is obtained by the relation $\mathcal{LR} = \mathcal{LQL}^{-1}\mathcal{Q} = \mathcal{L}(1-\mathcal{P})\mathcal{L}^{-1}\mathcal{Q} = \mathcal{Q}$. To this end, the solution $|\mathcal{W}\rangle\rangle$ in Eq. (3.27) is equivalent to the inverse \mathcal{R} [67]. At the end of the calculation we fix the solution by projection out of the steady state by condition $\langle\langle e|\mathcal{W}\rangle\rangle\rangle = \text{Tr}\left\{\mathcal{RJ}\rho_{\text{st}}\right\} = 0$, accomplished by premultiplication of projector $\mathcal{Q}|\mathcal{W}\rangle\rangle$.

Charge full counting statistics

Charge FCS through a double quantum dot was studied earlier in Refs. [69, 70, 71, 72, 73, 68, 67, 74, 75]. Here we provide a quick review of the relations for the electric current and current noise through the DQD using the master equation formalism. The current operator is defined as $\hat{I} = e\Gamma_r |R\rangle\langle R| = e\Gamma_r c_r^{\dagger} c_r$. The dc current is given by the expectation value of \hat{I} with respect to the steady state solution $\rho_{\rm st}$ for the density matrix,

$$I = e\Gamma_r \text{Tr}\{|R\rangle \langle R| \rho_{\text{st}}\}. \tag{3.28}$$

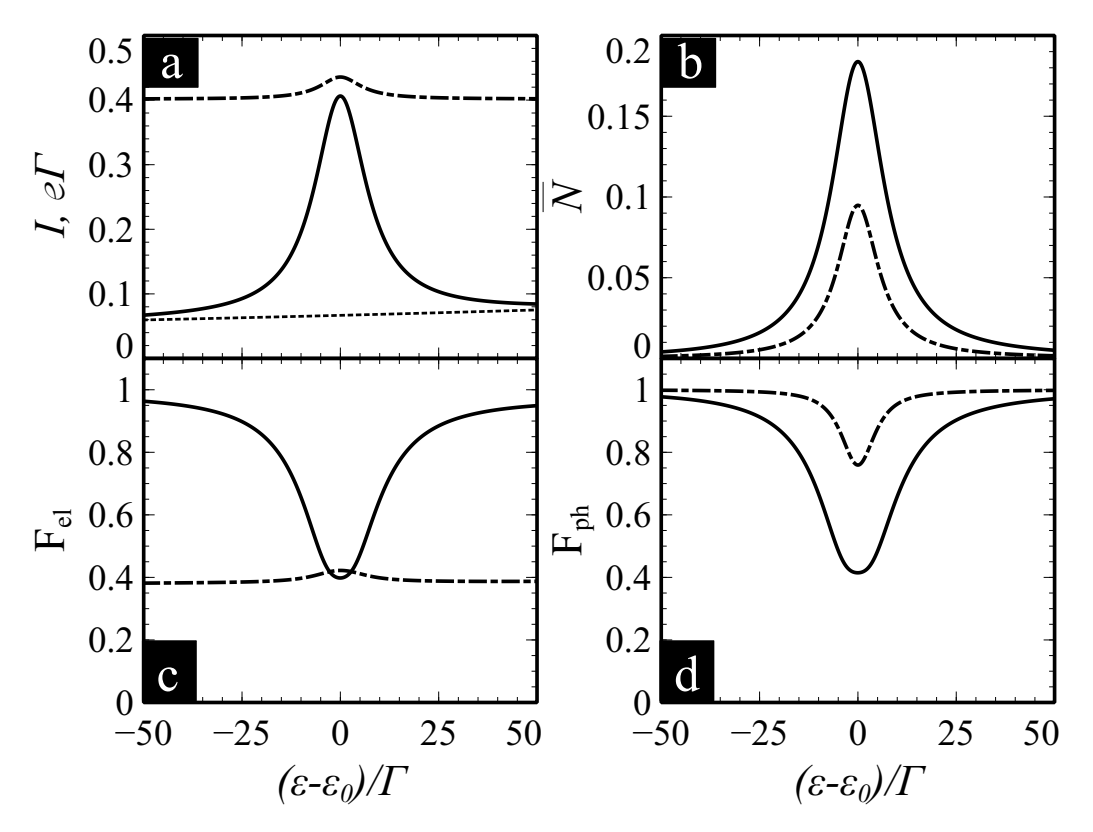


Figure 3.2: Dependences of (a) the electric current I through the DQD, (b) the average photon number \bar{N} in the resonator, (c) the electron Fano factor $F_{\rm el}$ and (d) the Fano factor $F_{\rm ph}$ for emitted photons are shown as functions of the electrostatic bias $\hbar\varepsilon$ near the resonance at $\varepsilon_0 = -\sqrt{\omega_0^2 - 4T^2}$. Solid (dashed) lines represent the case for $\gamma_r = 0$ ($\gamma_r = 2\Gamma$). Other system parameters are $\Gamma_{l,r} = \Gamma$, $\omega_0 = 800\Gamma$, $T = 200\Gamma$, $g_0 = 5\Gamma$, $\kappa = 2\Gamma$ and $\gamma_{\phi} = 0$. Dotted line in panel (a) refers to elastic electric current through a non-interacting DQD.

The spectral density of the current fluctuations is defined by the relation

$$S(\omega) = \int_{-\infty}^{\infty} \langle \langle \hat{I}(t)\hat{I}(t+\tau)\rangle \rangle e^{i\omega t} dt, \qquad (3.29a)$$

$$\langle\langle \hat{I}(t)\hat{I}(t+\tau)\rangle\rangle = \langle \hat{I}(t)\hat{I}(t+\tau)\rangle - I^2.$$
 (3.29b)

The first term in Eq. (3.29b) accounts for the concurrence of two electrons at times t and $t + \tau$

$$\langle \hat{I}(t)\hat{I}(t+\tau)\rangle = I^2 g_{\rm el}^{(2)}(t,\tau) + eI\delta(\tau), \tag{3.30}$$

where the second order correlation function $g_{\rm el}^{(2)}(\tau)$ is given by

$$g_{\rm el}^{(2)}(\tau) = \frac{\operatorname{Tr}\left\{c_r^{\dagger} c_r e^{\mathcal{L}\tau} \left(c_r \rho_{\rm st} c_r^{\dagger}\right)\right\}}{\operatorname{Tr}\left\{c_r^{\dagger} c_r \rho_{\rm st}\right\}^2}.$$
(3.31)

The last term in Eq. (3.30) represents counting the same electron at t and $t + \tau$.

Using Eqs. (3.29) and (3.31), we can write the current noise spectral function in the form:

$$S(\omega) = I^2 \int_{-\infty}^{\infty} \left(g_{\text{el}}^{(2)}(\tau) - 1 \right) e^{i\omega\tau} d\tau + eI. \tag{3.32}$$

This result shows that the second order correlation function $g_{\rm el}^{(2)}(\tau)$ is related to the current noise in both frequency and time domains. In particular, the Fano factor $F_{\rm el}$ of the charge current that characterizes the low frequency limit of $S(\omega)$ is [72]

$$F = \frac{S(0)}{eI} = 1 + \frac{2I}{e} \int_{-\infty}^{\infty} \left(g_{\text{el}}^{(2)}(\tau) - 1 \right) d\tau.$$
 (3.33)

The formalism discussed above can be further generalized to study cross-correlation functions of electron charge transfer and photon emission¹ Experimental observation of such cross-correlations is a challenging task, but can be achieved by combining charge sensing measurements [76] and photon detection [57].

3.3 Ideal Photon Counter

In this section we consider a system consisting of an ideal photon counter and a DQD with equal tunneling rates through left and right contacts, $\Gamma_{l,r} = \Gamma$, and the interdot tunneling amplitude $\mathcal{T} = 200\Gamma$. We take $\omega_0 = 800\Gamma$, and the electron-photon bare coupling $g_0 = 5\Gamma$.

In Figure 3.2 we present (a) dependence of electric current $I = e\Gamma_r \langle c_r^{\dagger} c_r \rangle_{\rm st}$, (b) the average number of photons in the resonator, $\bar{N} = \langle a^{\dagger} a \rangle_{\rm st}$, (c) the Fano factor of electronic current, $F_{\rm el}$, and (d) the Fano factor for photon flux, $F_{\rm ph}$. For the former two quantities, we evaluate $\rho_{\rm st}$ and take corresponding expectation values. Solid lines in Figure 3.2 are evaluated for an ideal quantum dot with $\gamma_r = \gamma_{\phi} = 0$. In this case, the amplitudes of electric current and the photon flux have a well pronounced peak at the resonant condition $\Omega = \omega_0$, while away from the resonance, photon production is suppressed, $\bar{N} \to 0$, and the current approaches $I_0 = eT^2\Gamma/(\varepsilon^2 + 3T^2)$ (a dotted line in Figure 3.2a) for elastic electron transfer through a DQD decoupled from the resonator [77]. Fano factors for both electric

¹to be discussed elsewhere.

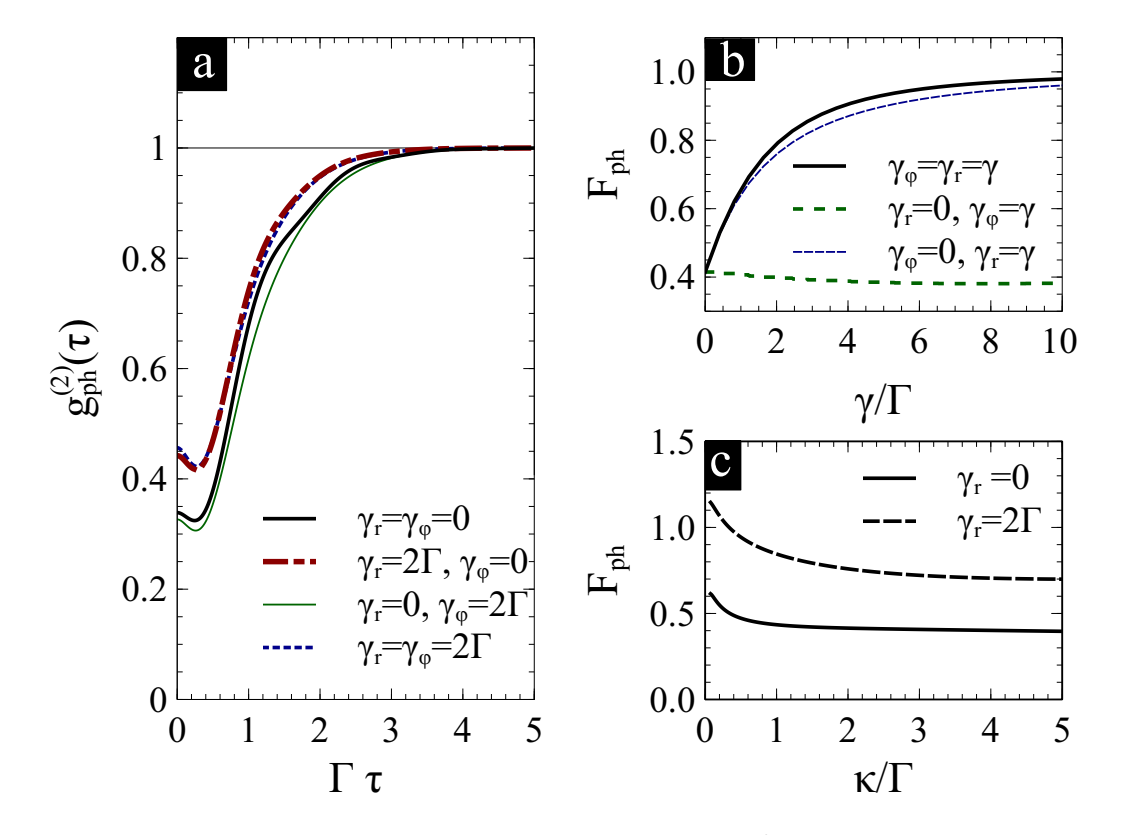


Figure 3.3: (a) The second order correlation function $g_{\rm ph}^2(2)(\tau)$ for photons as a function of time τ at resonant condition $\Omega=\omega_0$ for different values of energy, γ_r , and phase, γ_ϕ , relaxation rates. (b) The photon Fano factor $F_{\rm ph}$ as a function of relaxation rate γ in three cases $\gamma_r=\gamma_\phi=\gamma$ (solid line), $\gamma_r=\gamma$ and $\gamma_\phi=0$ (dotted line), $\gamma_\phi=\gamma$ and $\gamma_r=0$ (dashed line). (c) $F_{\rm ph}$ as a function of photon detection rate κ shows a flat behavior for $\kappa\gtrsim\Gamma$. Other system parameters in both panels are $\Gamma_{l,r}=\Gamma$, $\omega_0=800\Gamma$, $\mathcal{T}=200\Gamma$, $g_0=5\Gamma$, $\kappa=2\Gamma$ and $\gamma_\phi=0$ [for (a) and (b)].

current and photon flux are reduced below 1/2, indicating sub-Poissonian statistics with strong suppression of charge and photon noise at the resonance.

Inelastic relaxation facilitates electron transfer through the DQD and increases the electric current above I_0 even far away from the resonance, $|\Omega - \omega_0| \gg \Gamma$. In the presence of such background current, only a weak enhancement of the current occurs at $\Omega = \omega_0$. The electron Fano factor is reduced below unity for $\gamma_r \neq 0$, and a resonant electron transfer with photon emission does not significantly affects $F_{\rm el}$, see Figure 3.2c. We observe a resonant emission in the photon flux, see dashed line in Figure 3.2b, but the photon Fano factor, $F_{\rm ph}$, is closer to the value for the Poissonian statistics, F = 1.

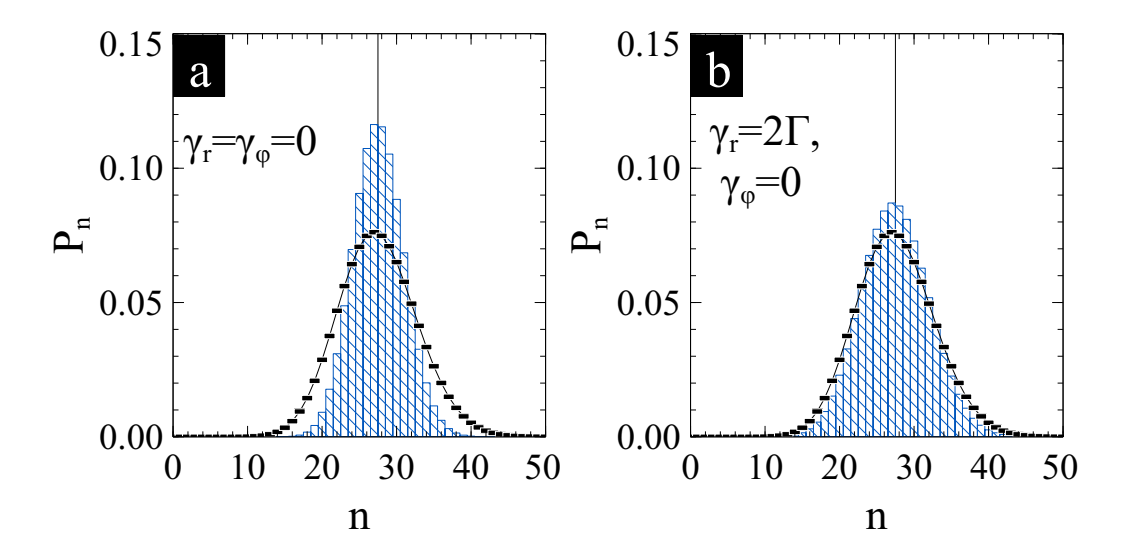


Figure 3.4: Probabilities P_n to have n emitted photons during time t at resonance $\Omega = \omega_0$ for (a) an ideal DQD without decoherence of electronic states, $\gamma_r = \gamma_\phi = 0$ and $t = 75/\Gamma$; (b) a DQD with inelastic relaxation $\gamma_r = 2\Gamma$, $\gamma_\phi = 0$ and $t = 145/\Gamma$. Other system parameters in both panels are $\Gamma_{l,r} = \Gamma$, $\omega_0 = 800\Gamma$, $\mathcal{T} = 200\Gamma$, $g_0 = 5\Gamma$ and $\kappa = 2\Gamma$. A thin curve in both panels represents the corresponding Poisson distribution $P_n^{(P)} = e^{-\bar{n}}\bar{n}^n/n!$ with $\bar{n} = \sum_n n P_n$ equal to the average number of emitted photons.

To evaluate the second order correlation function $g_{\rm ph}^{(2)}(\tau)$ shown in Figure 3.3a, we compute $\rho_{\rm st}$ and diagonalize the total Liouvillian superoperator \mathcal{L} to obtain $\exp{(\mathcal{L}\tau)}$. The thick solid line shows $g_{\rm ph}^{(2)}(\tau)$ for an ideal DQD, $\gamma_{\rm r}=\gamma_{\phi}=0$. The probability to observe two photons simultaneously is reduced, $g_{\rm ph}^{(2)}(0)<1$, indicating photon antibunching. As τ becomes longer than $\sim 1/\Gamma$, function $g_{\rm ph}^{(2)}(\tau)$ increases and eventually approaches its asymptote, $g_{\rm ph}^{(2)}(\tau \to \infty)=1$. The integral in Eq. (3.25) with such $g_{\rm ph}^{(2)}(\tau)$ is negative and $F_{\rm ph}<1$ (sub-Poissonian) 2 .

In the presence of inelastic relaxation in the DQD, $g_{\rm ph}^{(2)}(0)$ increases and $g_{\rm ph}^{(2)}(\tau)$ reaches its long-time asymptotic value 1 at a shorter time scale. However, pure dephasing, γ_{ϕ} , does not significantly change the shape of $g_{\rm ph}^{(2)}(\tau)$, because individual photon emission is phase-destructive. We also investigate the dependence of $F_{\rm ph}$ on inelastic, γ_r , and dephasing, γ_{ϕ} in Figure 3.3b. The inelastic relaxation, $\gamma_r = \gamma$ and $\gamma_{\phi} = 0$, recovers $F_{\rm ph}$ to its Poissonian

²the modified BR equations can be numerically solved using standard integration methods for a system of linear differential equations with time-dependent coefficients. Alternatively, we obtained same results using the BR functions of the QUTIP package [45] with a proper adjustment of the system Hamiltonian and the interaction term, see *e.g.* Eqs. (4.19) and (4.12), for time-dependence of the eigenstate basis.

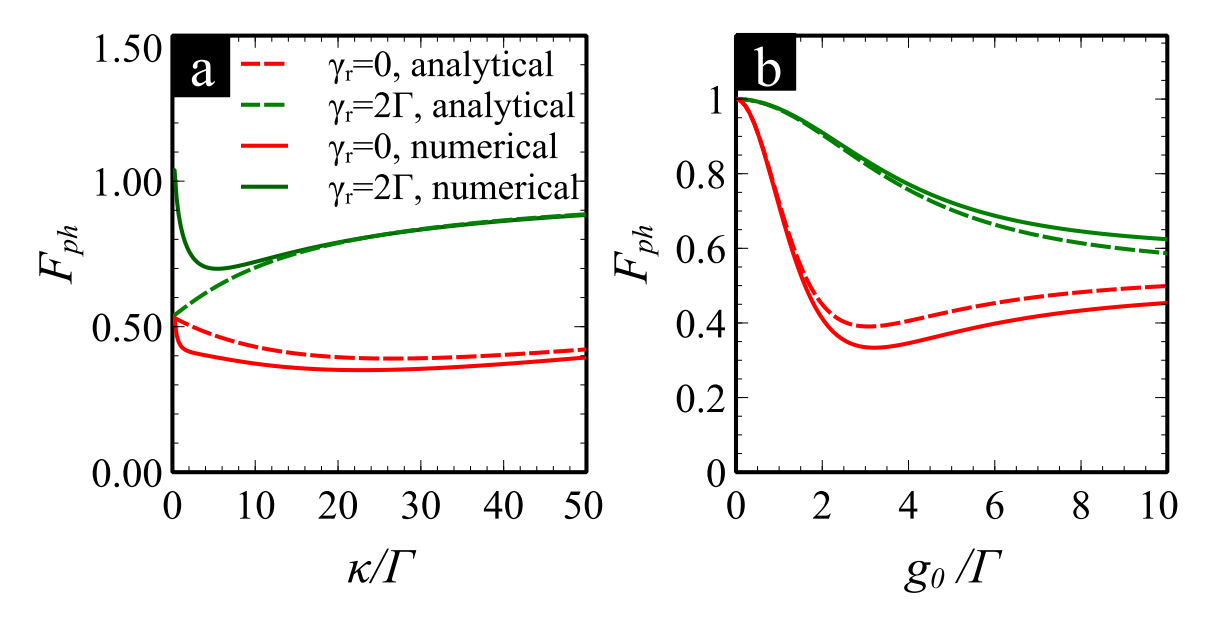


Figure 3.5: Dependence of photon noise Fano factor on (a) photon detection rate κ and (b) the bare coupling constant g_0 . In panel (a), the bare coupling constant is fixed $g_0 = 5\Gamma$ and in panel (b) the photon detection rate is fixed $\kappa = 10\Gamma$. Solid (dashed) lines represent results for numerical (analytical) calculations with method described in Sec. 3.2(Sec. 3.4). Other system parameters are $\Gamma_{l,r} = \Gamma$, $\omega_0 = 800\Gamma$, $\mathcal{T} = 200\Gamma$. Both plots indicate that the analytical results agree with numerical in the limit $\kappa \gtrsim g_0$, Γ .

value, $F_{\rm ph}=1$, as a consequence of the reduced memory of the system, $g_{\rm ph}^{(2)}(\tau) \to 1$, due to inelastic relaxation. Pure dephasing, $\gamma_{\phi}=\gamma$ and $\gamma_{r}=0$, has weak effect on $F_{\rm ph}$ even for large values of γ_{ϕ} , as dephasing does not change $g_{\rm ph}^{(2)}(\tau)$ to modify the integral in Eq. (3.25) for $F_{\rm ph}$. The addition of dephasing to relaxation, $\gamma_{\phi}=\gamma_{r}=\gamma$, makes no significant corrections to $F_{\rm ph}$ when compared to $F_{\rm ph}(\gamma_{r},0)$.

The dependence of the photon Fano factor on the photon detection rate κ is also studied. As κ decreases, the average photon number in the resonator increases. At large \bar{N} , photons already present in the resonator cause stimulated emission by the DQD [32, 35]. For an ideal DQD without energy relaxation, $\gamma_r = 0$, the photon Fano factor grows fast for $\kappa \lesssim \Gamma$; see Figure 3.3c. On the other hand, if the energy relaxation in the DQD is significant, the photon Fano factor can exceed unity and the photon field exhibits properties of a thermal state. In this respect, inelastic processes in the DQD enhance photon noise. For a strong photon detection rate, $\kappa \gtrsim \gamma_r$, g, and consequently a low photon number in the resonator,

the back-action of the photon field on electrons is negligible.

In Sec 3.4 we apply the adiabatic elimination method [59, 34, 78] to study photon statistics emitted by a quantum dot.

Next, we present the distribution function of the photon counts n over time t. For this purpose, we compute $\tilde{\rho}(t,s)$ with matrix exponent $\exp{[\mathcal{M}(s)t]}$ and integrate over counting field χ , see Eq. (3.15) and Eq. (3.19). For $\gamma_{\rm r} = \gamma_{\phi} = 0$, we take $t = 75/\Gamma$ and the distribution $P_n(t)$ is shown in Figure 3.4a. The average value of photon counts, $\langle n \rangle = \sum_n n P_n \simeq 27.6$ is consistent with $\langle n \rangle = \bar{N}\kappa t$ with $\bar{N} = 0.184$ and their variance $\langle n^2 \rangle - \langle n \rangle^2 \simeq 11.6$, in turn gives $F_{\rm ph} = 0.42$, both of which coincide with previous calculation, see Figure 3.2b,d at $\varepsilon = \varepsilon_0$. We present the Poisson distribution with the same expectation value $\langle n \rangle$ by narrow black dots in Figure 3.4a. P_n is closer to the Poisson distribution for a system with relaxation $\gamma_{\rm r} = 2\Gamma$ [see Figure 3.4b], where $t = 145/\Gamma$, $\langle n \rangle \simeq 27.6$ ($\bar{N} = 0.095$) and $F_{\rm ph} = 0.76$.

3.4 Adiabatic elimination of photon degrees of freedom

In the limit of strong photon detection rate, $\kappa \gg \gamma, g, \Gamma$, the photon field decays so fast that the density matrix can be approximately factorized as

$$\rho(t) \simeq \rho_{\rm D}(t) \left(|0\rangle\langle 0| \right), \tag{3.34}$$

where $|0\rangle$ is the vacuum state of the photon in the transmission line and $\rho_{\rm D}(t)$ is the reduced density matrix of the DQD. Thus we can adiabatically eliminate the photon mode, and obtain the equation of motion for the reduced density matrix $\tilde{\rho}_{\rm D}(t,s)$ in the interaction picture [59],

$$\dot{\tilde{\rho}}_{\mathrm{D}}(t,s) = \Gamma_{l} \mathcal{D}(c_{l}^{\dagger}) \tilde{\rho}_{\mathrm{D}}(t,s) + \Gamma_{r} \mathcal{D}(c_{r}) \tilde{\rho}_{\mathrm{D}}(t,s)$$

$$+ \gamma_{*} \mathcal{D}(\sigma^{-}) \tilde{\rho}_{\mathrm{D}}(t,s) + (s-1) \mathcal{J}(\sigma^{-}) \tilde{\rho}_{\mathrm{D}}(t,s),$$

$$(3.35)$$

where $\gamma_{\rm ph} = 4g^2/\kappa$ is the photon-induced relaxation rate associated with the spontaneous emission in this large κ limit and $\gamma_* = \gamma_r + \gamma_{\rm ph}$. Therefore photon absorptions can be

reflected by the jump superoperator $\mathcal{J}(\sigma^-)\tilde{\rho}_D(t,s) = \gamma_{\rm ph}\sigma^-\tilde{\rho}_D(t,s)\sigma^+$. In the basis $\rho_D = (\rho_0, \rho_g, \rho_{ge}, \rho_{eg}, \rho_e)^T$, the matrix $\mathcal{M}(s)$ in Eq. (3.12) is given by:

$$\mathcal{M}(s) = \frac{1}{4} \begin{pmatrix} -4\Gamma_{l} & -2\Gamma_{r}C_{\theta,-} & -\Gamma_{r}S_{\theta} & -\Gamma_{r}S_{\theta} & 2\Gamma_{r}C_{\theta,+} \\ 2\Gamma_{l}C_{\theta,+} & 2\Gamma_{r}C_{\theta,-} & -\Gamma_{r}S_{\theta} & -\Gamma_{r}S_{\theta} & 4\gamma_{r} + 4s\gamma_{\text{ph}} \\ -2\Gamma_{l}S_{\theta} & -\Gamma_{r}S_{\theta} & -2\Gamma_{r} - 2\gamma_{*} & 0 & -\Gamma_{r}S_{\theta} \\ -2\Gamma_{l}S_{\theta} & -\Gamma_{r}S_{\theta} & 0 & -2\Gamma_{r} - 2\gamma_{*} & -\Gamma_{r}S_{\theta} \\ -2\Gamma_{l}C_{\theta,-} & 0 & -\Gamma_{r}S_{\theta} & -2\Gamma_{r}C_{\theta,+} - 4\gamma_{*} \end{pmatrix},$$

$$(3.36)$$

where $S_{\theta} = \sin \theta$ and $C_{\theta,\pm} = \cos \theta \pm 1$.

To calculate the generating function $\mathcal{G}(s,t)$ and its derivatives, we take the Laplace transform of the generalized density matrix, Eq. (3.14),

$$\tilde{\rho}(z,s)_{\rm D} = (z - \mathcal{M}(s))^{-1} \tilde{\rho}(0,s)_{\rm D}.$$
 (3.37)

Since the long time behavior of the solution is determined by the residue of the generating function at the pole near z=0, i.e., $\mathcal{G}(t,s)\sim g(s)e^{z_0t}$ with g(1)=1, we can expand the pole around s=1:

$$z_0 = \sum_{i>0} c_i (s-1)^i, \tag{3.38}$$

and obtain, from Eq. (3.19), the first two moments, $\langle \langle n^i \rangle \rangle = \langle (n - \langle n \rangle)^i \rangle$:

$$\langle \langle n \rangle \rangle = \frac{\partial g}{\partial s} \Big|_{s=1} + c_1 t,$$
 (3.39)

$$\langle \langle n^2 \rangle \rangle = \left. \frac{\partial^2 g}{\partial s^2} \right|_{s=1} - \left[\left(\frac{\partial g}{\partial s} \right)^2 - \frac{\partial g}{\partial s} \right]_{s=1} + (c_1 + 2c_2) t, \tag{3.40}$$

which give the mean and variance of the probability distribution, respectively. In the asymptotic limit, $t \to \infty$, all the information about the moments is included in the expansion coefficients c_i . For instance, the Fano factor is given by [34, 78]

$$F \equiv \frac{\langle n^2 \rangle - \langle n \rangle^2}{\langle n \rangle} = 1 + \frac{2c_2}{c_1}.$$
 (3.41)

To find the coefficients c_1 and c_2 , we consider the equation

$$\det \left(z_0 \hat{1} - \mathcal{M}(s)\right) = 0, \tag{3.42}$$

with $z_0 = c_1(s-1) + c_2(s-1)^2 + \mathcal{O}(s-1)$. Then we can expand Eq. (3.42) in powers of s and let the coefficients for each power of s-1 be zero. This procedure generates a set of equations with c_i to arbitrarily large i. We provide two examples below.

First, we consider $\Gamma_l = \Gamma_r = \Gamma$ and $\theta \to \pi$ with fixed coupling constant g, the case in which the two levels in the DQD are weakly overlapping, and we obtain

$$c_1 = \frac{\gamma_{\rm ph} \Gamma}{2\gamma_* + \Gamma},\tag{3.43}$$

$$c_2 = -\frac{\gamma_{\rm ph}^2 \Gamma(\gamma_* + 2\Gamma)}{(2\gamma_* + \Gamma)^3}.$$
(3.44)

The Fano factor is given by

$$F = 1 - \frac{2\gamma_{\rm ph}(\gamma_* + 2\Gamma)}{(2\gamma_* + \Gamma)^2} < 1, \tag{3.45}$$

corresponding to the sub-Poissonian noise. When the DQD is tuned to its charge degeneracy, $\theta = \pi/2$, the solutions then read

$$c_1 = \frac{\gamma_{\rm ph}\Gamma(\gamma_* + 2\Gamma)}{6\gamma_*^2 + 11\gamma_*\Gamma + 4\Gamma^2},\tag{3.46}$$

$$c_2 = -\frac{\gamma_{\rm ph}^2 \Gamma(\gamma_* + 2\Gamma) \left(4\gamma_*^3 + 14\gamma_*^2 \Gamma + 31\gamma_* \Gamma^2 + 20\Gamma^3\right)}{\left(6\gamma_*^2 + 11\gamma_* \Gamma + 4\Gamma^2\right)^3}.$$
 (3.47)

The Fano factor in this case is

$$F = 1 - \frac{2\gamma_{\rm ph} \left(4\gamma_*^3 + 14\gamma_*^2 \Gamma + 31\gamma_* \Gamma^2 + 20\Gamma^3\right)}{\left(6\gamma_*^2 + 11\gamma_* \Gamma + 4\Gamma^2\right)^2},\tag{3.48}$$

again, giving the sub-Poissonian noise. In both cases, Fano factors are below 1 for $\gamma_{\rm ph} \neq 0$, indicating that it is the interaction between photons and electrons that gives rise to the sub-Poissonian statistics.

As mentioned above, this analytical method is valid in the limit when κ is large. We hereby make a comparison between analytical and numerical results, see Figure 3.5. In both plots, we do not consider dephasing effects. The calculations indicate that the analytical method presented above agrees with numerical results in the limit $\kappa \gtrsim g_0, \Gamma$.

3.5 Photon Counting Statistics Measured By Josephson Photomultipliers

In this section, we demonstrate that emitted photon statistics can be measured and justified by actual devices. A possible measurement is based on recently developed Josephson photomultipliers (JPM) [57, 79]. In these devices the Josephson coupling E_J dominates over charging energy E_c , therefore it is convenient to write the Hamiltonian of the JPM in terms of the phase operator ϕ across the Josephson junction:

$$H_{\rm JPM} = -\frac{E_c}{2} \frac{d^2}{d\phi^2} - E_J \left(\cos\phi - \frac{I}{I_0}\phi\right),\tag{3.49}$$

where I is the biased current and I_0 is the critical current of the junction. For $I \lesssim I_0$, the potential energy takes a "washbroad" shape, with a few discrete energy levels in the minima separated from the continuum. In this manner, we can tune the biased current such that only two phase states are bounded in the local minima.

Next we couple the microwave resonator to the JPM with Jaynes-Cummings type interaction. The total Hamiltonian is then written as

$$\tilde{H} = H + \hbar g_{\text{JPM}} (a^{\dagger} v^{-} + a v^{+}) + \frac{\hbar \omega_{\text{JPM}}}{2} v_{z}, \qquad (3.50)$$

where H is the Hamiltonian Eq. (3.3), g_{JPM} the coupling constant between the JPM and a resonator mode, and the Pauli matrices v^{\pm} and v_z are defined in the basis of eigenstates of the JPM spanned by $|E\rangle$ and $|G\rangle$. In a similar manner, the dynamics of the system is governed by the following master equation

$$\dot{\rho} = \mathcal{L}\rho = -\frac{i}{\hbar}[\tilde{H}, \rho] + \mathcal{D}_{\text{tot}}\rho,$$
 (3.51a)

$$\mathcal{D}_{\text{tot}}\rho = \kappa_0 \mathcal{K}(a)\rho + \mathcal{D}_{\text{DOD}}\rho + \mathcal{D}_{\text{JPM}}\rho, \tag{3.51b}$$

where

$$\mathcal{D}_{JPM}\rho = \gamma_{t}\mathcal{K}(|V\rangle\langle E|)\rho + \gamma_{d}\mathcal{K}(v^{-})\rho + \gamma_{cap}\mathcal{K}(|G\rangle\langle V|)\rho$$
(3.51c)

with $|V\rangle$ referring to a voltage regime of the junction, γ_t is the tunneling to this regime from the excited state and γ_{cap} is the capturing rate from the voltage regime to the ground state.

By defining state $|V\rangle$, we imply that the junction is out of the Hilbert space of two localized states $|G\rangle, |E\rangle$ near a local minima of the Josephson energy and does not correspond to a particular quantum state. While the junction evolves out of these two states, a finite voltage develops that can be identified by the measurement circuit as a photon detection signal. Then, the dissipation in the circuit leads to recapturing the junction in its ground state and the operation cycle closes. For this measurement scheme, we use the similar formalism introduced in Section 3.2 to calculate the Fano factor and FCS associated with the jump operator $\mathcal{J}\rho = \gamma_{\rm t}|V\rangle\langle E|\rho|E\rangle\langle V|$.

Black thick lines in Figure 3.6 correspond to the JPM measurement without energy relaxation and thin line are taken from Figure 3.2d and correspond to the Fano factor measured by an ideal photon counter for the same set of parameters of the DQD. Even though Rabi splitting appears due to coupling between JPM and microwave mode, a fairly good agreement between the ideal and JPM models of the photon counter indicates that sub-Poissonian statistics of photon emission by a DQD can be experimentally observed. The green lines in Figure 3.6 represent the measured Fano factor with energy relaxation rate $\gamma_d = 1.5\Gamma$ in the JPM, indicating that energy relaxation of the measurement device would spoil the noise characteristics. This is reminiscent of reduction of quantum efficiency of measurement device [58]. The FCS of JPM recordings is shown in Figure 3.7 for cases $\gamma_r = 0, 2\Gamma$, both of which agree with Fano factor calculation in Figure 3.6.

3.6 Conclusions

We investigated the statistics of photons emitted by a biased DQD coupled to a lossless resonator. We calculated the time correlation function $g_{\rm ph}^{(2)}(\tau)$ and found that photons exhibit antibunching, $g^{(2)}(\tau) < g^{(2)}(\tau \to \infty) = 1$. We also calculated photon counting statistics $P_n(t)$ of observing n photons during a fixed time interval t. We find that distribution $P_n(t)$ shows a sub-Poissonian statistics if measured by an ideal photon counter. We also demonstrate that photon full counting statistics can be accurately studied experimentally by utilizing a Josephson photomultiplier [57, 79].

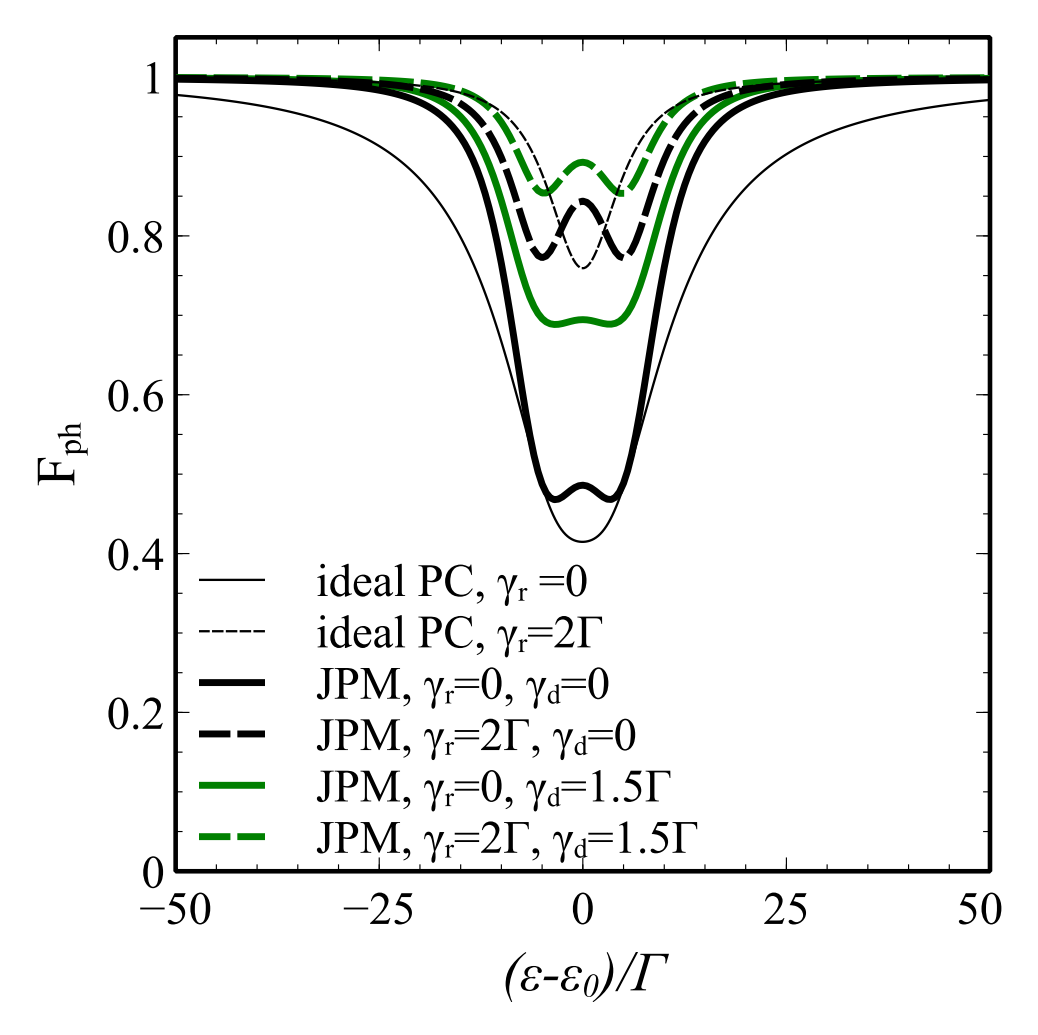


Figure 3.6: Comparison of Fano factor measured by an ideal photon detector and JPM with the same set of parameters of a DQD. Other additional parameters for JPM model are $g_{\rm JPM}=5\Gamma,~\omega_{\rm JPM}=\omega_0,~\kappa_0=0.6\Gamma,~\gamma_{\rm cap}=1.5\Gamma$ and $\gamma_{\rm t}=1.5\Gamma.$ When we introduce the energy relaxation rate $\gamma_d=1.5\Gamma$ for the JPM, the resultant Fano factor (green lines) increase towards unity.

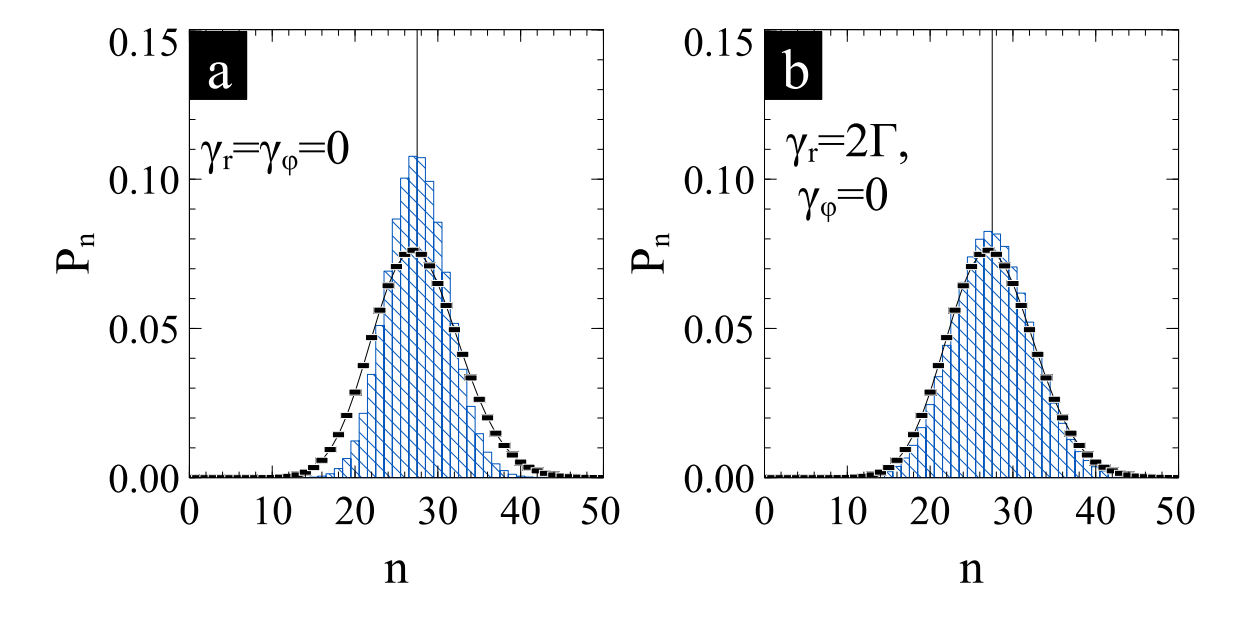


Figure 3.7: Probabilities P_n to have n JJ recordings during time t at resonance $\Omega = \omega_0$ for (a) an ideal DQD without decoherence of electronic states, $\gamma_r = \gamma_\phi = 0$ and $t = 132/\Gamma$; (b) a DQD with inelastic relaxation $\gamma_r = 2\Gamma$, $\gamma_\phi = 0$ and $t = 293.3/\Gamma$. Other system parameters in both panels are $\Gamma_{l,r} = \Gamma$, $\omega_0 = 800\Gamma$, $\mathcal{T} = 200\Gamma$, $g_0 = 5\Gamma$ and $\kappa = 2\Gamma$. A thin curve in both panels represents the corresponding Poisson distribution $P_n^{(P)} = e^{-\bar{n}}\bar{n}^n/n!$ with $\bar{n} = \sum_n n P_n$ equal to the average number of emitted photons.

In recent experiments, decoherence rates were comparable to the strength of the electronphoton coupling. For this reason, we investigated the effect on charge and photon statistics
of pure dephasing in the DQD and energy relaxation. We found that pure dephasing does
not significantly modify the charge transfer or photon emission statistics, but the inelastic
relaxation processes result in several drastic changes (see Figure 3.2): (i) The electric current and its noise acquire strong background as the inelastic processes facilitate the charge
transfer throughout the DQD, and the peak in I and the pit in F_{el} at the resonant condition $E_e - E_g = \hbar \omega_0$ are flattened. (ii) The photon number \bar{N} at the resonance is suppressed as
the effective photon source is reduced due to additional channels for the $e \to g$ transition
via inelastic events. (iii) Photon Fano factor $F_{\rm ph}$ as a function of the level spacing is flatten
as well. In the presence of inelastic electron relaxation, the memory time of the DQD is
reduced, which increases the photon correlation function $g_{\rm ph}^{(2)}$ at short time scales[see Fig-

ure 3.3a] and brings the photon Fano factor to its Poisson value, $F_{\rm ph}=1$, as shown in Figure 3.2.

Chapter 4

Nonadiabatic dynamics of a slowly driven dissipative two-level system

4.1 Introduction

The increasing demand for accurate control of quantum devices using high-fidelity control protocols [80, 81, 82, 83, 84] has stimulated interest in the study of the dynamics of quantum systems in response to slowly varying Hamiltonian. Moreover, rapid progress in the field of adiabatic quantum computing has fueled further interest in and need for more careful analysis of the dynamics of quantum systems whose parameters vary slowly in time. [85] In addition, decoherence in any real quantum system sets a rigid constraint on the time interval during which a quantum protocol must be carried out, limiting all protocols to intermediate time intervals that are shorter than the decoherence time. At these intermediate time scales, both non-adiabatic corrections and coupling to the environment become equally important.

The previous analysis [80, 81, 86, 87] of the qubit dynamics with time-dependent Hamiltonians was based on the Lindblad master equation [88, 89] that describes the interaction with environment in terms of dephasing and transition processes characterized by phenomenological decoherence rates. An alternative microscopic approach, formulated as a perturbative theory for a quantum system with a time-independent Hamiltonian

interacting with its environment, introduces the Bloch–Redfield (BR) master equation [90, 91, 92, 93, 94]. If the Hamiltonian of the system changes in time, the BR approach has to be modified to properly account for a non-adiabatic corrections.

In this chapter we extend the BR approach to account for slow evolution of the system Hamiltonian in the presence of the environment. The main concept of the BR theory is based on the identification of decoherence processes in terms of the matrix elements for transitions caused by environment in the eigenstate basis of the quantum system [90, 91, 94]. For the Hamiltonian that varies with time, one can still use a basis defined by eigenvectors of the Hamiltonian [95, 96, 92, 97, 98, 99, 100, 101, 102, 103], where the Hamiltonian is always represented by a diagonal matrix $\tilde{H} = UHU^{\dagger}$, where the unitary transformation U denotes a transition from the original basis to the eigenstate basis. Time-dependence of U produces an extra term in the time evolution of the quantum system that is effectively described by the new Hamiltonian $\tilde{H} - iU\partial_t U^{\dagger}$. This expression is not necessarily diagonal and another basis transformation is required. Such series of diagonalization transformations can be continued indefinitely, but for slowly changing Hamiltonian, the series can be truncated after a finite number of transformations neglecting terms of the higher order in time-derivatives of the parameters in the Hamiltonian. In addition to changes in the effective spectrum of the system, matrix elements representing coupling between the quantum system and its environment are also modified, resulting in a redefinition of the transition rates for the system.

We focus our analysis on the dynamics of a two-level quantum system — a qubit or a spin-1/2 system — in the presence of time-dependent field, which we refer to below as the control field of the qubit. We study the dynamical response of the transverse magnetization to quench velocity of the control field. The transverse magnetization measurements can provide the value of the Berry curvature of a quantum system [87, 104] and, consequently, characterize topological properties of a ground state of the system.

Since any real qubit is always coupled to its environment, it is necessary to perform detailed analysis of the non-adiabatic dynamics of a qubit system in the presence of dissi-

pation. To this end, we investigate the effect of pure dephasing and energy relaxation due to the Ohmic bath on the qubit polarization. Our results indicate that the decoherence suppresses the transient wiggles of the out-of-plane qubit projection, thereby bringing up the linear relation between the qubit response and the quench velocity. Thus, the dissipation facilitates the Berry curvature measurement based on the non-adiabatic response, proposed in Ref. [104]. Furthermore, our study is also applicable to other experimental techniques that are based on an interference effect for the Berry phase measurement in qubits since the drive parameter was changed slowly in measurements reported in Ref. [105], see also Refs. [106, 100, 107] for theoretical analysis of the influence of environment on the Berry phase.

We also apply the modified BR equation to the Landau–Zener (LZ) problem [108, 109, 110, 111 in a qubit coupled to environment at arbitrary temperature. The LZ problem in a quantum system coupled to its environment has attracted significant interest recently, where the environment was considered either as a source of classical noise [112, 113], or quantum fluctuations that cause transitions between qubit states [114, 115, 116, 101, 117, 118, 119, 120, 121, or pure dephasing [122, 86]. More recently, the LZ interferometry has attracted a growing interest [123, 124, 125, 126, 127, 128, 129, 130]. Here we focus on the role of quantum fluctuations in the environment that cause transitions between the eigenstates of the qubit in the LZ problem. We argue that during the LZ transition, the matrix elements of the coupling between the qubit and its environment must be considered in the basis of eigenstates of the full qubit Hamiltonian and therefore, the matrix elements acquire an explicit time dependence due to rotation of the eigenstate basis in addition to straightforward dependence on the energy difference between the eigenstates. This treatment modifies the previous results of Refs. [114, 115, 116] and generalizes the results of Refs. [101, 119], where a similar basis transformation was naturally included in the calculations. We disregard the effect of the Lamb-Stark shift on the qubit spectrum due to coupling to the environment, considered in Ref. [120], since this can be included in the redefined control field of the qubit. We focus solely on the transition effects due to non-unitary evolution of the qubit density

matrix. We consider the quantum fluctuations of the environment that are fixed along the direction of the control field at very long initial and final moments of the LZ transition so that the matrix element that characterizes the transition between qubit states at long times is absent and environment produces dephasing only. For arbitrary direction of the fluctuating field, the transition remains effective over long time and will effectively bring the qubit to the ground state for zero temperature environment. We also consider "dephasing" coupling [122, 86] when the quantum fluctuations occur only in the direction parallel to the direction of the control field in the parameter space of the qubit Hamiltonian. Our result is in agreement with Ref. [86] of the same problem within Lindblad master equation, in the limit of a high-temperature environment.

This chapter is organized as follows. In section 4.2, we present a formalism of the BR equations in transformed basis for time-dependent Hamiltonians. In section 6.2, we study the evolution of a qubit whose control field rotates in a plane with a constant magnitude and consider different directions of the environmental coupling field. In section 4.4, we consider the LZ problem in the presence of zero and finite temperature environment and show that transition is dominated by thermal excitation of the qubit at finite temperatures. In section 4.5, we analyze the non-adiabatic effects within the Lindblad formalism. We end with conclusions in section 6.5.

4.2 Bloch–Redfield approach to time-dependent Hamiltonians

We consider a spin coupled to a bath of harmonic oscillators. The full Hamiltonian $\hat{H} = \hat{H}_0 + \hat{H}_{int} + \hat{H}_{env}$ is a sum of the Hamiltonian for the spin in the magnetic field $\mathbf{b}(t)$

$$\hat{H}_0 = -\frac{1}{2}\mathbf{b}(t)\cdot\hat{\sigma},\tag{4.1}$$

the interaction Hamiltonian of the spin with the environment [18]

$$\hat{H}_{\text{int}} = \sum_{q} \lambda_{q} \mathbf{n} \cdot \hat{\sigma} \, \frac{\hat{a}_{q} + \hat{a}_{q}^{\dagger}}{2} \tag{4.2}$$

and the bath Hamiltonian

$$\hat{H}_{\text{env}} = \sum_{q} \hbar \omega_q (\hat{a}_q^{\dagger} \hat{a}_q + 1/2). \tag{4.3}$$

Here we assume that each environment oscillator interacts with the spin as a quantized magnetic field $\lambda_q(\hat{a}_q^{\dagger} + \hat{a}_q)/2$ in the common direction \mathbf{n} , \hat{a}_q^{\dagger} and \hat{a}_q are raising and lowering operators of the field.

The reduced density matrix $\hat{\rho}$ of the spin is determined by tracing out environment degrees of freedom of the full density matrix $\hat{\rho}_{\text{full}}$. The full density matrix satisfies the unitary master equation

$$\frac{d\hat{\rho}_{\text{full}}(t)}{dt} = \frac{1}{i\,\hbar} \left[\hat{H}(t), \hat{\rho}_{\text{full}}(t) \right]. \tag{4.4}$$

There are several approaches to obtain the corresponding equations for time evolution of the reduced density matrix for the qubit. Here we consider the limit of weak coupling of a qubit to the environment, when the density matrix is defined by the BR equations, [90, 91] see also Refs. [92, 94, 101] where a diagrammatic technique was developed to treat the weak coupling to environment.

The environmental effects are characterized by the spectral density function of the coupling $J(\epsilon) = \pi \sum_q \lambda_q^2 \delta(\epsilon - \hbar \omega_q)$. A generic spectral function has a power law dependence on energy at small energies, $J(\epsilon) \sim \epsilon^s$, and vanishes rapidly for energies above the ultraviolet cutoff E_c . Here, we consider the Ohmic (s = 1) environment with exponential high-energy cutoff:

$$J(\epsilon) = 2\pi\alpha\epsilon \exp(-\epsilon/E_c), \tag{4.5}$$

where the dimensionless parameter α defines the strength of coupling between the qubit and its environment and E_c is the cutoff. We restrict ourself to the weak coupling limit, $\alpha \ll 1$. Our approach can be adapted to non-Ohmic environments by utilizing the corresponding spectral functions $J(\epsilon)$ in the calculations below.

In general, the effect of weak environment on the qubit dynamics is twofold. On one hand, the qubit Hamiltonian is renormalized by the environment modes with $\epsilon < E_c$,

known as the Lamb and Stark effects. On the other hand, when we integrate out the environmental degrees of freedom, we also obtain non-unitary terms in the evolution of the quantum system. Both of these effects are accounted for by the BR equation [91, 90, 94] for the qubit density matrix $\hat{\rho}(t)$.

We first consider the case of a constant external magnetic field along \hat{z} direction, $\mathbf{b} = b\hat{\mathbf{z}}$. Then, the BR equation has the following form in the eigenstate basis

$$\begin{pmatrix} \dot{\rho}_{00}(t) \\ \dot{\rho}_{11}(t) \end{pmatrix} = \begin{pmatrix} -\Gamma_e & \Gamma_r \\ \Gamma_e & -\Gamma_r \end{pmatrix} \begin{pmatrix} \rho_{00}(t) \\ \rho_{11}(t) \end{pmatrix}, \tag{4.6a}$$

$$\dot{\rho}_{01}(t) = (i\epsilon - \Gamma_2)\rho_{01}(t), \tag{4.6b}$$

$$\dot{\rho}_{10}(t) = (-i\epsilon - \Gamma_2)\rho_{10}(t). \tag{4.6c}$$

We obtained the above equations within secular approximation that neglects fast oscillating terms with frequencies larger than the decoherence rates.

The equation in the matrix form, Eq. (4.6a), determines the evolution of diagonal elements of the density matrix. The relaxation and excitation rates, Γ_r and Γ_e , are defined by the spectral density $J(\epsilon)$ at the energy corresponding to the energy difference between two states of the qubit:

$$\Gamma_r = \frac{n_x^2 + n_y^2}{2\hbar} J(\epsilon)(N(\epsilon) + 1), \tag{4.7a}$$

$$\Gamma_e = \frac{n_x^2 + n_y^2}{2\hbar} J(\epsilon) N(\epsilon), \tag{4.7b}$$

and $N(\epsilon) = 1/[\exp(\epsilon/T) - 1]$ is the Planck's function. The factor $n_x^2 + n_y^2$ indicates that only the component of the fluctuating environment field that is perpendicular to the direction of the control field **b** gives rise to the qubit flip processes.

The off-diagonal elements of the density matrix are characterized by the decoherence rate Γ_2 and pure dephasing rate Γ_{φ} given by

$$\Gamma_2 = \frac{1}{2} (\Gamma_r + \Gamma_e) + \Gamma_{\varphi}, \quad \Gamma_{\varphi} = n_z^2 J_0.$$
 (4.7c)

The decoherence stems from two processes — the qubit flip processes with rate $\Gamma_r + \Gamma_e$, and pure dephasing which is not responsible for energy transitions at low frequency with

rate $J(\epsilon \simeq 0) \equiv J_0$. The only source of pure dephasing is the fluctuating fields of the environment along the external field **b**, hence the factor $\cos \theta$ in the definition of the pure dephasing term, $\Gamma_{\varphi} \propto n_z^2$.

The renormalization of the qubit Hamiltonian by the environment due to the Lamb or Stark effects are determined by the imaginary part of the environmental correlation function, as discussed in Ref. [94]. Explicitly, the renormalized qubit energy ϵ is

$$\epsilon = b + \delta \epsilon, \quad \delta \epsilon = -P \int \frac{d\omega}{4\pi} \frac{J(\omega) \coth(\omega/2T)}{\omega - b},$$
 (4.8)

where P denotes the Cauchy principal value. Below, we assume that the control field **b** already includes renormalization effects from the environment. The goal of this chapter is to investigate the features of the qubit evolution originating from decoherence characterized by rates Γ_r and Γ_e , respectively. The significance of the effect of the Lamb and Stark shifts on the evolution of the qubit was demonstrated in Ref. [120] in the context of the LZ problem.

We note that the qubit density matrix can be defined in terms of the magnetization in x, y and z directions as

$$\hat{\rho}(t) = \frac{1}{2} \left(1 + \mathbf{m}(t) \cdot \sigma \right). \tag{4.9}$$

Then the BR equations, Eq. (4.6), acquire a more common form of the Bloch equations

$$\dot{m}_z = (\Gamma_r - \Gamma_e) - (\Gamma_r + \Gamma_e)m_z, \tag{4.10a}$$

$$\dot{m}_x = -i\epsilon m_y - \Gamma_2 m_x \tag{4.10b}$$

$$\dot{m}_y = i\epsilon m_x - \Gamma_2 m_y. \tag{4.10c}$$

The above BR equations were obtained in the basis of qubit eigenstates. In case when the control field $\mathbf{b}(t)$ changes in time, we perform transformation $\hat{U}_1(t)$ of the basis that keeps the qubit Hamiltonian diagonal. This basis is commonly referred to as adiabatic. The corresponding transformation has two consequences.

The first consequence of $\hat{U}_1(t)$ transformation is that the Hamiltonian in the new basis acquires an extra term originating from the time dependence of the transformation $\hat{U}_1(t)$.

Thus, the qubit Hamiltonian in the new basis is

$$\hat{H}_0^{U_1}(t) = -\frac{\epsilon(t)}{2}\,\hat{\sigma}_z - i\hat{U}_1(t)\dot{\hat{U}}_1^{\dagger}(t)\,. \tag{4.11}$$

The resulting Hamiltonian still may remain non-diagonal due to the Berry connection term, $i\hat{U}_1(t)\dot{\hat{U}}_1^{\dagger}(t)$. We can introduce a new transformation $\hat{U}_2(t)$ that diagonalizes the right hand side of (4.11), but this transformation generates a new term $i\hat{U}_2(t)\dot{\hat{U}}_2^{\dagger}(t)$ and the "diagonalization" series of transformations $\hat{U}_n(t)$ does not stop for an arbitrary time evolution of $\mathbf{b}(t)$, because the Berry connection terms appearing in each consecutive diagonalization transformation acquires an extra time derivative. However, for slow time evolution, the series of transformations can be truncated by the first one or two transformations. Since the BR treatment of environmental effect requires anyway that the system changes in time slower than the rates given by Eqs. (4.7) and (4.7c) in the master equation, the truncation to a limited number of transformations $\hat{U}_n(t)$ under slow evolution of $\mathbf{b}(t)$ is justified. Also, in a special case of constant rotation of $\mathbf{b}(t)$ in a plane, the second transformation \hat{U}_2 is time-independent and transformation series stops after this second basis rotation.

The second consequence of the basis transformations is the modified interaction term in that the coupling between the qubit and its environment

$$\tilde{H}_{\text{int}} = \sum_{q} \lambda_q \mathbf{n}'(t) \hat{\sigma} \frac{\hat{a}_q + \hat{a}_q^{\dagger}}{2}, \quad \mathbf{n}'(t) \hat{\sigma} = \mathbf{n} \hat{V}(t) \hat{\sigma} \hat{V}^{\dagger}(t)$$
(4.12)

is modified from the initial coupling operator $\mathbf{n} \cdot \sigma$ to the environment field by the transformation matrix $\hat{V}(t) = \hat{U}_n(t) \dots \hat{U}_1(t)$. This transformation changes the corresponding "projection" factors $n_{\{x,y,z\}}$ in Eqs. (4.7) as well as the spectral weights $J(\epsilon)$.

Modification of the coupling between the qubit and its environment, introduced by Eq. (4.12), swaps components of the fluctuating field responsible for the pure dephasing and transition processes. For example, in case of a fixed external field $\mathbf{b} \| \mathbf{e}_z$, fluctuations along \mathbf{e}_z give rise to pure dephasing and do not cause transition processes between qubit eigenstates. However, as $\mathbf{b}(t)$ rotates while \mathbf{n} remains in \mathbf{e}_z direction, the fluctuating component along field $\mathbf{b}(t)$ is the only one responsible for the dephasing with the corresponding rate proportional to the spectral weight of its low-frequency fluctuations J_0 , while the com-

ponent of the fluctuating field perpendicular to **b** will produce qubit flip processes with the rate characterized by the spectral weight of fluctuating field with the energy equal to the energy of qubit flip $J(\epsilon(t))$. The second unitary transformation further mixes matrix elements of the coupling to environment representing qubit flip processes and pure dephasing.

Below, we present explicit expressions for the rates in Eqs. (4.7) for two special cases of evolution of $\mathbf{b}(t)$ for different types of environment. We focus on the effect of qubit flip processes due to environment and assume that $J_0 = 0$ in most numerical solutions. We note that the pure dephasing produced by the low frequency noise of the environment can be successfully described in terms of fluctuations of the classical field and may also include non–Markovian time correlations that are omitted in the BR approach. Effects of classical noise were discussed in Refs. [131, 122, 132, 112, 133, 113] for the LZ transition and in Refs. [106, 100] for Berry phase measurements.

4.3 Qubit rotation in a plane

We first consider a qubit with the Hamiltonian characterized by a time-dependent field in x-z plane: $\mathbf{b}(t) = \Delta \{\sin \theta(t), 0, \cos \theta(t)\}$. By definition, $\theta(t) = 0$ for t < 0. The transformation to adiabatic basis is defined by:

$$\hat{U}_1(t) = \exp(i\hat{\sigma}_y \theta(t)/2) \tag{4.13}$$

and the resulting qubit Hamiltonian has the form

$$\hat{H}_0^{U_1} = -\frac{\Delta \hat{\sigma}_z + \dot{\theta}(t)\hat{\sigma}_y}{2}.\tag{4.14}$$

Here, the second term is responsible for the non-diagonal form of the Hamiltonian for timedependent rotation angle $\theta(t)$ and causes the resultant field to point out of the rotation plane of $\mathbf{b}(t)$. This Hamiltonian has eigenvalues $\varepsilon_{\pm} = \pm \sqrt{\Delta^2 + \dot{\theta}^2}/2$ and eigenvectors, which are different from the vectors of the adiabatic basis. The latter two represent spin states in the (x-z) plane with $m_y = 0$. On the contrary, the qubit in the ground state $|g\rangle$ of the Hamiltonian (4.14) has a non-zero expectation value of the polarization m_y in the direction perpendicular to the (x-z) plane of the control field **b**:

$$m_y = \langle g | \hat{\sigma}_y | g \rangle = -\frac{\dot{\theta}}{\sqrt{\Delta^2 + \dot{\theta}^2}}.$$
 (4.15)

In the limit of slow rotations, $\dot{\theta}(t) \ll \Delta$, this result is consistent with a more general expression that connects a generalized force $f_i = -\langle g|\partial \hat{H}(\mathbf{X})/\partial X_i|g\rangle$ to time-dependent parameters $\mathbf{X}(t)$ of the Hamiltonian through the Berry curvature F_{ij} as [104, 87]

$$f_i = -\langle g | \frac{\partial \hat{H}(\mathbf{X})}{\partial X_i} | g \rangle = \sum_j F_{ij} \dot{X}_j(t).$$
 (4.16)

Comparing Eq. (4.15) and Eq. (4.16), we identify $f_y = m_y/2$, $\dot{X} = \dot{\theta}$ and $F_{y\theta} = 1/(2\Delta)$. Explicitly, the coefficient of the linear term in the rate of change of the magnetic field, *i.e.* $\Delta\Omega$, is the Berry curvature $1/2\Delta^2$. Indeed, this value of the Berry curvature gives the Berry phase $\Phi = \pi$ for one full rotation of the control field in the (x - z) plane after its integration over the half-sphere, $\int_{S(\mathbf{b})} ds/(2\Delta^2) = \pi$. This relation holds for an isolated qubit controlled by field $\mathbf{b}(t)$, assuming that $\mathbf{b}(t)$ is a slowly varying function of time with continuous higher derivatives.

However, if the rotation of the control field **b** starts instantaneously with constant angular velocity $\dot{\theta}(t) = \Omega$, *i.e.* $\theta(t) = \Omega t$, the rotation is equivalent to a quantum quench in the representation of Eq. (4.14) from $\dot{\theta} = 0$ to $\dot{\theta} = \Omega$. The qubit that was initially in the ground state of the original time-independent Hamiltonian, $-b\hat{\sigma}_z/2$, is in the superposition of eigenstates of the new Hamiltonian and exhibits precession around new direction of the effective field $(0, \Omega, b)$. This precession causes oscillations of

$$m_{\nu}(t) = \text{Tr}\{\hat{\sigma}_{\nu}\hat{\rho}(t)\} \tag{4.17}$$

around its average value given by Eq. (4.15), as illustrated in Figure 4.1(a). Here we use $\Omega = 0.2\Delta$ for a qubit decoupled to the environment. The qubit trajectories on the Bloch sphere in the original state basis is a cycloid along the equator in the plane of rotation of the control field and the "height" of the cycloid is proportional to Ω .

¹A simple realization of this setup for superconducting qubits is to apply a microwave pulse in the resonance of the original qubit energy splitting to let the qubit relax to its ground state in the rotated basis, and then to produce excitation with the same amplitude but shifted in frequency by Ω .

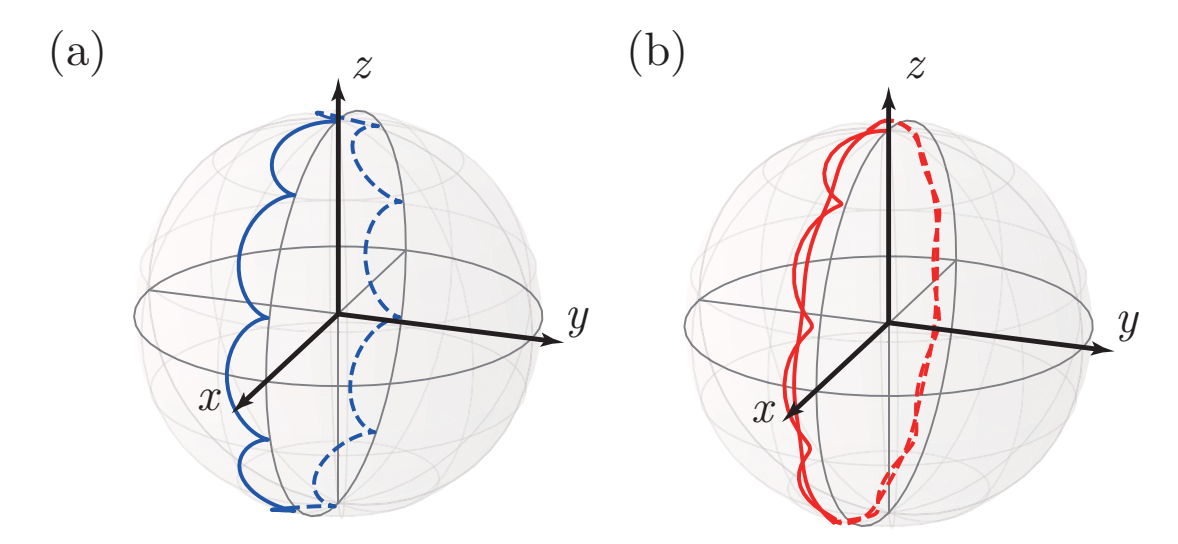


Figure 4.1: The Bloch sphere representation of the qubit state in the diabetic basis with $\Omega = 0.2\Delta$ and initial condition z = 1 for (a) $\alpha = 0$ and (b) $\alpha = 0.02$ at T = 0. For the dissipationless dynamics the trajectory of the qubit state form cycloids along the equator y = 0. However, for the dissipative dynamics the cycloidal trajectory flattens to a circular one with a finite value $m_y(\infty)$.

In the rest of this section, we analyze the effect of the environment on qubit response to rotating control field. We demonstrate that a qubit coupled to a zero-temperature environment relaxes towards the lower eigenstate of Hamiltonian (4.14) and for long time limit after the rotation started, the qubit state obeys Eq. (4.15). For rotation with constant angular velocity Ω , the transformed Hamiltonian, Eq. (4.14) is time independent and can be diagonalized by the second basis transformation

$$\hat{U}_2 = \cos \eta / 2 - i\hat{\sigma}_x \sin \eta / 2, \quad \tan \eta = \Omega / \Delta. \tag{4.18}$$

The qubit Hamiltonian in a new basis after a full transformation $\hat{V}(t) = \hat{U}_2 \hat{U}_1(t)$ becomes fully diagonal with time-independent eigenvalues:

$$\hat{H}_0^V = \hat{U}_2 \hat{H}_0^{U_1} \hat{U}_2^{\dagger} = -\frac{W}{2} \hat{\sigma}_z \,, \quad W = \sqrt{\Delta^2 + \Omega^2}. \tag{4.19}$$

We can apply the BR equation for the qubit density matrix, where the rates in Eq. (4.6) are defined by the interaction term H_{int} , Eq. (4.2), with $\sigma \cdot \mathbf{n}$ replaced by its transformation under $\hat{V}(t)$ according to Eq. (4.12). The result of the $\hat{V}(t)$ transformation depends

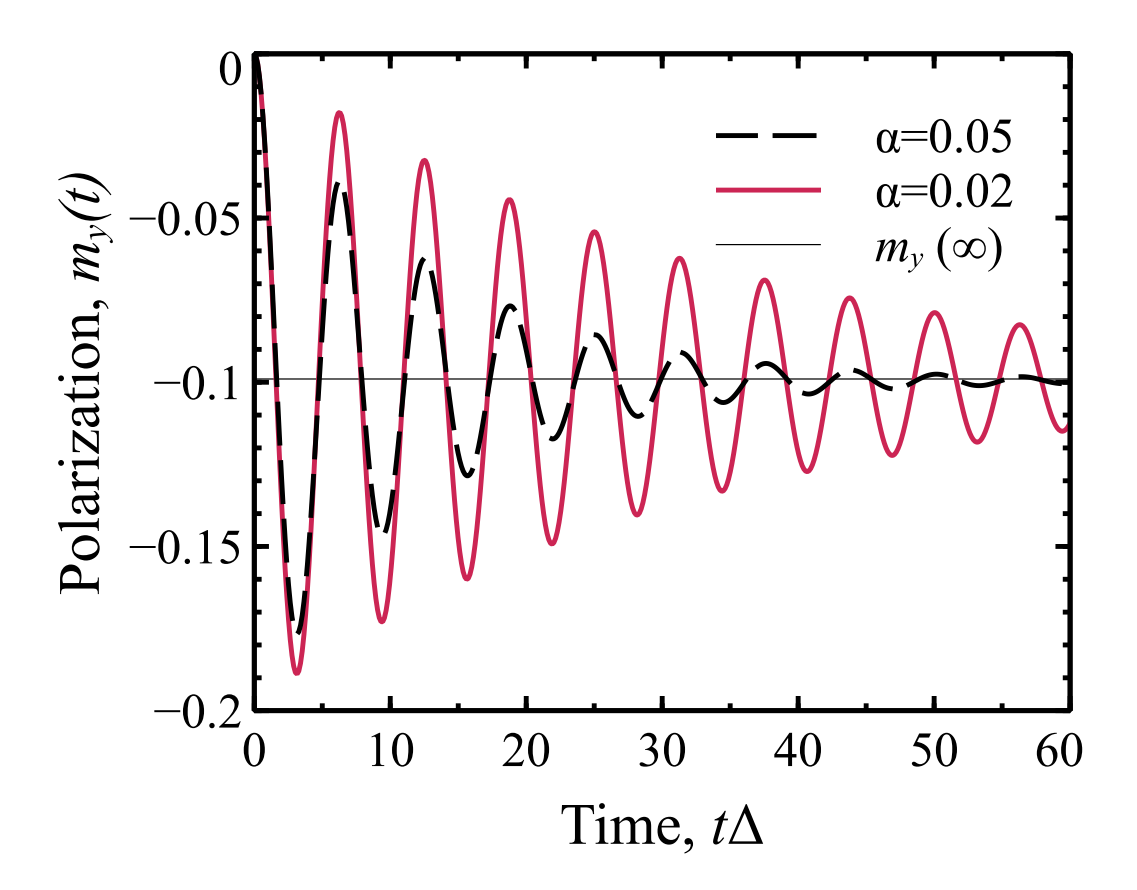


Figure 4.2: Time dependence of the out-of-plane polarization, $m_y(t)$, at zero temperature of environment for $\alpha = 0.02$ (solid line) and $\alpha = 0.05$ for fluctuating environment field out of the plane of rotation, $\mathbf{n} = \hat{\mathbf{y}}$. The pure dephasing rate is zero, $J_0 = 0$. The frequency of rotation of the control field is $\Omega = 0.1\Delta$. The thin horizontal line represents the asymptotic values of $m_y(\infty)$.

on the original orientation of the vector \mathbf{n} in the qubit space. Below, we consider three orientations of \mathbf{n} . We note that for the limit $\Omega \ll \Delta$ considered in this section, the shift of eigenvalues of Hamiltonian (4.19) and modification of the coupling to environment by the second transformation $\hat{U}_2 \simeq 1$ is not significant and can be disregarded to the lowest order in Ω .

Environment field perpendicular to the rotation plane

We first consider the case when the coupling between the qubit and its environment is determined by the vector $\mathbf{n} = \hat{\mathbf{y}}$ perpendicular to the plane of rotation of the external field

 $\mathbf{b}(t)$. For time independent Hamiltonian, this coupling causes qubit flip processes and the corresponding decoherence rates are defined by the environment spectral function at the excitation energies equal to the qubit energy splitting. For time-dependent Hamiltonian with rotating $\mathbf{b}(t)$, we have to write the qubit coupling operator $\mathbf{n} \cdot \boldsymbol{\sigma}$ in the rotated basis that diagonalizes the original Hamiltonian. As we discussed above, the transformation is a product of two consecutive transformations. The first transformation, $\hat{U}_1(t)$ to the adiabatic basis does not change the coupling operator $\hat{U}_1(t) \mathbf{n} \cdot \boldsymbol{\sigma} \hat{U}_1^{\dagger}(t) = \hat{\sigma}_y$. The second transformation results in

$$\hat{\Sigma}_y = \hat{V}(t)\,\hat{\sigma}_y \hat{V}^{\dagger}(t) = \hat{\sigma}_y \cos \eta + \hat{\sigma}_z \sin \eta. \tag{4.20}$$

Here, the first term represents the qubit flip process, while the second term preserves the qubit orientation and causes pure dephasing. The corresponding rates in the BR equations are given by

$$\Gamma_r = \frac{\cos^2 \eta}{2} J(W)[N(W) + 1],$$
(4.21a)

$$\Gamma_e = \frac{\cos^2 \eta}{2} J(W) N(W), \tag{4.21b}$$

$$\Gamma_2 = \frac{\Gamma_r + \Gamma_e}{2} + \frac{\sin^2 \eta}{2} J_0, \tag{4.21c}$$

with W and η defined by Eqs. (4.19) and (4.18). The qubit dynamics is characterized by the relaxation and excitation rates proportional to the spectral function J(W) of environment at energy W, these rates appear with factor $\cos^2 \eta = \Delta^2/W^2$ and recover the case of the qubit with a time-independent Hamiltonian with $\mathbf{b} \perp \mathbf{n}$ when only environment modes in resonance with the qubit contribute to the qubit dynamics. At finite Ω , however, the pure dephasing mechanism arises after transformation \hat{U}_2 and originates from the low frequency modes of the environment with spectral density J_0 . The pure dephasing rate contains factor $\sin^2 \eta = \Omega^2/W^2$ which is small for slow rotation with $\Omega \ll \Delta$.

The Bloch equations Eq. (4.10) with rates given by Eq. (4.21) can be solved to get the qubit density matrix $\hat{\rho}^{U_2}(t)$ in the secondly rotated basis. In conjunction with the initial condition, the time evolution of $m_y(t)$ is then obtained by $\text{Tr}[\hat{\Sigma}_y\hat{\rho}(t)]$, see Figure 4.1(b) for

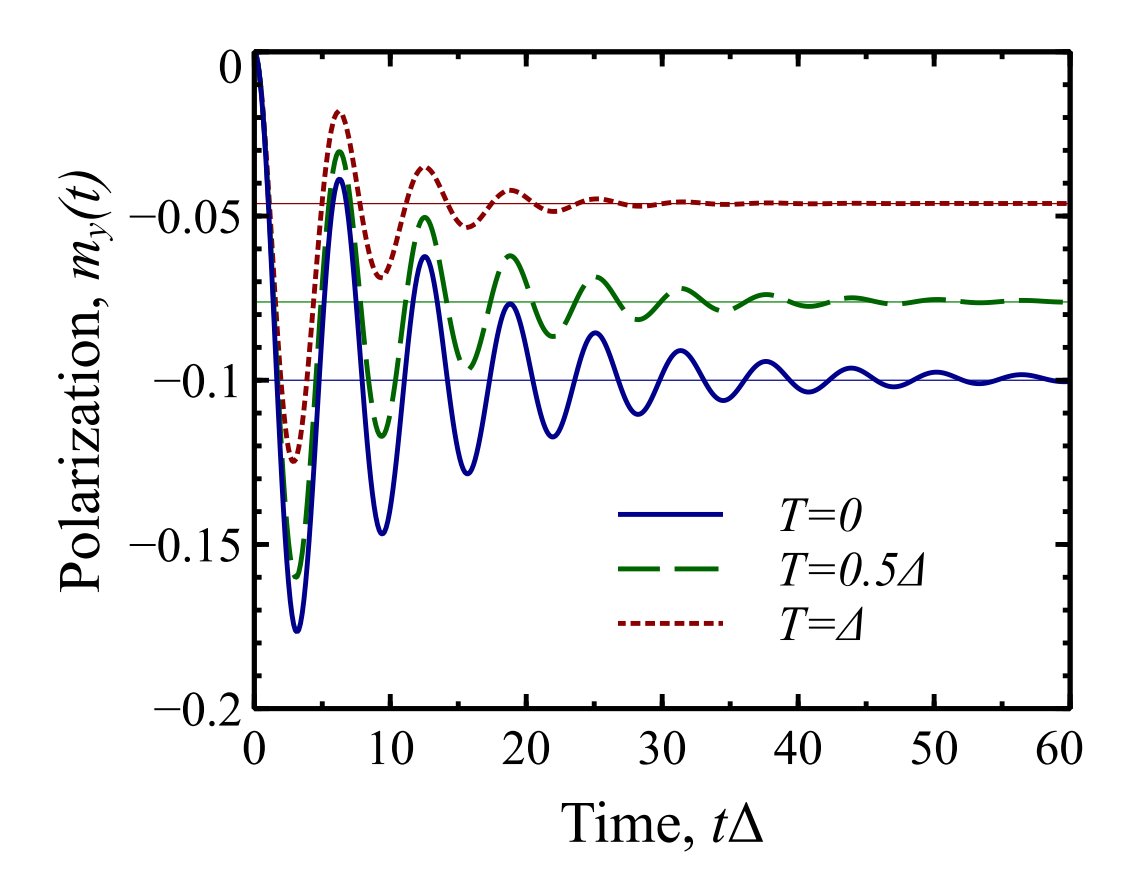


Figure 4.3: Time dependence of the out-of-plane polarization, $m_y(t)$, at various temperatures of environment: T=0 (solid line), $T=0.5\Delta$ (dashed line) and $T=\Delta$ (dotted line) for fluctuating environment field out of the plane of rotation, $\mathbf{n}=\hat{\mathbf{y}}$. The pure dephasing rate is zero, $J_0=0$. The frequency of rotation of the control field is $\Omega=0.1\Delta$. The coupling to environment $\alpha=0.05$. The thin horizontal lines represent the asymptotic values of $m_y(\infty)$ at different temperatures.

 $\Omega = 0.2\Delta$ and $\alpha = 0.02$. Initially, after the rotation starts, the qubit state at the Bloch sphere exhibits wiggles, similar to those in Figure 4.1(a) for an isolated system. As rotation continues, wiggles flatten out and the quit evolution on the Bloch sphere becomes a circle cross-section of the sphere by an x-z plane shifted along y-axis.

First, we provide an exact analytical solution by choosing the initial state to be a thermal state $\rho^{(0)}(0) = 1/2 + \tanh(W/2T)\sigma_z/2$. Defining $m_0 = \tanh(W/2T)$, the initial condition for the Bloch equation becomes $m_z(0) = m_0 \cos \eta$, $m_x(0) = 0$ and $m_y(0) = m_0 \sin \eta$.

Integrating the Bloch equation with the above initial condition yields

$$m_y(t) = -m_0 \sin \eta$$

$$\times \left(1 - 2\sin^2 \frac{\eta}{2} e^{-\Gamma_{\text{tot}}t} - \cos \eta e^{-\Gamma_{\text{tot}}t/2} \cos Wt \right),$$
(4.22)

where $\Gamma_{\text{tot}} = \Gamma_r + \Gamma_e$ and we assumed $J_0 = 0$. In the long times limit, $t \to \infty$, $m_y(t)$ reaches its stationary state solution

$$m_y(\infty) = -\frac{\Omega}{W} \tanh \frac{W}{2T} \simeq -\frac{\Omega}{\Lambda} \tanh \frac{\Delta}{2T},$$
 (4.23)

regardless of the form of the initial state. The significance of this expression is that the dynamical transverse response of the qubit subject to a rotating magnetic field is a consequence of the geometric phase effect in the sense that the stationary value $m_y(\infty)$ does not depend on the strength of the coupling to environment. Therefore, $m_y(\infty)$ is purely geometrical and immune to quantum zero-temperature fluctuations of the environment.

Next, in order to get the numerical solution of the BR equations (4.6) we utilize standard integration methods for a system of linear differential equations with time-dependent coefficients. Alternatively, we obtain the same results using the BR functions of the QuTiP package [45, 134] with a proper adjustment to the system Hamiltonian and the interaction term, see Eqs. (4.12) and (4.19), for time-dependence of the eigenstate basis, as presented in Figs. 4.2 and 4.3. We verified that the results shown in the plots are identical to numerical integration of the BR equations with the rates given by Eqs. (4.21). In both plots, the initial condition of the density matrix is chosen to be the ground state at t = 0 when $\mathbf{b} \parallel \mathbf{e}_z$. We obtain plots consistent with the analytical result, Eq. (4.22), for the thermal state of the density matrix at t = 0.

In Figure 4.2, we present the time evolution of $m_y(t)$ for several values of the coupling to the environment. From the plot it is clear that the role of the environment is to suppress transient wiggles of m_y and to bring the system to the steady state, defined by Eq. (4.23) with $\tanh(\Delta/2T) \to 1$. However, the transverse magnetization is fragile to thermal fluctuations, since these fluctuations create excitation to the higher energy state. The result is shown in Figure 4.3, where we fix α and plot $m_y(t)$ for different temperatures

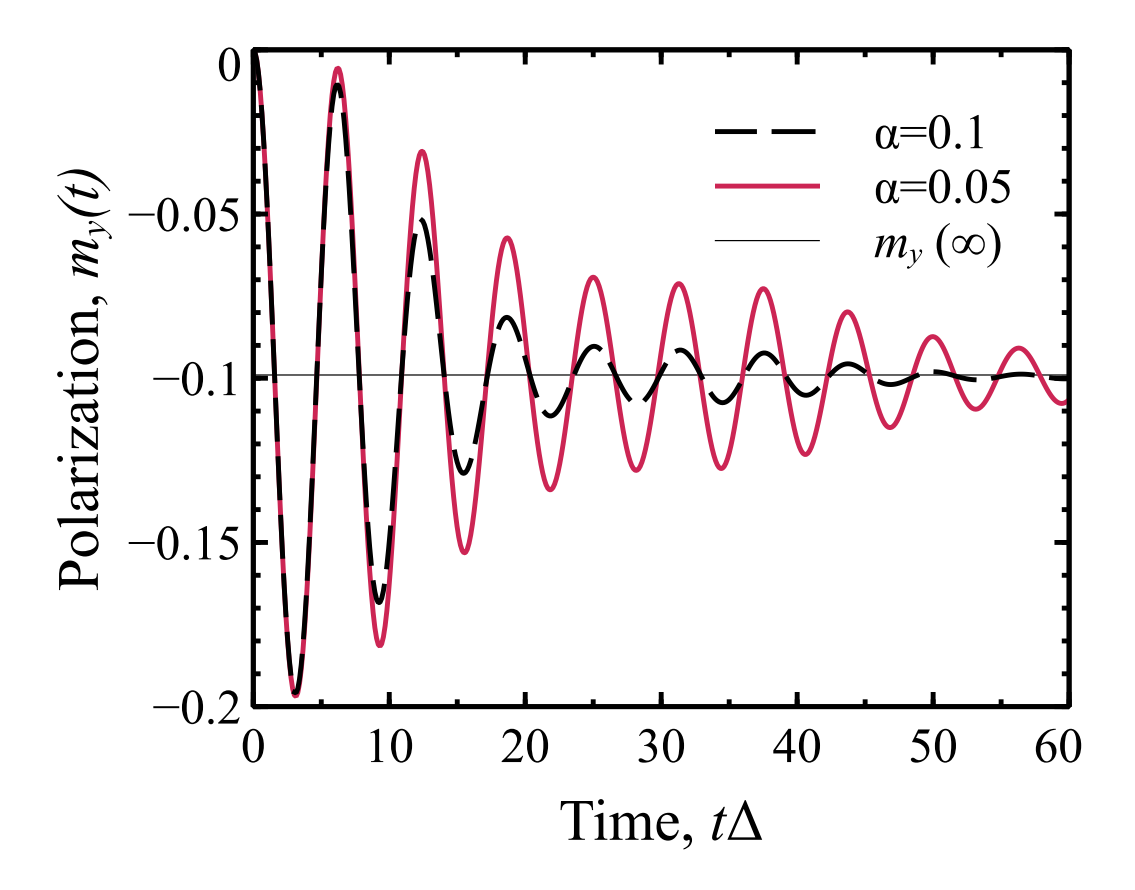


Figure 4.4: Time dependence of the out-of-plane polarization, $m_y(t)$, at zero temperature of environment, for $\alpha = 0.05$ (solid line) and $\alpha = 0.1$ (dashed line) for fluctuating environment field in the plane of rotation, $\mathbf{n} = \hat{\mathbf{z}}$. The pure dephasing rate is zero, $J_0 = 0$. The frequency of rotation of the control field is $\Omega = 0.1\Delta$. The relaxation is reduced for time intervals when $\Omega t \simeq \pi n$. The thin horizontal line represents the asymptotic values of $m_y(\infty)$.

 $T=\{0,1/2,1\}\Delta$. We note that since the dephasing rate, $\Gamma_2=(\Gamma_r+\Gamma_e)/2$ grows with the temperature, the oscillations decay faster for higher temperatures. Also, at finite temperatures, the spin has nonzero probability to stay in the excited state, the asymptote of $m_y(t\to\infty)$ is reduced in agreement with Eq. (4.23).

Environment field in the rotation plane

We now consider the qubit interacting with environment field in the plane of rotation. We take $\mathbf{n} = \mathbf{e}_z$ and for $\mathbf{b} \| \mathbf{e}_z$ the coupling to the environment results in pure dephasing and is characterized by the low frequency spectral density J_0 . As \mathbf{b} rotates, the effect of environment

ronment alternates between pure dephasing and qubit transitions between eigenstates. We obtain this variation in qubit flip and dephasing rates already after applying transformation $\hat{U}_1 = \exp(i\hat{\sigma}_y\theta/2)$ to the interaction Hamiltonian of the qubit and environment, Eq. (4.2). However, for rotating $\mathbf{b}(t)$ we have to take into account the gauge term $-i\hat{U}_1(t)\partial_t\hat{U}_1^{\dagger}(t)$ in Eq. (4.11) by applying the second transformation \hat{U}_2 to $\hat{H}_{\rm int}$. We obtain

$$\hat{V}(t)\hat{\sigma}_z\hat{V}^{\dagger}(t) = -\hat{\sigma}_x\sin\Omega t - (\hat{\sigma}_y\sin\eta - \hat{\sigma}_z\cos\eta)\cos\Omega t \tag{4.24}$$

that contains matrix elements for qubit flip processes at any moment of time. The corresponding rates in the Bloch–Redfield equations are

$$\Gamma_r = \frac{G(t)}{2} J(W)[N(W) + 1],$$
(4.25a)

$$\Gamma_e = \frac{G(t)}{2} J(W) N(W), \tag{4.25b}$$

$$\Gamma_2 = \frac{\Gamma_r + \Gamma_e}{2} + J_0 \cos^2 \eta \cos^2 \Omega t, \tag{4.25c}$$

where $G(t) \equiv \sin^2 \eta + \sin^2 \Omega t \cos^2 \eta$ and thus the qubit flip rates are nonzero as a function of time.

The evolution of the qubit in this case corresponds to precession of a spin in the magnetic field with initial state distinct from its new ground state after the quench. Namely, its dynamics will correspond to suppression of off-diagonal elements of its density matrix with the rate $\Gamma_2(t)$ and equilibration of the diagonal elements of ρ with rates $\Gamma_{r/e}(t)$. We emphasize that in this case all decoherence rates are time-dependent.

We calculate time-dependence of $m_y(t)$ by numerically solving the BR equations with the rates given by Eq. (4.25). We present the result of integration in Figure 4.4 for two different values of α at zero temperature and find clear evidence that the decoherence rates are roughly one half smaller compared to the result of previous subsection for the same value of α . Meanwhile, in Figure 4.5 we fix α and plot $m_y(t)$ for different temperatures. At time longer than the relaxation time $1/\Gamma_2$, $m_y(t)$ becomes constant with its value $m_y(\infty) =$ $-\Omega/W \tanh(W/2T)$, see Eq. (4.23)

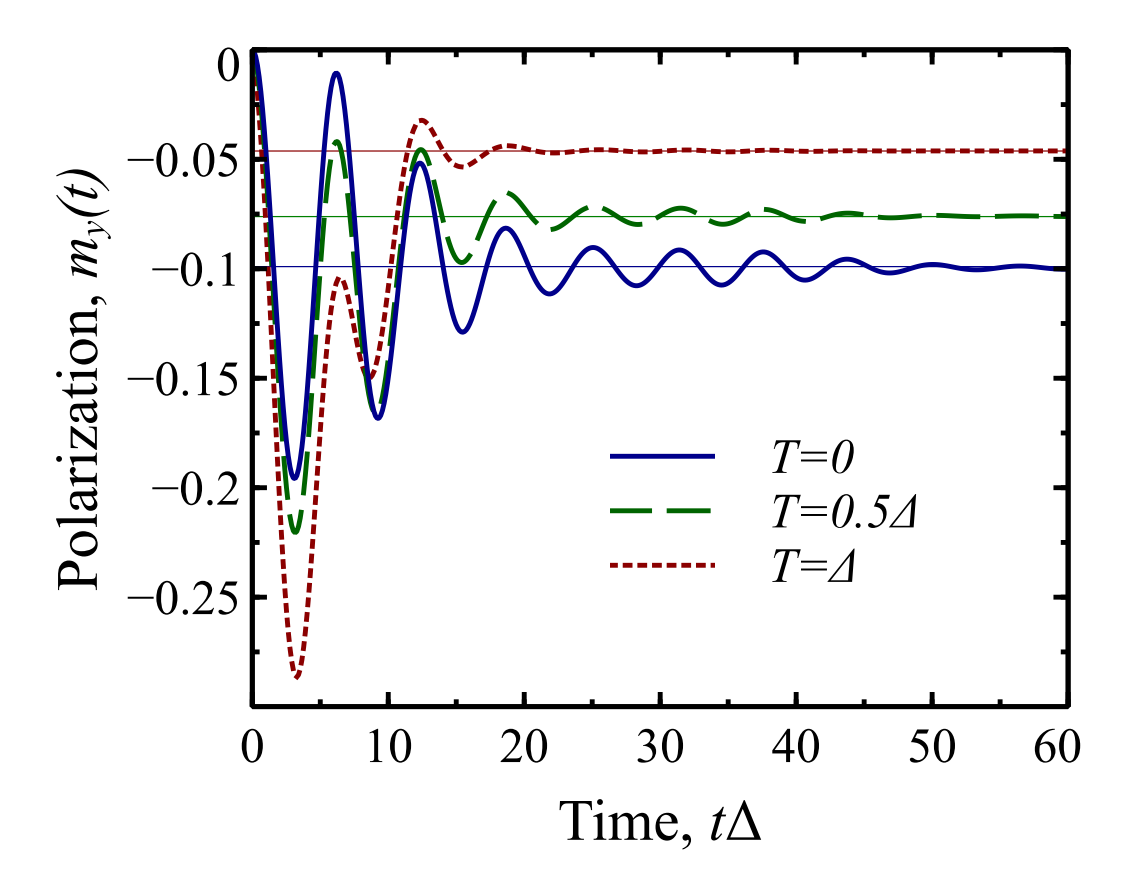


Figure 4.5: Time dependence of the out-of-plane polarization, $m_y(t)$, for $\alpha = 0.1$ and T = 0 (solid line), $T = 0.5\Delta$ (dashed line) and $T = \Delta$ (dotted line) in case when fluctuating environment field is in the plane of rotation, $\mathbf{n} = \hat{\mathbf{z}}$. The pure dephasing rate is zero, $J_0 = 0$. The frequency of rotation of the control field is $\Omega = 0.1\Delta$. The thin horizontal lines represent the asymptotic values of $m_y(\infty)$ at different temperatures.

Longitudinal coupling to environment

We also consider a somewhat artificial scenario when the coupling vector $\mathbf{n} = \sin \Omega t \, \mathbf{e}_x + \cos \Omega t \, \mathbf{e}_z$ in Eq. (4.2) rotates together with the external field $\mathbf{b}(t)$ ². For a stationary Hamiltonian this environment does not produce qubit flip processes and results in pure dephasing, when the diagonal elements of the density matrix do not change and only off diagonal elements decrease with time. In case when the direction of the control field rotates with frequency Ω , the basis transformation term in Eq. (4.11) introduces qubit flip processes

²This case may be realized if the interaction of the environment with the qubit is introduced through a fluctuating field along the external field $\mathbf{b}(t)$, e.g. when $\mathbf{b}(t)$ is realized as two quadratures of microwave pulse driving a qubit and the environment is described by longitudinal quantum fluctuations of the pulse.

for this coupling with the rates in Eqs. (4.6) given by

$$\Gamma_r = \frac{\sin^2 \eta}{2} J(W)[N(W) + 1],$$
(4.26a)

$$\Gamma_e = \frac{\sin^2 \eta}{2} J(W) N(W), \tag{4.26b}$$

$$\Gamma_2 = \frac{\Gamma_r + \Gamma_e}{2} + \cos^2 \eta J_0. \tag{4.26c}$$

For slow rotation $\Omega \ll \Delta$, we have $\sin \eta \ll 1$ and qubit flip processes are small. In this case, dephasing will suppress precession on time scale $\sim 1/J_0$, and further equilibration of the system occurs on a longer time scale $\sim \Delta/\pi\Omega^2$. We describe the evolution of a qubit coupled to high-temperature environment using a dephasing Lindblad model in Sec. 4.5.

Coupling to a strongly damped Quantum oscillator

In this subsection we consider the interaction of a qubit with a single damped quantum harmonic oscillator. This model can be used to describe environment with a sharp spectral function $J(\epsilon)$. The interaction part of the Hamiltonian is similar to Eq. (4.2):

$$\hat{H}_{\text{int}} = \frac{\lambda}{2} (\hat{a} + \hat{a}^{\dagger}) \mathbf{n} \cdot \sigma \tag{4.27}$$

and the single-mode Hamiltonian of the oscillator is $\hat{H}_{\text{o/c}} = \omega_0(\hat{a}^{\dagger}\hat{a} + 1/2)$. We describe dissipation of the oscillator using the Lindblad relaxation operators for the full density matrix $\bar{\rho}(t)$ of the qubit and the oscillator system:

$$\dot{\bar{\rho}}(t) = -i[\hat{H}(t), \bar{\rho}] - \kappa \left(\hat{a}^{\dagger} \hat{a} \bar{\rho} + \bar{\rho} \hat{a}^{\dagger} \hat{a} - 2\hat{a} \bar{\rho} \hat{a}^{\dagger} \right)$$

$$(4.28)$$

This equation is a standard Lindblad master equation with time dependent Hamiltonian. The difference with the previous calculations of this Section is that we keep a full quantum mechanical treatment of the qubit interaction with the oscillator and perform all transformations of the qubit basis for the full Hamiltonian of the qubit and the oscillator. At the same time, we assume that the Lindblad superoperator for the relaxation of the harmonic oscillator, represented by the last term in Eq. (4.28), is not affected by these transformations.

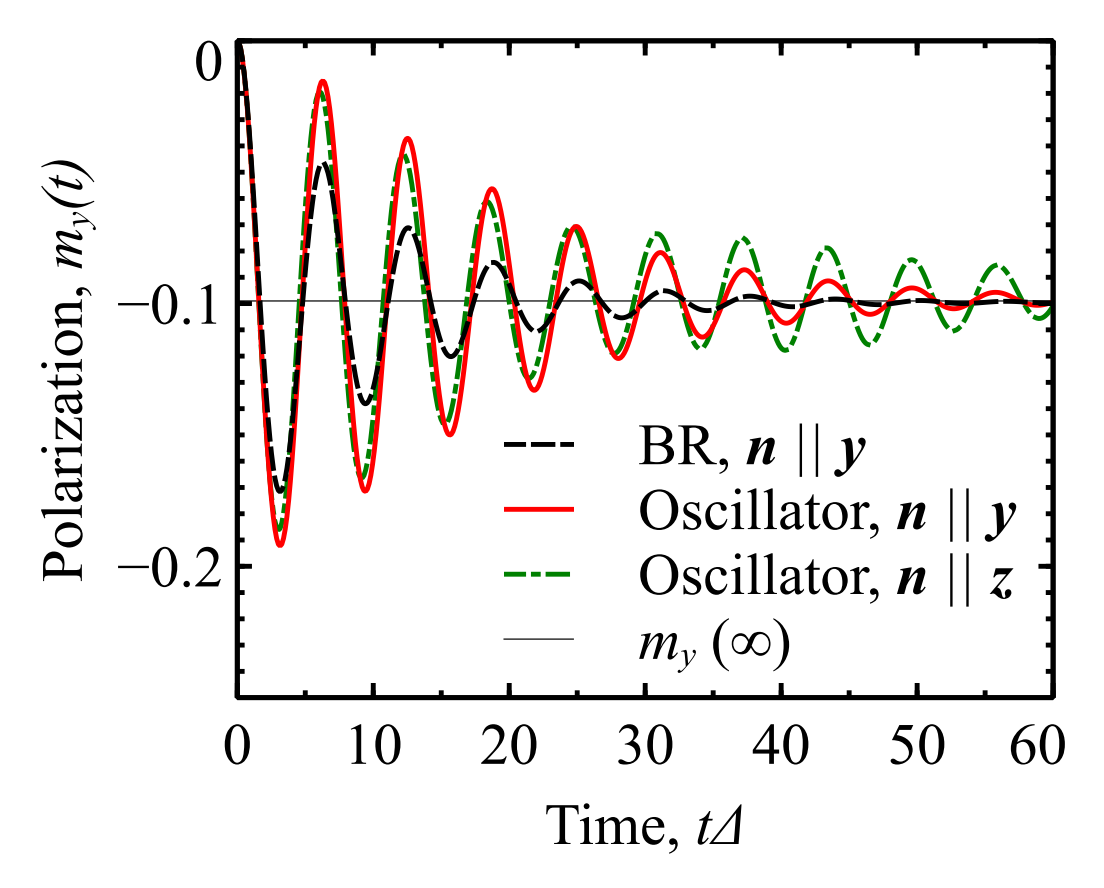


Figure 4.6: Time dependence of the out-of-plane polarization, $m_y(t)$, at zero temperature of environment for a qubit coupled to a damped harmonic oscillator with damping rate $\kappa = 0.2\Delta$ and coupling constant between the qubit and environment $\lambda = 0.1\Delta$. Coupling vector $\mathbf{n} \parallel \hat{\mathbf{y}}$ (solid line) and $\mathbf{n} \parallel \hat{\mathbf{z}}$ (dash-dotted line). For comparison, the solution for the Bloch–Redfield equation is presented (dashed line) with $\alpha = 0.03$ and $J_0 = 0$. The rotation angular velocity is $\Omega = 0.1\Delta$. The thin horizontal line represents the asymptotic values of $m_y(\infty)$.

We evaluate the qubit projection perpendicular to the rotation plane of the control field as a function of time. Figure 4.6 shows the comparison between calculation of Bloch-Redfield equations and damped quantum oscillator with different coupling directions at zero temperature. All three curves saturate at universal value $m_y(\infty) = -\Omega/W$. It is worth pointing out that the $\mathbf{n} \parallel \hat{\mathbf{z}}$ coupling results in time-dependent transition rates that are at minimum when $\mathbf{b} \parallel \mathbf{n}$ and at maximum when $\mathbf{b} \perp \mathbf{n}$, as one can conclude from the amplitude of oscillations of $m_y(t)$ for $\mathbf{n} \parallel \mathbf{e}_z$. Effectively, the overall relaxation is slower than that of the case $\mathbf{n} \parallel \hat{\mathbf{y}}$ and the amplitude of oscillating m_y at $t\Omega = n\pi$ decays insignificantly. The

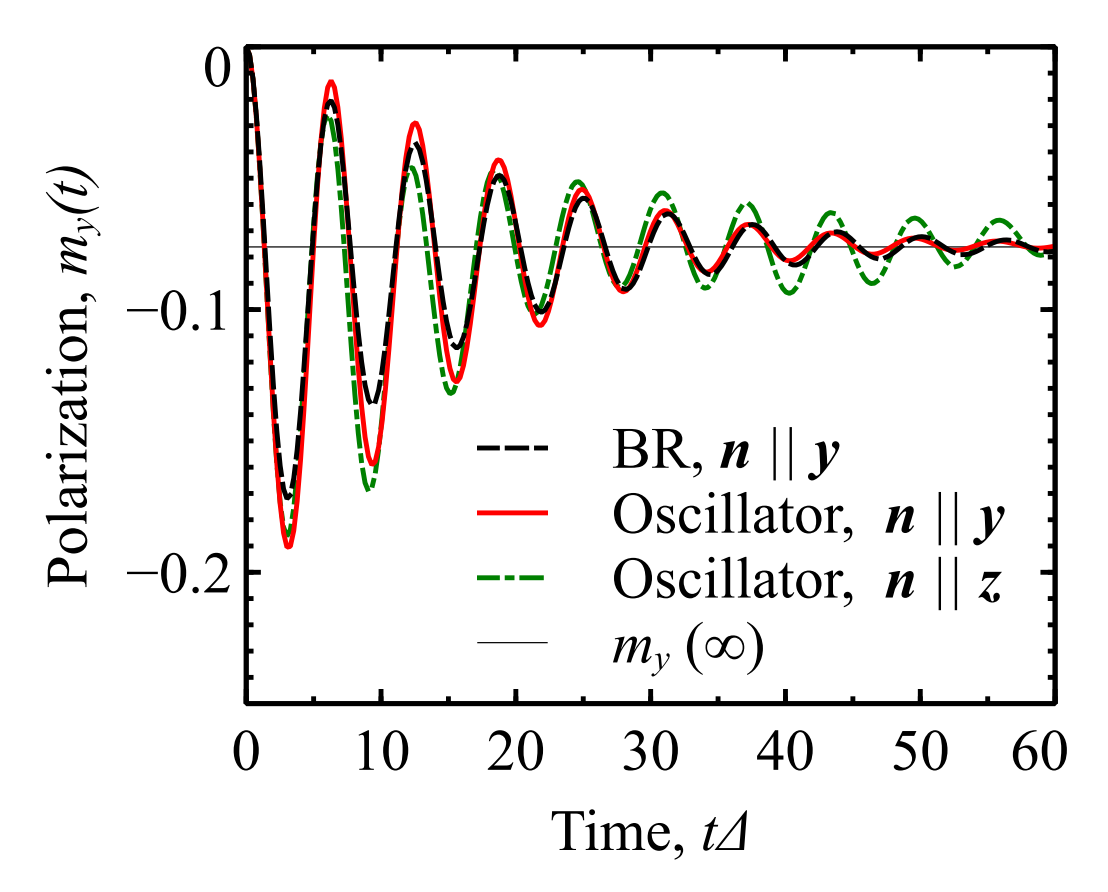


Figure 4.7: Time dependence of the out-of-plane polarization, $m_y(t)$, at environment temperature $T=0.5\Delta$ for a qubit coupled to a damped harmonic oscillator with damping rate $\kappa=0.2\Delta$ and coupling constant between the qubit and environment $\lambda=0.1\Delta$. Coupling vector $\mathbf{n} \parallel \hat{\mathbf{y}}$ (solid line) and $\mathbf{n} \parallel \hat{\mathbf{z}}$ (dash-dotted line). For comparison, the solution for the Bloch–Redfield equation is presented (dashed line) with $\alpha=0.03$ and $J_0=0$. The rotation angular velocity is $\Omega=0.1\Delta$. The thin horizontal line represents the asymptotic values of $m_y(\infty)$.

calculations at finite temperature $T=0.5\Delta$ are plotted in Figure 4.7 and in all cases $m_y(\infty)$ is consistent with Eq. (4.23).

4.4 Landau–Zener Transition

In this section we consider the Landau–Zener transition in a qubit coupled to its environment. The external field in the qubit Hamiltonian (5.3) has the following form $\mathbf{b}(t) = \{\Delta, 0, vt\}$, where Δ is the minimal level separation and v characterizes the rate at which the Hamiltonian changes. For the Landau–Zener problem, the qubit is initially in the

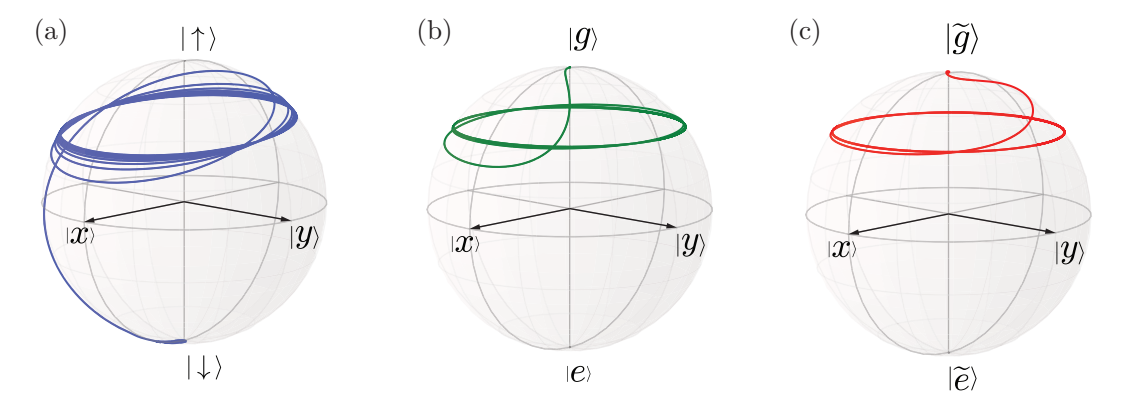


Figure 4.8: Representation of a qubit state during the Landau–Zener process on the Bloch sphere in (a) diabatic basis of states $|\uparrow\rangle$ and $\downarrow\rangle$ along fixed $\hat{\mathbf{z}}$ axis; (b) adiabatic basis of the ground, $|g\rangle$, and excited, $|e\rangle$, states; (c) in the "improved" eigenstate basis, $|g\rangle$ and $|e\rangle$, obtained from the diabetic basis by U_2 transformation. In the diabatic basis the trajectory of qubit state moves across the sphere from state $|\downarrow\rangle$ (ground state at $t\to-\infty$) towards $|\uparrow\rangle$ and slowly approaches the circle of constant precession at $t\to\infty$. The trajectory in the adiabatic basis and eigenstate basis shows a simpler trajectory and fast switch to the constant precession circle. Level-crossing speed $v=0.5\Delta^2$ and no coupling to environment.

ground state $|g\rangle$ with the density matrix $\hat{\rho}(t \to -\infty) = |g\rangle\langle g|$. The task is to find the probability of the system to be in the excited state $|e\rangle$ which is given by $P_{\infty} = \lim_{t \to +\infty} \langle e|\hat{\rho}(t)|e\rangle$.

Effects of the environment on qubit's dynamics can be separated into pure dephasing of the qubit state during the LZ process and inelastic qubit flips. When we consider a qubit coupled to its environment that causes qubit flip processes, we have to be careful with the formulation of the LZ problem. Indeed, the LZ process is formally infinitely long and the qubit flip processes accompanied by the energy exchange will result in equilibration of the qubit system with its environment. In particular, for the zero temperature environment, the qubit will relax to the ground state even if it was temporarily excited during the LZ process. For environment at finite temperature, the qubit state will tend to thermal state $\hat{\rho}(t) = \text{diag}\{\rho_{00}, \rho_{11}\}$ with $\rho_{11}/\rho_{00} = \exp(-E(t)/T)$. But as formally $E(t) \to \infty$ for long times t, the qubit will relax to the ground state and we find $P_{\infty} = 0$.

Previous considerations, see e.g. [114], predicted $P_{\infty} \to 0$ for the Ohmic environment with large high-frequency cutoff in the environment modes.³ But in this case the problem

³Notice that the projection of the coupling vector between a qubit and the environment does not change in time in Ref. [114] as required for the proper treatment of environment–qubit interaction.

looses its meaning since the LZ transition is shadowed by trivial relaxation of a quantum system to its ground state by releasing its energy to the environment. One can reformulate the problem in terms of finite time LZ process, which may be experimentally relevant situation in some cases. Alternatively, one can assume that the environment spectral function has a relatively low cutoff at high frequencies $E_c \sim \Delta$ and the relaxation is absent after time $t \gtrsim E_c/v$. Here, we consider a special orientation of the coupling vector with environment when $\mathbf{n} \| \mathbf{e}_z$, where \mathbf{e}_z is defined by $\hat{\mathbf{b}}(t \to \pm \infty) \| \mathbf{e}_z$. In this situation, the relaxation processes becomes weak at long times $|t| \gg \Delta/v$. This type of coupling is expected to be dominant in qubits with relatively long energy relaxation times, but with short dephasing time due to dominant coupling with the fluctuating field parallel to the qubit field along \mathbf{e}_z .

We utilize the Bloch–Redfield approach to the problem of Landau–Zener transitions in the presence of environment with $\mathbf{n} = \mathbf{e}_z$. In principle, we need to write the BR equations in the basis where the transformed qubit Hamiltonian is diagonal after an infinite series of basis transformations given by \hat{U}_n , which can be an infinite series. However, under the condition $v \lesssim \Delta^2$, the series of basis transformations can be limited by $\hat{U}_2(t)\hat{U}_1(t)$.

The first transformation changes the representation from diabatic basis of states $|\uparrow\rangle$ and $|\downarrow\rangle$ along \mathbf{e}_z to the adiabatic basis of the ground, $|g\rangle$, and excited, $|e\rangle$, states, where the Hamiltonian is diagonal. The first transformation matrix $\hat{U}_1(t)$ has the same form as in Eq. (4.13) except the rotation angle $\theta(t)$, which is now defined as

$$\cos \theta(t) = -\frac{vt}{\sqrt{v^2 t^2 + \Delta^2}}. (4.29)$$

The transformed Hamiltonian in the adiabatic basis has the form [96, 99, 98, 97]

$$\hat{H}_0^{U_1} = -\frac{E(t)}{2}\hat{\sigma}_z - \frac{v\Delta}{2E^2(t)}\hat{\sigma}_y, \quad E(t) = \sqrt{v^2t^2 + \Delta^2}.$$
 (4.30)

The second transformation is chosen to diagonalize matrix $\hat{H}_0^{U_1}$ and has the form

$$\hat{U}_2(t) = \exp\left(-\frac{i\eta}{2}\hat{\sigma}_x\right), \quad \tan\eta(t) = \frac{v\Delta}{E^3(t)}.$$
 (4.31)

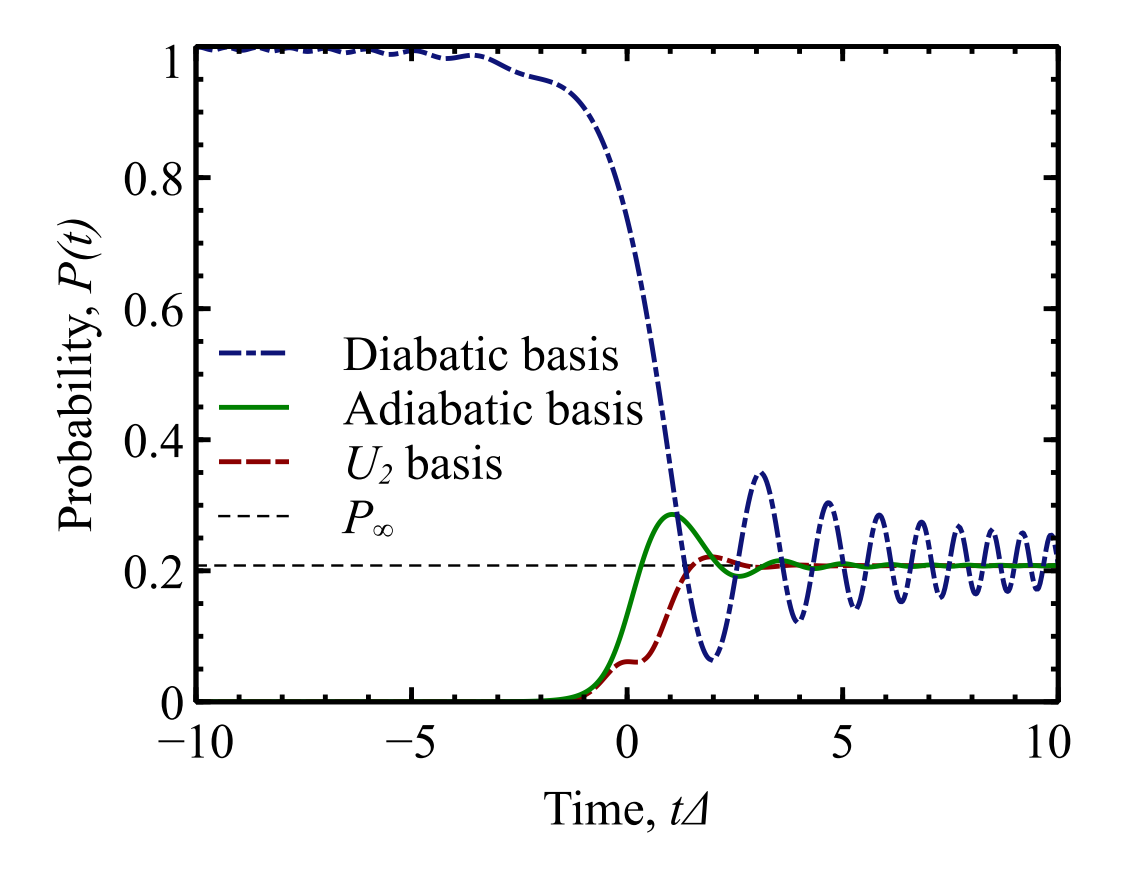


Figure 4.9: projection of a qubit state during the Landau–Zener process on the Bloch sphere on $|\downarrow\rangle$ state in the diabatic basis (dash-dotted line) and on the ground state in the adiabatic basis (solid line) and the "improved" eigenstate basis (dashed line). In the diabatic basis the projection of the qubit state shows long oscillations with amplitude decreasing as a power law in time, while the eigenstate projections quickly reach the asymptotic value. Level-crossing speed $v=0.5\Delta^2$ and no coupling to environment.

The Hamiltonian in this "improved eigenstate" basis has the form

$$\hat{H}_0^{U_2} = -\frac{W(t)}{2}\hat{\sigma}_z - \frac{\dot{\eta}}{2}\hat{\sigma}_x, \tag{4.32a}$$

$$W(t) = \sqrt{E^2(t) + \frac{v^2 \Delta^2}{E^4(t)}}, \quad \dot{\eta} = \frac{3v^3 \Delta t}{E^3(t)W^2(t)}.$$
 (4.32b)

Without dissipation, the LZ problem is equivalent in all three representations, with a properly written Hamiltonian, i.e., Eq. (5.3) for the diabatic basis, Eq. (4.30) for the adiabatic basis, and Eq. (4.32a) for "improved eigenstate" basis. In all representations, the qubit follows the appropriate instantaneous control field $\tilde{\mathbf{b}}(t)$, but since this field is time-dependent, the qubit deviates from the instantaneous direction of $\tilde{\mathbf{b}}(t)$ and acquires an

additional precession around the control field. When the original field eventually reaches its final direction, $\mathbf{b} \| \mathbf{e}_z$ at $t \gg \Delta/v$, the direction of the control field becomes time independent and the qubit simply precesses around \mathbf{e}_z with a non-zero projection of its state on the excited state, given by the known expression [108, 109, 111]

$$P_{\infty}^{LZ} = \exp\left(-\frac{\pi\Delta^2}{2v}\right). \tag{4.33}$$

Note that in Figure 4.8 this precession remains in all three considered representations, but the overall trajectories are smoother in the transformed representations. As we look at the projection of the qubit state on the "excited state" $P(t) = \langle e|\hat{\rho}(t)|e\rangle$ in the appropriate basis, see Figure 4.9, the oscillations decrease faster in the transformed representations, because the control field $\mathbf{b}(t)$ aligns faster with its final direction. We also note that since the control field remains aligned with its initial direction longer in transformed basis, the numerical computation can run over shorter time intervals thus making computation faster and more accurate.

Next, we take into account interaction with the environment within the Bloch–Redfield approach. The coupling to the environment is modified in the diagonal basis of the Hamiltonian, see Eq. (4.12) and Ref. [97]. Under the Markovian approximation and to the second order in the coupling to environment, we obtain the corresponding BR equations in the form

$$\dot{\rho}_{00} = i\frac{\dot{\eta}}{2}(\rho_{01} - \rho_{10}) - \Gamma_e \rho_{00} + \Gamma_r \rho_{11}, \tag{4.34a}$$

$$\dot{\rho}_{11} = -i\frac{\dot{\eta}}{2}(\rho_{01} - \rho_{10}) + \Gamma_e \rho_{00} - \Gamma_r \rho_{11}, \tag{4.34b}$$

$$\dot{\rho}_{01} = -(\Gamma_2 + iW(t))\rho_{01} + i\frac{\dot{\eta}}{2}(\rho_{00} - \rho_{11}), \tag{4.34c}$$

$$\dot{\rho}_{10} = -(\Gamma_2 - iW(t))\rho_{10} - i\frac{\dot{\eta}}{2}(\rho_{00} - \rho_{11}), \tag{4.34d}$$

where W(t) and $\dot{\eta}$ are given by Eq. (4.32b). The rates for the above equations are

$$\Gamma_r = \frac{G_{LZ}(t)}{2} J(W(t))[N(W(t)) + 1],$$
(4.35a)

$$\Gamma_e = \frac{G_{LZ}(t)}{2} J(W(t)) N(W(t)), \qquad (4.35b)$$

$$\Gamma_2 = \frac{\Gamma_r + \Gamma_e}{2} + J_0 \cos^2 \eta \cos^2 \theta(t), \tag{4.35c}$$

where $G_{LZ}(t) = \sin^2 \eta + \sin^2 \theta(t) \cos^2 \eta$ is a function of time-dependent basis rotation angles $\theta(t)$ and $\eta(t)$ defined by Eqs. (4.29) and (4.31). We note that the above equations for BR rates are given by truncation of transformation series of interaction Hamiltonian, Eq. (4.12), up to the second order, $\hat{V} = \hat{U}_2(t)\hat{U}_1(t)$. An equivalent approach with only first order transformation $\hat{V} = \hat{U}_1(t)$ was studied in Ref. [129]. Therefore, the rates are defined within $\mathcal{O}(\eta^2) \lesssim \mathcal{O}(v^2/\Delta^4)$ accuracy. The unitary evolution described by either $\hat{H}_0^{U_1}$ or $\hat{H}_0^{U_2}$ has no approximations and is valid for arbitrary values of v. We emphasize that once the basis transformation gives rise to non-zero decoherence rates, the qualitative results are similar regardless of our choice of the BR rates in the basis obtained after either \hat{U}_1 or $\hat{U}_2\hat{U}_1$ transformations. The rates in the \hat{U}_1 basis are given by Eq. (4.35) with $\eta = 0$. We now discuss solution of Eq. (4.34).

Zero temperature dissipative environment

We first consider the zero temperature environment and set $J_0=0$ to focus solely on qubit flips rather than dephasing. We numerically integrate the BR equation (4.34) and plot the probability of the system to be in the excited state $P_e(t)=\langle e|\rho(t)|e\rangle$ as a function of time in Figure 4.10 for $\alpha=0.05$. For numerical integration, we used both direct integration of linear differential equations (4.34) and the QuTiP's package for numerical solution of the Bloch–Redfield equations [45, 134], obtaining identical results. As the qubit levels go over the avoided crossing, the probability of the qubit to be in the excited state increases, roughly following the same function of time as $P_e(t)$ for an isolated qubit, $\alpha=0$. As the levels further depart from each other, the relaxation of the qubit from the excited state becomes the dominant process in the qubit dynamics, and $P_e(t)$ monotonically decreases and becomes constant once the level separation $\sim vt$ exceeds the ultraviolet cutoff E_c , or $t \gtrsim E_c/v$ and the qubit is effectively decoupled from the environment. In Figure 4.10 we compare the behavior of $P_e(t)$ for different values of E_c . For finite ultraviolet cutoff $E_c=5\Delta$, the probability $P_e(t)$ saturates for $t\Delta\gtrsim 10$. For $E_c\to\infty$, the probability $P_e(t)$ slowly decreases for all $t>\Delta/v$.

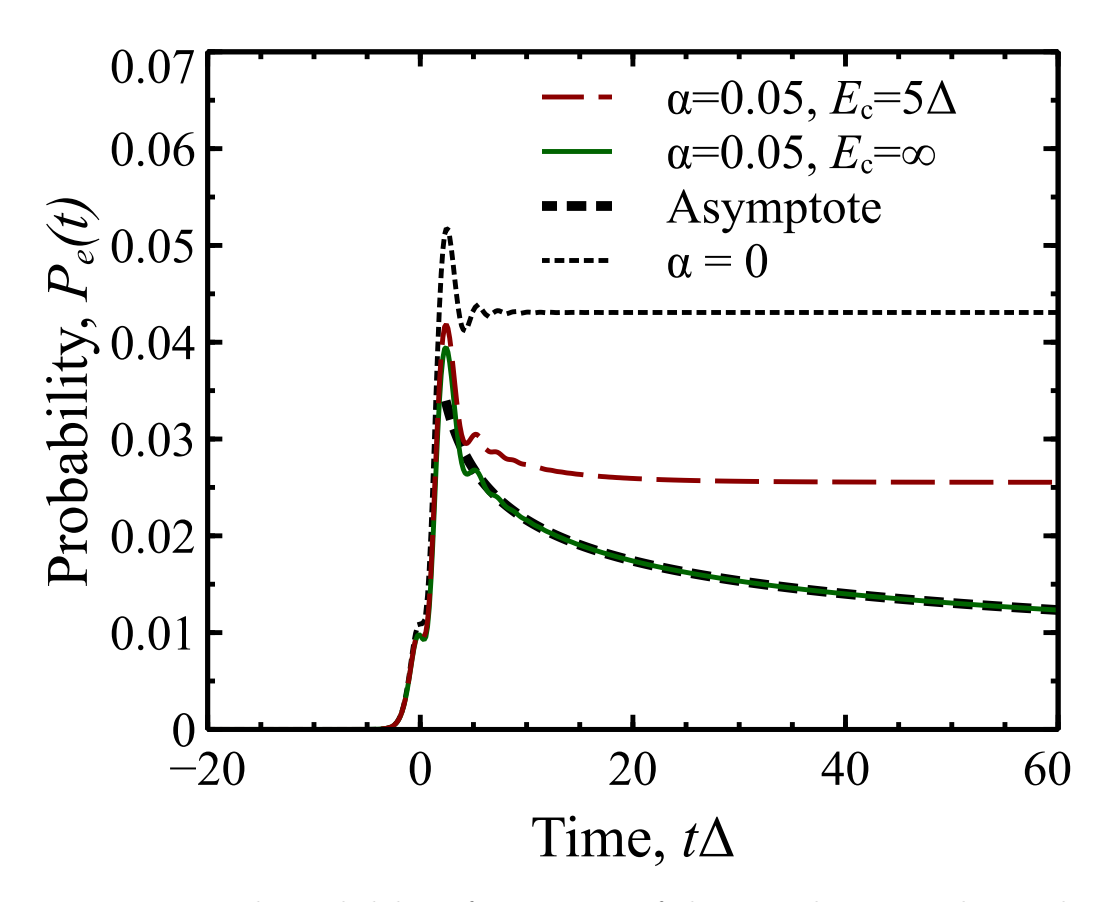


Figure 4.10: The probability of occupation of the excited state in the Landau–Zener transition in the U_2 basis. The temperature of environment is zero, T=0, the level velocity is $v=0.5\Delta^2$. We assume that the dephasing is absent, $J_0=0$. The asymptotic curve for $E_c=\infty$ is given by Eq. (4.36b) with a proper choice of integration constant C.

To evaluate this suppression, we can utilize Eqs. (4.34) in the asymptotic regime for $t \gg v/\Delta$, when $\Gamma_r(t) \gg \dot{\eta}(t)$. We write

$$\frac{dP_e(t)}{dt} = -\frac{\Delta^2}{2v^2t^2}J(vt)P_e(t),$$
(4.36a)

$$P_e(t) = C \exp\left(-\frac{\pi\alpha\Delta^2}{v}\ln\frac{vt}{\Delta}\right) \propto t^{-\pi\alpha\Delta^2/v}.$$
 (4.36b)

where we used the relaxation rate Γ_r from Eq. (4.35a). The latter equation demonstrates that even for environment with $\mathbf{n} \| \mathbf{e}_z$, the relaxation on long times scales is important. Formally, the power–law dependence of $P_e(t)$ on time originates from the slow converging integral $\int dt J(vt)/v^2t^2 \sim \ln vt/\Delta$ due to linearly increasing environment spectral function $J(\epsilon)$ with energy. With a proper choice of integration constant C, we obtain a good agree-

ment between computed $P_e(t)$ in Figure 4.10 and asymptote, defined by Eq. (4.36b).

This power-law dependence stops and reaches a fixed value P_{∞} when the qubit level separation exceeds the environment ultra-violet cutoff at times $t \gtrsim E_c/v$. We evaluate the long time asymptotic value of $P_e(t \gg E_c/v) = P_{\infty}$ by taking into account the high energy cutoff in the environment spectral function, Eq. (4.5). We obtain

$$P_{\infty}(T=0) = C\Pi, \quad \Pi = \exp\left\{-\frac{\pi\alpha\Delta^2}{v}\ln\frac{2E_c}{e^{\gamma}\Delta}\right\},$$
 (4.37)

where $\gamma \simeq 0.577$ is the Euler's constant, the integration constant $C \sim P_{\infty}^{LZ}$ and factor Π describes suppression of the excited state due to slow relaxation while qubit level separation increases from its minimum Δ to values above the cutoff energy E_c , see Appendix A for the derivation of Eq. (4.37).

Equations (4.36) are valid for $\alpha \ll 1$. For larger values of α , one has to take into account the renormalization of qubit Hamiltonian when the off-diagonal matrix element in the original Hamiltonian Δ_r is given by the following self-consistent relation [18]

$$\Delta_r = \Delta \exp\left(-\frac{1}{2} \int_0^\infty \frac{J(\omega)}{\omega^2 - \Delta_r^2} d\omega\right) \tag{4.38}$$

with solution $\Delta_r = \Delta(\Delta/E_c)^{\alpha/(1-\alpha)}$. Hence the relaxation rate is [119]

$$\Gamma_r(E) = \frac{\pi \Delta_r}{2\Gamma(2\alpha)} \left(\frac{E}{\Delta_r}\right)^{2\alpha - 1} \tag{4.39}$$

where $\Gamma(x)$ is the gamma-function. The integration over time with $E(t) \simeq vt$ gives [119]

$$\rho_{11}(t) = C' \exp\left(-\frac{\pi \Delta_r^2}{4\alpha \Gamma(2\alpha)v} \frac{(vt)^{2\alpha}}{\Delta_r^{2\alpha}}\right). \tag{4.40}$$

Notice that in the limit $\alpha \ll 1$, $\Delta_r = \Delta$, the relaxation rate Γ_r reduces to $\Gamma_r(E) = \pi \alpha \Delta^2/E$ in agreement with the relaxation rate in Eq. (4.36a). Similarly, Eq. (4.40) becomes Eq. (4.36b)

Finite temperatures

At finite temperatures, the excitation and relaxation rates may exceed $\dot{\eta}$ terms for strong enough coupling of the qubit to its environment and slow drive v. In this case, we disregard

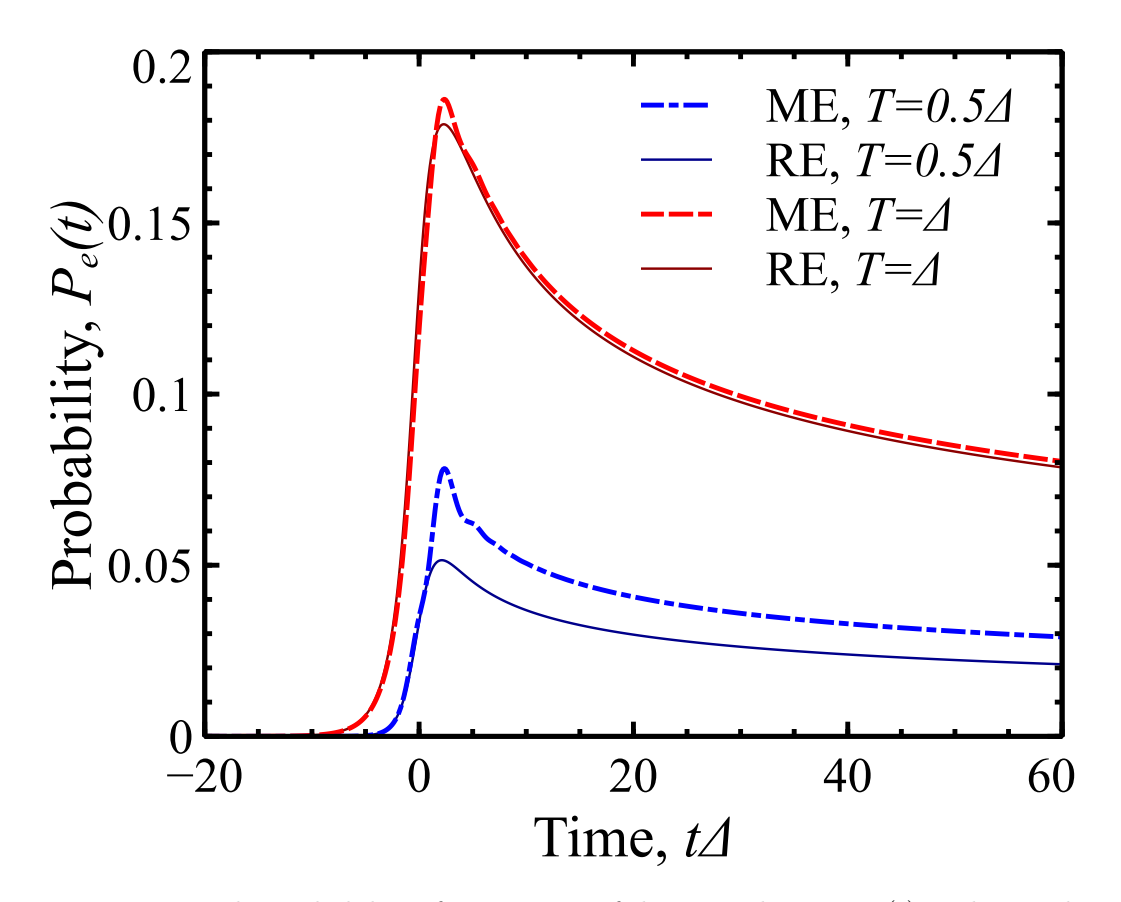


Figure 4.11: The probability of occupation of the excited state, $P_e(t)$ in the Landau–Zener transition in the U_2 basis at finite temperature of environment for $v = 0.5\Delta^2$, $\alpha = 0.05$ and $J_0 = 0$. The solid lines represent solutions of rate equations (4.41) that show good agreement with the BR equations at higher temperatures.

 $\dot{\eta}$ terms in Eq. (4.34) and the diagonal elements of the density matrix satisfy the rate equations. Since the rate equations preserve the trace of the density matrix, $P_g(t) + P_e(t) = 1$, with $P_g(t) = \langle g|\rho(t)|g\rangle$, we introduce $m(t) = P_g(t) - P_e(t)$ and obtain the differential equation for m(t):

$$\frac{1}{\Gamma_0} \frac{dm}{dt} = 1 - m \coth \frac{W(t)}{2T}, \quad \Gamma_0 = \pi \alpha W(t) G_{LZ}(t),$$

$$G_{LZ}(\tau) = \frac{\Delta^2 (v^2 + (v^2 \tau^2 + \Delta^2)^2)}{v^2 \Delta^2 + (v^2 \tau^2 + \Delta^2)^3}.$$
(4.41)

The initial condition is $m(t_i) = 1$ for $t_i = -\infty$. While we can write a formal solution to Eq. (4.41), the solution is not well defined due to logarithmic divergence of $\int_{t_i} \Gamma_0(t) dt$ for the spectral function $J(\varepsilon)$ without a cutoff. We present the result of numerical solution of

Eqs. (4.34) and the rate equations in Figure 4.11. We notice that for higher temperatures, these two solutions are indistinguishable because the thermal effects dominate only in short time scales |vt| < T such that the time window is long enough for the qubit to be thermalized and its off-diagonal elements of density matrix vanish.

Integrating Eq. (4.41) over t yields the following solution of $P_{\infty} = 1/2 - m(\infty)/2$:

$$P_{\infty} = \int_{-\infty}^{\infty} \Gamma_e(t) e^{-\int_t^{\infty} \Gamma_0(t') \coth \frac{W(t')}{2T} dt'} dt.$$
 (4.42)

The integral over time t is understood as thermal activation processes with rate $\Gamma_e(t)$ and integral in the exponent can be considered as contribution of relaxation processes after thermalization. For weak coupling $\alpha \ll 1$ and not very high temperatures $\alpha T \ll v/\Delta$, the integral in the exponential is a slow function of t. Therefore, we can replace the lower bound of the integration by t = 0. We obtain P_{∞} in the limit of low temperatures $T \ll \Delta$

$$P_{\infty} \simeq \frac{2\pi\alpha\Delta^2}{v} \sqrt{\frac{\pi T}{2\Delta}} e^{-\Delta/T} \Pi, \tag{4.43}$$

and in the limit of higher temperatures $T \gg \Delta$

$$P_{\infty} \simeq \frac{2\pi^2 \alpha T \Delta}{v} \Pi, \tag{4.44}$$

where Π is defined by Eq. (4.37). The details of the derivation of the above equations are presented in Appendix 4.7. We remind that Eqs. (4.42) – (4.44) are valid when the rate equations (4.41) are a good approximation to the BR equations (4.34). In this case, the transition of the system to the excited state is a consequence of incoherent excitation by environment of the qubit, and is not the coherent phenomenon that leads to the excitation in the Landau–Zener transition of an isolated quantum system. However, the excitation processes only happen when the adiabatic eigenstates of the qubit have a non-zero matrix elements with the coupling to environment, the latter happens when the "control field" $\hat{\mathbf{b}}$ is not parallel to the environment field which happens during time Δ/v , when the excitation rate can be estimated as $\pi \alpha T$, resulting in the excitation probability $\propto \alpha T \Delta/v$, cf. to Eq. (4.44). As the level separation E(t) exceeds temperature, only relaxation process remains that causes transitions to the ground state. The effect of this relaxation is represented by the exponential factor in Eqs. (4.43) and (4.44), cf. to Eq. (4.36b).

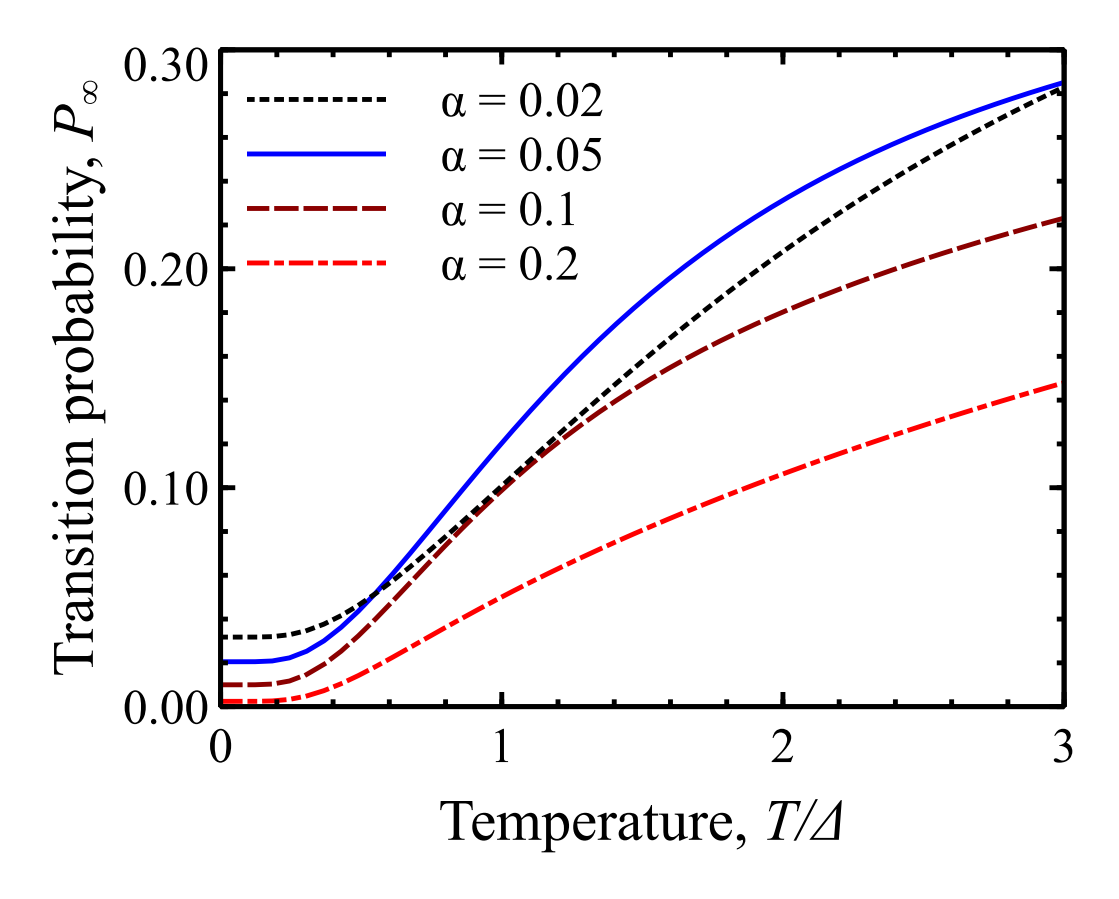


Figure 4.12: Transition probability P_{∞} as a function of environment temperature T, at different values of coupling between the qubit and the environment for $\mathbf{n} \| \hat{\mathbf{z}}$. Level-crossing speed $v = 0.5\Delta^2$, the high energy cutoff for the environment is $E_c = 10\Delta$ and $J_0 = 0$. We take $P_{\infty} = P_e(t = 4E_c/v)$.

From the above analysis, we conclude that a finite temperature of the environment leads to the "equilibration" between the ground and excited states of the qubit, and as temperature increases, the probability of the transition to the excited state in the LZ process increases monotonically, cf. Refs. [96, 97]. This behavior is demonstrated in Figure 4.12, where P_{∞} is shown as a function of T for several values α of coupling between the qubit and its environment. We also note that the temperature effects appear at $T \gtrsim \Delta$, at smaller T, values of P_{∞} are characterized by the excitation through unitary evolution with the subsequent relaxation.

When we consider P_{∞} as a function of coupling α for several values of T, we observe a more complicated behavior. For T=0, shown by the solid line in Figure 4.13, the

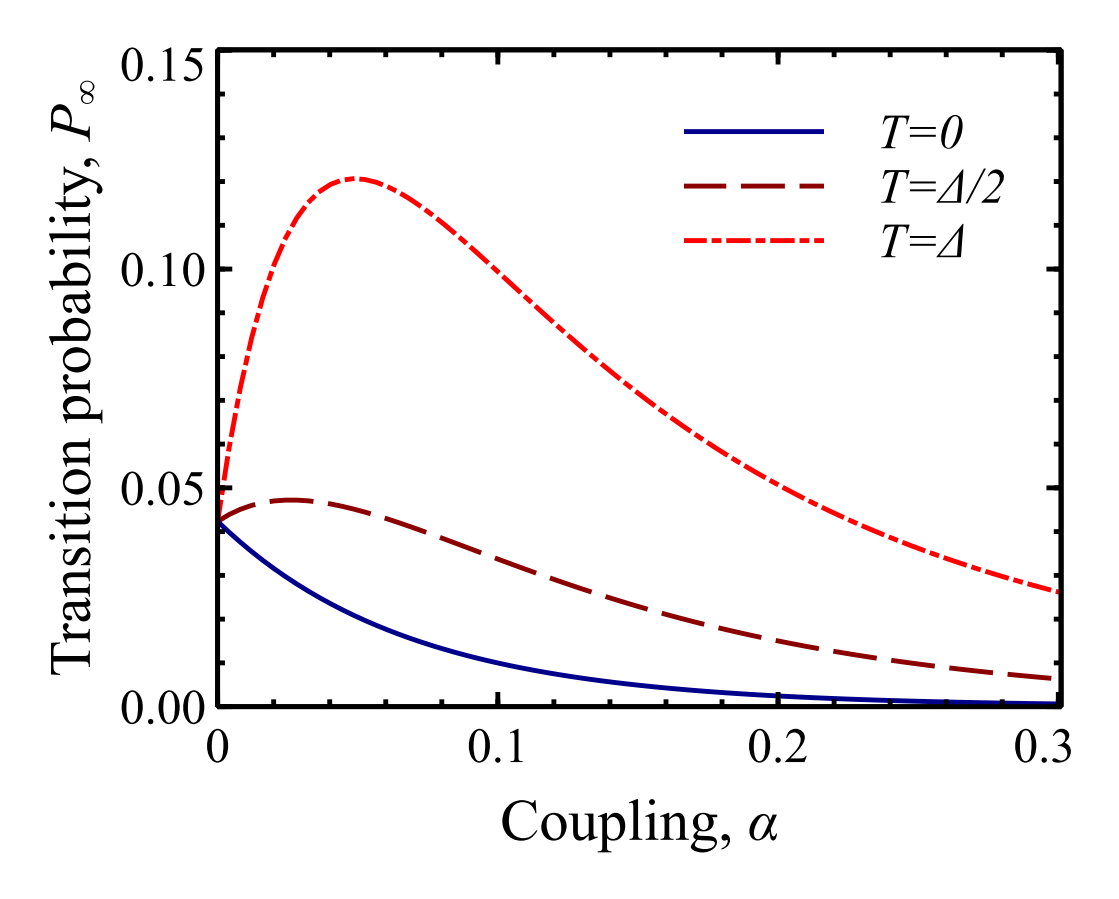


Figure 4.13: Transition probability P_{∞} as a function of the coupling parameter of the qubit and the environment, α , at different environment temperatures for $\mathbf{n} \| \hat{\mathbf{z}}$. Level-crossing speed $v = 0.5\Delta^2$, the high energy cutoff for the environment is $E_c = 10\Delta$ and $J_0 = 0$. We take $P_{\infty} = P_e(t = 3E_c/v)$.

transition probability P_{∞} monotonically decreases from its value P_{∞}^{LZ} , Eq. (4.33), as α increases, in agreement with Eq. (4.37). At finite temperatures, P_{∞} increases for smaller values of α , as the excitation process becomes more efficient and provides extra boost for transitions to the excited state in addition to that produced by unitary dynamics. However, this boost is only a linear function of α , see Eqs. (4.43) and (4.44), and at stronger values of α the exponential dependence of Π on α results in decreasing P_{∞} as α increases. The non-monotonic dependence of P_{∞} on α can be understood as a competition between energy relaxation and driving was analyzed in Ref. [117].

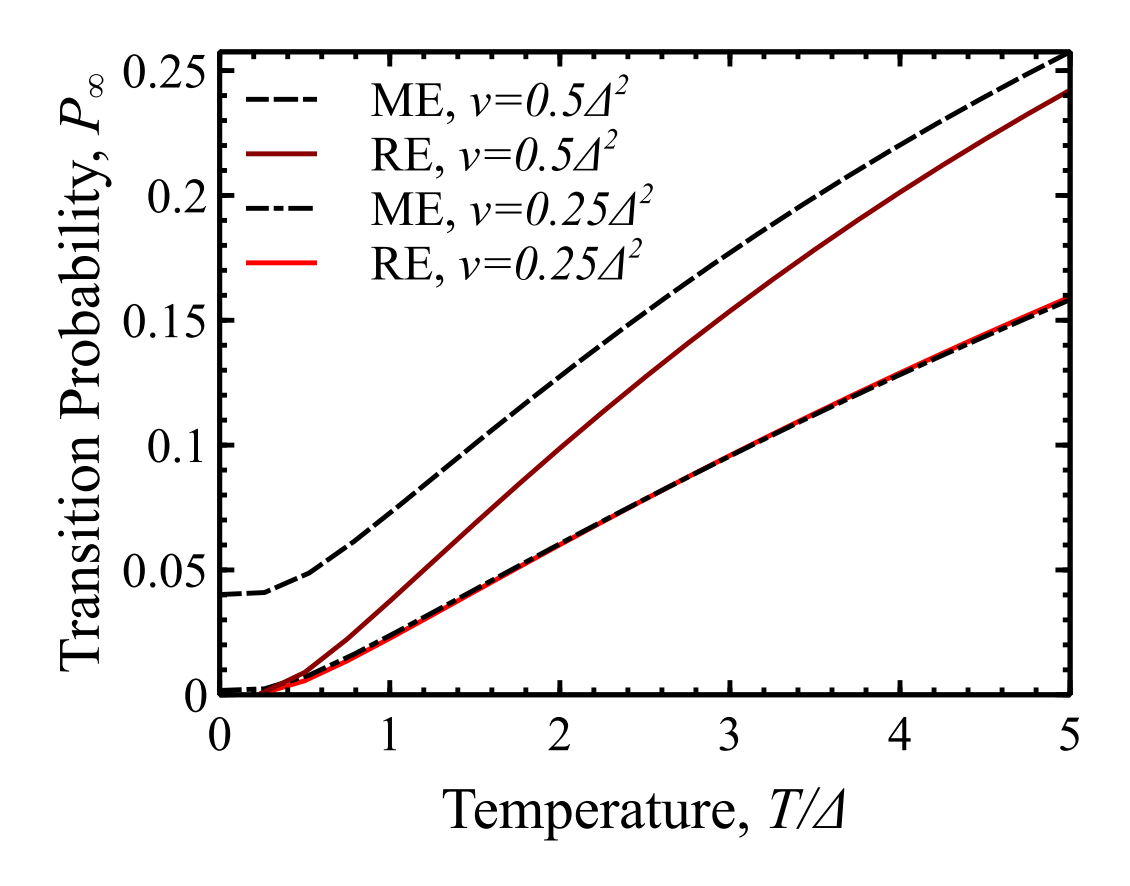


Figure 4.14: Transition probability P_{∞} as a function of environment temperature T for $\mathbf{n} \| \hat{\mathbf{b}}$, at different values of drive velocity. The high energy cutoff for the environment is $E_c = 10\Delta$ and $J_0 = 0$. The solid lines represent solutions of rate equations Eq. (4.41). We take $P_{\infty} = P_e(t = 4E_c/v)$.

Longitudinal coupling

We also consider the environment that produces fluctuating field along the direction of the control field, $\mathbf{n} \| \mathbf{b}$, in the Landau–Zener problem. The decoherence rates in the BR equations (4.34) are given by

$$\Gamma_r = \frac{\sin^2 \eta}{2} J(W(t))[N(W(t)) + 1],$$
(4.45a)

$$\Gamma_e = \frac{\sin^2 \eta}{2} J(W(t)) N(W(t)), \tag{4.45b}$$

$$\Gamma_2 = \frac{\Gamma_r + \Gamma_e}{2} + J_0 \cos^2 \eta. \tag{4.45c}$$

For this configuration of coupling between the qubit and environment, the matrix elements for transitions between different eigenstates of the qubit caused by the environment are small and the qubit flip rates $\Gamma_{r,e}$ are proportional to $\sin^2 \eta \lesssim v^2 \Delta^2 / E^6(t) \leq v^2 / \Delta^4$ and vanish fast for $|t| \gtrsim \Delta/v$ as $\Gamma_{r,e} \sim \Delta^2/v^4 t^6$. Such fast decrease of the qubit flip rates in time simplifies either numerical or analytical integration of the BR equation and makes P_{∞} independent from the high-energy cutoff E_c .

In particular, for finite temperatures, when the BR equations can be reduced to the rate equations, time evolution of $m(t) = P_g(t) - P_e(t)$ is given by Eq. (4.41) with $G_{LZ}(t) = \sin^2 \eta$. The general solution of the rate equation takes similar form to Eq. (4.42):

$$P_{\infty} = \int_{-\infty}^{\infty} \Gamma_e(t) e^{-\int_t^{\infty} \Gamma_l(t') \coth \frac{W(t')}{2T} dt'} dt,$$

$$\Gamma_l = \pi \alpha W(t) \sin^2 \eta(t).$$
(4.46)

Performing time integration in Eq. (4.46) gives for $T \ll \Delta$:

$$P_{\infty} = \alpha v \sqrt{\frac{\pi^3}{32T\Delta^3}} \exp\left(-\frac{\Delta}{T}\right) \exp\left(-\frac{2\pi\alpha v}{3\Delta^2}\right). \tag{4.47}$$

For high temperatures, $T \gg \Delta$, we obtain (see Appendix B)

$$P_{\infty} = \frac{1}{2} \left[1 - \exp\left(-\frac{3\pi^2}{4} \alpha \frac{Tv}{\Delta^3} \right) \right]. \tag{4.48}$$

As we mentioned above, the results in Eqs. (4.46) and (4.48) are independent from the cutoff energy E_c . Equation (4.47) shows that P_{∞} vanishes in the low temperature limit, unless we take into account non-adiabatic unitary evolution of the quantum state in the LZ problem. In the limit of high temperatures $T \gg \Delta$, but still weak coupling, $\alpha vT \ll \Delta^3$, we obtain the linear dependence of P_{∞} on T:

$$P_{\infty} = \frac{3\pi^2}{8} \alpha \frac{Tv}{\Delta^3},\tag{4.49}$$

which follows from Eq. (4.48).

Since simple form of P_{∞} can not be obtained in the intermediate temperature regime, we numerically calculate the solution of rate equation as well as that of Bloch-Redfield equation for comparison, see Figure 4.14. When the level-crossing speed v is small enough, the transition is mainly due to thermalization at short times and energy relaxation at longer times. In this regime, the rate and BR equations are in a very good agreement, as demonstrated in Figure 4.14 for $v=0.25\Delta^2$. However, as the level–crossing speed increases, the non-adiabatic unitary evolution also contributes to the transition to the excited state increasing the probability for a system to be in the excited state. Since the non-adiabatic unitary evolution is not incorporated in the rate equations, the equations underestimate the probability of the excitation in the LZ process, compare the solid and dashed curves in Figure 4.14 for $v=0.5\Delta^2$.

4.5 Lindblad dephasing evolution

We compare the results obtained from the BR equations in the case of longitudinal coupling with the theory based on the Lindblad equation for pure dephasing operators. For both problems, the qubit Hamiltonian can be parametrized by the control field $\mathbf{b} = E(t)\{\sin\theta, 0, \cos\theta\}$, where E(t) is the magnitude of the control field equal to the qubit level separation. The corresponding equation for the density matrix in the adiabatic basis has the form:

$$\dot{\rho} = \frac{iE(t)}{2} [\sigma_z, \rho] + \frac{i\dot{\theta}}{2} [\sigma_y, \rho] + \frac{\gamma}{2} (\sigma_z \rho \sigma_z - \rho). \tag{4.50a}$$

In the component form the above equation is

$$\dot{\rho}_{00} = \frac{\dot{\theta}}{2}(\rho_{01} + \rho_{10}), \quad \dot{\rho}_{11} = -\frac{\dot{\theta}}{2}(\rho_{01} + \rho_{10}), \tag{4.50b}$$

$$\dot{\rho}_{01} = (iE(t) - \gamma)\rho_{01} - \frac{\dot{\theta}}{2}(\rho_{00} - \rho_{11}), \tag{4.50c}$$

$$\dot{\rho}_{10} = (-iE(t) - \gamma)\rho_{10} - \frac{\dot{\theta}}{2}(\rho_{00} - \rho_{11}). \tag{4.50d}$$

These equations are similar to Eqs. (4.6), but because they are not written in the eigenstate basis, the last two equations contain extra terms. Time derivatives of diagonal terms contain the off-diagonal terms of the density matrix multiplied by the quantity characterizing the off-diagonal part of the Hamiltonian, $\dot{\theta}$. Time derivatives of the off-diagonal components of the density matrix have the terms identical to those in Eqs. (4.6) and the extra terms characterized by the diagonal matrix elements and parameter $\dot{\theta}$. In this section we again consider the two cases: (1) the qubit rotation with a constant angular velocity $\dot{\theta} = \Omega$,

i.e. $\theta(t) = \Omega t$, and $E(t) = \Delta$; (2) the LZ problem with $E(t) = \sqrt{\Delta^2 + v^2 t^2}$ and $\theta(t) = \arctan \Delta/vt$.

Rotating field

When the control field rotates in (x-z) plane, $\mathbf{b}(t) = \Delta \{\sin \Omega t, 0, \cos \Omega t\}$, the effective Hamiltonian is time independent. To make a comparison with the calculation of BR equations, one can look for a quasi-stationary state solution of the density matrix at time scale $t \sim 1/\gamma$ with ansatz that the off-diagonal elements are $\rho_{01/10} \propto \Omega$. We disregard Ω^2 terms for $\dot{\rho}_{00/11}$ and take $\rho_{00} = 1$. Then, we have $\rho_{01} = \Omega/2(i\Delta - \gamma)$, $\rho_{10} = \Omega/2(-i\Delta - \gamma)$ and the out of plane qubit projection is [87]

$$m_y(L) = -\frac{\Omega}{2} \frac{\Delta}{\Delta^2 + \gamma^2}.$$
 (4.51)

We argue, however, that the above expression does not hold for authentic steady state, $\dot{\hat{\rho}} = 0$, at longer times and for general configuration of the initial conditions. We present the result of numerical integration of the Lindblad equations (4.50) in Figure 4.15 for $\Omega = 0.1\Delta$ and $\gamma = 0.1\Delta$. In our calculation, we consider the case when the qubit is prepared in the ground state prior to rotation for t < 0. When the rotation starts, the Hamiltonian acquires extra terms $\sim \Omega$ and the qubit exhibits a precession around new direction of the control field. This precession is reduced by the decoherence with rate $\Gamma_2 \simeq \gamma$ and the oscillatory component in $m_y(t)$ vanishes for times $t \sim 1/\gamma$.

At longer times, the diagonal matrix elements start changing as well and the system will eventually relax to $\rho_{00} = \rho_{11} = 1/2$ and $\rho_{01} = \rho_{10} = 0$. The reason for this behavior is that at long times, the diagonal elements acquire significant changes even though these changes have small factor Ω^2 . In the language of the BR equation, the Lindblad pure dephasing operator contains relaxation and excitation components in the eigenstate basis of the transformed Hamiltonian \hat{H}_0^V and $\Gamma_e = \Gamma_r = \gamma \Omega^2/(\Delta^2 + \Omega^2)$, which is the high temperature limit because it does not distinguish processes with absorption or emission of environment excitations. Correspondingly, the density matrix reaches the high-temperature

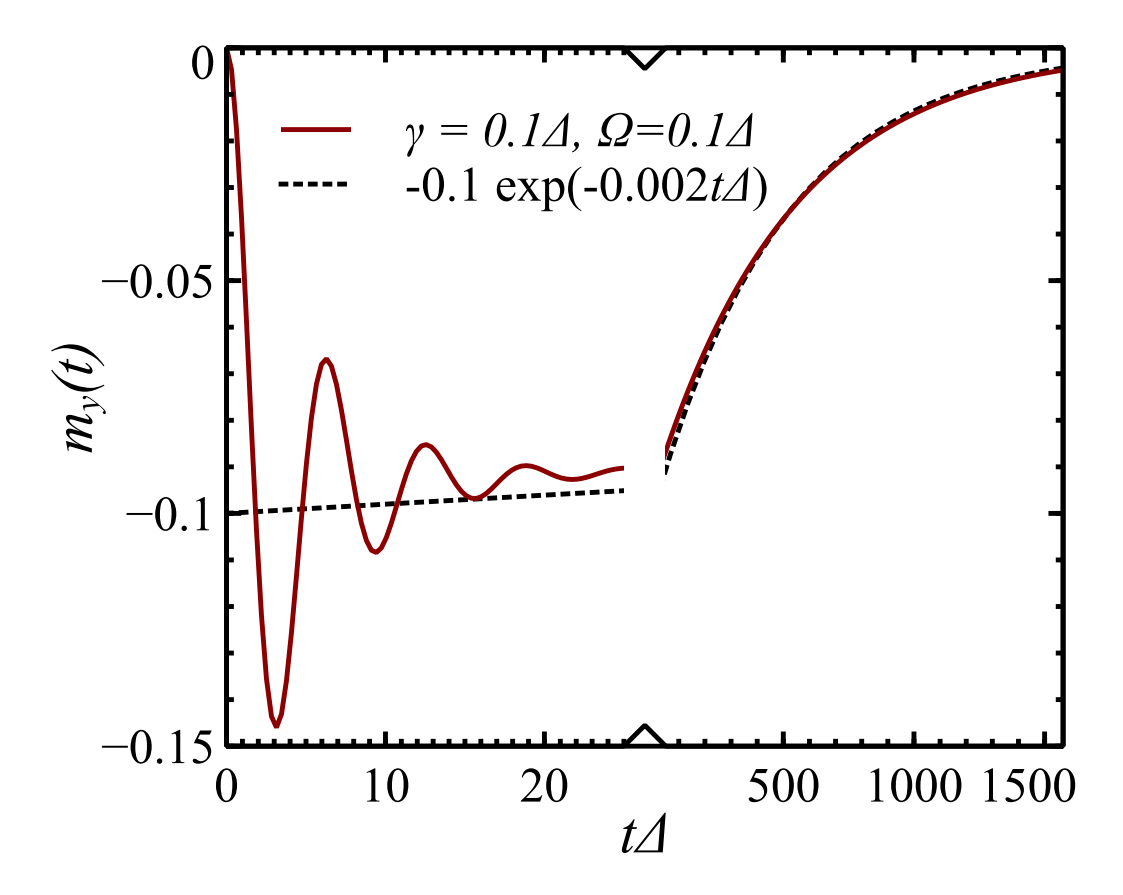


Figure 4.15: Polarization $m_y(t)$ as a function of time t for dephasing Lindblad evolution. The decoherence rate $\gamma = 0.1\Delta$ and rotation velocity $\Omega = 0.1\Delta$. After the rotation starts, polarization shows an oscillatory behavior originating from the qubit precession, at longer times the precession stops and the qubit relaxes to unpolarized state according to Eq. (4.52).

limit with equal probabilities of occupation of eigenstates of the qubit Hamiltonian

$$m_y^{(L)}(t) = -\frac{\Omega}{\sqrt{\Delta^2 + \Omega^2}} \exp\left(-\frac{2\Omega^2 \gamma t}{\Omega^2 + \Delta^2}\right). \tag{4.52}$$

This asymptotic behavior is consistent with the result obtained from the numerical solution of the Lindblad equation (4.50), shown in Figure 4.15.

Landau-Zener problem

The expression for Landau–Zener problem to the lowest order in v can be obtained from the explicit form of the Lindblad equation (4.50) with E(t) given by Eq. (4.30) and $\Omega = v\Delta/E^2(t)$. We assume that the changes in the system are slow and disregard $\dot{\rho}_{01}$ and $\dot{\rho}_{10}$

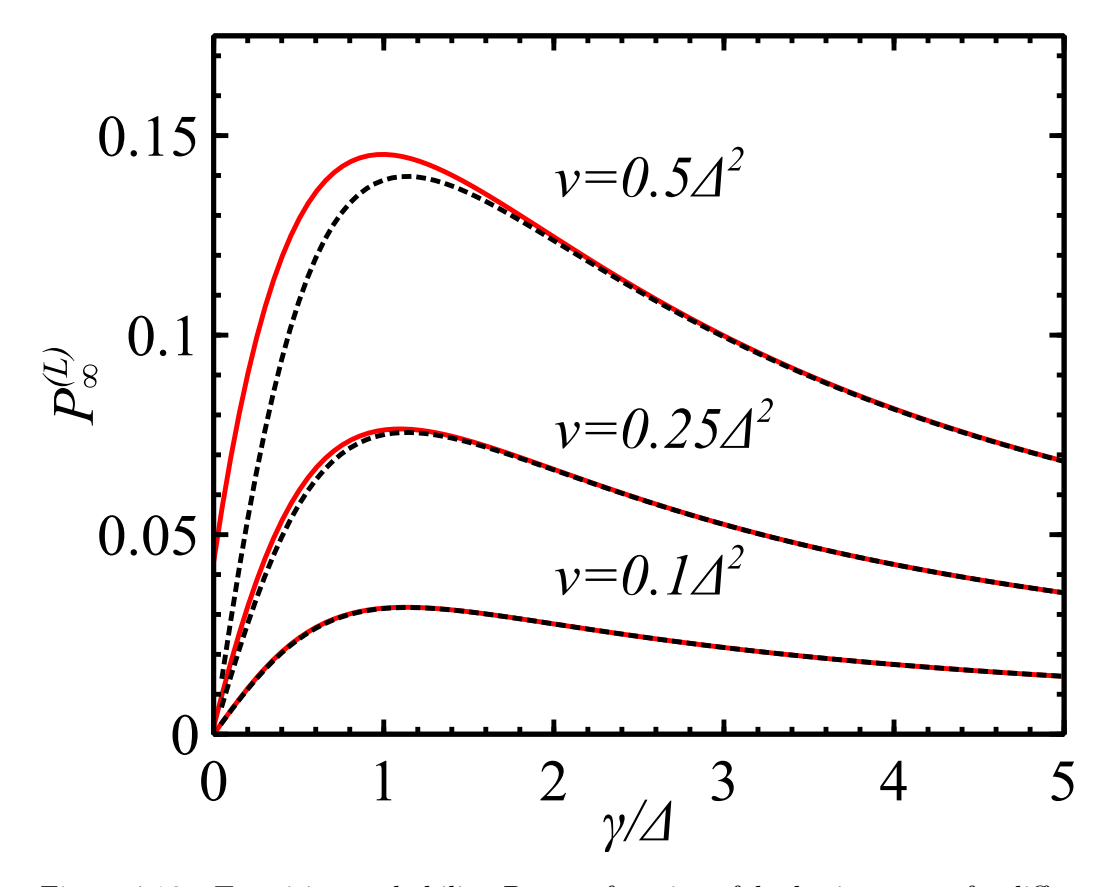


Figure 4.16: Transition probability P_{∞} as a function of daphasing rate γ for different level-crossing speeds $v/\Delta^2=0.1,\ 0.25,\ 0.5$. Solid lines are numerical solution of the Lindblad equation, Eq. (4.50), and dashed lines are given by Eq. (4.53).

in Eqs. (4.50). Then we find $\rho_{01} = \Omega/2(-iE + \gamma)[\rho_{00} - \rho_{11}]$ and $\rho_{10} = [\rho_{01}]^*$. Substituting these expressions to Eq. (4.50b), we obtain:

$$P_{\infty}^{(L)} = \frac{1}{2} \left[1 - \exp\left(-\gamma \int_{-\infty}^{\infty} \frac{v^2 \Delta^2}{E^4(t)} \frac{dt}{\gamma^2 + E^2(t)}\right) \right]$$
$$= \frac{1}{2} \left[1 - \exp\left(-\frac{\pi v}{2\Delta^2} R\left(\frac{\gamma}{\Delta}\right)\right) \right], \tag{4.53}$$

where

$$R(x) = \frac{2 + (x^2 - 2)\sqrt{x^2 + 1}}{x^3\sqrt{x^2 + 1}}. (4.54)$$

In the limit $v \ll \Delta^2$, we recover the result of Ref. [86]:

$$P_{\infty}^{(L)} = -\frac{\pi v}{4\Delta^2} R\left(\frac{\gamma}{\Delta}\right). \tag{4.55}$$

At small decoherence rate and slow drive, $\gamma \ll \Delta$, we take $R(x \ll 1) \simeq 3x/4$ and reproduce the previous result, Eq. (4.49), if we identify $\gamma = 2\pi\alpha T$. The agreement between Eqs. (4.49) and (4.53) has a simple interpretation. The Lindblad equation can be viewed as the high-temperature limit of the BR equation for the Ohmic environment [135]. The Lindblad equation (4.50) is written in the basis that does not completely diagonalize the Hamiltonian operator, and when we rewrite this equation in the basis diagonalizing matrix $E(t)\hat{\sigma}_z + \Omega\hat{\sigma}_x$, we arrive to the collapse operators that represent transition processes between the eigenstates with equal excitation and relaxation rates $\Gamma_{e,r}^{(L)} \approx \gamma(\Omega^2(t)/E^2(t))$. It is the excitation processes that cause transitions of the system to the excited state with the population of an excited state P_{∞} in accordance with Eq. (4.53). To account for finite temperatures, the Lindbladian operators are to be written in the eigenstate basis of the "dressed" Hamiltonian, see Ref. [136].

Large decoherence rate, $\gamma \gg \Delta$, suppresses the off-diagonal elements of the density matrix, and effectively reduces the excitation and relaxation rates $\sim \gamma \Omega^2/(E^2 + \gamma^2)$. As a result, the qubit is more likely to stay in its ground state without experiencing an excitation during the LZ avoided level crossing. The maximum of $R(x_m) \approx 0.42$ is reached at $x_m = 1.14$.

We compare Eq. (4.53) (dashed lines) with the result of numerical integration of the Lindblad equation (4.50) (solid lines) in Figure 4.16. We observe that at stronger decoherence rate, when the off-diagonal unitary terms in the evolution of the density matrix can be neglected in comparison with the decoherence terms, $\gamma \gg v/\Delta$ in the LZ problem, the two solutions are equivalent.

4.6 Discussion and Conclusions

In conclusion, we have presented a detailed analysis of the dynamics of an open quantum system in the presence of time-varying control field. Specifically, we formulated a time-dependent Bloch-Redfield approach to study the dynamics of a spin-1/2 system whose Hamiltonian varies slowly with time. Here we studied the dynamics in the presence of the

Ohmic environment, however, our formalism can be readily applied to non-Ohmic cases as well. Using modified BR approach, we investigated two problems. In the first problem, we studied the response of a qubit to a rotating control field of the qubit with a fixed magnitude. We noted that when the qubit basis is transformed to keep the effective Hamiltonian in the diagonal form, which is required for proper perturbative analysis of the coupling between the qubit and its environment, the transformed Hamiltonian acquires extra gauge terms. The gauge terms result in the modification of the qubit-environment coupling and are related to the renormalization of the mass and friction terms due to changing parameters of the Hamiltonian, cf. Ref. [137]. The exact form of the renormalization depends on a particular orientation of the control field with respect to the fluctuating environment field. We have illustrated this scenario by considering different orientations of the environment field: (1) control field and fluctuations are always perpendicular to each other, and the corresponding relaxation rates are time-independent; (2) control and fluctuation fields are parallel only at some moments of time, in which case the relaxation rates significantly oscillate in time; (3) fluctuations are always along the direction of the control field, then the relaxation rates are small in the parameter given by the ratio of the rotation velocity and level separation.

Our analysis offers a clear evidence of robustness of topological features against external noises. To see this one needs to consider a long time limit where the qubit density matrix reaches a steady state solution that at zero temperature coincides with the ground state of the effective Hamiltonian. When this ground-state qubit configuration is looked at in the original laboratory basis, the qubit has a constant projection in the direction perpendicular to the plane of rotation and the magnitude of the projection is proportional to the product of rotation velocity of the control field and the Berry curvature of the qubit ground state. In the long time limit, this response is unaffected by the environmental coupling field, at least for zero temperature environment. This relation of the response at long times and the Berry curvature can be utilized as a practical method for measurements of the Chern number [138] of a quantum system.

We also considered an environment with a very sharp spectral function. We represent

this environment by a quantum harmonic oscillator that has internal relaxation. In this case we solve the Lindblad master equation for the system of coupled qubit and oscillator and find that the results are qualitatively similar to the solution of the BR equation with properly chosen relaxation rates.

In the second example, we revisited the Landau–Zener problem. In this case, the modification of the matrix elements for transitions between eigenstates of the qubit Hamiltonian is essential, even though it was not always taken into account. [114, 116] The eigenstate basis that is necessary to use in treatment of interaction of the qubit with its environment is also convenient for numerical evaluation because in this basis the system behavior during the Landau–Zener level crossing is represented by a smooth function that quickly reaches its long-time asymptotic value.

For a qubit weakly coupled to the environment, the evolution, long after the level crossing, reduces to suppression of the off-diagonal elements of the density matrix and relaxation of the excited state to the ground state, the latter is accurately described by the rate equations. For the fluctuating field along the asymptotic direction of the control field, the relaxation rate decreases as the level separation increases due to suppression of the matrix elements of qubit transition between eigenstates caused by the environment. However, this suppression is not sufficient to cut the relaxation in the long time limit, and the relaxation results in a power law decay of the excited state, until the separation between the qubit states exceeds the ultra-violet cutoff of the environment.

At finite temperature, in addition to enhancement of decoherence rates for the qubit, the excitation processes produce transitions from the ground to the excited qubit states, eventually increasing the probability for the qubit to appear in the excited state after the transition. The BR equations accurately describe the crossover for the Landau–Zener transition in an isolated quantum system, Eq. (4.33), with unitary evolution, to the open system at arbitrary temperature, see Sec. 4.4.

Furthermore, we compare the results obtained from the generalized BR equations with that from the Lindblad master equation. In particular, we focused on the case of pure dephasing Lindblad superoperators, [86, 87] that are equivalent to the longitudinal coupling of the environment (fluctuating field of the environment is along the control field). We found that the two results are consistent in the high temperature limit, when the Lindblad and BR equations are equivalent, but application of the Lindblad equation for a system coupled to low temperature environment may result in unphysical solutions.

Finally, we note that the generalization of the Bloch–Redfield equations can be applied to accurately evaluate the fidelity of quantum gates. By taking into account proper modification of the transition and dephasing rates caused by time-varying parameters in the Hamiltonian, optimization techniques for gate operations can be further improved. Similarly, the BR equations for time-dependent Hamiltonian are also required for accurate description of protocols for adiabatic quantum computing and the Berry phase measurement in recent experiments. [139].

4.7 appendix

Solution of rate equations for the avoided level crossing

Here we evaluate the integral in Eq. (4.42). Notice that while the integral over t' in the exponent,

$$I_1(t) = \int_t^\infty \Gamma_0(t') \coth \frac{W(t')}{2T} dt'$$
(4.56)

originates on long interval from $\sim \Delta/v$ to E_c/v , the second integral converges for time $|t| \lesssim T/v$, for not very large temperatures, we can replace the low limit of integration in Eq. (4.56) by t=0. In this case, we have

$$P_{\infty} = e^{-I_1(0)}I_2, \quad I_2 = \int_{-\infty}^{\infty} \Gamma_e(t)dt,$$
 (4.57)

where $W(t) = \sqrt{\Delta^2 + v^2 t^2 + v^2 \Delta^2/(\Delta^2 + v^2 t^2)^2} \simeq \sqrt{\Delta^2 + v^2 t^2}$, $\Gamma_e(t) = G_{LZ}(t)J(W(t))N(W(t))/2$, $\Gamma_0 = G_{LZ}(t)J(W(t))/2$ with $G_{LZ} \simeq \Delta^2/(\Delta^2 + v^2 t^2)$ and $J(\omega) = 2\pi\alpha\omega \exp(-\omega/Ec)$. First, let us change the integration variable $t = \sqrt{s^2 - \Delta^2}/v$ such that $dt = s/v\sqrt{s^2 - \Delta^2}ds$ and

the integral in the exponential then reads

$$I_1(0) = \int_{\Lambda}^{\infty} \frac{\pi \alpha \Delta^2}{v\sqrt{s^2 - \Delta^2}} \coth \frac{s}{2T} \exp(-s/E_c) ds. \tag{4.58}$$

This integral can be evaluated in two cases. First, we consider the low temperature limit $T \to 0$, in which the hyperbolic cotangent $\coth s/2T \to 1 + 2\exp(-s/T)$. Therefore, the integral is obtained

$$I_1(0) = \frac{\pi \alpha \Delta^2}{v} \left[2K_0(\Delta/T) + K_0(\Delta/E_c) \right],$$
 (4.59)

where $K_0(x)$ is the 0th order modified Bessel function of the second kind with the following asymptotes: $K_0(x) \simeq \sqrt{\pi/2x} \exp(-x)$ for $x \gg 1$ and $K_0(x) \simeq -\ln(xe^{\gamma/2})$ for $x \ll 1$, $\gamma \simeq 0.577$ is the Euler constant. As the result, for $T \ll \Delta$, we have

$$I_1(0) \simeq \frac{\pi \alpha \Delta^2}{v} \left[\sqrt{\frac{2\pi T}{\Delta}} e^{-\Delta/T} + \ln(2E_c/\Delta) - \gamma \right].$$
 (4.60)

The first term can be disregarded for $T \ll \Delta$.

At higher temperatures, there is a stronger contribution to $I_1(0)$ originating from short time interval $|t| \lesssim T/v$. We can estimate this contribution as

$$\delta I_1 = \frac{\pi \alpha \Delta^2}{v} \int_{\Delta}^{\infty} \frac{2T}{s\sqrt{s^2 - \Delta^2}} ds = \frac{\pi \alpha \Delta^2}{v} \frac{\pi T}{\Delta}.$$
 (4.61)

We emphasize that this is the contribution which we do not evaluate correctly when replace Eq. (4.42) by Eq. (4.57). Therefore, we can treat the above expression for δI_1 as the boundary of applicability of our approximation, indicating that transition from Eq. (4.42) to (4.57) is justified not for very high temperatures, such that $\delta I_1 \ll 1$.

Next, we evaluate the integral

$$I_2 = \int_{-\infty}^{\infty} \Gamma_e(t)dt = 2\int_{\Delta}^{\infty} ds \frac{2\pi\alpha\Delta^2}{v\sqrt{s^2 - \Delta^2}} \frac{\exp(-s/E_c)}{\exp(s/T) - 1}.$$
 (4.62)

As before, we first consider the low temperature limit, $T \ll \Delta$, in which we approximate $1/[\exp(s/T) - 1] \simeq \exp(-s/T)$. Then the integral becomes

$$I_2 \simeq \frac{2\pi\alpha\Delta^2}{v} K_0(\Delta/T) \simeq \frac{2\pi\alpha\Delta^2}{v} \sqrt{\frac{\pi T}{2\Delta}} e^{-\Delta/T}.$$
 (4.63)

In the high temperature limit, we utilize $1/[\exp(s/T) - 1] \simeq T/s$, and we obtain

$$I_2 = \frac{\pi^2 \alpha T \Delta}{v}. (4.64)$$

This equation is valid for high temperature limit $T \gg \Delta$, provided that our substitution of Eq. (4.42) by (4.57) is justified, or $\alpha T \ll v/\Delta$.

To sum up, we evaluated P_{∞} in the limits of low and moderately high temperatures. The results are presented by Eqs. (4.43) and (4.44).

Solution of rate equations for the avoided level crossing for environment with longitudinal coupling

For the longitudinal coupling, the transition probability P_{∞} in limit of low temperatures $T \lesssim \Delta$ can be evaluated similarly to the calculations in Appendix A. We replace Eq. (4.46), where the integral over time t converges fast for $|t| \lesssim T/v$, by the following expression

$$P_{\infty} = I_2 e^{-I_1}, \quad I_2 = \int_{-\infty}^{\infty} \Gamma_e(t) dt$$
 (4.65)

$$I_1 = \int_0^\infty \Gamma_l(t)dt,\tag{4.66}$$

where in the last integral we take the lower limit of integration to zero and $\coth W/2T \to 1$. In the above expression, $W(t) = \sqrt{\Delta^2 + v^2 t^2 + v^2 \Delta^2/(\Delta^2 + v^2 t^2)^2} \simeq \sqrt{\Delta^2 + v^2 t^2}$, $\Gamma_e(t) = G_{LZ}(t)J(W(t))N(W(t))/2$, $\Gamma_0 = G_{LZ}(t)J(W(t))/2$ with $G_{LZ} \simeq v^2 \Delta^2/(v^2 t^2 + \Delta^2)^3$ and $J(\omega) = 2\pi\alpha\omega \exp(-\omega/Ec)$. Similarly, let us change the integration variable $t = \sqrt{s^2 - \Delta^2}/v$ such that $dt = s/v\sqrt{s^2 - \Delta^2}ds$. The integral I_1 then reads

$$I_1 = \int_{\Delta}^{\infty} \frac{\pi \alpha \Delta^2 v}{s^4 \sqrt{s^2 - \Delta^2}} ds = \frac{2\pi \alpha v}{3\Delta^2}.$$
 (4.67)

We note that this integral converges fast and the high-energy cutoff of the environment can be omitted. Similarly, the integral over $\Gamma_e(t)$ can be rewritten as

$$I_{2} = \int_{\Delta}^{\infty} \frac{2\pi\alpha\Delta^{2}v}{s^{4}\sqrt{s^{2} - \Delta^{2}}} \frac{ds}{\exp(s/T) - 1}$$

$$\simeq \int_{\Delta}^{\infty} \frac{\sqrt{2}\pi\alpha\Delta^{3/2}v}{s^{4}\sqrt{s - \Delta}} \exp(-s/T) ds$$

$$\simeq \alpha v \sqrt{\frac{\pi^{3}}{32T\Delta^{3}}} \exp(-\Delta/T).$$
(4.68)

In the high temperature limit, we follow a different approach. We assume that the environment is at high temperature and the relaxation rates are enhanced by factor T/W(t). In this case, we also have a fast convergence of integrals $\int \Gamma_0(t)dt$ at $|t| \lesssim \Delta/v$ and for $T \gg \Delta$, we can simplify the rate equation (4.41) to

$$\frac{dm}{dt} = -2\pi\alpha T \frac{v^2 \Delta^2}{W^2(t)E^4(t)} m(t). \tag{4.69}$$

This equation can be integrated to find m(t) with initial condition $m(-\infty) = 1$, and used to define $P_{\infty} = (1 - m(+\infty))/2$:

$$P_{\infty} = \frac{1 - e^{-I_3}}{2}, \quad I_3 = 2\pi\alpha T \int_{-\infty}^{\infty} \frac{v^2 \Delta^2 dt}{W^2(t) E^4(t)}.$$
 (4.70)

For $v \ll \Delta^2$, we obtain

$$I_3 = \frac{3\pi^2}{4} \frac{\alpha T v}{\Delta^3},\tag{4.71}$$

arriving to Eq. (4.48).

Chapter 5

Response to a local quench of a system near many body localization transition

5.1 Introduction

Localization phenomena in disordered quantum systems has over half century history starting with the seminal work by Anderson [140]. A system of non-interacting electrons in one and two dimensions exhibit localization at zero temperature as follows from the scaling considerations[141]. The role of electron-electron interactions, however, is ambiguous. The onset of localization, known as weak localization [142], is destroyed by electron-electron interaction at finite temperatures [143] as the interaction results in dephasing of electron wave functions. At the same time, electron-electron interactions give rise to the Coulomb gap at the Fermi energy, driving the system to localization [144]. Recent development in theory of localization in disordered system of interacting electrons was put forward in the work of Basko, Aleiner and Altshuler [145]. This chapter proposed an infinite order perturbation theory in the electron-electron interaction and determines an energy threshold. Below the threshold, the interactions between electrons cannot facilitate electron hopping

between localized single electron states and systems remains localized. As energy of the electron system increases above the threshold value, a large phase space of the system allows electrons to rearrange and form an extended many-electron quantum state. This many-electron quantum state corresponds to dephasing in a single electron language.

Along with more theoretical studies of localization in many body systems [146, 147], experimental observation of localization remains a challenging task due to electron-phonon interaction that effectively spoils many-particle states of the electron system in real metals. The interest in search of systems that might exhibit many-body localization (MBL) has shifted to ultra-cold atomic gases [148], trapped ions [149, 150] and artificial quantum systems composed of several interacting qubits [151]. Systems that contain relatively small number of quantum particles, such as qubit chains and trapped ions, have another advantage as their individual elements can be controlled and measured with high precision as well as these systems can be simulated numerically by exact diagonalization of corresponding Hamiltonians or by approximate methods with controllable accuracy. Thus, more recent theoretical work was focused on studies of interacting one dimensional spins chains [152, 153, 154, 155, 156, 157, 158, 159, 160, 161]. Numerical and theoretical studies [152, 153, 154, 155, 156, 157, 158, 159, 160, 161] have shown that spin systems containing more than ten spins and involving more than a thousand of many-body eigenstates show MBL behavior in sufficiently strong disorder.

A model that captures effects of interactions and disorder in a fermonic system is the onedimensional hopping Hamiltonian for spinless electrons with periodic boundary conditions $(c_{L+1} = c_1)$,

$$H_0 = \sum_{l=1}^{L} \left[J c_{l+1}^{\dagger} c_l + h_l n_l + J' n_l n_{l+1} \right] + \text{h.c.},$$
 (5.1)

where c_l is the annihilation operator of electron on site l and $n_l = c_l^{\dagger} c_l - 1/2$ defines the site occupation. Parameter J describes the tunneling amplitude between neighboring sites, J' defines the interaction between fermions on neighboring sites and h_l is an energy of an electron on site l. The onsite fields h_i are independent random fields, uniformly distributed in the range [-W, W], where W is the disorder strength in the system. The Hamiltonian

(5.1) can be rewritten as an antiferromagnetic Heisenberg spin-1/2 chain of L spins with the periodic boundary condition $\vec{\sigma}_{L+1} = \vec{\sigma}_1$ and and random fields h_l along the z direction.

$$H_0 = \sum_{l=1}^{L} \left[J(\sigma_l^x \sigma_{l+1}^x + \sigma_l^y \sigma_{l+1}^y) + J' \sigma_l^z \sigma_{l+1}^z + h_l \sigma_l^z \right], \tag{5.2}$$

This model has been the focus of recent detailed studies [156]. The system is assumed to be tuned at half-filling, when the number of spinless electrons is L/2 for a system with the Hamiltonian (5.1) or $S_{\text{tot}}^z = \sum_l \sigma_l^z = 0$.

At weaker disorder, $W \lesssim J$, the system is in the delocalized regime and has several characteristics reminiscent of conduction phase of a disordered metal. In particular, the level statistics shows a distribution of level spacing similar to the Wigner-Dyson statistics with level repulsion. At strong disorder, on the other hand, the Hamiltonian (5.1) shows localized behavior, as the level spacings acquire a Poisson distribution with high probability to find two levels with a small level separation, and the dynamic susceptibility vanishes. According to previous numerical studies, the transition from the delocalized regime to the localized regime takes place at $W = W_c \simeq 3J$.

At strong disorder, $W > W_c$, the evolution of the system depends on the strength of interaction, J'. If a system is split into two subsystems and its wave function is prepared in a product state, the entanglement entropy quickly reaches a non-zero value and remains constant for longer times for non-interacting system, J' = 0, this value of the entanglement entropy remains independent of the system size L. When the interaction is turned on, $J' \neq 0$, the entanglement entropy shows growth on a logarithmic scale and saturates on a exponentially long time scale [156, 157]. The saturated value of the entanglement entropy scales linearly with the system size.

This intriguing system is currently can be investigated numerically using exact numerical diagonalization of the Hamiltonian for a system size $L \lesssim 16$. Further increase of the system size requires significant increase in computing power and memory requirements. At the same time, this system can be simulated using current state of quantum devices. Recently, a system of superconducting qubits with pairwise interaction between neighbors

was demonstrated to have long decoherence times and future efforts are focused on building larger systems of such qubits [151]. Alternative system considered for such simulations is a system of trapped ions [150, 149].

Regardless of a particular realization of the system for simulation, a plausible measurements, such as spectroscopy or transport, will result in violation of the particle conservation (for system (5.1)) or spin along z-axis (for system (5.2)). Previous studies have conjectured that the nature of two phases are distinguished by the validity of eigenstate thermalization hypothesis (ETH). Such attribution allows one to construct translational invariant Hamiltonians in which the onset of MBL phase transition is caused by interactions. Another idea to examine the relation between ETH and MBL states is to drive the system out of equilibrium and test if the phase transition is restored.

The MBL phase can be characterized by the existence of infinite number of local integrals of motion [152, 153, 154, 155], the entanglement structure [156, 157, 158, 159, 160, 161], as well as the spectral properties of eigenstates [147]. While these characteristics can be measured in principle, the corresponding experiments are very burdened as they require either a full quantum tomography or full energy spectroscopy of such systems. In this chapter we propose an alternative strategy to identify the localization in a disordered system of interacting spins. We first study the level spacing statistics of a Heisenberg spin chain in random magnetic field along z axis with turning on a local transverse field. Then, we switch to analyze the response of a pure state of this model to a sudden application of a magnetic field perpendicular to z that acts on a single qubit. We evaluate the inverse participation ratio of an eigenstate of unperturbed Hamiltonian in the basis of the perturbed Hamiltonian. The participation ratio is small in the delocalized regime when the initial state overlaps with many eigenstates of the new Hamiltonian. In the localized regime, an application of a local perturbation does not affect majority of eigenstates and the IPR increases rapidly. Points at which the IPR starts increasing fast form a curve in the energy vs disorder strength plane. This curve defines the upper and lower mobility edges.

Since the IPR is not easily measurable in experiments, we also investigate correlations

in single spin measurements before and after the onset of the local perpendicular field. The covariance between these two measurements is small for delocalized states, but rapidly increases for localized states, as an applied perpendicular magnetic field does not change significantly configuration of spins far away from the perturbation. The mobility edge obtained from the covariance is consistent with the mobility edge obtained through the IPR, as well as through analysis of the entanglement entropy [162, 163]. Moreover, at strong disorder in the localization regime, the response of the spins to the applied local field decreases exponentially as a function of the distance of the monitored spin from the perturbation. We utilize this exponential decay to evaluate the localization length as a function of disorder and demonstrate that the localization length diverges near the mobility edge.

5.2 Level Spacing Statistics of the MBL Hamiltonian

To be specific, consider a 1D Heisenberg spin chain with random on-site field in the z direction with periodic boundary condition, described by the Hamiltonian

$$H_0 = \sum_{i} h_i \sigma_z^{(i)} + J \sum_{i} \boldsymbol{\sigma}^{(i)} \cdot \boldsymbol{\sigma}^{(i+1)}, \tag{5.3}$$

where h_i on each site is a random variable distributed uniformly in the interval [-W, W] and $\sigma^{(i)}$ is the Pauli matrix for spin at site i. Throughout the chapter, we use J as a fundamental unit and set J=1, we also denote eigenstates of H_0 by $|\alpha\rangle$. In fact, there are two global conserved quantities in the system, namely the energy and the total spin in z direction $S_z = \sum_i \sigma_z^{(i)}$. Previous numerical [164, 161] and theoretical [165] studies were focused on the subspace $S_z = 0$, where the MBL phase develops at strong disorder with $W \gtrsim 3.4$.

Since the total spin along z direction is conserved, the natural approach is to truncate the Hamiltonian at half-filling. We start by analyzing the spectral properties of H_0 at half-filling by performing exact diagonalization (ED) of the Hamiltonian for L=14 sites. The standard approach is to compute the ratio of consecutive level spacings, defined by

 $r_n = \min(\delta_n, \delta_{n+1})/\max(\delta_n, \delta_{n+1})$, where δ_n is the energy separation between adjacent many-body eigenstates $\delta_n = E_{n+1} - E_n$. This quantity r_n has the advantage that it is dimensionless and independent of local density of states. Thus such a distribution permits a transparent distinction from the band edges to the dense part of the spectrum.

It is well-known that at strong disorder, the eigenvalues are uncorrelated and therefore the probability distribution of δ_n is Poisson, which corresponds to $P_p(r) = 2/(1+r)^2$. On the other hand, at weak disorder, the random matrix theory as a phenomenological approach is adopted. Here, the eigenvalues are correlated, which is highlighted by the onset of level repulsion, $P(r) \to 0$ at small r limit. However, it remains an open question to understand the discrepancies of spectral properties between GOE and MBL Hamiltonian at weak disorder in the thermodynamic limit. Therefore throughout our analysis, instead of comparison to GOE or correspondingly Wigner-Dyson statistics, the main concern is about the onset level repulsion. For this purpose, we extract the exponent of P(r) in the limit $r \to 0$:

$$\kappa = \lim_{r \to 0} \frac{d \ln P(r)}{d \ln r},\tag{5.4}$$

as a universal measure of level repulsion.

In the top panel of Figure 5.1, we present the probability distribution P(r) in the log-log scale. The data is obtained from ED for 10^4 disorder realizations with L=14 and several disorder strengths. At small r limit, there is a clear crossover from $\kappa \simeq 1$ at weak disorder (W=1) to $\kappa \simeq 0$ at strong disorder (W=30). In between the two limits, the fractional value of κ in [0,1] is attributed to mixing between correlated and uncorrelated states. In the inset, the same set of data of P(r) is plotted in linear to show the decreasing of the average value of r with increasing W. As discussed in Ref. [147], $\langle r \rangle$ grows smoothly from 0.38 for Poisson ensemble to 0.54 for GOE as a resemblance to the weak disorder Hamiltonian. Our numerical result agrees with this findings. In the bottom panel, we plot the dependence of κ as functions of W for L=10,12 and 14. For all three curves, the exponent κ drops from unity at weak disorder to zero at strong disorder. However, in contrast to the study of

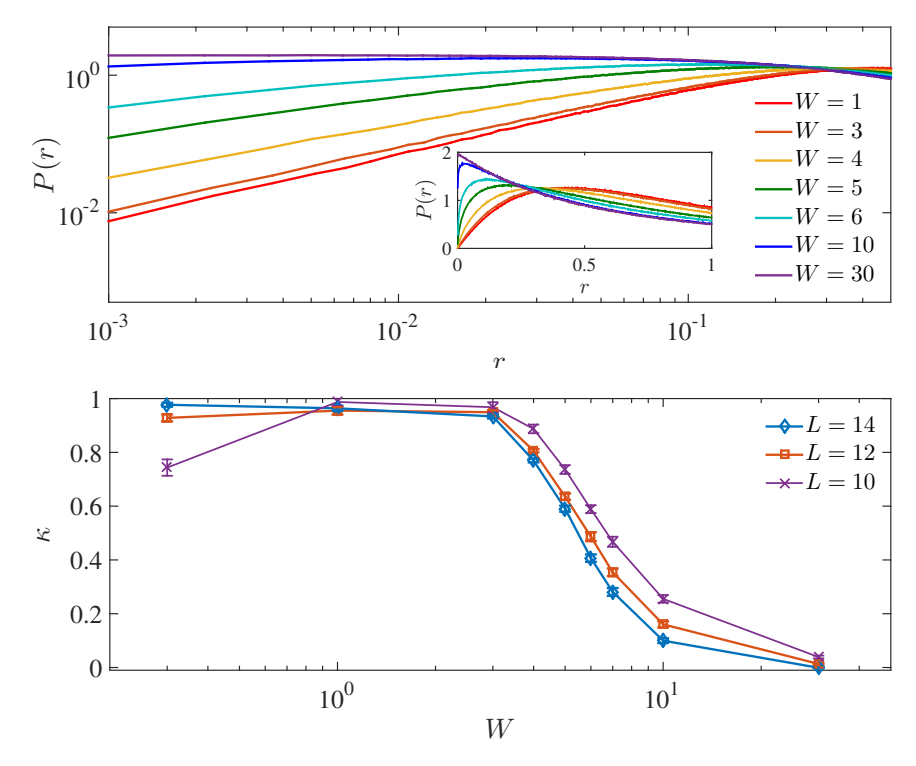


Figure 5.1: Level spacing statistics of the static Hamiltonian for 3 typical values of W = 0.3, 4, 30. Results are obtained with L = 14 spins, and are averaged over 10^4 realizations. The corresponding bare fittings with GSP distribution are also shown. In the strong disorder regime, the GSP distribution reduces to the well-known result with Poisson distribution. In contrast, at weak disorder, it remains unclear whether Wigner-Dyson, GSP or even more complicated distribution provides a correct result. Inset: the same set of data but plotted in log-log scale. Instead of the overall distribution of r, the slope of the linear dependence at small r limit is another method to obtain exponent α .

dynamic polarization in Ref. [164], in the critical regime, the curves with different system size are parallel other than crossing to each other.

5.3 Level Spacing Statistics of the Quenched Hamiltonian

Then, we study the case when Hamiltonian (5.3) suddenly acquires additional local perturbation breaking S_z conservation law. In particular, the new Hamiltonian is $\tilde{H} = H_0 + V$, where $V = f\sigma_x^{(i=0)}$, see Figure 5.2. As noted before, the total spin projection $S_z = \sum_i \sigma_z^{(i)}$ is a good quantum number for H_0 , therefore the perturbation term breaks the conservation of S_z . Quite generally, when the eigenstates are not correlated, the level spacings are

independently distributed upon varying external parameter(s). On the other hand, when the perturbation is turned on, the perturbed eigenstates acquires components set by the matrix elements of the perturbation term, divided by the differences in energies. In this manner, the level spacing statistics is no longer independent. One can check the statistics of the new eigenvalues of the perturbed Hamiltonian, similar as the procedure in the previous section. In our numerics, in order to evidence the spectral properties of the entire spectrum in which all families of total S_z is included, we first examine the distribution of the difference in indexes for states in the $S_z = 0$ sector.

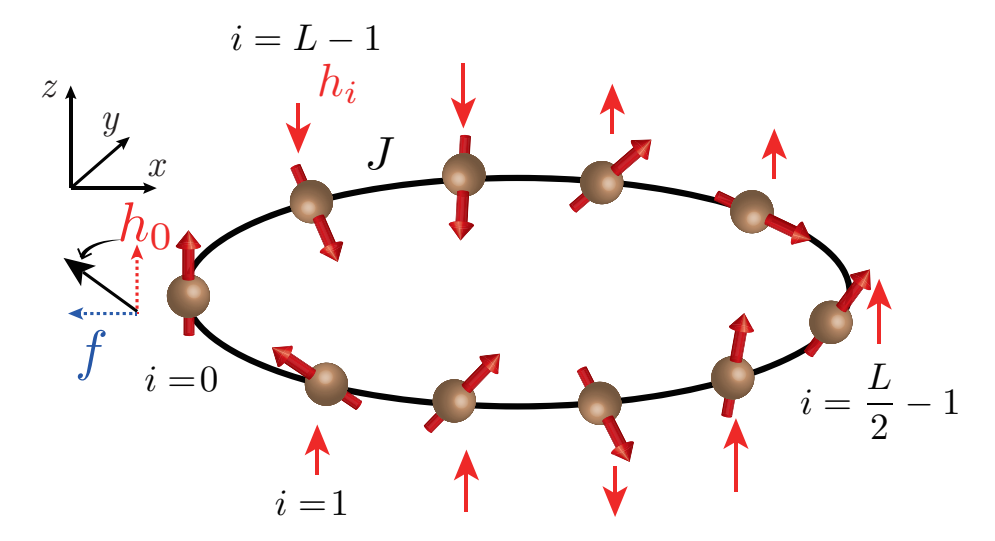


Figure 5.2: Schematic of the one-dimensional spin-1/2 chain with periodic boundary condition. Along the chain, each spin is subject to a random onsite field h_i along z direction and the spins are coupled by nearest neighbor Heisenberg interactions with strength J. At time t_0 when the local quench is turned on, a transverse magnetic field f is applied to one of the spin, labeled by i_0 .

Figure 5.3 shows the distribution of Δ index for both ergodic and localized regime. Here we find for the ergodic regime, there is an interesting repulsion of states with the same total spin. In other words, two adjacent eigenvalues are much more likely from two different families of S_z , rather than from the same value. Therefore, one can expect that the distribution of r for the entire spectrum are mainly dominated by the states with different S_z . States that are far apart in energy are far apart in the phase space as well, but the reverse is not true. Therefore in the ergodic regime, states with the same S_z are

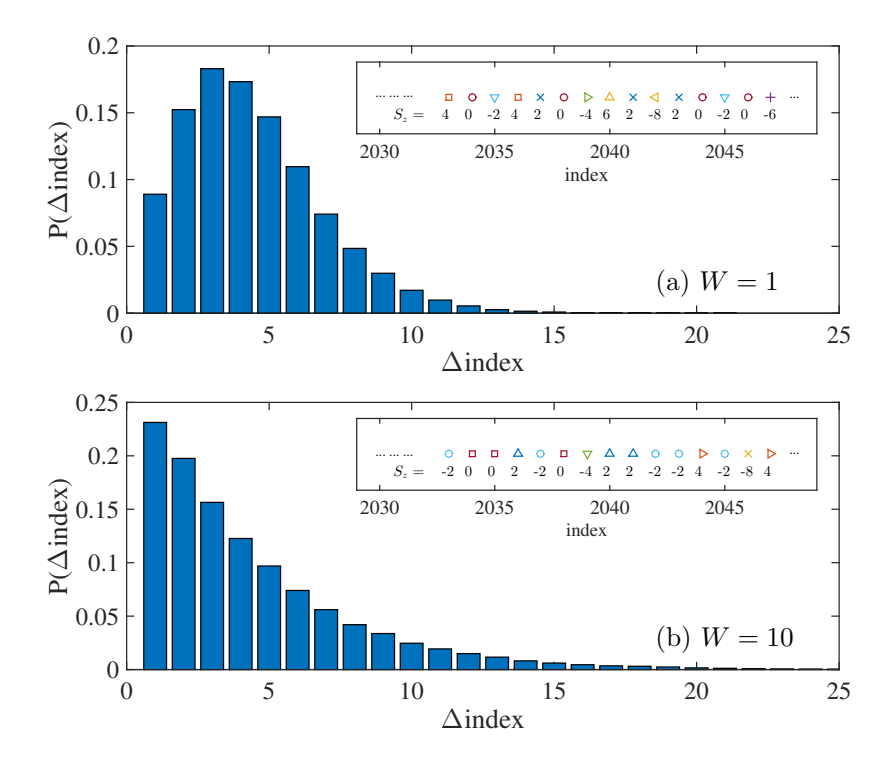


Figure 5.3: The distribution of Δ index for the $S_z = 0$ sector of the spectrum in (a) the ergodic regime, W = 1, or (b) the localized regime, W = 10. Data is obtained for L = 12 with 100 disorder realizations. Insets: the pattern of states labeled by different S_z in the middle of the band for one arbitrary disorder realization. Different markers correspond to different S_z . In the ergodic regime, states with the same S_z are more likely separated by at least one state with a different S_z , whereas for the localized regime, states with the same S_z more likely appear in adjacent pairs.

not grouped together. On the other hand, for the localized regime, the distribution is monotonic, indicating that states different S_z more likely appear in adjacent pairs. These differences in the distribution of Δ index, however, resulting both Poisson-like distribution for either weak or strong disorder. In the former case, selection rules between states with different S_z are vulnerable to the weak perturbation, whereas for the latter case, both intraand inter-couplings between states within different families are exponential small.

To reveal the non-trivial deviations in the distribution of r, we turn on the perturbation $f\sigma_x^{(1)}$. To this end, two eigenstates from different families of S_z are perturbed by the finite matrix elements given by σ_x . In this manner, in the phase space the boundary between states with quantum numbers S_z are blurred. In this case, the nature of the quantum states

can be examined without reliance on symmetry arguments or restriction of selection rules. After that, the connectivity of between states in the phase space is a criteria of localization. As shown in Ref. [166], for this particular spin model a tentative local conserved quantity of the MBL states are the local spins in z-direction, dressed by their neighbors with strengths set by the many-body localization length ξ . If ξ is comparable to the lattice spacing, local spins are oblivious to each other, so that the two configurations are not connected in the phase space. On the other hand, these operators become extended if the localization length is comparable to the system size and therefore looses its meaning.

Above arguments imply that within the entire spectrum of the driven Hamiltonian for a finite system highlights the remarkable role played by the perturbation. The role of the perturbation to distinguish the two phases can be seen as a reminiscent of its non-local response that forms a rearrangement of local conserved quantities. In the thermodynamic limit, the two phases can be recognized by if there is a orthogonal catastrophe due to small changes in the amplitude f. Unfortunately, this calculation is not permitted in the present work due to the limitation of computational resources, and remains an open question for future work.

In what follows, we consider the distribution function P(r) of the dimensionless parameter r with respect to various values of drive amplitude. As a result of increasing f, the quantum states unveil their nature of localization/delocalization. To see this, we vary the amplitude of the drive from f = 0 to f = 0.6J or more for each disorder realization with fixed parameters of the static Hamiltonian for both ergodic and localized regime. For each sample, we collect the data of r over all states and compute the histogram of r for both cases.

As expected, at f = 0, the distribution P(r) is Poisson-like statistics with minor deviations for both cases. While the external drive is turned on, the behavior of the statistics for W = 1 and W = 10 are qualitatively different. For strong disorder, W = 10, even though the perturbation induce a finite matrix element between states with different S_z , this effect on level spacing statistics is minor because a considerable portion of eigenstates are still

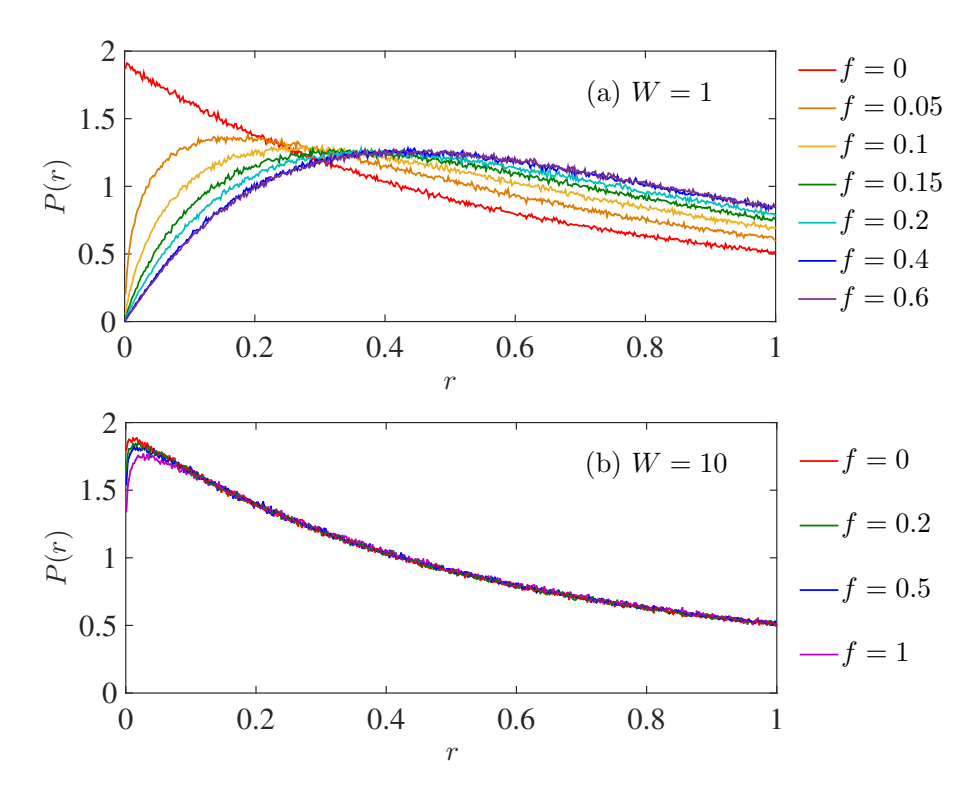


Figure 5.4: The probability distribution of r for (a) the ergodic regime, W = 1 and (b) the localized regime, W = 10 with varying amplitude of perturbation f. Data is obtained for L = 12 with 1000 disorder realizations.

being localized and thus remains uncorrelated. Consequently from the distribution function P(r) for finite drive amplitude at small r there is no apparent level repulsion developed. On the other hand for weak drive, W = 1, the effects of the perturbation is sensitive on the amplitude f. As f grows, signature of level repulsion quickly reveals up to f = 0.1J, as shown in Figure 5.4.

Quite interestingly, the onset of level repulsion can be quantified by looking at the following quantity "maximum distance" (MD) between cumulative distribution r, $Q(r) = \int_0^r P(r')dr'$ between Poisson and actual distribution P(r):

$$MD = \int_0^{r_0} |P_p(r) - P(r)| dr, \tag{5.5}$$

where $P_p(r) = 2/(1+r)^2$ is the Poisson distribution function for r and r_0 is the point of P(r) to maximize the cumulative distributions, i.e., the first intersection point of $P_p(r)$ and P(r). The advantage of this measure of similarity between different distribution function is

that the data of cumulative distribution is less noisy than P(r) itself, and it is also sensitive on the onset of level repulsion because only data in the small r limit is considered.

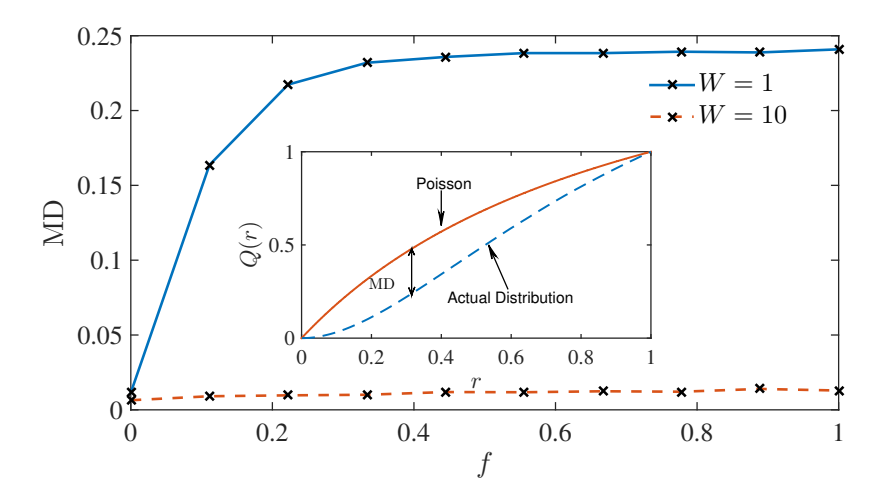


Figure 5.5: Dependence of MD on the amplitude of perturbation f for weak (W=1) and strong (W=10) disorder. As a measure of deviation from Poisson statistics, the MD for the ergodic regime is sensitive on f and grows quickly to $\simeq 0.24$, while for the localized regime MD roughly remains constant at a small value $\simeq 0.01$. Inset: The definition of MD is given by the maximum distance between cumulative distribution functions of r between Poisson statistics and actual statistics.

The dependence of MD on amplitude of drive has different behavior in the two phases, as shown in Figure 5.5. In our numerics, the cumulative distribution of Q(r) is obtained by the labels of the sorted data of r. In this manner, even for 100 disorder realizations, Q(r) is smooth enough for our computation purposes. For weak disorder, the MD quick saturates to $\simeq 0.24$ at $f \simeq 0.4J$, while for strong disorder MD remains constant at a small value $\simeq 0.01$.

It is worth pointing out that our numerical result agrees with the previous studies on the average of r, namely $\langle r \rangle \simeq 0.39$ for Poisson distribution and $\langle r \rangle \simeq 0.53$ for GOE. However, the reason why we use MD instead of $\langle r \rangle$ as a measure to distinguish the distributions is that the existence of universality for the entire spectrum at weak disorder is specious. Hence we are only simply interested in the deviation of the distribution from the Poisson one.

5.4 Long Time Dynamics of Local Quench

In this section we consider a system that was originally prepared as a pure state $|\psi\rangle$ in the subspace of states with $S_z|\psi\rangle = 0$ and calculate its response over a long time after the onset of $V = f\sigma_x^{(i=0)}$:

$$\langle \bar{O} \rangle = \lim_{T \to \infty} \frac{1}{T} \int_0^T \hat{O}(t) dt = \text{Tr} \overline{\rho(t)} \hat{O} = \text{Tr} \rho_{\text{DE}}^{|\psi\rangle} \hat{O},$$
 (5.6)

where $\rho(t) = \exp(-iHt)\rho(0) \exp(iHt)$ is the density matrix and $\rho_{\rm DE}^{|\psi\rangle} = \overline{\rho(t)}$ is the time-averaged density matrix initialized in a pure state, $\rho(0) = |\psi\rangle\langle\psi|$,

$$\rho_{\rm DE}^{|\psi\rangle} = \sum_{\alpha} P_{\tilde{\alpha}} \left| \langle \tilde{\alpha} | \psi \rangle \right|^2, \quad P_{\tilde{\alpha}} = |\tilde{\alpha}\rangle \langle \tilde{\alpha} | \tag{5.7}$$

and $P_{\tilde{\alpha}}$ is the projection operator on new eigenstates $|\tilde{\alpha}\rangle$ of \tilde{H} . The off-diagonal elements of $\rho_{\rm DE}^{|\psi\rangle}$ are averaged to zero and this density matrix is equivalent to a diagonal ensemble [167] where the off-diagonal elements are absent due to dephasing.

Below we concentrate on initial states $|\psi\rangle$ that coincide with eigenstates of the initial Hamiltonian H_0 and have $S_z = 0$. We denote these states by $|\alpha_0\rangle$, where the level index $\alpha_0 = 1, \dots, N(L, 0)$ runs over eigenstates of H_0 ordered with increasing values of eigenenergies, $N(L, S) = (2^L)!/[(2^{L-S})!(2^{L+S})!]$.

We demonstrate that the Hamiltonian with local perturbation, \tilde{H} , still exhibits the MLB phase. The first indicator of many-body localization we study is the inverse participation ratio (IPR), defined as

$$IPR_{\alpha_0} = \sum_{\tilde{\alpha}=1}^{2^L} |\langle \alpha_0 | \tilde{\alpha} \rangle|^4 = Tr \bar{\rho}_{DE}^{|\alpha_0\rangle} P_{\alpha_0}, \qquad (5.8)$$

where $P_{\alpha_0} = |\alpha_0\rangle\langle\alpha_0|$. The IPR is a measure of portion of the Hilbert space explored by the system after the perturbation V is turned on [168]. At weak disorder, the motion of the system is ergodic and the state travels over a large fraction of the Hilbert space and results in minimal values of the IPR about $\sim 2^{-L}$. On the other hand, in the strong disorder limit, the ergoicity breaks down and the many-body wavefunction evolves within a small section of the Hilbert space bounded by the local integral of motion [152, 165, 153]

For both limits, the distribution of $\log_2 \mathrm{IPR}_{\alpha_0}$ is highly concentrated and transition between these two limits can serve as an indicator of the mobility edge that separates localized and delocalized many body states. We note that the fluctuations of IPR are enhanced substantially near the mobility edge. Indeed, when $|\alpha\rangle$ is chosen to be close enough to the mobility edge, the excitations is a combination of delocalized and localized states. The compromise between them gives rise to diverging standard deviations in IPR.

To demonstrate the behavior described above, we perform exact diagonalization for L=12 spins and N=2000 realizations to obtain all the eigenstates $|\alpha\rangle$ s for H_0 and $|\tilde{\alpha}\rangle$ s for H to evaluate $\rho_{\rm DE}$. If the system is initialized with an eigenstate $|\alpha_0\rangle$ of H_0 with $S_z=0$, and as long as the quench is fast enough the system will be in the eigenstate $|\alpha_0\rangle$. We then evaluate both $|\alpha_0\rangle$ and $|\tilde{\alpha}\rangle$ that define the corresponding density matrix in diagonal ensemble as $\rho_{\rm DE}^{|\alpha_0\rangle}$.

The result of this analysis is presented in Figure 5.6. The average IPR as a function of disorder strength W and ϵ is plotted in Figure 5.6(a). The averaged value of IPR(W, ϵ) with respect to disorder realizations clear reveals the existence of a mobility edge that distinguishes delocalized states to localized states, here $\epsilon = \alpha_0/N(L,0)$ position of eigenstate within the energy band. To justify the nature of the mobility edge, we plot the histogram of the distribution of \log_2 IPR in Figure 5.6(b). In the weak and strong disorder limit, the distributions of \log_2 IPR are highly concentrated at somewhere $\propto L$ and 0 respectively. However, \log_2 IPR in the critical region is broadly distributed between the two limits with its standard deviation proportional to L and the standard deviation eventually diverges at the mobility edge in the thermodynamic limit. In fact, these critical fluctuations is a reminiscent of the many-body mobility edge which separates the two distinct phases. For this reason, we can use this approach to identify the phase boundary of an MBL transition. We note that similar divergence has been found in the fluctuations of the entanglement entropy [161].

In the lower panels Figure 5.6(c), we make two vertical cuts at fixed disorder strengths W = 3, 7 on the phase diagram. For moderate disorder strength W = 3 and in the presence

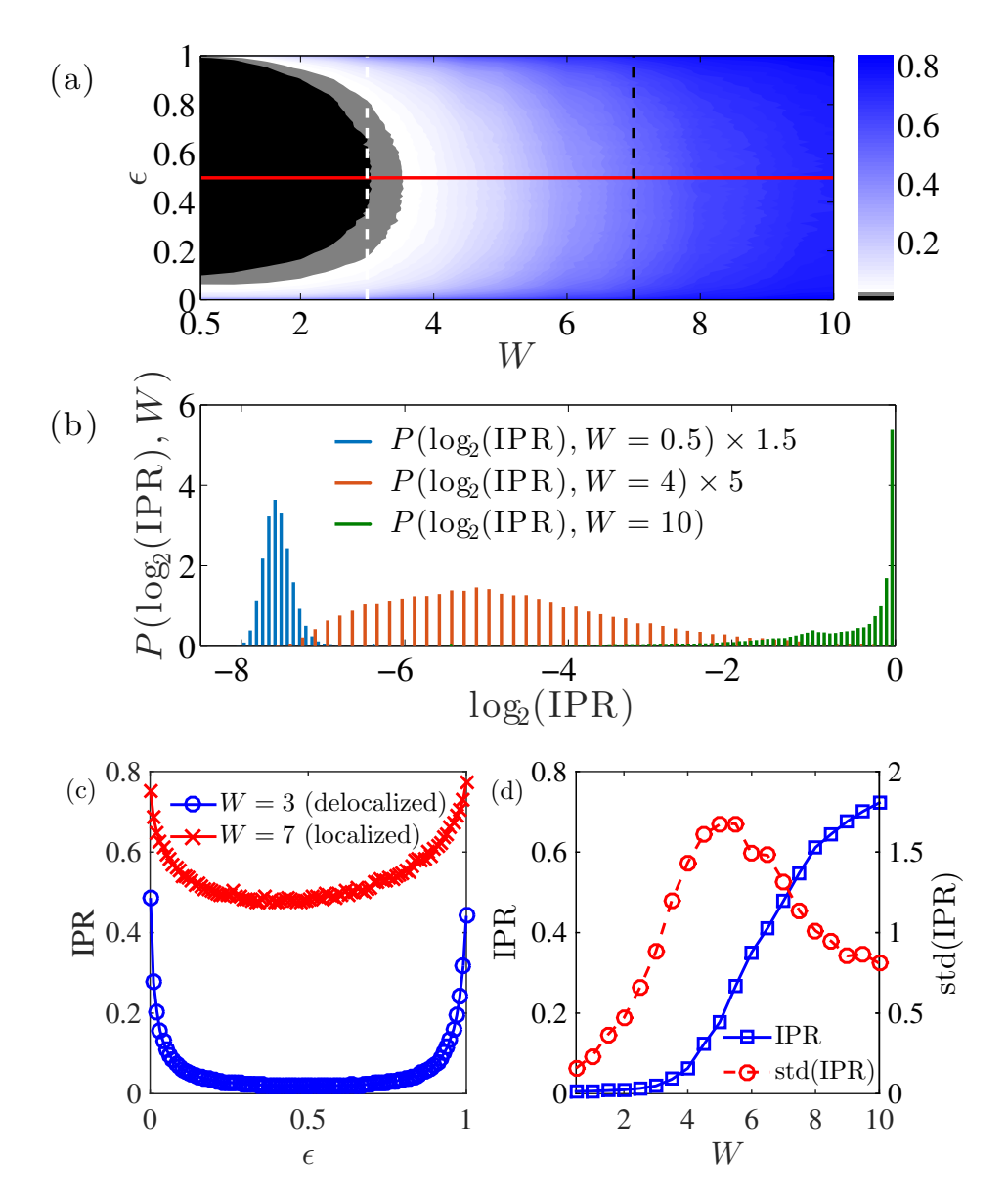


Figure 5.6: (a) Averaged participation ratio over disorder realizations as functions of disorder strength W and energy density ϵ for a system of L=12 and 1000 realizations. Marked by white color, the many body mobility edge encloses a region of delocalized states with IPR $\sim 2^{-L}$. The horizontal and vertical cut indicates the parameters for panel (c) and (d). (b) The histogram of \log_2 IPR in the middle of the band for W=0.5, 4 and 10. The distributions are concentrated for weak and strong disorder, but highly fluctuating in the critical region. (c) The IPR at fixed disorder W=3, for which case the states are delocalized in the middle of the band but localized in the edges, and W=7 where all states are localized. (d) The IPR and its standard deviation for fixed energy density $\epsilon=0.5$.

of mobility edge, the PR reaches ~ 0.4 in both edges in an unsymmetrical manner, but it sharply drops to $\sim 10^{-2}$ and forms a flat basin in the middle of the band. At strong disorder W=7, all states are localized and this can be justified by the large value of IPR throughout the band $\gtrsim 0.4$, indicating that the mobility edge is closed. When we fix the energy density at the middle of the band, $\epsilon=0.5$, we observe the stand deviation can identify that the mobility edge closes at the critical value $W_c \simeq 3.5$, accompanied by a kink in the standard deviation of IPR.

While the above approach to detect mobility edge through IPR is suitable for numerical calculations, it is hardly realized experimentally. For experimental detection of the mobility edge, we propose a different approach. We study the dynamics of single spins and investigate the correlation of the their expectation values $\langle \sigma_z^{(i)} \rangle$ before and after a local perturbation. Our motivation is based on the previous observations [169] that in the MBL regime the ETH is violated and information about the local observables at sufficiently long times can be traced back to its initial condition resulting in correlations between spin states before and after perturbation V is turned on. Otherwise, in the delocalized regime the motion is ergodic and all correlations with initial conditions are lost.

For an interacting system, the observables set by a finite degrees of freedom can be evaluated by the reduced density matrices in which the off-diagonal elements are essentially zero due to dephasing even if the system starts in some arbitrary pure state. One can measure the local observables in this steady state, and then apply the local perturbation to the Hamiltonian so that the system approaches a new quasistationary state in the eigenbasis of the perturbed Hamiltonian. In this sense, time averaged expectation values of a local operator are characterized by a diagonal ensemble $\rho_{\rm DE}$. In this case, a good description of response for arbitrary initial state can be obtained by analyzing correlations between expectation $P_{\alpha_0}^i$ of a local operator for an unperturbed system with Hamiltonian H_0 initialized in an eigenstate $|\alpha_0\rangle$ and its expectation value after system is perturbed, $Q_{\alpha_0}^i$. Here we introduced notations for the expectation values of $\langle \sigma_z^{(i)} \rangle$ of monitored spin i and initial system state $|\alpha_0\rangle$ as $P_{\alpha_0}^i$ and $Q_{\alpha_0}^i$ for a system before and after the local perturbation at

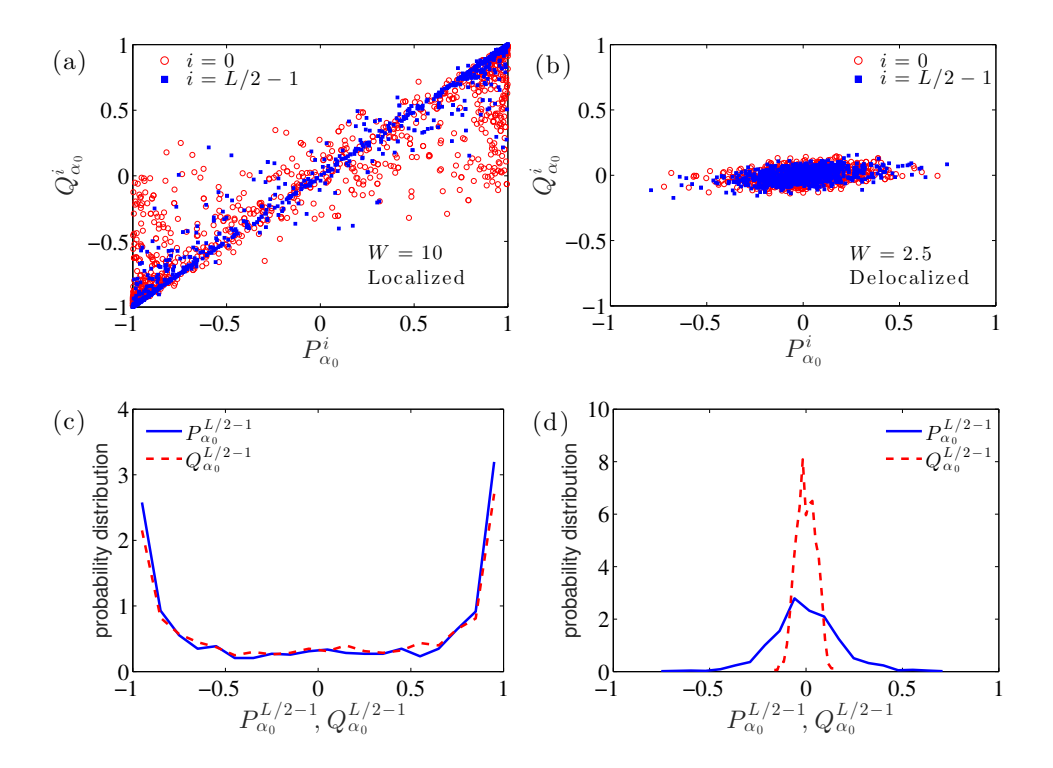


Figure 5.7: Scatter plot of $(P^i_{|\alpha\rangle}, Q^i_{|\alpha\rangle})$ for (a) the localized regime with W=10 and (b) the ergodic regime with W=2.5 for states $|\alpha\rangle$ in the middle of the band. Data obtained with L=12 and N=1000. The corresponding probability distribution of P_i and Q_i for (c) the localized regime in which the single spin measurement with and without a quench coincides with each other and for the (d) ergodic regime the disparity in the distribution with and without the quench indicates a thermalization.

site i' = 0 is turned on. These quantities are given by

$$P_{\alpha_0}^i = \langle \alpha_0 | \sigma_z^{(i)} | \alpha_0 \rangle, \tag{5.9a}$$

$$Q_{\alpha_0}^i = \sum_{\tilde{\alpha}} |\langle \alpha_0 | \tilde{\alpha} \rangle|^2 \langle \tilde{\alpha} | \sigma_z^{(i)} | \tilde{\alpha} \rangle = \text{Tr} \left\{ \bar{\rho}_{\text{DE}}^{|\alpha_0\rangle} \sigma_z^{(i)} \right\}.$$
 (5.9b)

Running over all eigenstates $|\alpha_0\rangle$ in the $S_z=0$ sector, we collect $P_{\alpha_0}^i$ and $Q_{\alpha_0}^i$ for a number of disorder realizations. In Figure (5.7), we present the scatter plot for pairs of $(P_{\alpha_0}^i, Q_{\alpha_0}^i)$ of spin i=0 (directly perturbed spin) and i=L/2-1 (the farthest spin from the local perturbation) in the middle of the band, $\alpha_0 \simeq N(L,0)/2$ for weak (W=2.5) and strong (W=10) disorder. In the localized phase at strong disorder, the eigenstates are product states consisting of physical spins $|\alpha\rangle = \bigotimes_i |\downarrow (\uparrow)\rangle_i$ and therefore the local spin

projection is good quantum number $P_{\alpha_0}^i \simeq \pm 1$.

In this sense, all eigenstates are interchangeable by disorder realizations, and thereby all states are localized at infinite temperature. Provided that the quench intensity f is small compared to the local onsite field, the eigenstate of the quenched Hamiltonian is perturbed to the order of $\mathcal{O}(f/W)$, resulting in an almost unchanged eigenstate with $Q_{|\psi\rangle} \simeq \pm 1$. On the scatter plot, each pair of $(P^i_{|\alpha\rangle}, Q^i_{|\alpha\rangle})$ is distributed along the line $P^i_{|\alpha\rangle} = Q^i_{|\alpha\rangle}$, indicating the two measurements being strongly correlated. In the delocalized regime at weak disorder (W=2.5), the eigenstate is a linear combination of a large number of product states, and therefore local spin projection is not good quantum number. The result of two sets of measurement form a elliptic cloud. This observation is an indicator of thermalization: upon thermalization, the distribution of single spin measurement for all possible spin configurations is centered at P(Q)=0 and narrowed down because the memory of the initial condition is lost. In Figure , we plot the distribution of P and Q for the both strong and weak disorders. Remarkably, the distributions are almost indistinguishable for W=10 and the contrast between the distribution in the ergodic regime W=2.5 is apparent due to the re-equilibration of the system after the local quench.

The correlation between $P_{|\psi\rangle}$ and $Q_{|\psi\rangle}$ can be characterized by the covariance: $C^i_{|\alpha\rangle} = \overline{(P^i_{|\alpha\rangle} - \overline{P^i_{|\alpha\rangle}}) \cdot (Q^i_{|\alpha\rangle} - \overline{Q^i_{|\alpha\rangle}})} = \overline{P^i_{|\alpha\rangle}Q^i_{|\alpha\rangle}}$, where $Q^i_{|\alpha\rangle}$ and $Q^i_{|\alpha\rangle}$ are averaged to zero with respect to disorder realizations. As an indicator of ergodicity breaking, the covariance is used to mapped out the phase diagram as a function W and ϵ , as shown in Figure 5.8. In the ergodic regime the averaged value \overline{C} approaches to 0 and eventually saturates to 1 deep in the localized regime where both Q and P takes the same value ± 1 . Similar to the IPR, this measure C can reveal the many-body mobility edge, marked in white.

With decreasing the spatial separation between the quenched spin and the monitored spin, we observe a larger deviation from the ideal case $P^i_{|\alpha\rangle} = Q^i_{|\alpha\rangle}$ because the quenched spin can be thermalized locally. At meanwhile, in the ergodic regime, the distribution of $(P^i_{|\alpha\rangle}, Q^i_{|\alpha\rangle})$ is insensitive to the spatial separations between quenched spin and monitored spin, suggesting that the response to the quench is uniform along the system. Indeed, the

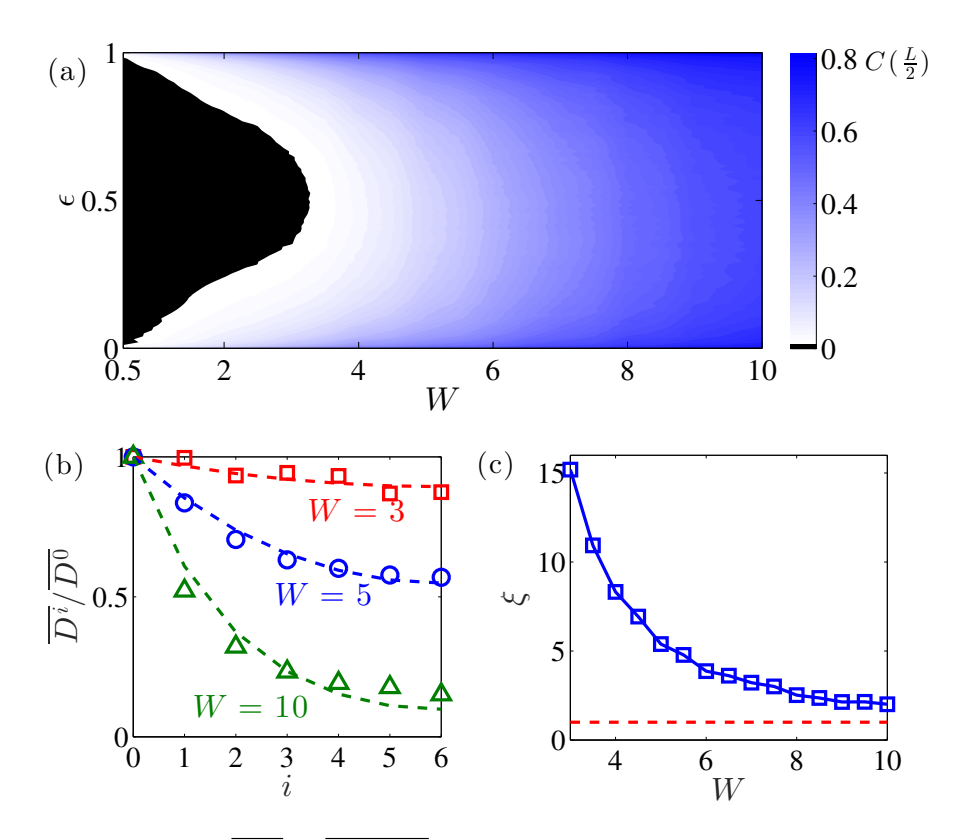


Figure 5.8: (a) Measure $\overline{C^i_{|\alpha\rangle}} = \overline{P^i_{|\alpha\rangle}Q^i_{|\alpha\rangle}}$ as functions of disorder strength W and energy density ϵ for L=12 and N=1000. The many-body mobility edge is marked in white. (b) "Euclidean distance" D^i as a function of distance between monitored spin and quenched spin (solid lines), and the corresponding fitting curve, Eq. (5.11) (dashed lines). (c) The many-body localization length ξ extracted from $D^{(i)}$ as a function of disorder strength. The dashed line corresponds to the $\xi=1$ to show that the at sufficiently strong disorder the system is localized in the atomic limit.

ensemble $P^i_{|\alpha\rangle}$ and $Q^i_{|\alpha\rangle}$) with respect to disorder realizations can be used to evaluate the many-body localization length. Intuitively the localization length is a scale below which spin texture form localized clusters and thereby the ergodicity is broken. Essentially deep in the localized regime, localization occurs in the atomic limit with localization length $\xi = 1$. With decreasing disorder, the localization length grows and once the scale is beyond the system size, the entire system cannot be decomposed into independent clusters and the ergodicity reoccurs. Therefore, the localization length is an indicator of the onset of MBL regime that can be determined by the spatial sensitivity of the response to the local quench. The deviation between the measurement $P^i_{|\alpha\rangle}$ and $Q^i_{|\alpha\rangle}$ averaged over disorder realizations

is given by "Euclidean distance":

$$D_{|\alpha\rangle}^{i} = \sqrt{\overline{(P_{|\alpha\rangle}^{i} - Q_{|\alpha\rangle}^{i})^{2}}}.$$
 (5.10)

We argue that in the localized regime $D^i_{|\alpha\rangle}$ is an exponentially decaying function with respect to the distance between spin i to the quenched spin:

$$\overline{D_{|\alpha\rangle}^{i}}/\overline{D_{|\alpha\rangle}^{0}} = e^{-i/\xi} + e^{-|L-i|/\xi} - e^{-L/\xi}, \tag{5.11}$$

where ξ is the localization length. The first two exponential terms in Eq. (5.11) arise from the periodic boundary condition, and the second term is a normalization constant. Therefore, we fit the undetermined parameter ξ for each disorder strength and for all spin indices i in $D^i_{|\alpha\rangle}$. In Figure 5.8(b) we present the ratio $\overline{D^i}/\overline{D^0}$ as a function of spatial separation i for several different disorder strengths W=3,5,10 in the middle of the band. In Figure 5.8(c), we illustrate the extracted localization length ξ from the scaling form of D^i . Due to the finite size of the system, at the critical disorder $W_c \simeq 3.3$ the localization length ξ does not diverge but remains a finite value larger than the system size, consistent with our argument above. On the other hand, ξ saturates to 1 deep in the localization regime, indicating that the localization effect occurs at atomic limit.

5.5 Summary

To summarize, we showed that as a result of local quench, the absence of thermalization can be characterized by the inverse participation ratio of the eigenstates of the quenched Hamiltonian into the unquenched eigenbasis in a many-body localized system. In particular, the IPR has critical fluctuations at the transition with disorder realizations in the thermodynamic limit and becomes more robust deep in both phases. Meanwhile, our analysis of the single spin measurements in the presence of quench provides a concrete example to perform experiment for better understanding of many-body localization length. In this scenario, performing measurements of z component of physical spins, other than more complicated measurement of many-particle entanglement or pseudo-spins is sufficient, even for

a quantum system with short T_2 , as long as the relaxation time T_1 is long enough such that the diagonal ensemble is a good approximation of transient quantum state, a regime where quantum simulation of many-body system is currently accessible. Our analysis demonstrated that for a realistic system that supports many-body localization, simple single spin measurement can reveal the indispensable characteristics, complementary to more sophisticated routes to check the growth of entanglement entropy [156, 157] or quantum revivals [170] under time revolution.

Chapter 6

Many-body localization in a quantum system subject to a local periodic drive

6.1 Introduction

In practice, one simplest scenario to study the dynamics of a quantum system is to apply a local harmonic drive to one of the spins. At long times after the drive is turned on, states that obey/disobey ETH would predict different expectation values for observables, whereas the former is insensitive to the specifics of the initial state and coincides with the prophecy of a thermal state at infinite temperature. This leads us to propose the description of the thermodynamics in terms of the time-averaged state, not of thermal ensembles.

The purpose of this chapter is to continue our discussion about the dynamical aspects of a MBL system, with an experimental accessible method to observe MBL phases by using a local harmonic drive on one of the spin. The Hamiltonian we consider is the following:

$$H = H_0 + f[\cos(\omega t)\sigma_x^{(1)} + \sin(\omega t)\sigma_y^{(1)}], \tag{6.1}$$

where f is the amplitude of the external drive and H_0 is the static MBL Hamiltonian.

Besides, one by-product of the formalism is that one can construct the long-time averaged density matrix using the Floquet basis. On one hand, such density matrix can be used to calculate the thermodynamic quantities that distinguish the two phases; on the other hand, by examining of the thermodynamic quantities with different initial conditions we conjecture there is a mobility edge in the spectrum of the static static Hamiltonian beyond which the states doe not obey ETH even for a less disordered Hamiltonian. The origin of such mobility edge is due to the finite size of the system and disappears in the thermodynamic limit.

The chapter is structure as follows: We first derive a formalism that can be used to analyze the AC driving scenario for the model, 6.1, within Floquet theory. In particular, we study the response of the quantum system by evaluating the average quantum infidelity between the evolution of the system with and without an AC drive. Next, we use the formalism to evaluate the thermodynamic characteristics at long times, which can reveal the validity or breakdown of ETH in different phases.

6.2 Evolution in the Floquet Representation

Now we analyze the response of a quantum system Eq. (5.2) in the presence of a harmonic drive, Eq. (6.1) with period $\tau = 2\pi/\omega$. For a periodic drive, the evolution operator $U(t = n\tau)$ after n periods can be represented as the nth power of the Floquet operator $U_f(\tau)$ per one period τ : $U(t = n\tau) = U_f^n$. The Floquet operator is unitary and has a set of eigenvectors, that form a Floquet basis:

$$U_f|\alpha\rangle = e^{-i\Omega_\alpha t}|\alpha\rangle,\tag{6.2}$$

where we use greek indices to numerate Floquet basis, $\alpha = 1, \dots, 2^L$, and Ω_{α} are quasienergies. After n periods of the drive, the system evolves from its initial state $|\psi_0\rangle$ to the state

$$|\psi(n\tau)\rangle = U_f^n |\psi_0\rangle, \quad U_f = e^{-i\Omega_\alpha t} |\alpha\rangle\langle\alpha|$$
 (6.3)

with U_f written in the Floquet basis.

To evaluate the Floquet operator, we notice that the transformation

$$U_1(t) = \exp\left(-\frac{i\omega t}{2} \sum_{l=1}^{L} \sigma_z^{(l)}\right)$$
(6.4)

removes explicit time-dependence in the full Hamiltonian of the system, Eq. (6.1):

$$\tilde{H} = U_1 H U_1^{\dagger} - i U_1 \dot{U}_1^{\dagger} = \tilde{H}_0 + \frac{f}{2} \sigma_x^{(1)}, \quad \tilde{H}_0 = H_0 - \sum_l \frac{\omega}{2} \sigma_z^{(l)}.$$
 (6.5)

After this transformation, the Floquet operator can be defined as an exponent of timeindependent Hermitian operator

$$U_f = \exp(-i\tilde{H}\tau)U_1(\tau), \tag{6.6}$$

where $U_1(\tau) = (-1)^L \mathbb{1}$, and $\mathbb{1}$ is the identity matrix. Using Eq. (6.6), we find that the Floquet basis is simply given by the eigenstates of the transformed Hamiltonian (6.5), $H_F = \tilde{H}$.

The effect of a harmonic drive on a state of the system can be defined the displacement of this state $|\psi_f(\tau)\rangle$ after one period of the drive from the free evolution over the period τ of the same state $|\psi_0(\tau)\rangle$. For an arbitrary initial state $|\psi_i\rangle$, the state after one period is $|\psi_f(\tau)\rangle = U_f|\psi_i\rangle$ for a harmonic drive with amplitude f, and $|\psi_0(\tau)\rangle = U_0|\psi_i\rangle$, where $U_0 = U_{f\to 0} = \exp(-iH_0\tau)$. The corresponding distance between the two states in the Fubini-Study metric is simply determined by the overlap of these two states:

$$F_{\psi_i} = |\langle \psi_0(\tau) | \psi_f(\tau) \rangle|^2 = |\langle \psi_i | \mathcal{U} | \psi_i \rangle|^2, \tag{6.7}$$

where we introduced a unitary operator

$$\mathcal{U} = U_0^{\dagger} U_f \tag{6.8}$$

representing a mismatch between the evolution of the system with and without drive.

We characterize a typical response of an arbitrary state to the drive over a single period in terms of the uniform average over initial states $|\psi_i\rangle$ of the overlap F_{ψ_i} . The corresponding average, known as a quantum fidelity between two unitary operations, is completely defined in terms of operator \mathcal{U} as [171]

$$\bar{F} = \frac{M + |\operatorname{Tr}\{\mathcal{U}\}|^2}{M(M+1)} \tag{6.9}$$

and $M = 2^L$ is the dimensionality of the Hilbert space.

The matrix element of \mathcal{U} taken between the energy eigenstate $|i\rangle$ of the static Hamiltonian H_0 and the Floquet state $|\alpha\rangle$ has the form

$$\langle i|\mathcal{U}|\alpha\rangle = A_i^{\alpha} \exp(-i(\Omega_{\alpha} - E_i)\tau), \quad A_i^{\alpha} = \langle i|\alpha\rangle,$$
 (6.10)

where A_i^{α} is the overlap amplitudes between energy eigenstates of the static Hamiltonian and the Floquet states. This relation leads to the matrix elements of \mathcal{U} in the energy eigenstate basis of H_0 :

$$\mathcal{U}_{ij} = \langle i|\mathcal{U}|j\rangle = \sum_{\alpha} \exp(-i(\Omega_{\alpha} - E_i)\tau)(A_i^{\alpha})^* A_j^{\alpha}.$$
 (6.11)

According to this equation, the evolution of the system reduces to a search of the components A_i^{α} of the Floquet states in the basis of the static Hamiltonian, and the corresponding eigenenergies and quasi energies. Below we present numerical evaluation of these matrix elements and argue that the statistical properties A_i^{α} change across the many body localization transition. We also show later in this chapter that in the long time limit, the Floquet amplitudes define thermodynamic characteristics of the system such as absorbed energy and the change in entropy and, consequently, these characteristics also change across the transition.

For quantitative analysis of the effect of the drive on the system, we consider a Hermitian matrix

$$\mathcal{T} = i\frac{1-\mathcal{U}}{1+\mathcal{U}} \tag{6.12}$$

instead of the unitary matrix \mathcal{U} . A simple choice of the norm as $\propto \text{Tr} \{\mathcal{T}^2\}$ can be interpreted as the power of the drive applied to the system. This is especially meaningful in the limit of weak drive when \mathcal{T} is linear in the drive amplitude f. In its eigenvector basis, operator \mathcal{U} is presented by a diagonal matrix with elements $e^{i\delta_a}$ $(a=1,\ldots,M)$ and \mathcal{T} is also diagonal with diagonal elements $[\mathcal{T}]_{aa} = \tan(\delta/2)$. The norm of \mathcal{T} is

$$\operatorname{Tr}\left\{\mathcal{T}^{2}\right\} = \sum_{a=1}^{M} \tan^{2} \frac{\delta_{a}}{2} \tag{6.13}$$

and Tr $\{\mathcal{T}^2\} \to \infty$ when one of the scattering phases reaches the unitary limit, $\delta_a = \pi$, so that corresponding eigenvector $|a\rangle$ of \mathcal{U} completely flips just after a single period of the drive, $\mathcal{U}|a\rangle = -|a\rangle$. This strong effect of the system states does not necessarily reduce fidelity \bar{F} , however, the system rearrangement over energy states $|i\rangle$ of the stationary Hamiltonian H_0 per cycle of the drive becomes significant if $\langle i|a\rangle \neq 0$ for many states $|i\rangle$.

Utilizing Eq. (6.10) and (6.12), we can write the system of linear equations for the Floquet amplitudes A_i^{α} :

$$\sum_{i} \langle i | \frac{\tan((\Omega_{\alpha} - E_i)\tau/2) + \mathcal{T}}{1 - i\mathcal{T}} | j \rangle A_j^{\alpha} = 0.$$
 (6.14)

This equation can be reduced to a hopping problem[172] of a particle with on-site energy $\tan((\Omega_{\alpha} - E_i)\tau/2)$ and hopping amplitude \mathcal{T} between sites in the Hilbert space:

$$\left[\tan\frac{(\Omega_{\alpha} - E_i)\tau}{2} + \mathcal{T}\right] |\chi_{\alpha}\rangle = 0, \tag{6.15}$$

where $|\chi_{\alpha}\rangle = \sum_{j} (1 - i\mathcal{T})^{-1} |j\rangle A_{j}^{\alpha}$ is an eigenstate at zero energy existing for a set of quasienergies Ω_{α} of the Floquet operator U_{f} . Equation (6.14) is in particular useful in the limit of weak drive when it establishes a simple relation between the Floquet amplitudes A_{i}^{α} and hopping amplitudes \mathcal{T}_{ij} .

6.3 Relation between Floquet amplitudes and hopping matrix

In this subsection, we consider in detail the limit of weak external drive, taking into account only the linear in drive amplitude f terms in the hopping matrix \mathcal{T} and the unitary matrix \mathcal{U} . First, we expand the operator \mathcal{U} , defined by Eq. (6.8), to the lowest order in f, and obtain the following expression for the hopping matrix:

$$\mathcal{T} = -\frac{if\tau}{2} \times \left(\sigma_x^{(1)} + i\tau[\tilde{H}_0, \sigma_x^{(1)}] + \frac{(i\tau)^2}{2!} [\tilde{H}_0, [\tilde{H}_0, \sigma_x^{(1)}]] + \dots\right).$$
(6.16)

This expression indicates that the matrix elements of \mathcal{T}_{ij} can be easily written in the eigenstate basis of Hamiltonian \tilde{H}_0 in terms of $\langle i|\sigma_x^{(1)}|j\rangle$. Here we present an alternative derivation of \mathcal{T}_{ij} . We notice that for f=0, the Floquet states $|\alpha\rangle$ and eigenvectors of stationary Hamiltonian \tilde{H}_0 as well as quasienergies Ω_{α} and energies \tilde{E}_i coincide,

$$\langle i | \alpha_{f=0} \rangle = \delta_{i\alpha}, \quad \Omega_{\alpha} = \tilde{E}_{\alpha} \pmod{2\pi/\tau}.$$
 (6.17)

We consider Eq. (6.14) up to the first order in \mathcal{T} and apply Eq. (6.17) to find a relation between off diagonal elements of matrices $A_i^{j\neq i}$ and \mathcal{T}_{ji} written in the eigenstate basis:

$$\mathcal{T}_{ij} = iA_i^{\alpha \to j} \sin \frac{\pi(\tilde{E}_i - \tilde{E}_j)}{\omega} e^{i\pi(\tilde{E}_i - \tilde{E}_j)/\omega}.$$
 (6.18)

To the lowest order in f, overlap between Floquet states and eigenstates of \tilde{H}_0 can be evaluated from the first order perturbation theory as $A_{i\neq j}^{\alpha\to j}=(f/2)\langle i|\sigma_x^{(1)}|j\rangle/(\tilde{E}_i-\tilde{E}_j)$. Note that while the difference between eigenenergies E_i of H_0 and \tilde{E}_i of \tilde{H}_0 is not important in Eq. (6.18), this difference is important in the denominator of $A_{i\neq j}^{\alpha\to j}$, that represents transition between states with different values of total spin along the z-axis, due to absorption or emission of energy $\hbar\omega$. We obtain the following expression for matrix elements of the hopping matrix in the basis of eigenstates of H_0 that coincides with eigenstates of \tilde{H}_0 :

$$\mathcal{T}_{ij} = \frac{f}{2} \frac{\langle i | \sigma_x^{(1)} | j \rangle}{\tilde{E}_i - \tilde{E}_j} \sin \frac{\pi (\tilde{E}_i - \tilde{E}_j)}{\omega} e^{i\pi (\tilde{E}_i - \tilde{E}_j)/\omega}. \tag{6.19}$$

At weak drive, $\mathcal{U} = 1 + 2i\mathcal{T} - 2\mathcal{T}^2 + \dots$ and we obtain an expression for the average fidelity

$$\bar{F} = \frac{M + M^2 - 4M \text{Tr} \mathcal{T}^2}{M(M+1)} \simeq 1 - 4p, \quad p = \frac{\text{Tr} \{\mathcal{T}^2\}}{M+1},$$
 (6.20)

and the average displacement of the states per period of the drive, or infidelity, is proportional to the dimensionless power p of the drive, $1 - \bar{F} = 4p$, provided that $p \ll 1$. In the above expression we disregarded terms that contain $(\text{Tr}\{\mathcal{T}\})^2$ since $\text{Tr}\{\mathcal{T}\}$ vanishes to the linear order in f, cf. Eq. (6.18)

We apply Eq. (6.18) to argue that the infidelity $1 - \bar{F}$ is a universal, M-independent measure of the effect of a harmonic drive on the system in either ergodic or MBL regimes.

We write

$$p \le \frac{1}{M} \sum_{i} \sum_{\alpha \ne i} |A_i^{\alpha}|^2 = \frac{\sum_{i} P_{\text{esc}}^{(i)}}{M} = \overline{P_{\text{esc}}^{(i)}}, \tag{6.21}$$

where $\overline{P_{\rm esc}^{(i)}}$ is the escape probability $P_{\rm esc}^{(i)} = 1 - |A_i^i|^2$ of the system from initial state $|i\rangle$ at long drive time, averaged over states $|i\rangle$.

We can provide more accurate estimate of infidelity $\bar{\epsilon}$ by applying Eq. (6.19):

$$p \simeq \frac{\pi^2 f^2}{4\omega^2 M} \sum_{i \neq j} \frac{\sin^2(\pi (E_i - E_j)/\omega)}{[\pi (\tilde{E}_i - \tilde{E}_j)/\omega]^2} \left| \langle i | \sigma_x^{(1)} | j \rangle \right|^2. \tag{6.22}$$

First, we evaluate the average value of p over realizations of the random magnetic field for ergodic regime of weak disorder $W \lesssim J$. At frequencies of the drive exceeding the mean level spacing, $\omega \gtrsim \overline{(E_i - E_j)}$, we omit the energy dependent factor and estimate \overline{p} as

$$\overline{p} \propto \frac{\pi^2 f^2}{4\omega^2}.\tag{6.23}$$

Here we assumed that a typical matrix element for $i \neq j$ can be estimated as

$$\sum_{i \neq j} \left| \langle i | \sigma_x^{(1)} | j \rangle \right|^2 \simeq \sum_{i,j} \left| \langle i | \sigma_x^{(1)} | j \rangle \right|^2 = M. \tag{6.24}$$

In the limit of strong disorder, the distribution of p is more complicated. As we demonstrate below from numerical analysis, the distribution becomes extremely wide and its average value actually looses its meaning. More meaningful is the distribution of the logarithm of p, $\lg(p)$. The logarithmic distribution is a common characteristic of strongly disordered, glassy systems that exhibit a wide hierarchy of scales. In our case, the broad distribution is formed due to rival realizations of the random magnetic field. For some realizations the spin states are strongly localized and effectively decoupled from the rest of the system, for other realizations the system develops a resonance between spins in the chain and may result in the dimensionless power exceeding the average power in the ergodic regime, cf. Eq. (6.23).

The contribution from configurations representing localized spins dominates for average value of $\lg(p)$, and results in monotonically decreasing value of ensemble averaged $\overline{\lg(p)}$. For localized states in case when the local magnetic field for a driven spin is strong, $|h_1| \gg J$, the eigenstates $|i\rangle$ are factorized and we can reduce the evaluation of p in Eq. (6.22) as

$$p \simeq \frac{f^2}{4M} \frac{M}{2} \frac{\sin^2(\pi h_1/\omega)}{h_1^2} \left| \langle \downarrow | \sigma_x^{(1)} | \uparrow \rangle \right|^2. \tag{6.25}$$

Assuming that the localized configurations give the main contribution to $\overline{\lg(p)}$, we integrate $\lg(p)$ given by Eq. (6.25) over uniformly distributed h_1 and obtain

$$\overline{\lg(p)} \propto -2\lg \frac{W}{J}.\tag{6.26}$$

We note that our estimates for p in the limit of weak or strong disorder are independent on the dimensionality of the $M = 2^L$, see Eqs. (6.23) and (6.25).

6.4 Statistical properties of the hopping matrix

In this section, we numerically evaluate statistical properties of the strength $p \propto \text{Tr} \{\mathcal{T}^2\}$ of the hopping matrix. We evaluate matrix \mathcal{T} directly from Eq. (6.12), by computing the matrix exponents for evolution matrices U_0 and U_f , and therefore, our computation is not restricted to the weak drive limit considered in the previous section. For $f \ll J$, we obtained the bilinear response of $p \propto f^2$ and recover all relations between the Floquet amplitudes A_i^{α} , quasienergies and matrix elements of $\sigma_x^{(1)}$ between unperturbed eigenstates of H_0 that we discussed in the previous section. We also observed that the bilinear regime is satisfied for average value of p or $\lg(p)$ for $f \lesssim J$, and chose $f = J/\sqrt{10}$ for analysis of p at different values of disorder strength W. This choice of f allows us to compare some conclusions from the previous section with the numerical results, and at the same time demonstrates that the properties of p remain similar at moderate drive amplitudes, $f \simeq J$. At stronger drive, multi photon processes become important and their analysis deserve a separate discussion.

First, we study the probability distributions of P(p) of the drive strength p over ensemble realizations of the random field $\{h_i\}$ defined by a constant distribution of local fields within the interval $|h_i| \leq W$. Because our numerical analysis required evolution of matrix exponent and inverting matrices, to reach a large number of realizations $N = 10^4$, we took the system size L = 10. We present the normalized histogram in the top panel of Figure 6.1 for weak and moderate strength of disorder. As the strength of disorder increases, the distribution broadens and shifts to smaller values of p. However, while more realizations have smaller value of p, there are some realizations at moderate disorder that exhibit p

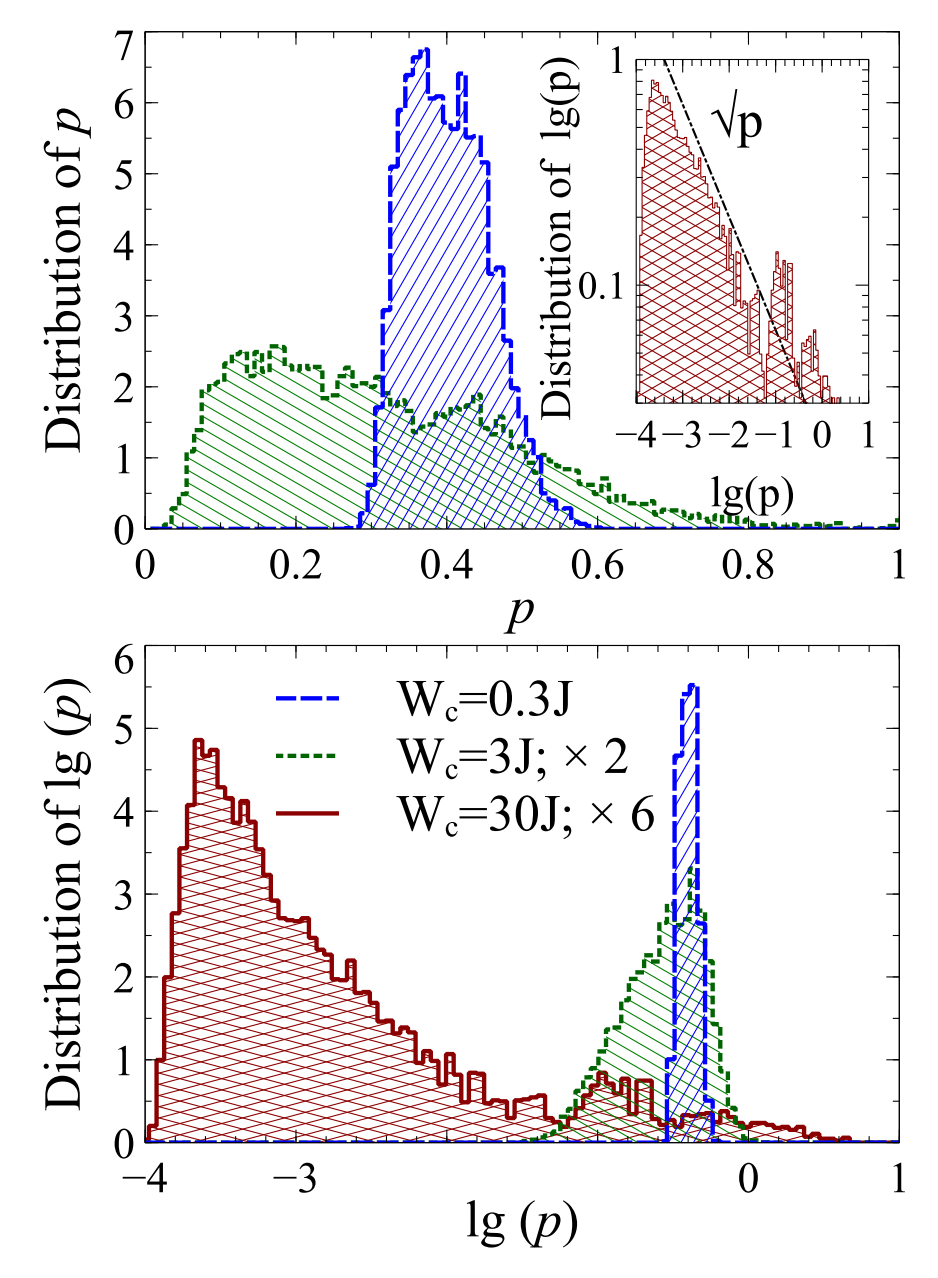


Figure 6.1: Distribution of dimensionless power p, Eq. (6.20), over $N=10^4$ realizations of the random magnetic field $\{h_i\}$ for a system with L=10 spins. The top panel shows the distribution of the power itself for W/J=0.3 (blue long-dashed line) and W/J=3 (green short-dashed line), while the bottom panel shows the distribution of $\lg p$ for all three values of disorder for three values of the disorder strength W/J=0.3, 3 and 30 (red solid line). We scaled the distribution curves for W/J=3 by factor two and for W/J=30 by factor six. The inset shows the logarithm of the distribution of $\lg p$ for W/J=30 and the dash-dotted line represents the slop $\sim p^{-1/2}$. The drive amplitude $f=J/\sqrt{10}$ and $\omega=J$.

exceeding maximal values of p in weakly disordered system, see the tail to the right in the top panel of Figure 6.1. This behavior becomes even more pronounced at strong disorder, W = 30J, when the distribution collapses to extremely small values of p, but its tail extends to larger values of p than the values found for weak and moderate disorder.

We characterize the distribution in the strong disorder limit by $\lg(p)$. In such logarithmic presentation, we can compare all three cases of weak, moderate and strong disorder on the same plot, as shown in the bottom panel of Figure 6.1. At strong disorder, distribution of $\lg(p)$ shows that in most realizations, the drive power p is significantly reduced below its values for the ergodic regime. at the same time, we find the tail that extends to larger values of p, which are not realized at weaker disorder. In these rear events, p > 1 and our bilinear analysis is not applicable, in particular, relation (6.20) between the infidelity $1 - \bar{F}$ and the dimensionless power is no longer valid, even though p has no upper bound. For realizations with large values of p, the system exhibits occasional resonances between spins in the chain that lead to strong coupling of the drive to the spin system. In this case, the spin system subject to a drive strongly deviates from its free evolution.

We plot the logarithm of the distribution of $\lg(p)$ in the limit of strong disorder in the inset in Figure 6.1 and observe that the right slope is consistent with $\sim -(1/2)\lg(p)$. This behavior implies that the probability distribution function for p decays as a power law $\propto p^{-3/2}$, and we conclude that the distribution of p is Pareto type. Such slow power law decrease makes the cumulants ill-defined, including the expectation value, unless the power law terminates at larger p. According to Figure 6.1, the power law terminates at sufficiently large p, making the expectation value of p over disorder sensitive to the rare large realizations of p. This sensitivity to rear fluctuations of p does not allow us to numerically study average value of p at strong disorder, as even for a very large number of samples, $N \gtrsim 10^4$ for smaller systems, L = 6, the average value of p was not converging well.

To characterize the effect of disorder strength on the dimensionless power, we numerically evaluate $\overline{\lg(p)}$ that represents the expectation value of $\lg(p)$. The result is presented in Figure 6.2. We observe that $\overline{\lg(p)}$ does not strongly depend on the system size L, as points

for L=8, 10 and 12 are aligned along the same curve. At weak disorder, $\overline{\lg(p)}$ changes weakly with disorder strength, as demonstrated by the nearly flat values of $\overline{\lg(p)}$ for disorder strength corresponding to the ergodic regime with $W \lesssim 3J$. At stronger disorder, in the localization regime $W \gtrsim 3J$, $\overline{\lg(p)}$ decreases linearly in $\sim -2\lg(W/J)$, in agreement with estimate (6.26).

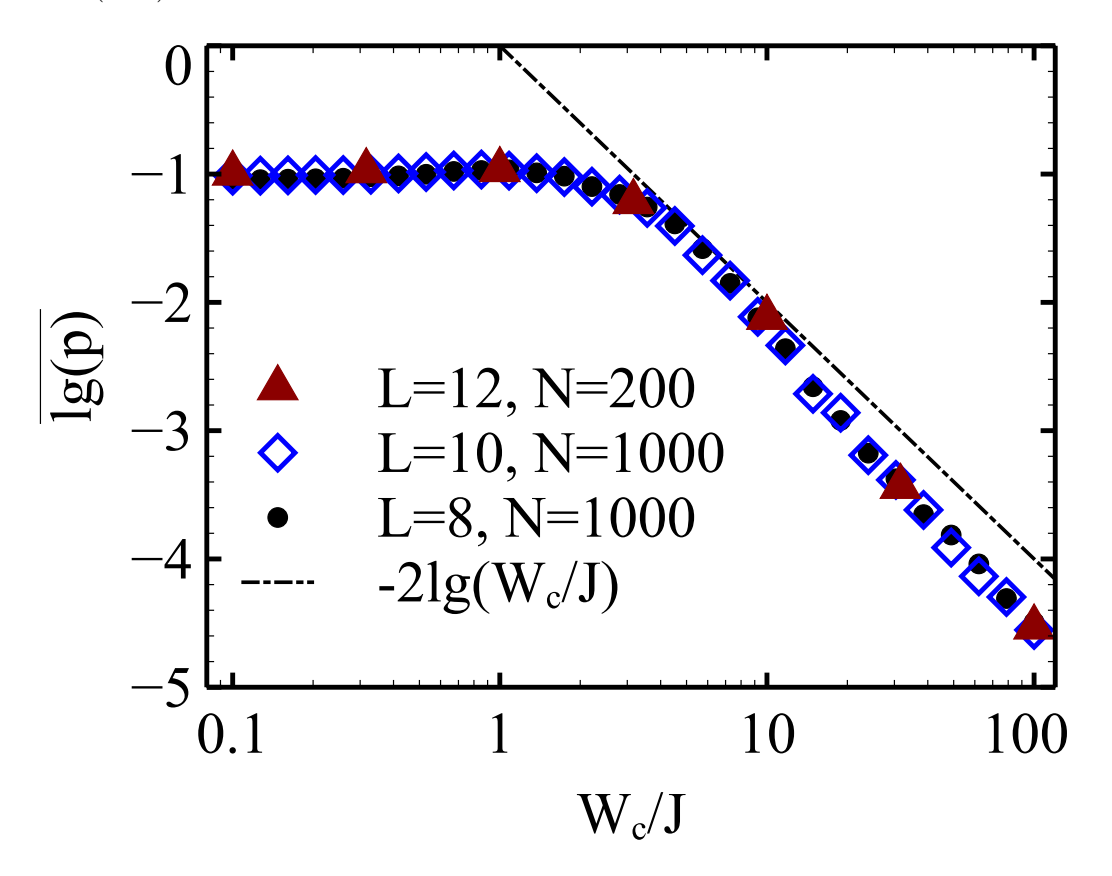


Figure 6.2: Average value of the logarithm of dimensionless power, $\lg(p)$, as a function of disorder strength W for a spin system of size L=8 (circles), L=10 (diamonds) and L=12 (triangles). The average is evaluated over $N=10^3$ samples for L=8, 10, and for N=200 for L=12. The drive amplitude $f=J/\sqrt{10}$ and $\omega=J$.

As shown in Refs.[162, 163], with extensive numerical simulations the phase diagram of delocalization/localization can be visualized by quantities of interests as functions of disorder strength W with energy resolutions; in particular, the many-body mobility edge can be understood as boundary between the two phases. This procedure can be applied to the numerical simulation of \mathcal{T}^2 as well, as shown in Figure 6.3. To be specific, we evaluate

 \mathcal{T}^2 for each disorder realization in the eigenbasis of H_0 with total $S_z=0$. These eigenstates are labeled from $\alpha=1\cdots I$, with $I=L!/(L/2)!^2$ the total number of states, according to the descendant order of their eigenvalues. After taking disorder average over $\lg \mathcal{T}^2$, we plot the result as functions of both W and the energy density ϵ defined by the corresponding label α/I . With energy resolution, we are able to map out the phase diagram of the system whereas the two phases are separated by the mobility edge. Recall that the matrix \mathcal{T} is interpreted as hopping amplitude between Floquet states to the static eigenstates; threfore, the frequency of the drive is chosen to be slow, $\omega=0.01J$ in order to prevent unwanted optical resonances. On the other hand, if the frequency is comparable to J, a localized state below the mobility edge could be in resonance with a delocalized state within the mobility edge, and this process will mix the two states. In this sense, if a great number of optical resonances occur when the frequency of drive is comparable to mean level spacings, the mobility edge looses its meaning and \mathcal{T}^2 will not be a function of ϵ any more.

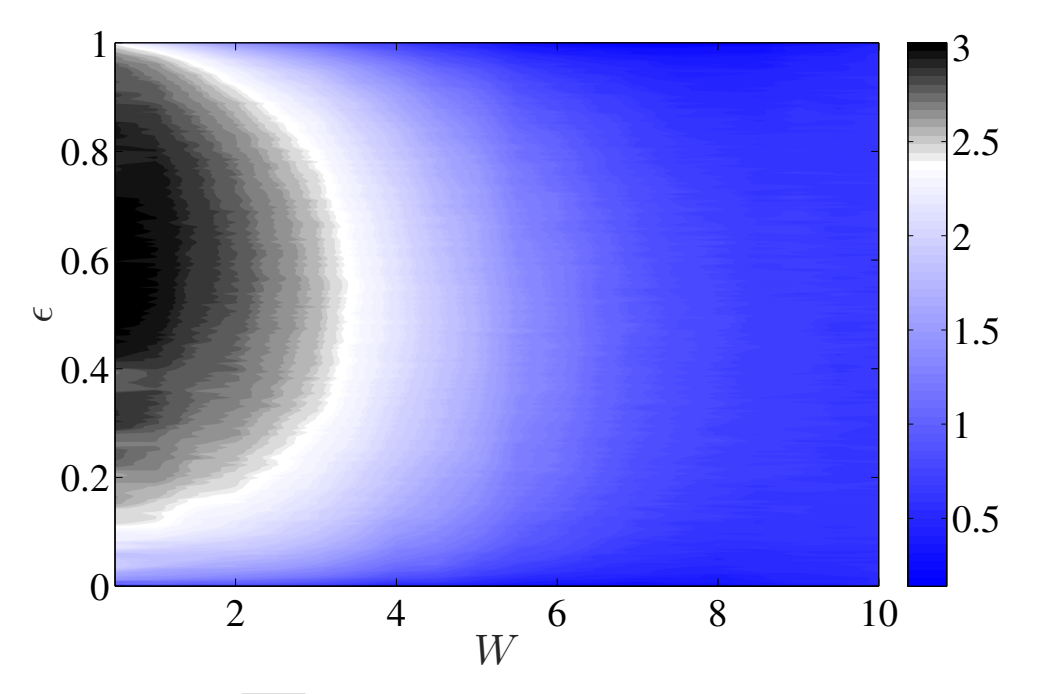


Figure 6.3: Measure $\overline{\lg \mathcal{T}^2}$ as functions of disorder strength W and energy density ϵ for L=10 and N=4000. The many-body mobility edge is marked in white.

6.5 Thermodynamic characteristics

Time evolution

A quantum state of the system (6.1) driven by a harmonic perturbation after n periods is defined by the unitary transformation of its initial state $|\psi_0\rangle$ given by Eq. (6.3). Using this expression for the state, we can evaluate a value of any observable M at time $t = n\tau$ as

$$\langle M(t_n) \rangle = \text{Tr} \{ M \rho_n \},$$
 (6.27)

where the stroboscopic density matrix operator with initial condition $|\psi_0\rangle$ is given by

$$\rho_n = \sum_{\alpha,\beta} e^{-i(\Omega_\alpha - \Omega_\beta)n\tau} |\alpha\rangle\langle\alpha|\psi_0\rangle\langle\psi_0|\beta\rangle\langle\beta|.$$
 (6.28)

For the purposes of practicality, one can study the time-average of an observable,

$$\langle \overline{M(t_n)} \rangle = \text{Tr} \{ M \overline{\rho} \}, \quad \overline{\rho}_{|\psi_0\rangle} = \sum_{\alpha} |\langle \alpha | \psi_0 \rangle|^2 |\alpha\rangle \langle \alpha |,$$
 (6.29)

where the off-diagonal elements of the density matrix are averaged out. If $|\psi_0\rangle = |\psi_i\rangle$ is an eigenstate of time-independent Hamiltonian, $|\langle \alpha | \psi_i \rangle|^2 = |A_i^{\alpha}|^2$ are the Floquet amplitudes defined in Eq. (6.10).

The fact that the time averaged density matrix is diagonal in the Floquet basis facilitates the calculations of time average values of observables, $\langle M(t_n) \rangle$, which can be treated as thermodynamic characteristics of the system, depending on the nature of the density matrix $\bar{\rho}$. Essentially, since the spectrum of the static Hamiltonian Given that ETH is valid in the ergodic regime, the density matrix $\bar{\rho}$ is a thermal state with some temperature T. Therefore the average values of the observables coincide with the thermal state at T. On the other hand, in the localized phase, deviations of these average values from that given by the thermal state can be viewed as a diagnosis of invalidity of ETH.

In the thermodynamic limit, the overall spectrum is universal. Therefore for delocalized regime, we expect that all the Floquet basis are equally distributed in the eigenstate basis, such that the coefficient $A_{i\alpha} \sim 1/\sqrt{N}$, and the IPR vanishes as IPR $\sim 1/N$. On the other hand, for the localized regime, each Floquet basis has a good one-to-one correspondence

with the eigenstate basis in the sense that after one period of driving, the wavefunction of the system is localized in the Hilbert space and hopping amplitudes to other eigenstates are exponentially small with space size. Therefore, we expect $A_{i\alpha} \simeq \delta_{i,\alpha}$, and the IPR is of order unity.

Energy Fluctuations

Next we consider the fluctuations of the energy absorbed/emitted by the system in the presence of the external drive at long times. Since the external drive can be seen as an energy source, provided that ETH is valid, the system would approach to a thermal state with infinite temperature, $\rho(T \to \infty) = \hat{1}/M$, regardless of the initial state.

The absorbed or emitted energy of the steady state is given by the difference $\text{Tr}(H\hat{\rho}(\infty))$ E_i , with energy of the initial state E_i . In general the width of the distribution in eigenstates are determined by whether the system is ergodic or localized. In particular, for our current setting with $f \gtrsim J$ the system saturates to a thermal state with infinite temperature. Therefore in the thermodynamic limit the width of the distribution in eigenstates is comparable to the bandwidth. To this end, we can introduce the following dimensionless quantity Q to make a fair comparison between different system size:

$$Q = \sqrt{\frac{var\left[\operatorname{Tr}(H\bar{\rho}_{|\psi_{i}\rangle} - E_{i}\right]}{var\left[\operatorname{Tr}(H\hat{\rho}(\beta \to 0)) - E_{i}\right]}}$$

$$= \sqrt{\frac{var\left[\operatorname{Tr}(H\bar{\rho}_{|\psi_{i}\rangle} - E_{i}\right]}{var\left[E_{i}\right]}}$$
(6.30)

$$= \sqrt{\frac{var\left[\text{Tr}(H\bar{\rho}_{|\psi_i\rangle} - E_i\right]}{var\left[E_i\right]}}$$
(6.31)

where $\hat{\rho}(\beta \rightarrow 0) = \hat{1}/N$ is the density matrix at infinite temperature, and var is the variance over index i. In Figure 6.4 we present the result of energy absorption, with different amplitudes of drive and system sizes. As a measure of overlap between themal state and density matrix at long times, the quantity Q decays exponentially in the localized regime, indicating that the system violates ETH.

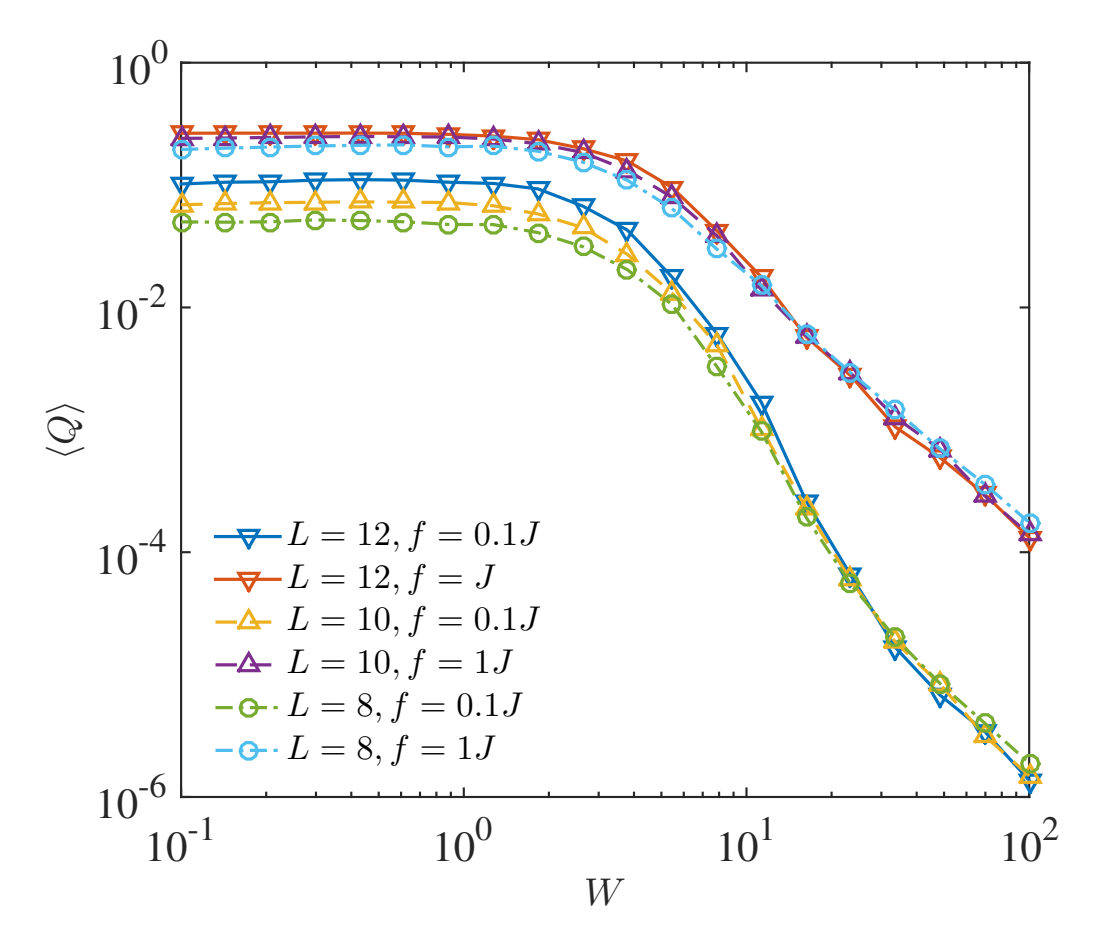


Figure 6.4: Average value of the normalized absorbed energy Q evaluated by using Eq. (6.39) as functions of the disorder strength W for a spin system of size L=8, L=10 and L=12. The average is evaluated over $N=10^4$ samples for L=8,10 and N=200 for L=12 and drive amplitudes are f=0.1J and f=J. The dependence of Q on W in the localized regimes suggests that an exponential small overlap between thermal state with infinite temperature and actual density matrix.

Spin Diffusion

Finally we evaluate the total spin projection in z direction, $S_z = \sum_i s_z^i$ by averaging over the initial eigenstates with $S_z = 0$. Since S_z is a good quantum number for the static Hamilonian while rotating field in xy plane would break the conservation of S_z , the wave function acquires components with nonzero S_z .

If the eigenstates are uniformly occupied for a thermal state with infinite temperature,

the expectation value of S_z^2 is

$$\overline{S_z^2} = \frac{1}{2^L} \sum_{n=0}^L \binom{L}{n} (L - 2n)^2 = L. \tag{6.32}$$

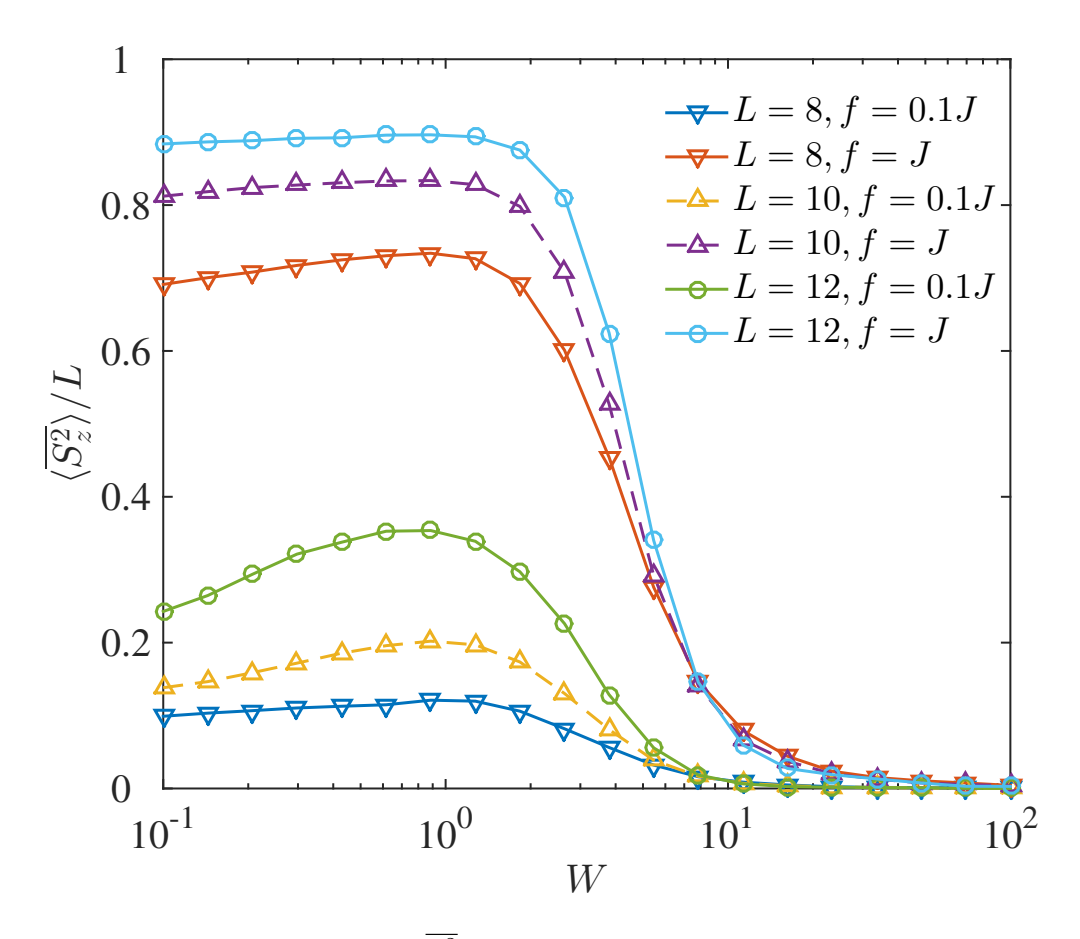


Figure 6.5: Expectation value of $\overline{S_z^2}$ as functions of disorder strength W for a spin system of size L=8,10 and 12. Parameters are the same as Figure 6.4

Even though through Sec.(6.3) we find there is still a good correspondence between Floquet basis and eigenbasis, averaging observables defined by the time-averaged density matrix over initial conditions chosen as all eigenstates is close to that of a thermal state with infinite temperature in the thermodynamic limit.

Therefore we calculate the following quantity

$$\overline{\langle S_z^2 \rangle} / L = \frac{1}{NL} \sum_{i=1}^N \text{Tr} \left(S_z^2 \bar{\rho}_{|\psi_i\rangle} \right), \tag{6.33}$$

where $\bar{\rho}_{|\psi_i\rangle}$ is the time-averaged density matrix with initial eigenstate $|\psi_i\rangle$ and N is the total number of eigenstates in the sector $S_z = 0$.

In Figure (6.5) we present the result of numerical calculation of $\overline{\langle S_z^2 \rangle}/L$ with two amplitudes of the drive. We see that in the ergodic regime, the expectation value of $\overline{\langle S_z^2 \rangle}/L \to 1$ in the long time limit. On the other hand, in the localized regime the wavefunction are localized and therefore the expectation value of S_z^2 remains zero.

Bures distance and inverse partition ratio

We characterize the deviation of the time average density matrix $\bar{\rho}_{|\psi_0\rangle}$ from the initial density matrix $\rho_0 = |\psi_0\rangle\langle\psi_0|$ using the Uhlmann fidelity[173]

$$F(\psi_0) = \left[\text{Tr} \left\{ \sqrt{\sqrt{\rho_0} \bar{\rho}_{|\psi_0\rangle} \sqrt{\rho_0}} \right\} \right]^2. \tag{6.34}$$

that defines the Bures angle between the two density matrices as $\theta_B = \arccos \sqrt{F(\psi_0)}$ [174]. In our case, the Bures angle can be viewed as a measure of displacement of time-averaged density matrix from its configuration before the onset of the drive. Due to a simple form of ρ_0 , we have

$$F(\psi_0) = \sum_{\alpha} |\langle \alpha | \psi_0 \rangle|^4, \quad F_i = \sum_{\alpha} |A_i^{\alpha}|^4.$$
 (6.35)

Below we consider only special cases when $|\psi_0\rangle$ is taken as one of eigenstates $|i\rangle$ of time-independent Hamiltonian, (5.2). In this case, the fidelity $F(\psi_i) = F_i$ is determined by the Floquet amplitudes, as shown by the second equation (6.35). After averaging over all eigenstates of time-independent Hamiltonian, we arrive to the expression for the inverse partition function, as defined in the previous chapter

$$IPR = \frac{1}{N} \sum_{\alpha, i} |A_{i\alpha}|^4, \tag{6.36}$$

where $|i\rangle$ is the set of eigenstates of static Hamiltonian.

However, in reality levels close to the band edges are not universal and contribute to finite size effects, which can be reduced by averaging the value of the IPR over all eigenstates. In Figure 6.6 we show the IPR as functions of the disorder strength W for different system

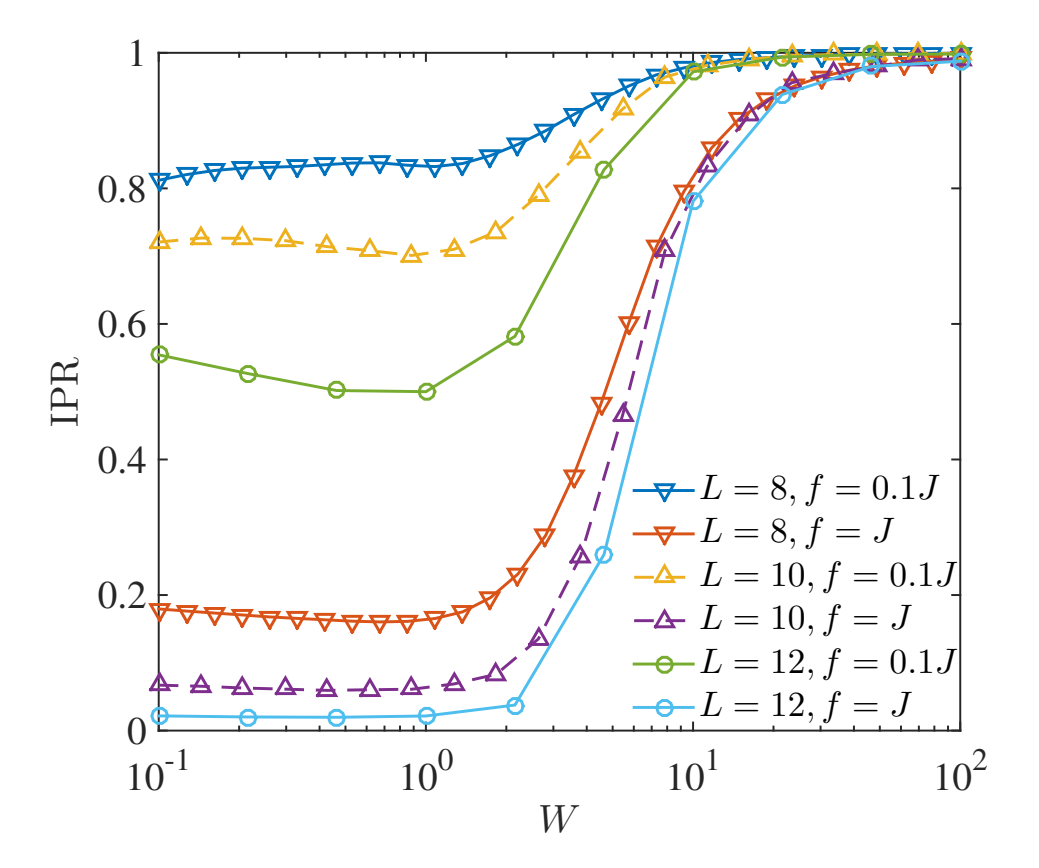


Figure 6.6: Average value of the IPR over all eigenstates defined in Eq.(40), as functions of disorder strength W for a system of size L=8, L=10 and L=12. Parameters are the same as Figure 6.4

size and drive amplitudes. Since the system saturates for $f \gtrsim J$, the case f = J is close to ideal estimation of IPR that increases from 1/N to unity. At weaker drive, the one-to-one correspondence between Floquet states and eigenstates is restored even in the ergodic regime, hence the IPR approaches to unity.

Finally, we notice that the inverse partition ratio also defines the change in the linear entropy of the system under the harmonic drive. For a pure state, the linear entropy is zero, but becomes positive for the time-average density matrix $\bar{\rho}_i$:

$$S_{\text{lin}}^{(i)} = 1 - \text{Tr}\left\{\bar{\rho}_i^2\right\}.$$
 (6.37)

We average this expression over all eigenstates $|i\rangle$ the time-independent Hamiltonian (5.2)

and obtain

$$\overline{S_{\text{lin}}} = 1 - IPR. \tag{6.38}$$

Von Neumann entropy

In this section we discuss the von Neumann entropy $S = \text{Tr} \{\rho \ln \rho\}$ of the time-average density matrix $\bar{\rho}_{|\psi_0\rangle}$ for initial state $|\psi_0\rangle$. Because $\bar{\rho}_{|\psi_0\rangle}$ is diagonal in the Floquet basis, the entropy is given by

$$S_{|\psi_0\rangle} = -\sum_{\alpha} |\langle \alpha | \psi_0 \rangle|^2 \ln(|\langle \alpha | \psi_0 \rangle|^2), \tag{6.39}$$

which is an observable.

The entropy reaches a maximum when an initial state $|\psi_0\rangle$ has equal overlap with all Floquet states, namely, $|\langle \alpha | \psi_0 \rangle|^2 \simeq 2^{-L}$. The value of maximal entropy is $S_{\text{max}} = L \ln(2)$. On the other hand, if for one value of α , we have $|\langle \alpha' | \psi_0 \rangle| = 1$ and $|\langle \alpha \neq \alpha' | \psi_0 \rangle| = 0$, the time averaged density matrix $\bar{\rho}_{|\psi_0\rangle}$ represents a pure state and $S_{|\psi_0\rangle} = 0$.

Of course, the above estimation is only valid in the thermodynamic limit where finite size effects are eliminated. However, as discussed before, eigenstates close to the band edge are not universal, therefore thermodynamic quantities obtained through these states are not good characterizations. Hence to avoid these states, we average the von Neumann entropy with respect to all eigenstates as initial conditions.

As demonstrated in Sec.6.5, the system starts to saturate at $f \gtrsim J$, a parameter regime where the entropy would reaches maximum value in the thermodynamic limit. In Figure 6.7 we present our calculation of the averaged von Neumann entropy for two chosen amplitudes of drive. In the ergodic regime, the entropy shows finite size scaling and we expect that for f = J the it approaches to $L \ln 2 \simeq 0.69L$ in the thermodynamic limit. The entropy smoothly drops to zero regardless of system size and drive amplitude.

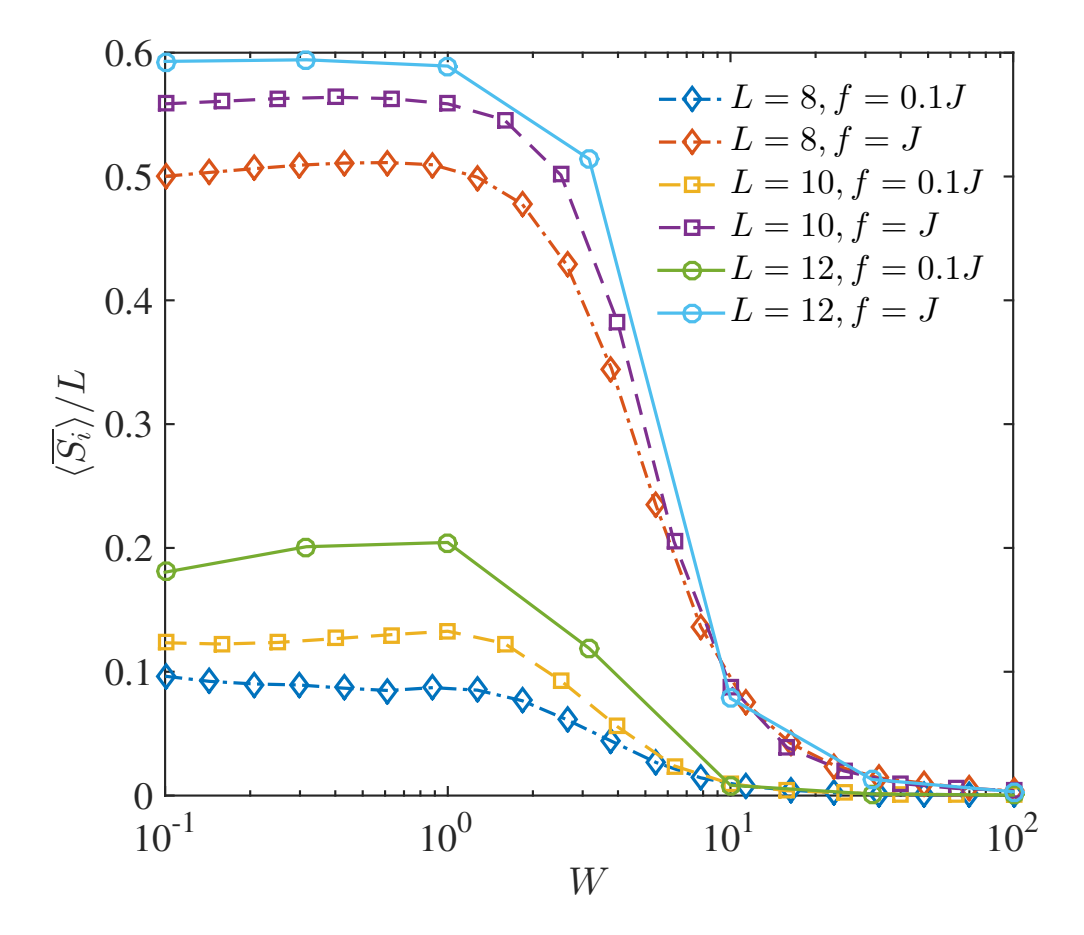


Figure 6.7: Averaged von Neumann entropy obtained by averaging over all eigenstates as initial conditions. At f = J we expect that the entropy approaches to $L \ln 2 \simeq 0.69L$ in the thermodynamic limit at weak disorder and drops to 0 at strong disorder. Parameters are the same as Figure 6.4.

6.6 Summary

In conclusion, we discussed spectral and dynamics of a quantum Heisenberg spin chain that is subject to a harmonic local drive. We have shown that, the many-body localization can be seen by the level spacings from the bulk of the static Hamiltonian. In the presence of the drive, a natural measure of the localized/ergodic phases is the quantum infidelity between evolution operator with and without the local drive. The distribution of the fidelity are qualitatively different in the two phases. For the ergodic regime the distribution of the infidelity is narrow and weakly depends on disorder, while for the localized regime the

distribution has an exponential small tail. It is surprising that the average value of the infidelity is independent of system size, indicating quantum simulation with $L\simeq 10$ spins would be sufficient to see the distinction between two phases.

In the thermodynamic point of view, the bulk part of the spectrum are expected to obey the ETH. For these states we have found that the average of observables approaches to that of a thermal state with infinite temperature in the thermodynamic limit.

Chapter 7

Conclusion

Over the course of this these, we have covered several different aspects of superconducting and semiconducting qubits, and presented several new and interesting results. In chapter 2, we discussed the quantum photovoltaic effects in a hybrid quantum system consist of a double quantum dot and a microwave resonator. In particular, we found that the spectrum of photovoltaic current exhibits multiple peak feature due to Rabi splitting determined by coupling strength and photon number, similar to the structure of a strongly coupled cQED. Furthermore, we explicitly showed where fundamental differences between classical and quantum photovoltaic effects arise from, in terms of various system parameters. Our analysis demonstrated that the Rabi splitting in the current spectrum is a consequence of entanglement between the DQD and the resonator.

In chapter 3, we have also looked at the similar DQD plus resonator system to determine the statistical properties of the emitted photons from a voltage biased DQD. While there had been evidences for lasing state in the presence of an external drive to the high Q microwave resonator, we have shown that interesting physics may appear when the drive is turned off. Specifically, we have shown that in contrast to the Poisson statistics for the coherent state, the noise of emitted photon arising from coherent charge transfer satisfies a sub-Poisson statistics when the energy relaxation rate of the DQD is much smaller than the dephasing rate. We have also shown that the statistics can be measured by a Josephson

photomulitiplier, which has been implemented experimentally.

In chapter 4, we have presented a detailed analysis of the dynamics of an open quantum system in the presence of a time-dependent control field. In principle, this approach can be applied to study the dynamics a spin one half in the presence of the Ohmic or non-Ohmic environment. We have shown that, the time-dependent parameters in the qubit Hamiltonian can be eliminated perturbatively by a series of digitalization procedures and under certain circumstances, this series is finite up to several orders. For the qubit dynamics in a rotating control field, there had been experimental studies suggesting robust quantization of Chern numbers at low temperatures with dissipative environments; our approach in parallel showed that this is the case, while Lindblad approach failed to predict the correct value at long times.

For the Landau-Zener problem, modifications of the matrix elements between eigenstates of the Hamiltonian was taken into account, because naturally in the Bloch-Redfield approach it is required to work in the eigenbasis of the qubit. In this basis, the fast oscillations between "spin up" or "spin down" is replaced by a fast monotonic behavior between ground and excited state. At zero temperature, the decay of the occupation of excited state exhibits a power law in time since the off-diagonal elements are suppressed. At finite temperature, thermal excitation process facilitates transitions from the ground to the excited state, resulting in monotonic increasing of its occupation as a function of temperatures.

The remaining chapters of the thesis are devoted to the discussion of many-body localization. In chapter 5, we have investigated the response of a MBL Hamiltonian under a local quench, in terms of inverse participation ratio, level spacing statistics, and in particular the single spin measurements. There exist a clear many-body mobility edge and localization length that appear to be measurable for certain experimental procedure; it is our desire that the single spin measurements can be performed using suitable spin systems. In chapter 6, we continue to discuss the dynamical aspects of an MBL system. Here we apply an AC drive to the system and apply the Floquet theory to present the result of quantum fidelity given by the evolution operator with or without the drive. Finally and perhaps most importantly,

we pointed out that for driven systems, the many-body localization transition can be well addressed when thermalization is absent correspondingly from the thermodynamic point of view.

Bibliography

- [1] R. P. Feynman, "Simulating physics with computers," *International Journal of Theoretical Physics*, vol. 21, pp. 467–488, May 1982.
- [2] D. Deutsch, "Quantum Theory, the Church-Turing Principle and the Universal Quantum Computer," *Proceedings of the Royal Society of London A: Mathematical, Physical and Engineering Sciences*, vol. 400, pp. 97–117, July 1985.
- [3] P. W. Shor, "Polynomial-Time Algorithms for Prime Factorization and Discrete Logarithms on a Quantum Computer," *SIAM J. Comput.*, vol. 26, pp. 1484–1509, Oct 1997.
- [4] L. K. Grover, "A Fast Quantum Mechanical Algorithm for Database Search," in STOC '96 Proceedings of the Twenty-eighth Annual ACM Symposium on Theory of Computing, pp. 212–219, ACM, May 1996.
- [5] E. Farhi, J. Goldstone, S. Gutmann, and M. Sipser, "Quantum Computation by Adiabatic Evolution," arXiv:quant-ph/0001106, Jan 2000.
- [6] E. Farhi, J. Goldstone, S. Gutmann, J. Lapan, a. Lundgren, and D. Preda, "A quantum adiabatic evolution algorithm applied to random instances of an NP-complete problem," *Science*, vol. 292, no. 5516, pp. 472–475, Apr 2001.
- [7] E. Knill, R. Laflamme, and G. J. Milburn, "A scheme for efficient quantum computation with linear optics," *Nature*, vol. 409, no. 6816, pp. 46–52, Jan 2001.
- [8] J. I. Cirac and P. Zoller, "Quantum computations with cold trapped ions," *Phys. Rev. Lett.*, vol. 74, pp. 4091–4094, May 1995.
- [9] D. Jaksch, J. I. Cirac, P. Zoller, S. L. Rolston, R. Côté, and M. D. Lukin, "Fast quantum gates for neutral atoms," *Phys. Rev. Lett.*, vol. 85, pp. 2208–2211, Sep 2000.
- [10] B. E. Kane, "A silicon-based nuclear spin quantum computer," *Nature*, vol. 393, pp. 133–137, May 1998.

- [11] D. Loss and D. P. DiVincenzo, "Quantum computation with quantum dots," *Phys. Rev. A*, vol. 57, pp. 120–126, Jan 1998.
- [12] J. M. Martinis, S. Nam, J. Aumentado, and C. Urbina, "Rabi oscillations in a large josephson-junction qubit," *Phys. Rev. Lett.*, vol. 89, p. 117901, Aug 2002.
- [13] J. Koch, T. M. Yu, J. Gambetta, A. A. Houck, D. I. Schuster, J. Majer, A. Blais, M. H. Devoret, S. M. Girvin, and R. J. Schoelkopf, "Charge-insensitive qubit design derived from the Cooper pair box," *Phys. Rev. A*, vol. 76, p. 042319, Oct 2007.
- [14] V. E. Manucharyan, J. Koch, L. I. Glazman, and M. H. Devoret, "Fluxonium: Single Cooper-Pair Circuit Free of Charge Offsets," *Science*, vol. 326, pp. 113–116, Oct 2009.
- [15] D. Vion, A. Aassime, A. Cottet, P. Joyez, H. Pothier, C. Urbina, D. Esteve, and M. H. Devoret, "Manipulating the quantum state of an electrical circuit," *Science*, vol. 296, pp. 886–889, May 2002.
- [16] R. Barends, J. Kelly, A. Megrant, D. Sank, E. Jeffrey, Y. Chen, Y. Yin, B. Chiaro, J. Mutus, C. Neill, P. O'Malley, P. Roushan, J. Wenner, T. C. White, A. N. Cleland, and J. M. Martinis, "Coherent Josephson qubit suitable for scalable quantum integrated circuits," *Phys. Rev. Lett.*, vol. 111, p. 080502, Aug 2013.
- [17] A. Das and B. K. Chakrabarti, "Colloquium: Quantum annealing and analog quantum computation," Rev. Mod. Phys., vol. 80, pp. 1061–1081, Sep 2008.
- [18] A. J. Leggett, S. Chakravarty, A. T. Dorsey, M. P. A. Fisher, A. Garg, and W. Zwerger, "Dynamics of the dissipative two-state system," Rev. Mod. Phys., vol. 59, pp. 1–85, Jan 1987.
- [19] C. Xu, A. Poudel, and M. G. Vavilov, "Nonadiabatic dynamics of a slowly driven dissipative two-level system," *Phys. Rev. A*, vol. 89, p. 052102, May 2014.
- [20] L. C. G. Govia, E. J. Pritchett, C. Xu, B. L. T. Plourde, M. G. Vavilov, F. K. Wilhelm, and R. McDermott, "High-fidelity qubit measurement with a microwave-photon counter," *Phys. Rev. A*, vol. 90, p. 062307, Dec 2014.
- [21] C. Xu and M. G. Vavilov, "Quantum photovoltaic effect in double quantum dots," *Physical Review B*, vol. 87, p. 035429, Jan 2013.
- [22] C. Xu and M. G. Vavilov, "Full counting statistics of photons emitted by a double quantum dot," *Phys. Rev. B*, vol. 88, p. 195307, Nov 2013.

- [23] W. G. van der Wiel, S. De Franceschi, J. M. Elzerman, T. Fujisawa, S. Tarucha, and L. P. Kouwenhoven, "Electron transport through double quantum dots," *Reviews of Modern Physics*, vol. 75, pp. 1–22, Dec 2002.
- [24] A. Wallraff, D. I. Schuster, A. Blais, L. Frunzio, R.-S. Huang, J. Majer, S. Kumar, S. M. Girvin, and R. J. Schoelkopf, "Strong coupling of a single photon to a superconducting qubit using circuit quantum electrodynamics.," *Nature*, vol. 431, pp. 162–7, Sep 2004.
- [25] A. Blais, R.-S. Huang, A. Wallraff, S. M. Girvin, and R. J. Schoelkopf, "Cavity quantum electrodynamics for superconducting electrical circuits: An architecture for quantum computation," *Physical Review A*, vol. 69, p. 062320, June 2004.
- [26] J. Q. You and F. Nori, "Atomic physics and quantum optics using superconducting circuits," *Nature*, vol. 474, pp. 589–97, June 2011.
- [27] T. Frey, P. J. Leek, M. Beck, A. Blais, T. Ihn, K. Ensslin, and A. Wallraff, "Dipole coupling of a double quantum dot to a microwave resonator," *Phys. Rev. Lett.*, vol. 108, p. 046807, Jan 2012.
- [28] M. R. Delbecq, V. Schmitt, F. D. Parmentier, N. Roch, J. J. Viennot, G. Fève, B. Huard, C. Mora, A. Cottet, and T. Kontos, "Coupling a quantum dot, fermionic leads, and a microwave cavity on a chip," *Phys. Rev. Lett.*, vol. 107, p. 256804, Dec 2011.
- [29] H. Toida, T. Nakajima, and S. Komiyama, "Vacuum Rabi Splitting in a Semiconductor Circuit QED System," *Phys. Rev. Lett.*, vol. 110, p. 066802, Feb 2013.
- [30] S. J. Chorley, J. Wabnig, Z. V. Penfold-Fitch, K. D. Petersson, J. Frake, C. G. Smith, and M. R. Buitelaar, "Measuring the complex admittance of a carbon nanotube double quantum dot," *Phys. Rev. Lett.*, vol. 108, p. 036802, Jan 2012.
- [31] K. D. Petersson, L. W. McFaul, M. D. Schroer, M. Jung, J. M. Taylor, A. A. Houck, and J. R. Petta, "Circuit quantum electrodynamics with a spin qubit," *Nature*, vol. 490, pp. 380–383, Oct 2012.
- [32] O. Astafiev, K. Inomata, A. O. Niskanen, T. Yamamoto, Y. A. Pashkin, Y. Nakamura, and J. S. Tsai, "Single artificial-atom lasing," *Nature*, vol. 449, pp. 588–90, Oct 2007.
- [33] L. Childress, A. S. Sørensen, and M. D. Lukin, "Mesoscopic cavity quantum electrodynamics with quantum dots," *Physical Review A*, vol. 69, p. 042302, Apr 2004.

- [34] R. Sánchez, G. Platero, and T. Brandes, "Resonance Fluorescence in Transport through Quantum Dots: Noise Properties," *Physical Review Letters*, vol. 98, p. 146805, Apr 2007.
- [35] P.-Q. Jin, M. Marthaler, J. H. Cole, A. Shnirman, and G. Schön, "Lasing and transport in a quantum-dot resonator circuit," *Physical Review B*, vol. 84, p. 035322, July 2011.
- [36] M. G. Vavilov and A. D. Stone, "Photovoltaic Current Response of Mesoscopic Conductors to Quantized Cavity Modes," *Physical Review Letters*, vol. 97, p. 216801, Nov 2006.
- [37] T. H. Stoof and Y. V. Nazarov, "Time-dependent resonant tunneling via two discrete states," *Physical Review B*, vol. 53, pp. 1050–1053, Jan 1996.
- [38] M. H. Pedersen and M. Büttiker, "Scattering theory of photon-assisted electron transport," *Physical Review B*, vol. 58, p. 12993, Nov 1998.
- [39] S.-H. Ouyang, C.-H. Lam, and J. Q. You, "Backaction of a charge detector on a double quantum dot," *Physical Review B*, vol. 81, p. 075301, Feb 2010.
- [40] A. Silva and V. E. Kravtsov, "Multiphoton processes in driven mesoscopic systems," *Physical Review B*, vol. 76, p. 165303, Oct 2007.
- [41] P. W. Brouwer, "Rectification of displacement currents in an adiabatic electron pump," *Physical Review B*, vol. 63, p. 121303, Mar 2001.
- [42] L. DiCarlo, C. M. Marcus, and J. S. Harris, "Photocurrent, Rectification, and Magnetic Field Symmetry of Induced Current through Quantum Dots," *Physical Review Letters*, vol. 91, p. 246804, Dec 2003.
- [43] M. G. Vavilov, L. DiCarlo, and C. M. Marcus, "Photovoltaic and rectification currents in quantum dots," *Phys. Rev. B*, vol. 71, p. 241309, Jun 2005.
- [44] S. M. Tan, "A computational toolbox for quantum and atomic optics," *Journal of Optics B: Quantum and Semiclassical Optics*, vol. 1, pp. 424–432, Aug 1999.
- [45] J. Johansson, P. Nation, and F. Nori, "QuTiP: An open-source Python framework for the dynamics of open quantum systems," *Computer Physics Communications*, vol. 183, pp. 1760–1772, Aug 2012.

- [46] R. Blatt, J. I. Cirac, and P. Zoller, "Trapping states of motion with cold ions," *Physical Review A*, vol. 52, pp. 518–524, July 1995.
- [47] M. Marthaler and M. Dykman, "Switching via quantum activation: A parametrically modulated oscillator," *Physical Review A*, vol. 73, p. 042108, Apr 2006.
- [48] M. Dykman, Fluctuating Nonlinear Oscillators. Oxford University Press, July 2012.
- [49] R. J. Glauber, "Coherent and Incoherent States of the Radiation Field," *Physical Review*, vol. 131, pp. 2766–2788, Sep 1963.
- [50] C. W. J. Beenakker and H. Schomerus, "Counting Statistics of Photons Produced by Electronic Shot Noise," *Physical Review Letters*, vol. 86, pp. 700–703, Jan 2001.
- [51] C. W. J. Beenakker and H. Schomerus, "Antibunched Photons Emitted by a Quantum Point Contact out of Equilibrium," *Physical Review Letters*, vol. 93, p. 096801, Aug 2004.
- [52] A. V. Lebedev, G. B. Lesovik, and G. Blatter, "Statistics of radiation emitted from a quantum point contact," *Physical Review B*, vol. 81, p. 155421, Apr 2010.
- [53] D. I. Schuster, A. A. Houck, J. A. Schreier, A. Wallraff, J. M. Gambetta, A. Blais, L. Frunzio, J. Majer, B. Johnson, M. H. Devoret, S. M. Girvin, and R. J. Schoelkopf, "Resolving photon number states in a superconducting circuit," *Nature*, vol. 445, pp. 515–518, Feb 2007.
- [54] M. Hofheinz, E. M. Weig, M. Ansmann, R. C. Bialczak, E. Lucero, M. Neeley, A. D. O'Connell, H. Wang, J. M. Martinis, and A. N. Cleland, "Generation of Fock states in a superconducting quantum circuit," *Nature*, vol. 454, pp. 310–314, July 2008.
- [55] J. Gabelli, L.-H. Reydellet, G. Fève, J.-M. Berroir, B. Plaçais, P. Roche, and D. C. Glattli, "Hanbury Brown\char21{}Twiss Correlations to Probe the Population Statistics of GHz Photons Emitted by Conductors," *Physical Review Letters*, vol. 93, p. 056801, July 2004.
- [56] E. Zakka-Bajjani, J. Ségala, F. Portier, P. Roche, D. C. Glattli, A. Cavanna, and Y. Jin, "Experimental Test of the High-Frequency Quantum Shot Noise Theory in a Quantum Point Contact," *Physical Review Letters*, vol. 99, p. 236803, Dec 2007.
- [57] Y.-F. Chen, D. Hover, S. Sendelbach, L. Maurer, S. T. Merkel, E. J. Pritchett, F. K. Wilhelm, and R. McDermott, "Microwave Photon Counter Based on Josephson Junctions," *Physical Review Letters*, vol. 107, p. 217401, Nov 2011.

- [58] A. Poudel, R. McDermott, and M. G. Vavilov, "Quantum efficiency of a microwave photon detector based on a current-biased Josephson junction," *Physical Review B*, vol. 86, p. 174506, Nov 2012.
- [59] H. J. Carmichael, Statistical Methods in Quantum Optics 2: Non-Classical Fields. Springer, Nov 2008.
- [60] T. Jeltes, J. M. McNamara, W. Hogervorst, W. Vassen, V. Krachmalnicoff, M. Schellekens, A. Perrin, H. Chang, D. Boiron, A. Aspect, and C. I. Westbrook, "Comparison of the Hanbury Brown–Twiss effect for bosons and fermions," *Nature*, vol. 445, pp. 402–405, Jan 2007.
- [61] K. Ikushima and S. Komiyama, "Photon generation by injection of electrons via quantum Hall edge channels," *Physical Review B*, vol. 84, p. 155313, Oct 2011.
- [62] J. Jin, M. Marthaler, P.-Q. Jin, D. Golubev, and G. Schön, "Noise spectrum of a quantum dot-resonator lasing circuit," New Journal of Physics, vol. 15, p. 025044, Feb 2013.
- [63] A. A. Clerk, M. H. Devoret, S. M. Girvin, F. Marquardt, and R. J. Schoelkopf, "Introduction to quantum noise, measurement, and amplification," *Reviews of Modern Physics*, vol. 82, pp. 1155–1208, Apr 2010.
- [64] C. Gardiner and P. Zoller, Quantum Noise. Springer, Oct 2004.
- [65] X. T. Zou and L. Mandel, "Photon-antibunching and sub-Poissonian photon statistics," *Physical Review A*, vol. 41, pp. 475–476, Jan 1990.
- [66] P. L. Kelley and W. H. Kleiner, "Theory of Electromagnetic Field Measurement and Photoelectron Counting," *Physical Review*, vol. 136, pp. A316–A334, Oct 1964.
- [67] C. Flindt, T. Novotný, and A.-P. Jauho, "Current noise in a vibrating quantum dot array," *Physical Review B*, vol. 70, p. 205334, Nov 2004.
- [68] C. Flindt, T. Novotný, and A.-P. Jauho, "Full counting statistics of nanoelectromechanical systems," *EPL (Europhysics Letters)*, vol. 69, p. 475, Feb 2005.
- [69] Y. M. Blanter and M. Büttiker, "Shot noise in mesoscopic conductors," Physics Reports, vol. 336, pp. 1–166, Sep 2000.
- [70] L. S. Levitov, "The statistical theory of mesoscopic noise," in *Quantum Noise in Mesoscopic Physics* (Y. Nazarov, ed.), Kluwer, Apr 2003.

- [71] J. Jin, M. Marthaler, P.-Q. Jin, D. Golubev, and G. Schn, "Noise spectrum of a quantum dot-resonator lasing circuit," *New Journal of Physics*, vol. 15, no. 2, p. 025044, 2013.
- [72] C. Emary, C. Pöltl, A. Carmele, J. Kabuss, A. Knorr, and T. Brandes, "Bunching and antibunching in electronic transport," *Physical Review B*, vol. 85, p. 165417, Apr 2012.
- [73] D. A. Bagrets and Y. V. Nazarov, "Full counting statistics of charge transfer in Coulomb blockade systems," *Physical Review B*, vol. 67, p. 085316, Feb 2003.
- [74] T. Brandes, "Waiting times and noise in single particle transport," *Annalen der Physik*, vol. 17, pp. 477–496, July 2008.
- [75] D. Marcos, C. Emary, T. Brandes, and R. Aguado, "Finite-frequency counting statistics of electron transport: Markovian theory," *New Journal of Physics*, vol. 12, p. 123009, Dec 2010.
- [76] S. Gustavsson, R. Leturcq, B. Simovič, R. Schleser, T. Ihn, P. Studerus, K. Ensslin, D. C. Driscoll, and A. C. Gossard, "Counting Statistics of Single Electron Transport in a Quantum Dot," *Physical Review Letters*, vol. 96, p. 076605, Feb 2006.
- [77] B. Elattari and S. A. Gurvitz, "Shot noise in coupled dots and the "fractional charges"," *Physics Letters A*, vol. 292, pp. 289–294, Jan 2002.
- [78] R. Sánchez, G. Platero, and T. Brandes, "Resonance fluorescence in driven quantum dots: Electron and photon correlations," *Physical Review B*, vol. 78, p. 125308, Sep 2008.
- [79] L. C. G. Govia, E. J. Pritchett, S. T. Merkel, D. Pineau, and F. K. Wilhelm, "Theory of josephson photomultipliers: Optimal working conditions and back action," *Phys. Rev. A*, vol. 86, p. 032311, Sep 2012.
- [80] H. Jirari and W. Pötz, "Optimal coherent control of dissipative N-level systems," *Physical Review A*, vol. 72, p. 013409, July 2005.
- [81] F. Motzoi, J. M. Gambetta, P. Rebentrost, and F. Wilhelm, "Simple Pulses for Elimination of Leakage in Weakly Nonlinear Qubits," *Physical Review Letters*, vol. 103, p. 110501, Sep 2009.
- [82] A. Poudel and M. G. Vavilov, "Effect of an Ohmic environment on an optimally controlled flux-biased phase qubit," *Physical Review B*, vol. 82, p. 144528, Oct 2010.

- [83] M. G. Bason, M. Viteau, N. Malossi, P. Huillery, E. Arimondo, D. Ciampini, R. Fazio, V. Giovannetti, R. Mannella, and O. Morsch, "High-fidelity quantum driving," *Nature Physics*, vol. 8, pp. 147–152, Dec 2011.
- [84] M. Thorwart and P. Hänggi, "Decoherence and dissipation during a quantum xor gate operation," *Phys. Rev. A*, vol. 65, p. 012309, Dec 2001.
- [85] A. M. Childs, E. Farhi, and J. Preskill, "Robustness of adiabatic quantum computation," *Physical Review A*, vol. 65, p. 012322, Dec 2001.
- [86] J. E. Avron, M. Fraas, G. M. Graf, and P. Grech, "Landau-Zener Tunneling for Dephasing Lindblad Evolutions," *Communications in Mathematical Physics*, vol. 305, pp. 633–639, May 2011.
- [87] J. E. Avron, M. Fraas, G. M. Graf, and O. Kenneth, "Quantum response of dephasing open systems," *New Journal of Physics*, vol. 13, p. 053042, May 2011.
- [88] G. Lindblad, "On the generators of quantum dynamical semigroups," Communications in Mathematical Physics, vol. 48, pp. 119–130, June 1976.
- [89] G. Lindblad, "Entropy, information and quantum measurements," Communications in Mathematical Physics, vol. 33, pp. 305–322, Dec 1973.
- [90] F. Bloch, "Generalized Theory of Relaxation," Physical Review, vol. 105, pp. 1206–1222, Feb 1957.
- [91] A. G. Redfield, "On the Theory of Relaxation Processes," *IBM Journal of Research and Development*, vol. 1, pp. 19–31, Jan 1957.
- [92] H. Schoeller and G. Schön, "Mesoscopic quantum transport: Resonant tunneling in the presence of a strong Coulomb interaction," *Physical Review B*, vol. 50, pp. 18436–18452, Dec 1994.
- [93] Y. Makhlin, G. Schön, and A. Shnirman, "Quantum-state engineering with Josephson-junction devices," *Reviews of Modern Physics*, vol. 73, pp. 357–400, May 2001.
- [94] Y. Makhlin, G. Schön, and A. Shnirman, "Dissipative effects in Josephson qubits," *Chemical Physics*, vol. 296, pp. 315–324, Jan 2004.
- [95] P. Ao and J. Rammer, "Influence of dissipation on the Landau-Zener transition," *Physical Review Letters*, vol. 62, pp. 3004–3007, June 1989.

- [96] P. Ao and J. Rammer, "Quantum dynamics of a two-state system in a dissipative environment," *Physical Review B*, vol. 43, pp. 5397–5418, Mar 1991.
- [97] M. Grifoni and P. Hänggi, "Driven quantum tunneling," Physics Reports, vol. 304, pp. 229–354, Oct 1998.
- [98] N. V. Vitanov, "Transition times in the Landau-Zener model," *Physical Review A*, vol. 59, pp. 988–994, Feb 1999.
- [99] S. N. Shevchenko, A. S. Kiyko, A. N. Omelyanchouk, and W. Krech, "Dynamic behaviour of Josephson-junction qubits: crossover between Rabi oscillations and Landau-Zener transitions," *Low Temperature Physics*, vol. 31, p. 569, Dec 2004.
- [100] R. S. Whitney, Y. Makhlin, A. Shnirman, and Y. Gefen, "Geometric Nature of the Environment-Induced Berry Phase and Geometric Dephasing," *Physical Review Let*ters, vol. 94, p. 070407, Feb 2005.
- [101] V. L. Pokrovsky and D. Sun, "Fast quantum noise in the Landau-Zener transition," Physical Review B, vol. 76, p. 024310, July 2007.
- [102] J. P. Pekola, V. Brosco, M. Möttönen, P. Solinas, and a. Shnirman, "Decoherence in Adiabatic Quantum Evolution: Application to Cooper Pair Pumping," *Physical Review Letters*, vol. 105, p. 030401, July 2010.
- [103] A. Saha, Y. Gefen, I. Burmistrov, A. Shnirman, and A. Altland, "A quantum dot close to Stoner instability: The role of the Berry phase," *Annals of Physics*, vol. 327, pp. 2543–2559, Oct 2012.
- [104] V. Gritsev and A. Polkovnikov, "Dynamical quantum Hall effect in the parameter space," Proceedings of the National Academy of Sciences of the United States of America, vol. 109, pp. 6457–62, Apr 2012.
- [105] P. J. Leek, J. M. Fink, a. Blais, R. Bianchetti, M. Göppl, J. M. Gambetta, D. I. Schuster, L. Frunzio, R. J. Schoelkopf, and a. Wallraff, "Observation of Berry's phase in a solid-state qubit," *Science*, vol. 318, pp. 1889–92, Dec 2007.
- [106] R. S. Whitney, Y. Makhlin, A. Shnirman, and Y. Gefen, "Berry phase with environment: classical versus quantum," *Theory of Quantum Transport in Metallic and Hybrid Nanostructures NATO Science Series*, vol. 230, p. 9, Jan 2006.
- [107] G. De Chiara, A. Lozinski, and G. M. Palma, "Berry phase in open quantum systems: a quantum Langevin equation approach," *The European Physical Journal D*, vol. 41, pp. 179–183, Aug 2006.

- [108] L. D. Landau, "A theory of energy transfer on collisions," Physikalische Zeitschrift der Sowjetunion, vol. 1, p. 88, 1932.
- [109] C. Zener, "Non-Adiabatic Crossing of Energy Levels," *Proceedings of the Royal Society A: Mathematical, Physical and Engineering Sciences*, vol. 137, pp. 696–702, Sep 1932.
- [110] E. C. G. Stückelberg, "Theorie der unelastischen Stösse zwischen Atomen," *Helvetica Physica Acta*, vol. 5, p. 369, 1933.
- [111] E. Majorana, "Atomi orientati in campo magnetico variabile," *Il Nuovo Cimento*, vol. 9, pp. 43–50, Feb 1932.
- [112] V. L. Pokrovsky and N. A. Sinitsyn, "Fast noise in the Landau-Zener theory," *Physical Review B*, vol. 67, p. 144303, Apr 2003.
- [113] M. B. Kenmoe, H. N. Phien, M. N. Kiselev, and L. C. Fai, "Effects of colored noise on Landau-Zener transitions: Two- and three-level systems," *Physical Review B*, vol. 87, p. 224301, June 2013.
- [114] M. Wubs, K. Saito, S. Kohler, P. Hänggi, and Y. Kayanuma, "Gauging a Quantum Heat Bath with Dissipative Landau-Zener Transitions," *Physical Review Letters*, vol. 97, p. 200404, Nov 2006.
- [115] M. Wubs, K. Saito, S. Kohler, Y. Kayanuma, and P. Hnggi, "Landau-Zener transitions in qubits controlled by electromagnetic fields," *New Journal of Physics*, vol. 7, p. 218, Oct 2005.
- [116] K. Saito, M. Wubs, S. Kohler, Y. Kayanuma, and P. Hänggi, "Dissipative Landau-Zener transitions of a qubit: Bath-specific and universal behavior," *Physical Review B*, vol. 75, p. 214308, June 2007.
- [117] P. Nalbach and M. Thorwart, "Landau-Zener transitions in a dissipative environment: Numerically exact results," *Phys. Rev. Lett.*, vol. 103, p. 220401, Nov 2009.
- [118] P. Nalbach and M. Thorwart, "Competition between relaxation and external driving in the dissipative Landau-Zener problem," *Chemical Physics*, vol. 375, pp. 234 242, Oct 2010.
- [119] P. P. Orth, A. Imambekov, and K. Le Hur, "Universality in dissipative Landau-Zener transitions," *Physical Review A*, vol. 82, p. 032118, Sep 2010.

- [120] R. S. Whitney, M. Clusel, and T. Ziman, "Temperature Can Enhance Coherent Oscillations at a Landau-Zener Transition," *Physical Review Letters*, vol. 107, p. 210402, Nov 2011.
- [121] Z. Sun, J. Ma, X. Wang, and F. Nori, "Photon-assisted Landau-Zener transition: Role of coherent superposition states," *Physical Review A*, vol. 86, p. 012107, July 2012.
- [122] E. Shimshoni and A. Stern, "Dephasing of interference in Landau-Zener transitions," *Physical Review B*, vol. 47, pp. 9523–9536, Apr 1993.
- [123] M. S. Rudner, A. V. Shytov, L. S. Levitov, D. M. Berns, W. D. Oliver, S. O. Valenzuela, and T. P. Orlando, "Quantum Phase Tomography of a Strongly Driven Qubit," *Physical Review Letters*, vol. 101, p. 190502, Nov 2008.
- [124] S. Ashhab, J. R. Johansson, A. M. Zagoskin, and F. Nori, "Two-level systems driven by large-amplitude fields," *Physical Review A*, vol. 75, p. 063414, June 2007.
- [125] S. Shevchenko, S. Ashhab, and F. Nori, "Landau-Zener-Stückelberg interferometry," *Physics Reports*, vol. 492, pp. 1–30, July 2010.
- [126] S. Gasparinetti, P. Solinas, and J. P. Pekola, "Geometric Landau-Zener Interferometry," Physical Review Letters, vol. 107, p. 207002, Nov 2011.
- [127] S. Ganeshan, E. Barnes, and S. Das Sarma, "Exact classification of Landau-Majorana-Stückelberg-Zener resonances by Floquet determinants," *Physical Review Letters*, vol. 111, p. 130405, Sep 2013.
- [128] F. Forster, G. Petersen, S. Manus, P. Hänggi, D. Schuh, W. Wegscheider, S. Kohler, and S. Ludwig, "Characterization of qubit dephasing by Landau-Zener-Stückelberg-Majorana interferometry," Phys. Rev. Lett., vol. 112, p. 116803, Mar 2014.
- [129] P. Nalbach, J. Knörzer, and S. Ludwig, "Nonequilibrium Landau-Zener-Stückelberg spectroscopy in a double quantum dot," *Phys. Rev. B*, vol. 87, p. 165425, Apr 2013.
- [130] X. Tan, D.-W. Zhang, Z. Zhang, Y. Yu, S. Han, and S.-L. Zhu, "Demonstration of geometric Landau-Zener interferometry in a superconducting Qubit," *Physical Review Letters*, vol. 112, p. 027001, Jan 2014.
- [131] Y. Kayanuma, "Nonadiabatic transitions in level crossing with energy fluctuation. I. analytical investigations," *Journal of the Physics Society Japan*, vol. 53, pp. 108–117, Jan 1984.

- [132] K. Saito and Y. Kayanuma, "Nonadiabatic transition probabilities in the presence of strong dissipation at an avoided-level crossing point," *Physical Review A*, vol. 65, p. 033407, Feb 2002.
- [133] J. I. Vestgården, J. Bergli, and Y. M. Galperin, "Nonlinearly driven Landau-Zener transition in a qubit with telegraph noise," *Physical Review B*, vol. 77, p. 014514, Jan 2008.
- [134] J. R. Johansson, P. D. Nation, and F. Nori, "QuTiP 2: A Python framework for the dynamics of open quantum systems," *Computer Physics Communications*, vol. 184, pp. 1234–1240, Apr 2013.
- [135] R. S. Whitney, "Staying positive: going beyond Lindblad with perturbative master equations," *Journal of Physics A: Mathematical and Theoretical*, vol. 41, p. 175304, May 2008.
- [136] S. N. Shevchenko, G. Oelsner, Y. S. Greenberg, P. Macha, D. S. Karpov, M. Grajcar, U. Hübner, A. N. Omelyanchouk, and E. Il'ichev, "Amplification and attenuation of a probe signal by doubly dressed states," *Phys. Rev. B*, vol. 89, p. 184504, May 2014.
- [137] L. DAlessio and A. Polkovnikov, "Emergent newtonian dynamics and the geometric origin of mass," *Annals of Physics*, vol. 345, no. 0, pp. 141 165, June 2014.
- [138] D. Xiao, M.-C. Chang, and Q. Niu, "Berry phase effects on electronic properties," Reviews of Modern Physics, vol. 82, pp. 1959–2007, July 2010.
- [139] S. Berger, M. Pechal, A. A. Abdumalikov, C. Eichler, L. Steffen, A. Fedorov, A. Wall-raff, and S. Filipp, "Exploring the effect of noise on the Berry phase," *Physical Review A*, vol. 87, p. 060303, June 2013.
- [140] P. W. Anderson, "Absence of diffusion in certain random lattices," *Phys. Rev.*, vol. 109, pp. 1492–1505, Mar 1958.
- [141] E. Abrahams, P. W. Anderson, D. C. Licciardello, and T. V. Ramakrishnan, "Scaling theory of localization: Absence of quantum diffusion in two dimensions," *Phys. Rev. Lett.*, vol. 42, pp. 673–676, Mar 1979.
- [142] B. L. Altshuler, D. Khmel'nitzkii, A. I. Larkin, and P. A. Lee, "Magnetoresistance and Hall effect in a disordered two-dimensional electron gas," *Phys. Rev. B*, vol. 22, pp. 5142–5153, Dec 1980.

- [143] B. L. Altshuler, A. G. Aronov, and D. E. Khmelnitsky, "Effects of electron-electron collisions with small energy transfers on quantum localisation," *Journal of Physics C: Solid State Physics*, vol. 15, p. 7367, Dec 1982.
- [144] A. L. Efros and B. I. Shklovskii, "Coulomb gap and low temperature conductivity of disordered systems," *Journal of Physics C: Solid State Physics*, vol. 8, p. L49, Feb 1975.
- [145] D. M. Basko, I. L. Aleiner, and B. L. Altshuler, "Metal-insulator transition in a weakly interacting many-electron system with localized single-particle states," *Annals* of *Physics*, vol. 321, pp. 1126–1205, May 2006.
- [146] I. V. Gornyi, A. D. Mirlin, and D. G. Polyakov, "Interacting electrons in disordered wires: Anderson localization and low-t transport," *Phys. Rev. Lett.*, vol. 95, p. 206603, Nov 2005.
- [147] V. Oganesyan and D. A. Huse, "Localization of interacting fermions at high temperature," *Phys. Rev. B*, vol. 75, p. 155111, Apr 2007.
- [148] M. Schreiber, S. S. Hodgeman, P. Bordia, H. P. Lüschen, M. H. Fischer, E. Altman, U. Schneider, and I. Bloch, "Observation of many-body localization of interacting fermions in a quasi-random optical lattice," arXiv:1501.05661, Jan 2015.
- [149] C. Senko, J. Smith, P. Richerme, A. Lee, W. C. Campbell, and C. Monroe, "Coherent imaging spectroscopy of a quantum many-body spin system," *Science*, vol. 345, pp. 430–433, July 2014.
- [150] R. Islam, C. Senko, W. C. Campbell, S. Korenblit, J. Smith, A. Lee, E. E. Edwards, C.-C. J. Wang, J. K. Freericks, and C. Monroe, "Emergence and frustration of magnetism with variable-range interactions in a quantum simulator," *Science*, vol. 340, pp. 583–587, May 2013.
- [151] R. Barends, L. Lamata, J. Kelly, L. Garcia-Alvarez, A. G. Fowler, A. Megrant, E. Jeffrey, T. C. White, D. Sank, J. Y. Mutus, B. Campbell, Y. Chen, Z. Chen, B. Chiaro, A. Dunsworth, I. C. Hoi, C. Neill, P. J. J. O'Malley, C. Quintana, P. Roushan, A. Vainsencher, J. Wenner, E. Solano, and J. M. Martinis, "Digital quantum simulation of fermionic models with a superconducting circuit," Nat. Commun., vol. 6, July 2015.
- [152] M. Serbyn, Z. Papić, and D. A. Abanin, "Local conservation laws and the structure of the many-body localized states," *Phys. Rev. Lett.*, vol. 111, p. 127201, Sep 2013.

- [153] A. Chandran, I. H. Kim, G. Vidal, and D. A. Abanin, "Constructing local integrals of motion in the many-body localized phase," *Phys. Rev. B*, vol. 91, p. 085425, Feb 2015.
- [154] V. Ros, M. Mueller, and A. Scardicchio, "Integrals of motion in the many-body localized phase," *Nuclear Physics B*, vol. 891, no. 0, pp. 420 465, 2015.
- [155] I. H. Kim, A. Chandran, and D. A. Abanin, "Local integrals of motion and the logarithmic lightcone in many-body localized systems," arXiv:1412.3073, Dec 2014.
- [156] J. H. Bardarson, F. Pollmann, and J. E. Moore, "Unbounded Growth of Entanglement in Models of Many-Body Localization," *Phys. Rev. Lett.*, vol. 109, p. 017202, July 2012.
- [157] M. Serbyn, Z. Papić, and D. a. Abanin, "Universal slow growth of entanglement in interacting strongly disordered systems," *Phys. Rev. Lett.*, vol. 110, p. 260601, June 2013.
- [158] A. Nanduri, H. Kim, and D. A. Huse, "Entanglement spreading in a many-body localized system," *Phys. Rev. B*, vol. 90, p. 064201, Aug 2014.
- [159] M. Serbyn, Z. Papić, and D. A. Abanin, "Quantum quenches in the many-body localized phase," Phys. Rev. B, vol. 90, p. 174302, Nov 2014.
- [160] R. Vosk and E. Altman, "Dynamical quantum phase transitions in random spin chains," *Phys. Rev. Lett.*, vol. 112, p. 217204, May 2014.
- [161] J. A. Kjäll, J. H. Bardarson, and F. Pollmann, "Many-body localization in a disordered quantum ising chain," *Phys. Rev. Lett.*, vol. 113, p. 107204, Sep 2014.
- [162] D. J. Luitz, N. Laflorencie, and F. Alet, "Many-body localization edge in the random-field heisenberg chain," Phys. Rev. B, vol. 91, p. 081103, Feb 2015.
- [163] I. Mondragon-Shem, A. Pal, T. L. Hughes, and C. R. Laumann, "Many-body mobility edge due to symmetry-constrained dynamics and strong interactions," arXiv:1501.03824, Jan 2015.
- [164] A. Pal and D. A. Huse, "Many-body localization phase transition," Phys. Rev. B, vol. 82, p. 174411, Nov 2010.
- [165] R. Vosk, D. A. Huse, and E. Altman, "Theory of the many-body localization transition in one dimensional systems," *ArXiv e-prints*, Dec 2014.

- [166] D. A. Huse, R. Nandkishore, and V. Oganesyan, "Phenomenology of fully many-body-localized systems," Phys. Rev. B, vol. 90, p. 174202, Nov 2014.
- [167] M. Rigol, V. Dunjko, and M. Olshanii, "Thermalization and its mechanism for generic isolated quantum systems," *Nature*, vol. 452, pp. 854–858, Apr 2008.
- [168] A. D. Luca and A. Scardicchio, "Ergodicity breaking in a model showing many-body localization," *Europhysics Letters*, vol. 101, no. 3, p. 37003, Feb 2013.
- [169] R. Nandkishore and D. A. Huse, "Many-body localization and thermalization in quantum statistical mechanics," Annual Review of Condensed Matter Physics, vol. 6, no. 1, pp. 15–38, Mar 2015.
- [170] R. Vasseur, S. A. Parameswaran, and J. E. Moore, "Quantum revivals and many-body localization," *Phys. Rev. B*, vol. 140202, no. 91, p. 5, Apr 2015.
- [171] L. H. Pedersen, N. M. Møller, and K. Mølmer, "Fidelity of quantum operations," *Phys. Lett. A*, vol. 367, pp. 47–51, July 2007.
- [172] P. Ponte, A. Chandran, Z. Papić, and D. A. Abanin, "Periodically driven ergodic and many-body localized quantum systems," *Annals of Physics*, vol. 353, pp. 196–204, Feb 2015.
- [173] A. Uhlmann, "The "transition probability" in the state space of a *-algebra," Reports Math. Phys., vol. 9, pp. 273–279, Apr 1976.
- [174] A. Uhlmann, "Geometric phases and related structures," Reports on Mathematical Physics, vol. 36, no. 23, pp. 461 481, Dec 1995.